



Power Modulation of Aluminium Reduction Cells – Operational Constraints and Process Limits

Author:

Reek, Till

Publication Date:

2015

DOI:

<https://doi.org/10.26190/unsworks/17334>

License:

<https://creativecommons.org/licenses/by-nc-nd/3.0/au/>

Link to license to see what you are allowed to do with this resource.

Downloaded from <http://hdl.handle.net/1959.4/54217> in <https://unsworks.unsw.edu.au> on 2024-04-28

Power Modulation of Aluminium Reduction Cells – Operational Constraints and Process Limits

Till Carsten Reek

A thesis submitted in fulfillment
of the requirements for the degree of
Doctor of Philosophy

School of Chemical Engineering

Faculty of Engineering

UNSW



The University of New South Wales
Sydney, Australia

February 2015

Abstract

Aluminium reduction cells are operated traditionally with an energy input as constant as possible. This is to reduce the variability of the process and simplify process monitoring and detection of abnormal situations.

Recent advances in control systems have decreased the number and magnitude of process excursions keeping a vast majority of reduction cells within optimum performance.

Reorientation in energy generation towards volatile renewable sources and changes in marketing mechanisms in Germany have led to an elevated and volatile electricity price resulting in an incentive to overcome the concept of constant energy input.

This thesis postulates theoretical aspects and boundaries of both possibility and magnitude of power modulation. With this objective material and thermal balances are built including side reactions and material introduced at ambient temperature and heated to process temperature which is otherwise not affected by the process, but nevertheless inevitable for continued operation.

These theories are compared with results found in experiments simulating aspects of power modulation undertaken on industrial reduction cells as well as during practical operation of a whole smelter with continuous power modulation. Key results of these investigations are:

1. Theoretical amount of extra energy that can be stored in the cell was determined to be 0.7 MWh for TRIMET Hamburg's modified P19 cell.. This amount was experimentally verified.
2. Side ledge shows a distinctly different behaviour if in contact with molten bath or molten metal. Previous considerations always assumed equilibrium when discussing side ledge. Experimental results show that there are significant dynamics influencing the shape of side ledge.

3. Cells show a significant capability of shedding additional heat in less than a day, stabilizing operation shortly after increased energy inputs.
4. Top cell cover contributes up to 50% to physical changes in the cell induced by energy imbalances.
5. For prolonged, severe energy reductions a shifting of work practices, especially anode change, is advisable to avoid superimposing effects reducing available energy in the cell needed for good operation.

Basic approaches for modelling and incorporating effects of power modulation into process control algorithms are derived from experimental results.

Changes in process efficiency found during continuous modulation are evaluated with regards to the economical impact on smelter operation showing that power modulation is a valid approach for reducing production costs. Other scenarios for generating revenue based on flexible smelter operation are highlighted.

To extend the capabilities for power modulation, engineering solutions available today, such as shell heat exchangers and dampers to control off-gas volume, are discussed with respects to their ability to vary and control heat loss from a cell. It is shown that shell heat exchangers are the only applicable system to actively vary heat loss.

The findings of this thesis can be used to optimize future designs and retrofits of cells by taking the variability of heat loss and the limits for energy storage into account to optimize the design to extend the possibilities for power modulation.

Two areas of future work are identified in this thesis. On the one hand, new process control strategies have to be developed if cells are to be operated with

the ability to vary heat loss. These strategies have to incorporate decision points when to increase and decrease heat loss intentionally. Also it has to be defined which continuous measurements to base this decision on and if new continuous measurements are needed.

The second are of interest is the extension of existing FEM models to reflect the dynamics detailed in this thesis to help predict changes in the cell. Existing MHD models could be extended to study the ledge dynamics at various heat inputs to also help optimizing cell relining for ledge stability at variable heat input.

Acknowledgement

“Remember that the most difficult tasks are consummated, not by a single explosive burst of energy or effort, but by the constant daily application of the best you have within you.”

Og Mandino

Such a work is not easily completed, especially if the work is done part time. For that reason there are many people to thank for their help, input and understanding.

First and foremost I'd like to thank Martin Iffert at Trimet Aluminium SE who paved the way for this thesis with regards to the university as well as with regards to the subject. Also many thanks for showing me the wisdom of writing a thesis while commuting between two plants, Martin! My thanks to Jörg Prepeneit for the continuous support during my time working for him at Trimet Hamburg.

Andreas Lützerath, Richard Meier and Helge Friedrich along with all the employees in the reduction department in Hamburg and especially in the process control department for bearing with me during all the experiments and trials necessary for this thesis. As they supported most of the practical work, this thesis would not have been possible without them.

At UNSW I'd like to thank Barry Welch, Maria Skyllas-Kazacos and Jie Bao for the supervision of my work and their continuous input on the content of the thesis. If they wouldn't have pushed for a lot of the additional content this work would have been considerably shorter.

Also at UNSW I'd like to thank Winnie Cheung for helping me around campus and having a good time as well as for the continuous confirmation that actually writing a thesis seems to be an impossible task for everybody.

My thanks to our post graduate coordinator, Ik Ling Lau, for all thankful reminders when I was approaching another deadline and helping with all the administrative issues that are hard to manage if not on-site.

Last but not least I'd like thank my wife Monika. Without her support not only this thesis would have been an even more difficult task than it was already.

Table of Contents

1	Introduction	1
2	Background.....	5
2.1	Overview of the Process	5
2.1.1	Temperature and Electrolyte Composition.....	8
2.1.2	Smelting, Energy Use and Metal Production.	10
2.1.3	Cell Voltage.....	14
2.1.4	Basics of Control.....	18
2.2	Evolution of cell designs	22
2.2.1	Alumina Feeding Mechanisms.....	24
2.2.2	End to End vs. Side by Side	25
2.2.3	Development in Relining Materials and Cathode Grades	27
2.2.4	Typical Modern Cell	30
2.2.5	The P19 cell used at Trimet Hamburg	30
2.3	Global Development of the Primary Aluminium Industry.....	34
2.3.1	Critical Resources of the Process	35
2.3.2	Trends in Cost Structure	43
2.3.3	Environmental Influence	44
2.4	Changing Trends in Energy Generation.....	46
2.4.1	Hydro Power	46
2.4.2	Nuclear, Coal and Oil Power.....	46
2.4.3	Geothermal Power	47
2.4.4	Wind Power.....	47
2.4.5	Solar Power	48

2.4.6	Summary on Renewable Energy Sources	49
2.5	“Energiewende”, Energy Reorientation	50
2.5.1	Change from Demand to Supply Driven Market.....	50
2.5.2	Change from Centralized to Decentralized Power Generation	52
2.5.3	Impact on Use Pattern	52
3	Material and Thermal Balances	54
3.1	Process Fundamentals	54
3.1.1	Operational Constraints	54
3.1.2	The Challenge of Power Modulation	62
3.2	Material and Thermal Balances	63
3.2.1	Envelope of the Material and Thermal Balance	64
3.2.2	Main Reactions	66
3.2.3	Side Reactions.....	69
3.2.4	Material Balance	71
3.2.5	Thermal Balance.....	77
3.3	Heat Loss.....	87
3.3.1	Experimental Cross-Check on the Cell Heat Loss Distribution	92
4	Power Modulation	98
4.1	History of Power Modulation	98
4.1.1	First Applications of Power Modulation	98
4.1.2	Energy Input Reduction	101
4.1.3	Modern Power Modulation	102
4.2	Possible Scope of Power Modulation	105
4.2.1	Thermal Operation Range for a Reduction Cell	106
4.2.2	Aim of Process Control Systems.....	106

4.2.3	Heat Capacity of an Calculation for the Aluminium Reduction Cell as it is installed in Hamburg	108
4.3	Affected Cell Voltage Components	113
4.3.1	Compensating Voltage Adjustments	117
4.3.2	Bath Voltage Drop.....	118
4.3.3	Cell Voltages Changes Induced by Changes of Line Current	122
4.4	Practical Limitations	125
4.4.1	Restrains in Equipment and Organisation.....	126
4.4.2	Constraints Imposed through Interfaces	127
4.5	Concepts of Implementing Power Modulation.....	128
4.5.1	Modulation with Minimal Impact on Thermal Balance	129
4.5.2	Modulation with Minimal Impact on the Cell	131
4.5.3	Changes in Alumina Feeding	133
4.5.4	Implementation at Trimet Hamburg.....	134
5	Cell Reaction to Altered Operating Conditions.....	136
5.1	Measurement Systems Used	136
5.1.1	Bath, Liquidus Temperature and Superheat	136
5.1.2	Side Ledge Measurement.....	137
5.1.3	Bath Inventory Measurement	145
5.2	Base Case Studies	147
5.2.1	Sensitivity of Side Ledge to Outside Temperature	147
5.2.2	Distribution of Ledge Thickness in a Cell	150
5.3	Cell Reactions to Single Periods of Increased Energy Input.....	153
5.3.1	Experimental Setup.....	153
5.3.2	Discussion of Experimental Results	156
5.4	Reversibility of Energy Increases.....	176

5.4.1	Experimental Setup.....	176
5.4.2	Discussion of Experimental Results.....	177
5.5	Potline Behaviour under Repeated Modulation.....	183
5.5.1	Experimental Setup.....	183
5.5.2	Discussion of Experimental Results.....	187
5.6	Conclusions on Cell Behaviour.....	190
5.6.1	Regression Analysis for Cell Reactions.....	190
5.6.2	Ledge Dynamics during Power Modulation.....	194
5.6.3	Impact of Melting Cover Material on Bath Inventory and Ledge Development.....	198
6	Economic Impact of Power Modulation.....	200
6.1	Energy Price Spread.....	200
6.2	Power Modulation with the Current Market Situation.....	204
6.3	Effect of Power Modulation on Productivity.....	206
6.4	Conclusions on Economical Impact and Future Prospects.....	212
7	Engineering Solutions to Promote Sustained Power Modulation.....	215
7.1	Controlled Side Wall Heat Loss.....	216
7.2	Controlled Top Heat Loss.....	219
8	Conclusions and Future Work.....	221
8.1	Capability of Energy Storage.....	223
8.2	Limiting Constraints for Power Modulation.....	224
8.3	Side Ledge Variability during Power Modulation.....	225
8.4	Effects on Process Efficiency and Means of Generating Additional Revenue.....	226
8.5	Design Improvements.....	226
8.6	Future Work.....	227
8.6.1	Process Control of Power Modulation.....	227

8.6.2	Impact on Cathode Performance	229
9	Bibliography	230

List of Figures

Figure 1.1:	Energy price fluctuations in 2008 as listed on the EEX.....	2
Figure 2.1:	Schematic of an Aluminium Reduction Cell	6
Figure 2.2:	NaF-AlF ₃ phase diagram with indication of the process window (Kvande 1983).....	9
Figure 2.3:	Pseudo-resistance curve depending on alumina concentration	21
Figure 2.4:	Drawing of the early cell designs used by ALCOA.....	22
Figure 2.5:	Schematics of a side-by-side potline (A) and an end-to-end potline (B)	26
Figure 2.6:	Anode numbering in the Hamburg cell with tap and measurement hole marked in red	32
Figure 2.7:	Modified Reynolds P19 cell design installed in Hamburg.....	32
Figure 2.8:	Comparison of global electricity prices, Germany equals 100 %, 2011 (Anonymous 2011)	38
Figure 2.9:	Comparison of electricity prices in Europe, Germany equals 100 %, 2011 (Anonymous 2011)	38
Figure 2.10:	Schematic of an open pit anode ring furnace (Lützerath 2012)	40
Figure 2.11:	Recent cost structure in a Central European smelter.....	43
Figure 2.12:	Degree of utilization of 16,000 MW installed wind energy generating power in Germany in 2006 (Pieper, Fleckenstein et al. 2007).....	48
Figure 2.13:	Total grid load and residual load (Schulz 2012).....	51

Figure 3.1:	Constraints of aluminium production.....	54
Figure 3.2:	Bath mass necessary to heat and dissolve one shot of alumina weighing 6 kg	56
Figure 3.3:	Phase diagram $\text{Na}_3\text{AlF}_6 - \text{Al}_2\text{O}_3$	57
Figure 3.4:	Effect of increased internal energy.....	58
Figure 3.5:	Effect of power modulation on process efficiency	63
Figure 3.6:	Heat Balance Boundary (Bruggeman 1998)	66
Figure 3.7:	Reaction potentials for CO_2 and CO formation depending on current density (Welch 2010).....	68
Figure 3.8:	Preferential reaction of different carbons in an anode (Fischer, Meier et al. 2006).....	69
Figure 3.9:	Exemplary increase in energy consumption as a result of increased carbon consumption (Welch 2013a).....	78
Figure 3.10:	Relation between net carbon consumption, current efficiency and energy to produce metal for the Hamburg cell	80
Figure 3.11:	Typical heat loss distribution as given by Bruggeman (Bruggeman 1998).....	89
Figure 3.12:	Heat flux measurement points at the cell bottom	93
Figure 4.1:	Comparison of the process Window of optimum performance with the real process room of a classical control system (left) and a modern one (right)	107
Figure 4.2:	Energy content of a reduction cell at 955 °C and 970 °C	112
Figure 4.3:	Shift in energy content while heating up from 955 °C to 970 °C.....	112

Figure 4.4:	Different investigations of anode polarization at 980 °C for cryolite-alumina melts with graphitic carbon electrodes (Welch 2003)	114
Figure 4.5:	Electrical conductivity of the bath depending on bath temperature	120
Figure 4.6:	Electrical conductivity of the bath depending on bath composition	120
Figure 4.7:	Cell voltage compared to calculated control voltage	124
Figure 4.8:	Schematic of modulated energy input and resulting energy states	125
Figure 4.9:	Effects of varying BFT on number of shots	134
Figure 4.10:	Critical anodic current density	135
Figure 5.1:	Ledge measurement system in a new cell	138
Figure 5.2:	Dial used for determination of the angle (left) and hook inside the cell (right).....	139
Figure 5.3:	Sketch of the set-up of the side ledge measurement	140
Figure 5.4:	Distribution of measured ledge thicknesses 10 cm above the cathode surface on all cells before an energy increase trial.....	144
Figure 5.5:	Comparison of the ledge thickness of all anodes and the selected measurement location for the January 2010 base case	145
Figure 5.6:	Measurement positions for the base case side ledge measurement.....	147
Figure 5.7:	Effect of different seasons on side ledge	148

Figure 5.8:	Pinch point of the side ledge	150
Figure 5.9:	Distribution of ledge thickness in a cell	151
Figure 5.10:	Metal velocity diagram of the Hamburg cell and bus bar schematics (Droste 1999).....	152
Figure 5.11:	Comparison of predicted and measured temperature Increase and bath inventory change.....	157
Figure 5.12:	Change in temperature and superheat vs deviation from nominal energy input introduced by current.....	158
Figure 5.13:	Superheat surface curve of energy density and trial time	160
Figure 5.14:	Coefficients of temperature and superheat increase per kWh of energy increase introduced by voltage addition.....	161
Figure 5.15:	Temperature and superheat reaction in relation to energy density introduced by voltage addition.....	162
Figure 5.16:	Temperature and superheat difference before 1 st and 2 nd repetition.....	163
Figure 5.17:	Temperature curve after voltage increase.....	167
Figure 5.18:	Superheat curve after voltage increase	167
Figure 5.19:	AlF ₃ -Levels during voltage increase.....	168
Figure 5.20:	Ledge profile after energy increase.....	170
Figure 5.21:	Ledge movement for different energy increases	171
Figure 5.22:	Ledge melting in the metal pad and bath area depending on additional energy input.....	172
Figure 5.23:	Linear regression for the overall ledge melting	172
Figure 5.24:	Cell voltage over the experiment.....	177

Figure 5.25:	Side ledge development during the trial, cell 138.....	180
Figure 5.26:	Side ledge development during the trial, cell 139.....	180
Figure 5.27:	Development of ledge thickness in the bath and metal.....	183
Figure 5.28:	Line current curve for the modulation schemes	186
Figure 5.29:	Energy cumulative sum for continuous modulation.....	187
Figure 5.30:	Shape of the side ledge after the high and low amperage phase.....	188
Figure 5.31:	Ledge movement (ledge growth positive) depending on maximum energy cumulative sum	189
Figure 5.32:	Areas for mechanisms of dissolving and melting ledge	195
Figure 5.33:	Time dependency of ledge in the metal pad after a change of heat input.....	198
Figure 6.1:	Average power price on a weekday in June 2008.....	201
Figure 6.2:	Power price on weekdays and weekends in June 2008 (Anonymous)	202
Figure 6.3:	Power prices during seasons in 2008 (Anonymous).....	202
Figure 6.4:	Price curve and resulting line current.....	203
Figure 6.5:	Average power price on a weekday in November 2013.....	204
Figure 6.6:	Resulting modulation profile.....	205
Figure 6.7:	Production data System I.....	208
Figure 6.8:	Production data System II.....	209
Figure 7.1:	Sketch of the working principle of the shell heat exchanger (Lavoie, Namboothiri et al. 2011).....	217

Figure 7.2:	Heat loss achievable with a shell heat exchanger.....	218
Figure 7.3:	Heat loss through the top of the cell at various suction rates ...	220

List of Tables

Table 2.1:	Effects of additives on physical and chemical properties (Haupin 1980).....	8
Table 2.2:	Composition of typical electrolyte (Grjotheim and Kvande 1993)	10
Table 2.3:	Conversion energies and reaction enthalpies for reaction in an aluminium smelting cell at 960 °C.....	14
Table 2.4:	Voltage and resistance breakdown for a Hamburg P19 cell.....	18
Table 2.5:	Cathode properties for grades sold today (SGL Carbon 2013)	28
Table 2.6:	Operating figures for TRIMET Hamburg's P19 cells	33
Table 2.7:	Comparison of electricity generation and aluminium production (Anonymous 2013c, Anonymous 2013d)	36
Table 3.1:	Difference in AlF_3 additions in primary and secondary alumina cells.....	72
Table 3.2:	Average analysis of alumina used by Trimet.....	73
Table 3.3:	Anode consumption	74
Table 3.4:	Impurities of a carbon anode.....	74
Table 3.5:	Material movement during one anode change	76
Table 3.6:	Material movement during anode change per ton of aluminium produced	76
Table 3.7:	Proportion for the reaction to produce aluminium	78
Table 3.8:	Material and heat balance for anode butts and cover	81

Table 3.9:	Material and heat for the dry scrubber process and AlF_3 -additions	83
Table 3.10:	Impurity reactions forming fluoride salts per t_{Al}	84
Table 3.11:	Impurity reactions forming elements per t_{Al}	84
Table 3.12:	Total energy needed in the reduction process for 93.5 % current efficiency.....	85
Table 3.13:	Results of 4 consecutive heat loss measurements	95
Table 4.1:	Details for power modulation at Alcanbrazil and Valesul	99
Table 4.2:	Details for power modulation at Hydro Aluminium Karmøy	102
Table 4.3:	Details for power modulation at Trimet Essen and AlDel	104
Table 4.4:	Mass, temperature and energy of materials used in the cell at 955 °C and 970 °C.....	109
Table 4.5:	Bath chemistry development on cell 113 without AlF_3 additions (Reek 2013).....	111
Table 4.6:	Comparison of voltage breakdown for different line currents ...	123
Table 5.1:	Measurement data for Figure 5.7	149
Table 5.2:	Additional heat input for investigating cell reactions.....	154
Table 5.3:	Voltage increase applied to study self-rebalancing	156
Table 5.4:	Temperature and superheat measurements from energy input trials.	157
Table 5.5:	Temperature and superheat before 1 st and 2 nd trial	163
Table 5.6:	Temperature and superheat development after voltage increase	165
Table 5.7:	Ledge profile in mm after energy increase	169

Table 5.8:	Bath inventory before and after the +10 kA for 8 hours trials ...	174
Table 5.9:	Experimental setup for 3 h voltage changes	177
Table 5.10:	Temperatures during the voltage compensation trial	178
Table 5.11:	Side ledge dimension during the trials	181
Table 5.12:	Development of ledge thickness in the bath and metal	182
Table 5.13:	Characterisation of four modulation schemes	184
Table 5.14:	Ledge movement during modulation	188
Table 6.1:	Production data System I	208
Table 6.2:	Production data System II	209
Table 6.3:	Adjusted productivity loss during power modulation	210
Table 6.4:	Net benefit of power modulation on production cost	211

Abbreviations and Constants

Abbreviation	Description	Unit
ΔT	Superheat	°C
η_{CE}	Current efficiency	--
ACD	Anode cathode distance	mm
AE	Anode effect	--
Bath	Industrial term for electrolyte	--
BFT	Base feed time	s
CPC	Calcined petroleum coke	--
CR	Cryolite ratio; n_{NaF}/n_{AlF_3}	--
CVD	Cathode voltage drop	mV
EEX	European Energy Exchange	--
GTC	Gas treatment center	--
MHD	Magneto-hydro-dynamic, modelling approach to estimate the stability of a cell design	--
PAH	Polycyclic aromatic Hydrocarbon	--
PCU	Process control unit	--
PFC	Perfluorinated carbon gases typically CF_4 and C_2F_6	--
T_{amb}	Ambient temperature	°C
T_{bath}	Temperature of the bulk of bath	°C
T_{liq}	Liquidus temperature	°C

Constant Description		Value and unit
$C_{p_{Al}}$	specific heat capacity of Al	1.18 J/(g * K)
$C_{p_{bath}}$	specific heat capacity of bath	1.89 J/(g * K)
EMF	Electro-Magnetic Force	1.60 V
F	Faraday's Constant	96,485 C/mol
$l_{anlength}$	length of the anode	1,495 mm
$l_{anwidth}$	width of the anode	795 mm
$l_{celllength}$	length of the cell	9.233 m
$l_{cellwidth}$	width of the cell	4.356 m
m_{Al}	Molar mass of aluminium	26.982 g/mol
m_{Sr}	Molar mass of Sr	87.62 g/mol
m_{SrCO_3}	Molar mass of SrCO ₃	147.63 g/mol
n_{anodes}	number of anodes	18
R	Universal Gas Constant	8.3144 J/(mol * K)
ρ_{bath}	density of liquid bath at 960 °C	2.1 g/cm ³
ρ_{Al}	density of liquid Aluminium at 960 °C	2.4 g/cm ³
λ_{Al}	thermal conductivity of Aluminium	237 W/(m * K)
λ_{bath}	thermal conductivity of bath	0.4 W/(m * K)
λ_{steel}	thermal conductivity of steel	49 W/(m * K)

1 Introduction

Aluminium production is a highly energy intensive electrolytic process. As aluminium oxide is an extremely stable chemical compound, a lot of electrical energy is needed to separate it. For this reason large sources of low priced electrical power were and still are driving forces for developing primary aluminium smelting capacities. With the growth of the industry to produce 50 million tons of aluminium per year in 2013, in correspondence with an increasing population and increasing living standards in the world, the availability of low priced energy is diminishing rapidly. In production areas established several decades ago, electricity prices have been rising substantially due to competitive demand. The cost of energy can constitute as much as 40 % of production costs. Even small price increases are difficult to compensate by increasing efficiency.

The introduction of renewable energy generation has further increased average production costs through levies and subsidies. In addition this has led to a dramatic increase in price fluctuation, as is illustrated in Figure 1.1 (Anonymous 2010) which shows the minimum, maximum and average price per MWh per day for the year 2008. Peak prices are repeatedly above 150 €/MWh with a single peak as high as 494 €/MWh on Nov 25th. In Germany the yearly average price for 2008 was 65.76 €/MWh while the average price spread – the difference between maximum and minimum hourly price per day – was 71.63 €/MWh. In effect price variability exceeded the average price.

These price fluctuations present an opportunity to lower energy costs if aluminium reduction cells are capable of operating with a non-constant energy input. In this case the cell has to act as an energy storage system, receiving surplus energy during low price periods, converting it into a combination of increased metal production and surplus heat, which increases the temperature of the cell. Consequently, during high price periods less energy is consumed by the cell, shedding heat and decreasing metal production.

This situation was the origin for the work detailed in this thesis.

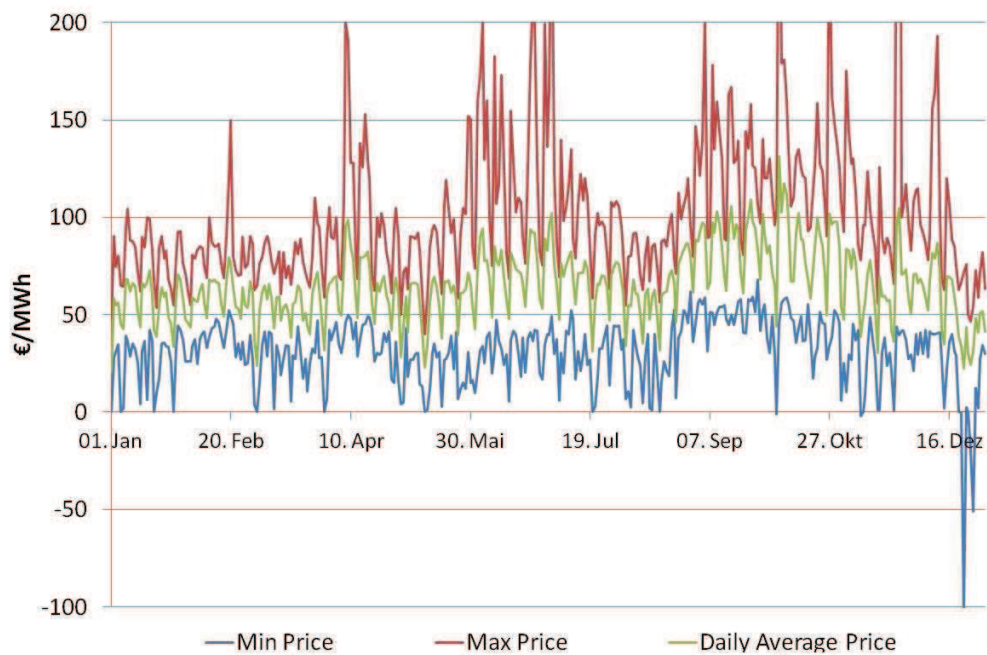


Figure 1.1: Energy price fluctuations in 2008 as listed on the EEX

This mechanism is subject to constraints of cell design and process dynamics as the cell is operating within a narrow process window spanned by efficiency, alumina dissolution and cell life.

An aggressive electrolyte is necessary to dissolve alumina. This electrolyte – cryolite, Na_3AlF_6 – is so corrosive, that most known materials cannot withstand contact with molten cryolite for an extended period of time. For this reason aluminium reduction cells operate closely above the melting point of the electrolyte. In addition, they are designed to lose heat through the vertical side wall so as to promote freezing of electrolyte onto the side wall material forming a protective side ledge. This so called side ledge protects the side wall refractory from exposure to and damage from the molten electrolyte. The continued existence of this ledge is heavily influenced by the temperature and composition of the electrolyte and hence is dependent on energy input. Thus, the necessity of the existence of side ledge is the upper limit of an energy

increase. If all side ledge is molten at one location within the cell, the electrolyte will damage the cell refractory and lead to premature failure.

The second major constraint is the energy necessary to heat all raw materials to the operating temperature of 960 °C. In case of alumina, which is the main material added to the process, it has to be dissolved into the electrolyte. For this to happen, enough energy has to be present in the electrolyte to rapidly heat and dissolve the added alumina. Sufficient mixing of alumina and electrolyte is necessary to facilitate the necessary heat transfer. The energy is stored in overheating the electrolyte beyond the liquidus temperature. This difference is the so-called superheat, ΔT . If the superheat is too small, the added alumina will not dissolve and will accumulate at the bottom of the cell, reducing the efficiency of the process.

With the traditional process control concept, aim was to keep the energy input into the cell as constant as possible to remove one variable from the control strategy and thus improve process efficiency. When moving to a variable energy input however, it is critical to ensure that the control system is keeping track of the accumulated energy deviation from nominal operation and that decisions are taken with regards to this parameter. For example a cell normally considered to have a high temperature of 970 °C might not be considered hot any more if the temperature was measured after a significant energy increase.

Effectively, the process control system has to incorporate energy deviation as an additional dimension.

The objective of this thesis is to investigate the feasibility of the aluminium reduction process to operate at varying energy input. The major questions to be answered are:

- How much energy can you store in each cell while maintaining thermal balance constraints?

- What are the limiting constraints existing in cell design and process organisation?
- What is the effect on process efficiency?
- Which simple, economical and retrofittable design variations exist that increase the feasibility of power modulation?

2 Background

Synopsis:

This chapter is a literature review and reflects on the history of aluminium production and the process as it is in use today. The challenges it is facing when confronted with changing availability of electrical energy are discussed.

2.1 Overview of the Process

Primary aluminium is solely produced by the Hall-Héroult-Process. The process is named after its inventors, American Charles Martin Hall and Frenchman Paul Héroult. Both discovered that aluminium oxide – called alumina – can be dissolved in molten cryolite (Na_3AlF_6) and electrolysed if a direct current is applied. A carbon crucible was used as an electrochemical cathode as well as to contain the molten cryolite and the produced molten aluminium. A prebaked carbon piece was used as an anode. The carbon anode is directly or indirectly electrochemically oxidized by electrical current, reacting with the oxide anion of the alumina dissolved in the electrolyte leading to a mixture of carbon monoxide and carbon dioxide evolving at the anode.

Both inventors discovered the process independently and nearly simultaneously. Both filed in 1886 and were awarded a patent describing this method (Héroult 1886, Hall 1889).

The two dominant reactions of the Hall-Héroult-Process are:



and



The fundamentals of producing aluminium have not changed since its invention. Even though the size of the cells has increased dramatically, the cell itself still uses a carbon lining to contain the melt and to conduct electricity out of the cell. Figure 2.1 shows a cross section of a modern aluminium reduction cell. To introduce electricity into the cell, several pre-manufactured carbon anodes are attached to steel yokes which also support the anodes in the cell. Typically cells contain two rows of carbon anodes with each row containing between eight and 24 anodes, and with each carbon block weighing between 500 and 1,500 kg depending on the cell amperage and design.

Earlier technologies also had cells with one large single anode that was self formed utilizing surplus heat generated by the cell. This type of cell is referred to as a Söderberg cell but it is unlikely that this technology will be built in any greenfield sites hereafter mainly due to pitch volatiles from the anode raw materials escaping into the ambient air.

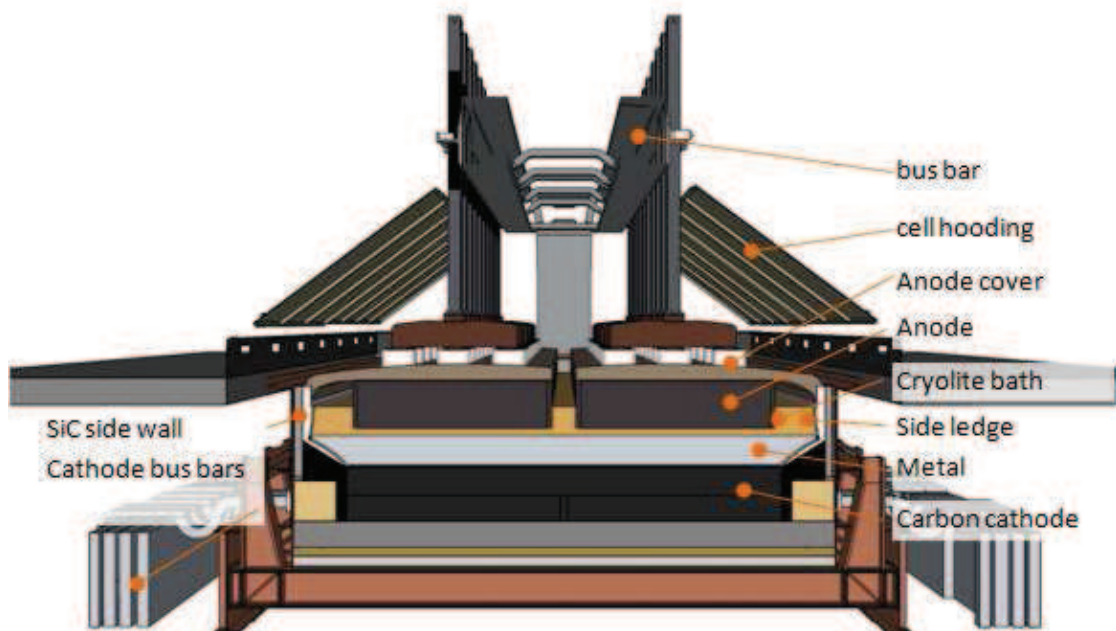


Figure 2.1: Schematic of an Aluminium Reduction Cell

The top of the anodes is covered by a mixture of alumina and frozen electrolyte to retain heat within the cell and to prevent ambient oxygen from reaching the hot anode surfaces. The top of the cell consists of structures for supporting and vertically moving the anodes, in addition to alumina hoppers and feeders as well as cell hooding and a connection to a central off gas treatment.

All electrical energy introduced into the cell within a boundary encompassing the anode top cover and the shell of the cell is used either for electrochemical as well as process reactions associated with aluminium production or as thermal energy necessary to preheat the input materials and provide the heat lost across that boundary. A constant line current is used for normal operation and one main operating target is to maintain a stable energy balance.

The carbon lining is encased in refractory material which is in turn housed in a steel shell. Embedded in the carbon are steel collector bars used to conduct the electricity out of the cell onto a bus bar system interconnecting the cells.

Towards the bottom of the cell, refractory material is used to prevent penetration of electrolyte below the carbon lining. Several layers of diffusion barrier and refractory bricks are used. Underneath is an insulation layer consisting of calcium silicate bricks or in older designs simply compacted alumina.

Accordingly the vertically oriented side-walls of the cell are designed to promote heat loss sufficiently to form a layer of frozen electrolyte – called side ledge – on the refractory. This is also necessary to protect the material from the highly corrosive electrolyte. Silicon carbide refractory is exclusively used for the side wall nowadays.

2.1.1 Temperature and Electrolyte Composition

Operation temperature ranges from 940 °C up to almost 980 °C, depending on technology and electrolyte composition used. Most smelters maintain target temperatures in the range of 955 – 965 °C (Utigard 1999). The chemical composition is such that its melting point is usually in the range of 5 – 10 °C below the operating temperature. This temperature difference is referred to in the industry as the superheat ΔT , which is variable to some degree.

The electrolyte consists mainly of cryolite as it is the only solvent for aluminium oxide. One of the disadvantages of cryolite is the steep liquidus curve in the process area as indicated on the phase diagram shown in Figure 2.2.

The reduction in liquidus temperature from 1010 °C for pure cryolite to 950 - 960 °C is achieved by additives. A general overview of the effect of additives used in the electrolyte is given in Table 2.1.

Table 2.1: Effects of additives on physical and chemical properties (Haupin 1980)

	Al ₂ O ₃ Sol.	Electrical Cond.	Density	Viscosity	Liquidus	Metal Sol.	Surface Tension	Vapour Pressure
AlF ₃	↓	↓	↓	↓	↘	↓	↓	↑
CaF ₂	↓	↓	↑	↗	↓	↓	↑	↓
Al ₂ O ₃	-	↓	↓	↗	↓	↓	↘	↓
Temp	↑	↑	↓	↓	-	↑	↓	↑

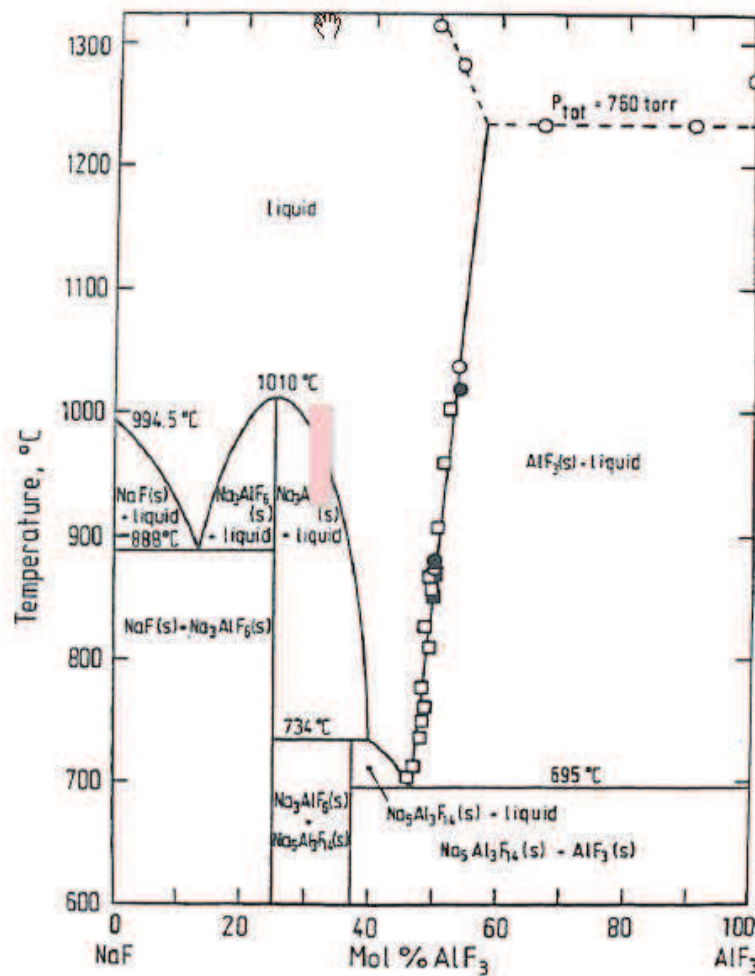


Figure 2.2: NaF-AlF₃ phase diagram with indication of the process window (Kvande 1983)

Usually only AlF₃ and alumina are added on purpose. Alumina is the reactant to produce aluminium and is continuously removed and added to the cell. AlF₃ reduces the liquidus temperature and the metal solubility of the electrolyte. Also the density is lowered resulting in a better separation of metal and electrolyte. It has to be added continuously to compensate for the sodium oxide content of the alumina. Alumina solubility and electrical conductivity are affected negatively by an increased AlF₃ content.

CaF₂ typically accumulates in the electrolyte due to impurities in the alumina. Due to its positive effect on metal solubility and liquidus temperature, it is added

in rare cases intentionally if the CaO content in the alumina is insufficient. A major disadvantage of CaF_2 is the increase of bath density which lessens the separation between metal and electrolyte and may cause operational problems if the CaF_2 content exceeds a critical limit, typically given at 7 %.

Other additives like MgF_2 or LiF were used in former times but are insignificant in today's industry. Table 2.2 gives an overview of the range of compositions used today (Grjotheim and Kvande 1993).

Table 2.2: Composition of typical electrolyte (Grjotheim and Kvande 1993)

Additive	Concentration
Al_2O_3	2 – 4 %
AlF_3	9 – 11 %
CaF_2	4 – 7 %
Na_3AlF_6	balance

2.1.2 Smelting, Energy Use and Metal Production.

Practical experience of the operation of aluminium smelting cells shows they are capable of operating over a range of line currents but for each operating current there is usually an optimum set of conditions that results in the maximum amount of metal that can be produced in any one time.

Some of these conditions are controlled by the kinetics, for example mixing and subsequent dissolution of alumina; others are controlled by the work practices which are carried out intermittently.

The assigned energy used by each smelting cell is broadly subdivided into two components:

- The external, used for interconnecting the cells to the DC supply
- The energy dissipated within the boundary conditions of the cell.

Thus the energy that has been introduced within the cell is given by

$$Q_{cell} = (U_{total} - R_{cell-cell} \cdot I) \cdot I \quad \text{Eq. 2.2}$$

With

Q_{cell}	energy input into the cell
U_{total}	gross cell voltage
$R_{cell-cell}$	bus bar resistance between cells
I	line amperage

This energy has a number of different destinations. These are:

1. The heat loss through the sidewall of the cell which is driven by the superheat of the liquid electrolyte and controlled by the thermal resistance resulting from the properties of the materials used. In addition it has a variable component with the thickness of the side ledge.
2. The heat loss through the bottom of the cell which is driven by the electrolyte temperature and the thermal resistance of the materials being used.
3. The heat loss through the top of the cell which is driven by electrolyte temperature, thermal conductivity and geometry of the anodes as well as thickness, composition and integrity of the anode cover. It is influenced by the suction rate of the dry scrubber, which is usually typically boosted when work is done on a cell to maximize capturing of emissions.

4. The heat loss during the work practices. This includes the materials being moved or removed, e.g. the hot anode butts and metal, but also the absorption of heat in a newly set anode or newly applied cover material. This figure is difficult to assess as material masses and temperatures are not registered at all or with insufficient quality.
5. The energy required to preheat the materials continuously added such as the smelter grade alumina. This is proportional to the operating line current and the current efficiency at any instance.
6. A major contributor to the energy consumption is the conversion energy from hot solid alumina into liquid aluminium and the carbon oxides that are evolved.
7. The raw materials contain approximately 5% impurities. These have conversion energy requirements as they are converted to different products and therefore they have a conversion energy requirement that is proportional to line current and operating current efficiency.
8. Transient stored energy which changes when process conditions and performance changes are creating an imbalance. The operating cells have a “stored energy” due to the states and phases of materials within the balance boundary and this buffers energy imbalances.

As will be discussed below in conjunction with the voltage, the aluminium smelting process requires energy to be transferred both thermally and electrochemically through the potential gradients at the anode and cathode. Therefore the smelting cells can be used to store or supply some of the thermal energy required during a transient period of operation as long as minimum voltage requirements to enable the reactions for reducing aluminium from alumina are met.

For aluminium smelting the conversion energy required is given by the enthalpy of the reaction starting with solid alumina at the cell temperature. The energy requirements for the various possible conversion reactions are given in the following table which is based on the HSC thermodynamic data base (Roine 2002). The table also includes the Gibbs energy changes for the reactions listed. E^0 is calculated using the formula Eq. 2.3, while the equivalent voltage to enable the reaction is calculated by Eq. 2.4.

$$E^0 = \frac{-\Delta G^0}{nF} \quad \text{Eq. 2.3}$$

$$E^0_{eq.} = \frac{-\Delta H^0}{nF} \quad \text{Eq. 2.4}$$

With	E^0	standard potential
	$E^0_{eq.}$	equivalent voltage
	ΔG^0	Gibb's energy
	ΔH^0	enthalpy
	n	number of electrons
	F	Faraday's Constant

Table 2.3: Conversion energies and reaction enthalpies for reaction in an aluminium smelting cell at 960 °C

Reactions	$\Delta G^0_{\text{reaction}}$ [kJ/mol]	$\Delta H^0_{\text{reaction}}$ [kJ/mol]	E^0 [V]	Equiv. Volts to enable
$Al_2O_3 + 3C \rightarrow 2Al + 3CO(g)$	621.5	1350.8	1.074	2.333
$Al_2O_3 + 1.5C \rightarrow 2Al + 1.5CO_2(g)$	689.5	1098.6	1.191	1.898
$Al_2O_3 + 3C + 2Na_3AlF_6 \rightarrow 4Al + 3COF_2(g) + 6NaF$	2157.6	2876.0	1.863	2.484
$C + 2COF_2(g) \rightarrow 2CO(g) + CF_4(g)$	-45.7	122.9	(-0.04)	(0.106)

Using the universally accepted practice of setting the potential of the aluminium electrode to zero, the maximum potential of the anode is constrained to below ~ 1.84 V on an operating cell to prevent co-evolution of the fluorocarbons. At this potential limit the electrodes have insufficient energy for complete conversion and therefore additional heat transfer is required, with the amount required being much greater as the proportion of carbon monoxide formed increases.

2.1.3 Cell Voltage

The cell voltage is made up of a combination of the thermodynamic potential, the ohmic resistance voltage drops associated with the electrode materials and electrolyte and the anodic and cathodic interfacial electrode potential gradients. Each electrode potential gradient is, subject to its magnitude, capable of providing the necessary energy to enable redox reactions, and simultaneously

provide additional energy (or driving force) to maintain the reaction rate. The reaction is occurring subject to there being enough additional energy to complete the various conversion reactions.

Thus giving the following equation for cell voltage:

$$U_{cell} = E_{anode} + E_{cathode} + I \cdot R_{cell} \quad \text{Eq. 2.5}$$

With	U_{cell}	cell voltage
	$E_{()}$	electrochemical potential
	I	amperage
	R_{cell}	ohmic resistance of the cell

Where the cell's ohmic resistance is comprised of the following contributions:

$$R_{cell} = R_{anode} + R_{bubble} + R_{electrolyte} + R_{cathode} + R_{external} \quad \text{Eq. 2.6}$$

Whilst various models have been developed for the bubble resistance there is no accurate data indicating how the bubble resistance varies with current density. It is known that it is modified substantially by having slots in the anodes for example, as this changes the bubble residence time and average volume. The operating current density, carbon quality of the anodes as well as the design, shape and burn-off profile also has an influence on the bubble layer resistance.

The voltage drops over all parts of the cell acting only as an electrical conductor are affected according to Ohm's Law. These are the anode voltage drop consisting of anode rod, yoke and transition joint, the stub to carbon voltage drop and the anode carbon itself, as well as the carbon cathode, steel collector bar and the external bus bar.

In a more detailed examination, the change in current will effect a change in heat generated in the conductor. This will lead to a change of temperature of the material and thus a change in conductivity and voltage drop. However the expected effects are minor compared to other factors such as ambient temperature acting onto the overall temperature of the bus bar system or the cell temperature acting on the anode carbon.

One critical point bearing consideration is the stub to carbon contact. The heat generated is considerably higher than at other interfaces. Due to the nature of the cast iron joint and the inferior anode properties due to the complex geometries at the stub hole, this area is sensitive to overheating. If considerably more heat is generated than can be conducted away from the top part of the anode or drained off through the anode yoke and rod assembly, there is danger of excessive air burn. Hamburg is operating an anodic stub current density of 16.5 A/cm^2 . The value is in the upper region of the typical operation area given as $8 - 20 \text{ A/cm}^2$ (Welch and James 2003).

The electrolyte ($R_{\text{electrolyte}}$) is dependent on cell and operating conditions such as temperature and interelectrode distance, chemical composition of both the solvent fluoride electrolyte and dissolved solute concentration.

Within Eq. 2.5 the anode potential (E_{anode}) is the sum of the Nernst or reversible decomposition potential of the saturated electrolyte, the impact of the dissolved oxide concentration at the anode interface deviating from saturation and the reaction activation overpotential (Richards and Welch 1964) required to maintain the imposed reaction rate (η_i) of each electrode reaction plus the applicable polarization for that reaction (E_i). Therefore we have

$$E_{anode} = E^0 - \frac{RT}{nF} \left(\frac{a_{CO_2}^3 \cdot (a_{Al_2O_3}^2)_{saturated}}{a_{Al_2O_3}^2} \right) + \eta_i \quad \text{Eq. 2.7}$$

With	E_{anod}	anode potential
	E^0	standard potential
	R	universal gas constant
	T	temperature
	F	Faraday's Constant
	n	number of electrons
	a_i	activity coefficient for the given species, which is approximately proportional to the degree of saturation

The magnitude of the electrode kinetic energy gradients of the electrode, referred to as overpotential or polarisation, is also dependent on a large number of process variables, and especially the overall redox reaction mechanism.

The anode overpotential is significantly higher in the current density range used by aluminium smelters because of the complex reaction mechanism associated with the formation of both, carbon dioxide as well as carbon monoxide, and its subsequent evolution. Dependable variables include the true surface area of the anode carbon, the solvent electrolyte composition, the operating current density, and alumina concentration. The over-potential is particularly sensitive to the alumina concentration and this sensitivity is used as a means of control for alumina additions to the electrolyte.

At the higher levels of the reported anode polarization range the electrode potential approaches values that can initiate the indirect formation of fluorocarbons and can thus constitute a limit on the combination of current density and alumina concentration, although operating towards a low concentration is desirable for the basic cell control strategy.

Cell voltage can be broken down into four major parts given in the following table (Depee, Agbenyegah et al. 2012). Due to a variable line current, it is more meaningful to express the parts as a resistance to illustrate the ohmic

behaviour. This applies to all except for the electrochemical voltage. The components of the breakdown of the cell voltage are either measured or estimated from the total cell voltage in the Hamburg cells which were used for this research. A more detailed breakdown of the cell voltage and its variability depending on line current is discussed in chapter 4.3.

Table 2.4: Voltage and resistance breakdown for a Hamburg P19 cell

	Resistance ($\mu\Omega$)	Voltage at 180 kA
Anode Voltage Drop	2.69	0.485 V
Bath Voltage Drop	8.61	1.55 V
Electrochemical Voltage	n/a	1.81 V
Cathode Voltage Drop	1.97	0.355 V
Total Cell Voltage		4.20

2.1.4 Basics of Control

As neither actual addition rate nor actual consumption of alumina is known due to the volumetric designed addition units on the one hand and the variations in current efficiency on the other hand, the alumina concentration in the cell is modulated around a value by cyclic over- and underfeeding around the actual consumption rate. Typically, an overfeed rate consists of alumina addition of 120 % to 150 % of nominal consumption rate, leading to an enrichment of alumina in the electrolyte. During underfeeding 50 to 70 % of nominal consumption are typically added, depleting the electrolyte of alumina. Some control systems, such as the one used at Trimet Hamburg, also use a base feed between over- and underfeed which is close to the nominal consumption.

The control signal is the change in cell voltage which arises almost totally from a change in the anode potential according to the Nernst equation and the various polarisations. The potential increases for a decrease in alumina concentration.

The aim is to limit this change to a potential below one where per-fluoro-carbon co-evolution can initiate. It is assumed that the cells operate at constant line current although in practice potlines do not operate at either constant current or constant voltage. The potline control system attempts to maintain the current constant, but the current fluctuates through the impact of other cells having anode effects, beam movements or similar disturbances, causing a change in cell voltage and subsequently in total line voltage. Because of this the cell voltage needs to be normalised to the average operating line current and this is done using a simplified voltage model whereby it is assumed that the current density dependent variables change linearly with current (anode and cathode polarisation, bubble resistance). Using this assumption a normalising voltage U_{norm} is estimated from a typical current versus voltage relationship (which is dominated by the ohmic components) and the voltage abscise determined by extrapolating back to zero amperage. This assumes that the electrode polarisations and bubble resistance vary linearly with current in the control region. Typical values of the extrapolated voltage range from 1.60 to 1.70 V. A constant value within this span is assumed and then a normalised voltage calculated according to Eq. 2.8.

During electrolysis with a modulated feed rate (where the dissolved alumina concentration changes) variations in cell voltage are dominated by changes in the anode potential which in turn are dominated by changes in alumina concentration. If there is a movement in the anode beam or differential consumption between the anode and growth of the metal pad, this will also bring about a small change in the cell voltage but the latter being linear, while voltage changes due to changes in alumina concentration are exponential in the targeted process area. Because of heat balance constraints the average voltage should also be controlled.

$$U_{norm} = (U_{meas} - EMF) \cdot \frac{I_{target}}{I_{meas}} + EMF$$

Eq. 2.8

With:	U_{norm}	normalized cell voltage
	U_{meas}	measured cell voltage
	I_{target}	targeted line amperage
	I_{meas}	measured line amperage
	EMF	electro-magnetic force, 1.60 V in Celtrol

One or more cells are controlled by an individual process control unit (PCU) monitoring cell voltage. Pseudo-resistance is calculated in dependence of a transmitted line current signal by Eq. 2.8 (Automated Systems Group 2007).

Variations are dominated by changes in the bath voltage drop and anode over potential. Both vary with alumina concentration, electrolyte temperature and composition. The bath voltage drop is also highly dependent on anode-cathode distance. To counteract this multivariate dependency, the PCU monitors both cell voltage and the derivation with respect to time. This is based on the assumption that only the alumina concentration varies within a short time frame.

Eq. 2.8 is a simplistic approximation designed to control a cell at or close to constant conditions. The main drawback is that the EMF sums up several effects depending on current density and concentrations and assumes these to be constant. Effects of changes in current density on cell voltage are detailed in chapter 4.3.

If the current is suddenly interrupted the resulting instantaneous new voltage is referred to as the back EMF which is the sum of the reversible potentials and the various contributions to the over potential. The concentration polarisation decays rapidly while the other components decay at different rates.

The PCU controls alumina additions. It subjects the cell to an underfeed-overfeed cycle inducing a variation in alumina concentration and thus in cell voltage. During underfeed the cell voltage increases, as the alumina concentration decreases. It is crucial to switch to overfeeding before the cell starts to decompose the electrolyte and enters a so-called anode effect (AE). In this case evolving perfluorinated carbon gases coat and isolate the anodes. Cell voltage increases to 20 – 40 V until the anode effect is terminated. Figure 2.3 illustrates the dependency of cell resistance on alumina concentration for neutral electrolytes. The alumina concentration for the initiation of an anode effect is not a hard limit, but also highly dependent on local current density.

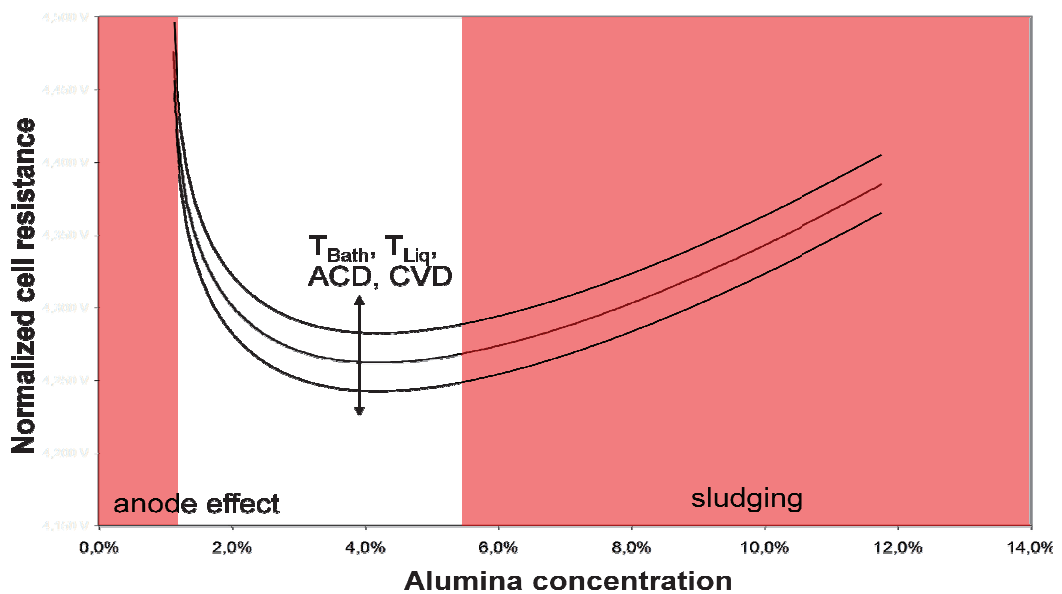


Figure 2.3: Pseudo-resistance curve depending on alumina concentration

The PCU monitors the cell for AEs and other exceptions. If an abnormality is detected a limited set of standard operating procedures is available to counteract the abnormality. In most cases however an operator will be notified to investigate and remove the cause.

2.2 Evolution of cell designs

The original aluminium reduction cell design was focused on making the process happen in the first place. A small carbon crucible was used to contain the melt and a pre-manufactured carbon electrode was used as an anode to introduce electricity into the melt. Elemental aluminium accumulated at the bottom of the cell. As the process was at this time a batch process, the cell was cooled sufficiently before it was broken apart and aluminium metal removed as solid globules. Due to the small amounts produced, the specific consumption of energy or anode material was not an issue.

Very soon after inception, the process moved to continuous operation with the crucible containing the melt determining the operational life time of a cell. Figure 2.4 shows a drawing of one of the early production rooms of ALCOA (Anonymous 2013a), which was founded on the patent of Charles Hall. Cell life exceeded the life time of a single anode already at this stage as can be seen in the varying setting height of the anodes. Neither bus bar configuration nor accessibility of the cell was important at this stage, as all work was done manually.

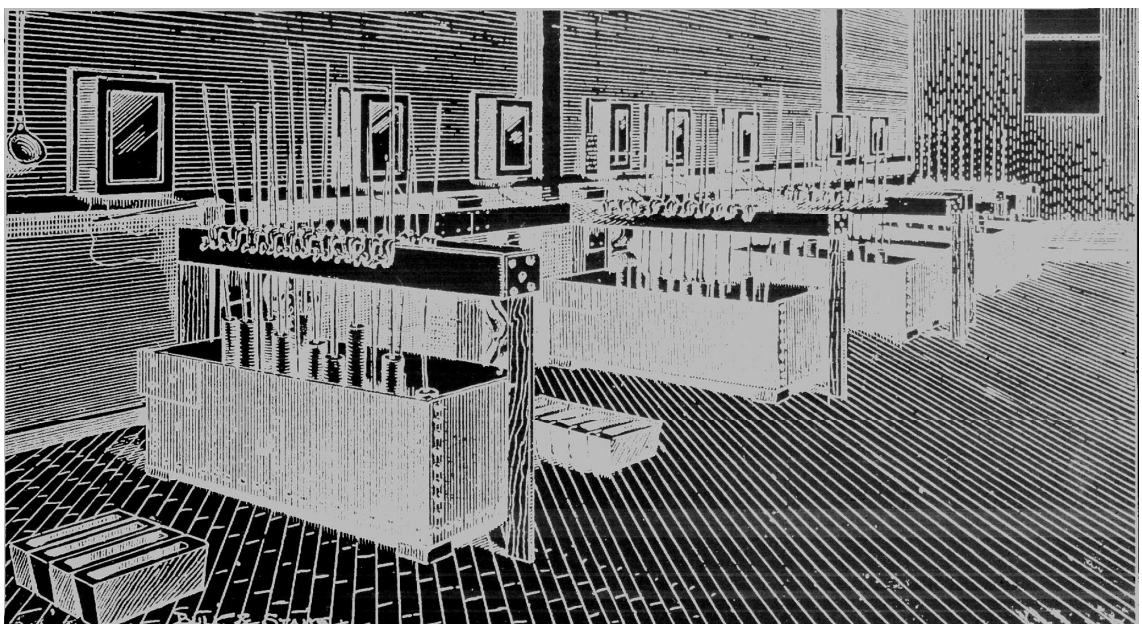


Figure 2.4: Drawing of the early cell designs used by ALCOA

The development immediately aimed at increasing the operational amperage of the cells to increase productivity. The major mean to increase amperage is to increase cell size, as the anodic current density is limited. With increasing cell size, operation procedures became more of a concern.

Special machinery – either floor operated or crane operated – was built to perform operational tasks at the cells. These tasks are:

- Anode change
- Metal tapping
- Alumina addition

The design of high amperage cells has accelerated over the last decades. Current increase was rather slow in the first half of the 20th century. The first ALCOA cells operated at 1.75 kA in 1890 (Beck 2008). In 1940 a typical modern cell was operating at 40 kA. In the late 1960s and early 1970s several technologies were introduced in the range of 130 – 160 kA. Some years later amperages beyond 200 kA were reported (Tabereaux 2000).

In 1981 Aluminium Pechiney developed their AP-30 cell technology operating at 300 kA which dominated green and brown field projects in the next 20 years. By continuously improving the design, amperage was and still is being pushed to 350 – 400 kA until today (Vanvoren, Homsı et al. 2001b, Martin, Fiot et al. 2009).

The most recent developments are in the area of 400 – 500 kA (e.g. RTA AP-50, Dubal DX and several Chinese technologies), with prototype cells operating at 600 kA. These technologies cannot be refitted in existing buildings and will only be used in either green field projects or major brown field reconstructions (Vanvoren, Homsı et al. 2001a, Kalban, Alfarsi et al. 2008).

2.2.1 Alumina Feeding Mechanisms

Until the implementation of the demand-feed-routine, alumina was added in large batches. An operator waited for an anode effect signalling the depletion of alumina. After quenching the anode effect, another large batch of alumina was added to the bath. There were two ways to handle alumina additions at that time. One solution was to use floor operated vehicles, called wheel breakers, which used a massive wheel to crush the anode cover along the side channel of the cell. Another vehicle applied new alumina cover to the broken side. This design is called side-worked cell. Due to the monolithic anode used in Söderberg cells, this was the main feeding mechanism used by that technology.

Anode quality was not as good as with a typical prebaked anode, however. Green paste on top of the Söderberg anode could not be compacted the same way as in a dedicated process. This resulted in anodes with a lower density, limiting current density and resulting in higher air burn and more carbon dust in the reduction line. In addition efficient emission capturing was difficult and treating the mixed off gas from reduction containing HF and anode baking containing PAHs proved difficult to treat.

Even though the Söderberg technology might have resulted in a more energy efficient overall process requiring less capital investments, the environmental disadvantages have led to a phasing out of the Söderberg technology. Starting in the 1970s the majority of cells built were of prebake designs. Existing Söderberg lines were either converted to prebake technology or shut down. Since the crisis in 2009 there are only a few Söderberg plants left in operation.

The second approach for alumina feeding used a pneumatic bar breaker in the center channel of the cell to crush the cover. Dosage units installed into the superstructure of the cell dumped alumina onto the bath through the broken crust.

After the implementation of demand-feed these methods became obsolete and the massive amounts of alumina being fed to the cells was replaced by the

trend towards adding small, controlled amounts of alumina very regularly to operate in a very narrow concentration window of alumina in the bath.

Wheel breakers and side operation were discarded in favour of so-called point feeder mechanisms adding typically less than 2 kg per shot. In some cases old centre work mechanisms have been converted to adopt the aims of point feeders without the need for major reconstruction of feeding mechanics. Such is the case in Hamburg.

The centre bar was shortened and four stubs were added to each cell, breaking the crust at designated places similar to point feeders. The alumina feeding mechanism for centre work is still in place, but the outlet for alumina was reduced in size to reproduce smaller dump weights.

2.2.2 End to End vs. Side by Side

Earlier cell designs for low amperage operation were not concerned with the magnetic field generated by the operating current. Two distinct cell configurations in pot lines evolved.

The first layout is the so-called “end-to-end”. In this case, cells are oriented with the short sides towards each other as illustrated in Figure 2.5 b). The advantage is the ease of access to the long side of cell. These cell designs were originally side-worked cells with vehicles performing crust breaking and anode change. The mechanical equipment installed at each cell could be limited to a minimum. The current flow however is disadvantageous. Current moves in a corkscrew path as it flows along the axis of the row of cells, but also perpendicular in two axes. One axis is horizontal as it moves out of the cell into the collector bars, and back in as it is led back to the anode beam. The other axis is vertically oriented as the current flows downwards through the anode rods and back up through the risers. This leads to a maximum in magnetic field generation. No end-to-end cell was designed for operation beyond 200 kA and only a few plants succeeded in pushing end-to-end cells beyond this amperage (Tarcy, Kvande et al. 2011).

In the other layout the long side of the cells face each other. Accordingly, this type of cells is called “side-by-side”, see Figure 2.5 a).

The advantage is the natural magnetic compensation if the cell is designed with side risers. Additionally to the axis along the potline, current flows only in one perpendicular axis. Current moves in a wave pattern downward along the anode rods and upwards through risers positioned between cells. The magnetic fields generated from these current flows compensate each other. Magnetic fields can be minimized even at high amperages. The highest amperage side-by-side cells operate between 500 and 600 kA today.

Instead of vehicle operation, these cells must be operated by cranes running above the cells as the lack of space between two cells prohibits the entry of vehicles. As the number of cranes per potline is limited, operation tends to be less flexible than in vehicle operated plants. To counteract this modern potlines use cranes only for pot tending and anode change. Metal tapping is done by vehicle and alumina distribution by air slide systems.

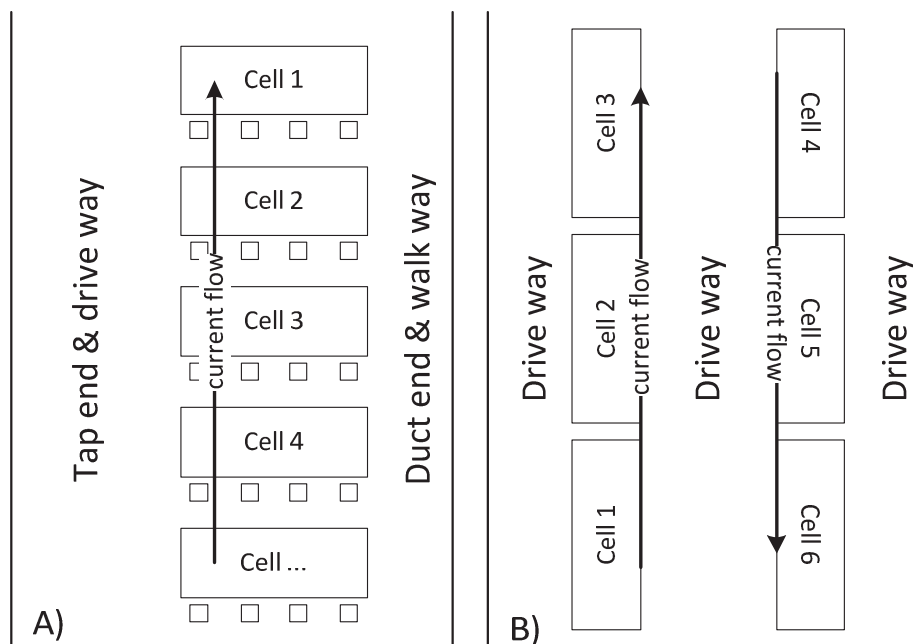


Figure 2.5: Schematics of a side-by-side potline (A) and an end-to-end potline (B)

Today side-by-side potlines are built exclusively. The Hamburg smelter is a magnetically compensated side-by-side technology. Side risers for magnetic compensation were installed during a retrofit in the 1990s.

2.2.3 Development in Relining Materials and Cathode Grades

Originally cells were lined with carbon and steel bars were embedded into the carbon lining to function as a conductor for current out of the cell. Alumina was used as an insulator at the bottom of the cell. The type of insulation applied determines the heat transfer and thermal balance of the cells.

2.2.3.1 Cathode Grades

Whereas cells were lined with a green ramming paste that calcined during preheat and operation, prefabricated carbon blocks were soon used. The first blocks were still made of anthracitic material. Amorphous material is beneficial with regards to mechanical properties and thus long lifetime of cells, but shows a significant aging effect as sodium penetrates into the cell. Additionally electrical and thermal conductivity are low.

To improve electrical and thermal conductivity graphitic raw material was introduced to the cathode. This led to semi graphitic cathodes grades with a graphite content of 30 – 70 % in the grains. These still showed superior mechanical properties but had already improved conductivity compared to an amorphous block.

The next development was a 100% graphitic raw material for cathodes. Mechanical properties are less pronounced than with a semi graphitic grade but electrical and thermal conductivity are higher. Due to the loss in cell life some smelters that reline in-situ in the pot room and operate cells that are not magnetically compensated consider this grade as sub-optimum. Other smelters convert to this grade under an initiative to increase production by increasing

amperage. The better conductivity allows more heat loss through the side wall while reducing electrical resistance of the relining.

To further improve conductivity, fully graphitized cathode blocks were made available by the suppliers. Manufactured from amorphous material this grade is graphitized after baking, giving the material a homogenous structure. Mechanical properties are slightly better compared to 100% graphitic blocks. Due to the graphitic structure of the cell, cathode resistance is low and heat conductivity is nearly one magnitude higher compared to other grades. This necessitates a different cell design favouring more heat loss through the lower side wall (Sorlie and Oye 1994, SGL Carbon 2013). A comparison of mechanical and physical properties of various cathode grades is given in Table 2.5 (SGL Carbon 2013).

Table 2.5: Cathode properties for grades sold today (SGL Carbon 2013)

Property	Unit	Semi-graphitic	100% graphitic	graphitized
Compressive Strength	MPa	32 – 35	23 – 26	33 – 35
Flexural Strength	MPa	6 – 9	7 – 8	10 – 11
Spec. electrical resistivity	$\mu\Omega\text{m}$	29 – 33	16 – 18	11 – 12
Thermal conductivity (30 °C)	W/(Km)	8 – 15	38 – 43	110 – 120
Ash content	%	3	0.7	0.3

2.2.3.2 Insulation Material

Smelter grade alumina was used primarily as thermal insulation material underneath the carbon cathode. The material is cheap and readily available in each smelter. During cell life bath material penetrates through the carbon cathode and infiltrates the insulation layer. This leads to a rapid drop in insulation quality and the cell loses more heat through the bottom of the cell, becoming more susceptible to forming bottom freeze.

To improve long term insulation, a refractory layer was introduced to prevent bath reaching the alumina. There are several designs of insulation layers in use today. One typical design uses a silicate rich refractory brick underneath the cathode in combination with a layer of steel sheets between the refractory and the insulation material to avoid bath penetration. Another approach uses two separate layers of refractory, the first rich in silicate, and the other rich in alumina.

As an insulation material either compacted, smelter grade alumina or calcium silicate slabs are used.

2.2.3.3 Side Wall Bricks

Side wall bricks are made from silicon carbide nearly exclusively today. Some smelters may still use carbon bricks as side wall protection. As SiC has superior heat conductivity and is more resistant against both bath attack and airburn, nearly all smelters converted to SiC side wall.

Material grades are very uniform in the market. However, there are experiments using SiC-bonded SiC brick instead of the usual nitride bond. Also there are tests impregnating the brick to improve the resistivity against bath attack. Both approaches have yet to find wider acceptance in the industry (LMRC 2012, Simonsen 2012).

2.2.4 Typical Modern Cell

Most modern cells developed in recent years show a common theme. All use a magnetically compensated side-by-side configuration and are crane operated. Anodes are prebaked and weight about 1 ton each. The number of anodes is determined by the amperage. Typically numbers are about 40 anodes per cell at an operating current of 350 – 500 kA.

Alumina is supplied by point-feeders using internal electronics to detect bath contact. The number of point feeders can be summarized as 1 point feeder per 50 to 100 kA line amperage.

Alumina is transported by an air slide to the cells to reduce the usage of cranes. Typically metal is tapped by truck for the same reason.

Off gas is collected by a dry scrubber using alumina to adsorb HF from the raw gas. During cell operations suction is boosted to provide acceptable levels of emission capturing.

2.2.5 The P19 cell used at Trimet Hamburg

The modified Reynolds P19 cell design installed in Trimet Hamburg differs on some significant points from a modern cell described in chapter 2.2.4.

Operational amperage is between 175 and 180 kA. 18 anodes are installed per cell with a size of 1495 x 795 x 650 mm, weigh 1.2 tons each. Magnetic compensation was introduced in the 1990's by removing downstream corner risers and installing upstream side risers.

For relining 100% graphitic cathodes are used with a double layer of refractory bricks and alumina as insulation material.

The original center bar breaker was modified to function as a point feeder, feeding at 4 spots in the center channel 1.5 kg alumina per spot per dump.

Both alumina delivery and tapping are done using a crane. The dry scrubber was continually upgraded and boosted suction was introduced to increase the capture efficiency of the cell.

Figure 2.7 shows a picture of the pot room in Hamburg and Table 2.6 shows typical data for the Hamburg smelter. In addition Figure 2.6 shows the numbering of anodes used at the Hamburg smelter for later references.

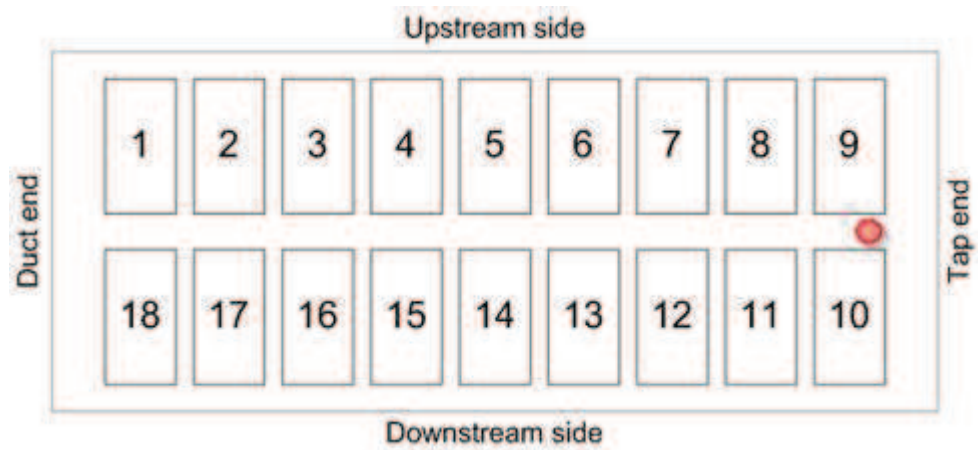


Figure 2.6: Anode numbering in the Hamburg cell with tap and measurement hole marked in red



Figure 2.7: Modified Reynolds P19 cell design installed in Hamburg

Table 2.6: Operating figures for TRIMET Hamburg's P19 cells

Line amperage	180 kA
Current efficiency	93.5 %
Cell voltage incl. externals	4.39 V
Energy consumption	13.99 MWh _{DC} /t _{Al}
Operating temperature	960 °C
Ambient temperature	25 °C
Anode rota	40 h
Anode weight	1200 kg
Gross carbon consumption	532 kg/t _{Al}
Net carbon consumption	419 kg/t _{Al}
Cover material per anode change	400 kg
Alumina content in cover material	50 %
Cover material spillage	20 %
Average cover material temperature	550 °C
Na ₂ O content in alumina	0.37 %

2.3 Global Development of the Primary Aluminium Industry

There is a common theme connecting most of the spatial development in the industry. As aluminium smelting is an energy intensive industry, plants were built historically at locations with easy and cheap access to energy. At the turn of the 20th century, this meant hydroelectric power generation. Originating in Europe from Héroult's patent, sites were found in the Alps' valleys and Norway, whereas Hall founded his first production site in Pittsburgh and later opened sites near the Niagara Falls.

Aluminium production at this time was in the 1,000 tons per year range and the metal was extremely expensive. Due to the lightness of the material, it was used in the aerospace industry early on, seeing a major production peak during both World Wars. After fighting ceased, production was cut back due to lack of demand and for cost reasons.

It took until the late '60s and early '70s to create a private demand that exceeded wartime needs. During these times many smelters were built with modern concepts. Many of these smelters are still in operation today. Trimet's smelters in Essen and Hamburg date back to this period of time for example. During this time the availability of oil and nuclear energy broke the link between hydroelectric power generation and the Hall-Héroult-Process.

In several instances an aluminium smelter was built right next door to a nuclear power plant to provide a base load consumer taking up the same amount of energy all the time. This was especially the case if the nuclear power plant was built to industrialize a former rural area.

The oil crisis in 1973 cut several of these projects short. Even though individual lines were already in operation, planned extensions were abandoned due to the increased price pressure.

The trend to build new smelters where electrical energy is cheaply and reliably available is unbroken until today. The most recent development in this area is the announcing, building or extending of several sites in the Middle East producing more than 1,000,000 tons of aluminium per year each. As a plant of

this size has to handle not only the necessary energy, but twice the amount of alumina and about 60 % of the amount in anodes, logistics are of major concern nowadays as well.

Plants in the Alps were supplied by train. All modern plants now operate their own port facility capable of handling ocean going ships. If a plant is built without access to a harbour, there is a bauxite mine and an alumina refinery close by to justify increased logistic costs for other raw materials and the final product.

One exception to this global move towards low energy cost countries is China. Even though China produced 19.754 million tons of aluminium of the global production of 45.207 million tons in 2012 (Anonymous 2013d), this is not driven by low energy prices but more by internal political mechanisms of the Chinese system. Another notable exception is Inner Russia where there is still potential for increased hydro electrical power generation and thus low cost energy, but transport costs for raw materials and products are considerably higher due to the remote location.

2.3.1 Critical Resources of the Process

The Hall-Héroult-Process uses electrical energy to decompose alumina electrolytically. Consumable carbon anodes are used. Thus, the 3 main resources for the process are electricity, alumina and carbon anodes.

However a highly skilled workforce is necessary for smooth operation as well.

2.3.1.1 Electrical Energy

Primary aluminium production is an energy intensive industry. In 2010, annual electricity generation worldwide was at 20,225 TWh. In comparison 41.15 million tons of primary aluminium was produced worldwide. Using an average

energy consumption of 14.777 MWh_{AC}/t_{Al}, total consumption was 608 TWh. This amounts to more than 3 % of the world electricity generation (Anonymous 2013c, Anonymous 2013d). This percentage has been stable since 2006 varying only by ± 0.1 %, even though specific energy consumption was decreased from more than 15.2 MWh_{AC}/t_{Al} on a global level since 2006. Details are given in Table 2.7. This highlights two different factors:

The aluminium industry as a whole is striving for excellence in energy efficiency, reducing specific energy consumption by 3 % in 6 years in total. This is achieved by both, improving process efficiency in existing technologies as well as replacing out-dated technologies by modern designs.

Aluminium demand is continuously growing over-proportionally when compared to e.g. electricity generation, as the percentage of energy being consumed for aluminium production of the total electricity production is constant while the specific energy consumption per ton of aluminium is decreasing.

Table 2.7: Comparison of electricity generation and aluminium production (Anonymous 2013c, Anonymous 2013d)

Year	Electricity generation	Aluminium production	Specific energy consumption	Share of world consumption
	TWh	Mill t	MWh _{AC} /t _{Al}	%
2006	18,014	33,983	15.206	2.869
2007	18,842	38,132	15.035	3.043
2008	19,157	39,491	15.010	3.094
2009	19,071	36,986	14.795	2,869
2010	20,225	41,153	14.777	3.007

Besides the magnitude of demand, there is one other requirement of the electricity supply. The power supply must have an extremely high availability.

Electrical energy is the sole source of heat used in the process. The electricity not only provides the energy to reduce aluminium, it is also used to heat the cells to the required temperature of about 960 °C. As the electrolyte is only a few degrees above its melting point at this temperature, longer interruption of the power supply leads to cooling and solidification of electrolyte in the cell. This reduces the conductivity of the reduction line during extended power outages. In extreme cases this can lead to a scenario where the continued operation is deemed impossible. Typically, this time frame is given as something between 4 to 6 hours.

If this time frame has expired, all cells have to cool to be manually cleaned from both solid metal and electrolyte. Then each individual cell has to be preheated and restarted. Depending on the size of the plant, this may take from several months to more than one year.

Specific demand of electricity for aluminium production is extremely high at just less than 15 MWh_{AC}/t_{Al}. Looking at the cost structure, energy can amount to more than 40 % of the costs of production in Central Europe.

Figure 2.8 and Figure 2.9 visualize the global and intra-European differences in energy prices (Anonymous 2011). It is easily understandable why primary aluminium production in Central Europe has been under heavy pressure in the last decade.

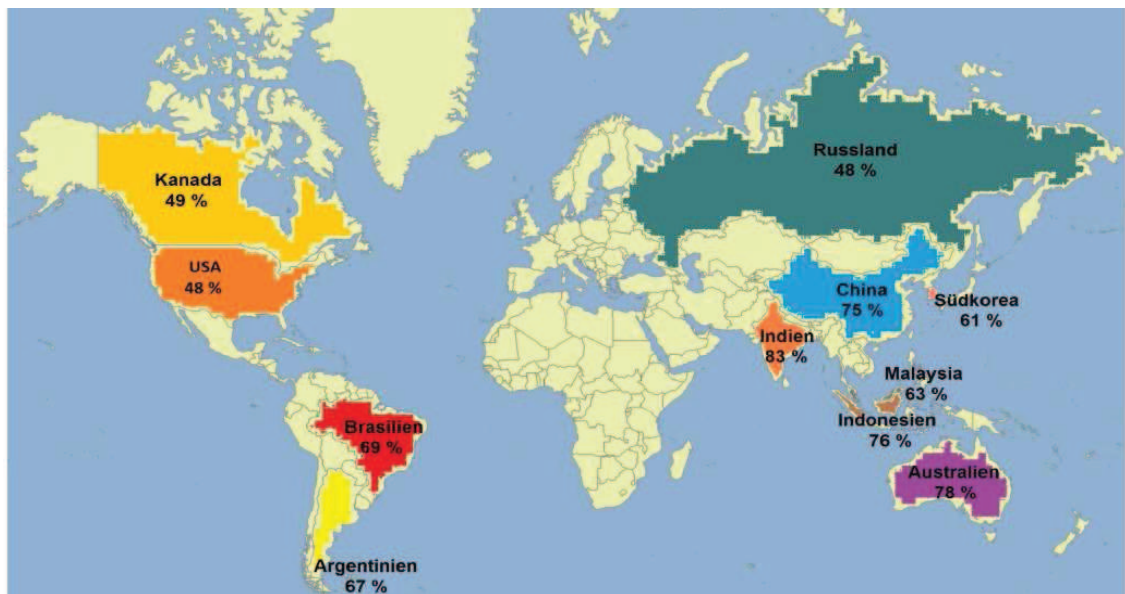


Figure 2.8: Comparison of global electricity prices, Germany equals 100 %, 2011 (Anonymous 2011)



Figure 2.9: Comparison of electricity prices in Europe, Germany equals 100 %, 2011 (Anonymous 2011)

2.3.1.2 Bauxite and Alumina

Aluminium is the most abundant metal in the earth's crust. At more than 8 % it is the third most abundant element. Due to its low electrochemical potential, there are no native deposits. It is always found in its oxidized state.

Typical alumina content of bauxite is 40 – 60 %. It co-deposits with iron oxide and silica, as well as with trace elements such as titanium, gallium and zinc. Depending on composition and trace elements it is considered usable in the Bayer process. Major mining sites for bauxite are in Guinea, Jamaica, Brazil, Australia and Africa for example. In some instances, especially in China and Russia, less suitable types of bauxite are mined and refined as the transport costs for high grade alumina would counter the lower acquiring costs from local sources.

In the Bayer process, alumina is dissolved in pressurized, hot, caustic soda solution. Other oxides are insoluble and removed as "red mud" by settling and filtration. Aluminium hydroxide is precipitated from the clarified solution by seeding with aluminium hydroxide crystals, cooling and reducing of pressure. The washed precipitate is calcined in rotary drum or flash calciners. In some cases, fluid bed reactors are used. Temperatures of up to 1200 °C are targeted to produce anhydrous alumina.

There is always sodium hydroxide co-deposited. Depending on the operation of the precipitator, typical sodium oxide content in the final product is in the range of 0.28 % to 0.5 %. Sodium oxide reacts with AlF_3 in the process forming electrolyte (Thonstad, Fellner et al. 2001, Beck 2008).

Due to the abundance of bauxite, alumina is the least critical of the mentioned raw materials, even though development of refining capacity is not always keeping pace with the increased smelting capacity.

2.3.1.3 Calcined Petroleum Coke and Anodes

In most cases the Hall-Héroult-Process uses prebaked carbon anodes that are continuously consumed as they react with oxygen forming at the anode. These anodes are manufactured from calcined petroleum coke, cleaned and crushed anode butts returned from the potroom and coal tar pitch as binder. The paste is prepared from specified grain size fraction mixed with hot pitch and vibro-compacted into the desired anode geometry.

After green forming, anodes are fired in ring furnaces at maximum temperatures of 1250 °C. In the ring furnace exhaust air is led counter-current to the baking process. Cool air is blown into chambers with hot baked anodes to preheat the gas. The heated air is then conducted into the chambers which are actively fired to achieve maximum temperature. The hot exhaust gas is passed over cool unbaked anodes to preheat them. Figure 2.10 shows a schematic of a modern anode ring furnace (Lützerath 2012).

A firing cycle typically lasts 16 days to 3 weeks as the heating and cooling gradients must be controlled stringently to prevent thermal cracking in the anodes (Grjotheim and Kvande 1993).

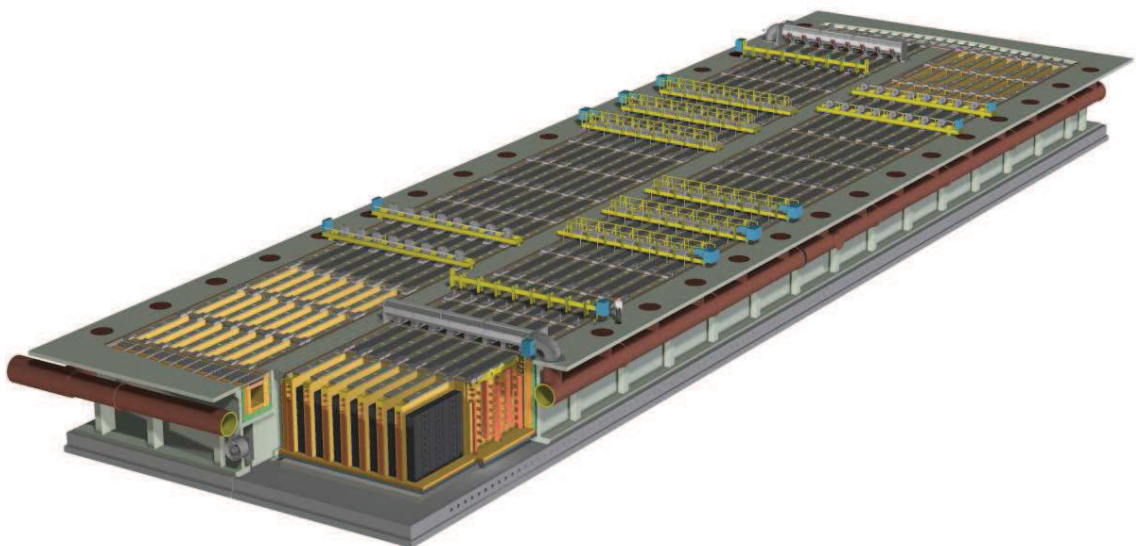


Figure 2.10: Schematic of an open pit anode ring furnace (Lützerath 2012)

Process control in the paste plant and during baking is critical to provide an anode that has satisfactory properties. However material characteristics of the raw material play a major part in determining the properties of the final product as well. E.g. sodium impurities are introduced through the recycled anode butts if the anode butts are cleaned poorly. This results in an increase in air reactivity of the anode (Fischer, Meier et al. 2006).

For the last decades, several major companies have researched to replace the sacrificial carbon anode with an inert anode. No attempt has been able to grow beyond laboratory scale so far, as on the one hand current density is typically lower and on the other hand process setup and control have to change dramatically to accommodate an inert anode (Welch 2009).

As petroleum coke – the major raw material for anode manufacturing – is a residual product in oil refineries, availability is heavily linked to the oil industry. With the exploitation of oil deposits not considered suitable a decade ago and with changes in the refineries themselves to improve the yield of higher margin products, coke quality is declining continuously. Sulphur content and content of trace elements such as vanadium, nickel and calcium are increasing continuously (Cannova, Sadler et al. 2007, Lindsay 2013). An increase in V, Ni and Ca result in an increased air and carbon dioxide reactivity of the anode and may impact the product portfolio of the cast house. Sulphur is usually strictly limited by the authorities with a strong tendency to reduce allowed sulphur content further.

It is more and more difficult for the carbon plants to produce anodes that satisfy the demands of the reduction department at competitive costs while staying within limits imposed by environmental regulations.

2.3.1.4 Workforce

Even though labour costs accounts for only about 5 % of the operating costs of a typical mid-European smelter (Figure 2.11), the workforce is pivotal for successful operation of any smelter. Technical issues in smelter operation and management are well discussed and documented with references too numerous to list. All this information is insignificant if it is not consistently applied to daily operation by all employees.

Whereas previously smelter personnel were typically recruited from the unskilled workforce, the trend in the last one to two decades has been to employ a growing percentage of skilled labourers. This trend extended to exclusively hiring operators skilled in a technical profession.

The reason for this is a shift in the perception and recognition of the work to be done in a reduction line. Whereas previously a mentality of “getting the work done” was prevalent in the industry, daily operation is being credited today with a major need for professionalism.

While locations of green field smelters are often chosen with regards to energy cost and availability, this has effects on the availability of personnel. Previously it was a common practice to build a green field smelter and power plant in a region to provide an industrial base for continued development. In this case skilled labour was difficult to employ as incentives were needed to move people to remote locations. Today these smelters are competing with industries which settled in the area later and offer more attractive jobs.

It takes time to fully train personnel for work in the pot rooms. In addition the process itself has a large internal time constant. It can take weeks to months until poor work practice shows in process data. In this respect the process is significantly different from e.g. manufacturing of semi-finished products. It is crucial to always have a mature workforce. This results in a growing incentive to retain fully trained employees and continuously motivate them to further improve.

2.3.2 Trends in Cost Structure

Today the largest share of expenses in aluminium production in Central Europe is associated with energy. This includes the working costs per MWh as well as grid usage costs, taxes and levies. Figure 2.11 illustrates a recent breakdown of costs for Trimet. Energy nowadays constitutes about 40 % of production costs, followed by alumina (30 %) and anodes (15 %). 5 % of overall costs are spent on personnel. The remaining 10 % cover all maintenance, investment and amortization.

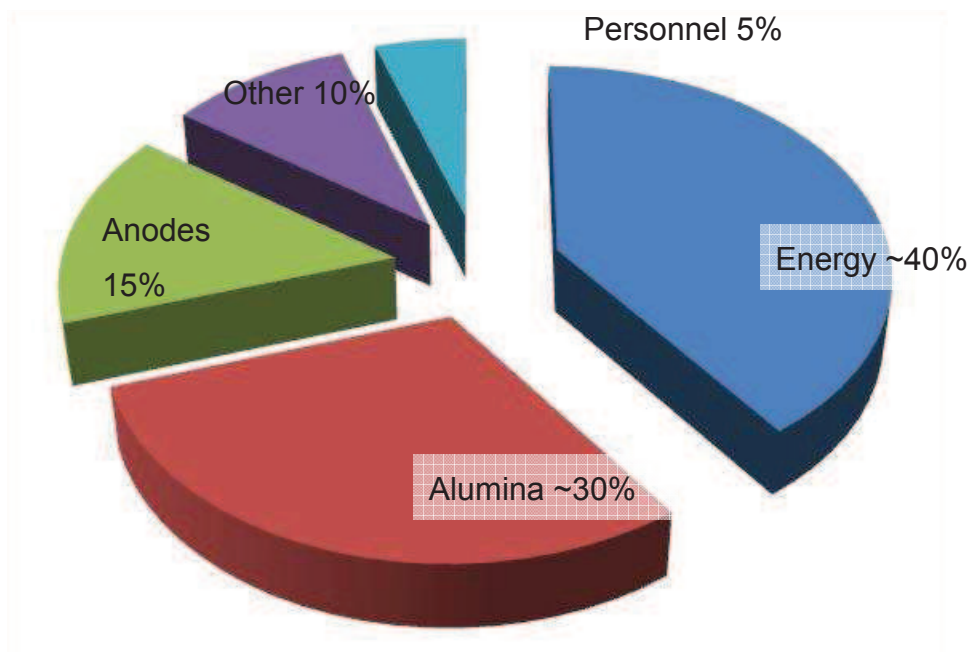


Figure 2.11: Recent cost structure in a Central European smelter

This breakdown is only valid for a smelter that has been in operation long enough to amortize its construction cost. Newly built smelters will have a larger share of amortization to include in the cost structure. Construction costs for smelters are quoted at 4,000 US\$ to 9,000 US\$ per ton annual production capacity (Vanvoren, Homsı et al. 2001a, Benkahla, Caratini et al. 2008). This is only slightly compensated for by the lower energy consumption of modern cell technology. While smelters built in the '70s can achieve 14.0 MWh_{DC}/t_{Al}, modern

smelters are reported to operate as low as 12.5 MWh_{DC}/t_{Al} (Thibeault, Bécasse et al. , Welch 2011). This is reducing the energy cost by only 5 % if the price per MWh is assumed to be constant. This reduces the energy costs from 40 % to 38 %.

For this reason locations for smelters must offer extremely competitive energy prices, as anodes and alumina are a globally traded resource with a virtually uniform global price.

This axiom has been true for the last half century all over the world. During this period the cost percentages for alumina and anodes have been nearly constant. However, the major shift has been from personnel and maintenance costs as well as amortization towards energy cost.

This trend is continuing and maybe even accelerating today. If it continues unabated the feasibility of aluminium production is at risk in Central Europe and other economic regions that are increasing taxation on energy.

2.3.3 Environmental Influence

2.3.3.1 Fluoride Emissions

Using large amounts of molten cryolite, gaseous fluoride emissions have always been a concern of the industry. Since the '70s various scrubbing systems have been in use. Whereas in earlier times, a wet scrubbing for roof ventilation was the norm, nowadays the off-gas of each individual cell is captured and conveyed to one or several dry scrubbing stations using alumina as an adsorbent for gaseous HF emission. In cooperation with alumina suppliers the physical properties of alumina have been enhanced to provide better HF adsorption by providing a larger surface area per weight unit of alumina. Simultaneously the calcining of alumina has been optimized to minimize crystal water content, which is a major contributor to the generation of HF (Iffert, Kuenkel et al. 2006, Iffert 2008).

The current situation in virtually all prebake anode pot lines is that the atmosphere is good enough that no roof ventilation scrubbing is necessary and personnel exposure to emissions is so limited that respiratory protection equipment can be limited to work practices that lead to above average exposure such as anode change.

2.3.3.2 Sulphur Emissions

The second major emission from pot lines is sulphur dioxide. Sulphur enters the process through the natural sulphur content of calcined petroleum coke used in anode manufacturing, as the calcining temperature of the anode bake furnace is – on purpose – insufficient to desulphurize coke. The sulphur content is carried over.

Sulphur is then oxidized in the cell along with anodic carbon. It is generally agreed that a certain amount of sulphur is beneficial for the reactivity of anode carbon (Hume, Fischer et al. 2006, Perruchoud, Meier et al. 2006). A sulphur content above 1.5 % is targeted.

Typically sulphur dioxide in the off-gas is not treated. Only a few smelters located on the sea shore are using sea water scrubbers for the off-gas to remove sulphur dioxide.

Sulphur emissions are restricted by the government by limiting the sulphur content in the anodes. In Germany the limit is 3.0 % sulphur. Initiatives are pushing for stricter limits as low as 1.5 %. With regards to the decreasing amount of low sulphur petroleum coke these initiatives have to be considered with care.

2.4 Changing Trends in Energy Generation

2.4.1 Hydro Power

Hydro power has been used to provide reliable and cheap energy since the end of the 19th century. The first European smelters were situated in Norway and the Alps region due to the availability of hydro power. In the case of the Alps region this was in disregard of the higher logistic costs of moving both raw materials and products by train. Even though investment costs for constructing dams are considerable, extremely low operating costs provide feasible returns on investment.

However as nearly all viable locations have been put to use decades ago, there is little room for expansion. Only some rivers in remote locations – such as Siberia or Central Africa – hold potential for significant hydro generation.

Besides lack of attractive locations for hydro power generation, increasing complexity of an approval process as well as protests by local citizens against massive infrastructure projects, there is little possibility to expand hydro power generation in Central Europe.

2.4.2 Nuclear, Coal and Oil Power

In the 1960s and 1970s logistics were deemed more important as smelters capacity per site increased. Additionally with the advent of nuclear power plants, cheap energy was no longer limited to hydro power. Smelters were built to provide a base load consumer for newly established nuclear power plants. Two examples of this strategy were the smelters in Angelesy, Wales, UK and Stade, northern Germany. Both plants featured their own harbour facilities for handling raw materials and an adjacent nuclear power plant in a location without other base load consumers.

These were not the only smelting sites developed in this time. Smelters were constructed in developed areas where energy was readily available due to coal

or lignite mining as well as oil extraction. Examples are the smelters in Central Germany, South Africa and Australia as well as the first smelting sites in the Middle East.

This trend holds true until today. Major smelting sites are developed where there is oil and gas readily available. A sizeable fraction of new sites are announced in the Middle East due to the availability of cheap gas. However due to the incentive to export gas to Europe and Japan, the Middle East is building nuclear power plants to fulfill their demand for cheap and reliable energy. This is also an effort to reduce the emissions of green house gases (Anonymous 2012).

2.4.3 Geothermal Power

Geothermal energy is readily available and cheap to convert to electricity. Availability is limited to certain geological locations though. Iceland for example generates a substantial amount of electricity from geothermal sources. In Iceland there were 1,707 MW of generation capacity installed at the end of 2006. Of these, 1,162 MW (68.1 %) were hydro and 432 MW (25.3%) were geothermal power (Ekeberg, Schaumburg-Müller et al. 2007).

Outside of suitable geological areas, geothermal power generation is not feasible on an infrastructural scale.

2.4.4 Wind Power

Wind and solar power can be feasible depending on location. In both cases it has to be kept in mind that both sources do not supply power constantly.

Wind energy is strictly limited to the actual wind at a particular moment. In case of insufficient wind – or wind speeds exceeding the upper operational limit – there is no generation from wind mills. Figure 2.12 illustrates the overall utilization of wind mills in Germany in 2006 (Pieper, Fleckenstein et al. 2007). It

is evident that wind power generation most of the time is only infinitesimal compared to the installed capacity.

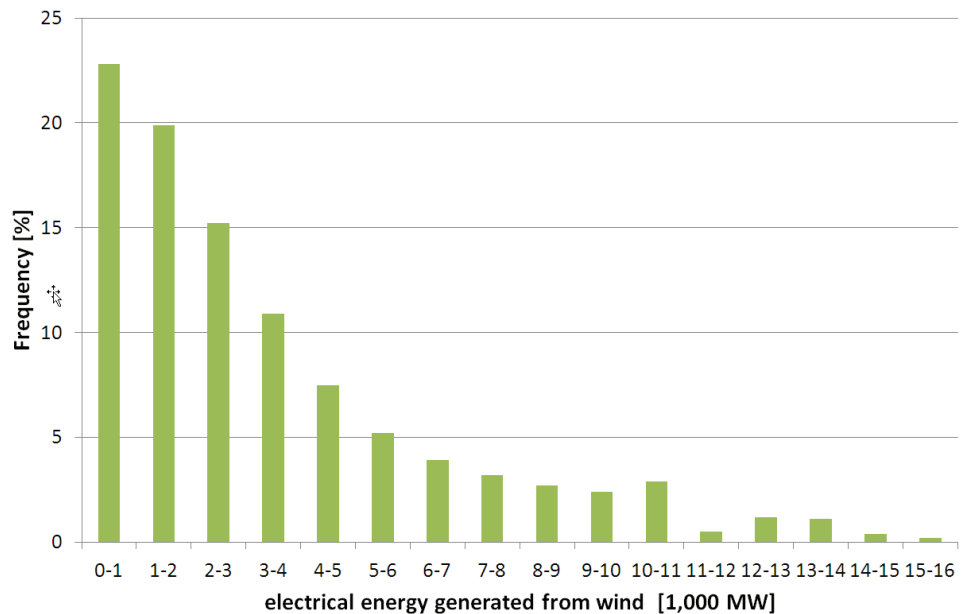


Figure 2.12: Degree of utilization of 16,000 MW installed wind energy generating power in Germany in 2006 (Pieper, Fleckenstein et al. 2007)

2.4.5 Solar Power

Solar power is also limited to the particular weather conditions. In certain areas – e.g. California, USA – there is a strong link between electricity generated from solar power and energy consumption by households powering up air condition systems.

With the development of molten salt heat storage there is also the possibility to extend the electricity generation time well into the night if a solar thermal power plant is upgraded accordingly. However the current technology is insufficient to bridge the whole night (Hoff 2011).

2.4.6 Summary on Renewable Energy Sources

In recent years there has been a push to reduce green house gas emissions. For energy generation this is equivalent to reducing CO₂ emissions. Discounting nuclear power the only viable alternative is renewable energy generation to reduce CO₂ emissions. The oldest renewable energy in use is hydro power, discussed in 2.4.1

Other well-used renewable energy sources are wind, solar and geothermal power. Depending on individual location these means of electricity generation are in use for an extended period of time as well.

Other means of generation are either in an experimental or prototype scale or their respective generation capacity is so limited that they do not provide a significant portion of the generated energy. This encompasses tidal power and biomass combustion.

All these generation means suffer from at least one, and often several, of the following constraints:

- difficulty to increase the generated capacity
- geographically limited
- fluctuating energy generation
- low energy generation capacity

2.5 “Energiewende”, Energy Reorientation

The German term “Energiewende” is difficult to translate. Literally the translation would be energy ‘reorientation, transition or change’. The term “Wende” in Germany refers to the collapse of the state of East Germany in 1989. Interestingly the term “Energiewende” is older – it originated from a book published in 1980 (Krause, Bossel et al. 1980). However, the significance attributed to the energy reorientation today is as high as the one attributed to the political change in 1989.

Today the term designates a significant change in energy policy. It encompasses a complete reorientation from a demand driven market to a supply driven market. It associates also a shift from centralized to decentralized power generation and a move away from fossil fuels to CO₂-emission-free technologies.

The effects of these changes are discussed in the following sub-chapters.

2.5.1 Change from Demand to Supply Driven Market

Traditionally a small number of power companies operated large, centralized power plants. According to the actual power demand of the larger area the utilization of the plants was adjusted. In off-peak times energy prices were extremely cheap as the alternative was to cut power generation and thus decrease efficiency of the plants.

Power consumers – such as aluminium smelters – which operate at a constant load and thus lead to a stabilisation of the power grid were honoured with reduced power prices.

Nowadays with an increased share of volatile renewable energies, this system is about to change. Coal-fired power plants are adjusted according to the changing energy generation by renewable energies. Figure 2.13 shows the total grid load and the residual load in Germany over an extended period of time

(Schulz 2012). The residual load is defined as the load that has to be provided by traditional power plants.

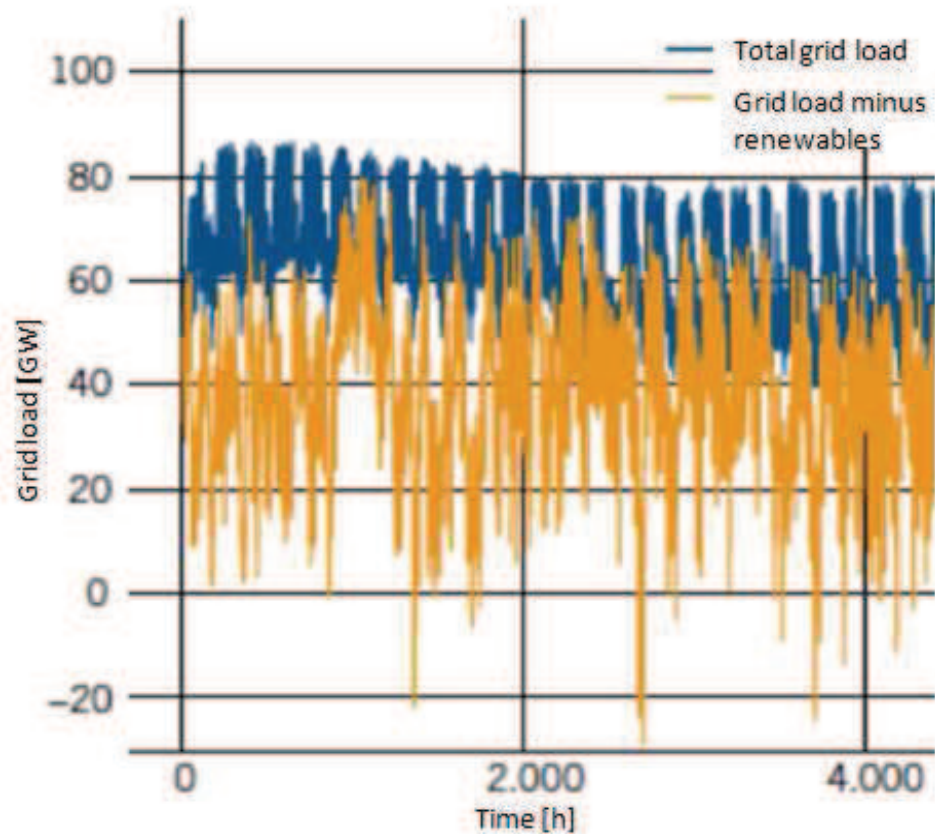


Figure 2.13: Total grid load and residual load (Schulz 2012)

A wide spread of load that has to be covered is easily visible from the figure, as well as a rapid change in load is necessary. Special consideration has to be given to the repeated times where the residual note is negative – renewable energy provides more electricity than needed. Due to the legal constellation in Germany, this power has to be bought by grid operating companies and distributed. Effectively this can lead to negative power prices listed on the exchange.

It should also be noted that at about 1,000 hours all renewable generation capacity supplied nearly no energy at all, necessitating a backup power supply in the form of conventional power plants. This is in line with data provided in Figure 2.12.

2.5.2 Change from Centralized to Decentralized Power Generation

With the adoption of different energy sources, another trend started growing as well. To link both electricity and heat generation, combined power and heat plants were built. In some cities – such as Hamburg and parts of the Rhine-Ruhr-Area, there were extensive networks for district heating already available. These were connected to the new highly efficient power plants.

As taxes and levies on electricity increased, small decentralized combined heat and power plants were constructed. As these typically belong to the owners of serviced property, no electricity tax has to be paid on power generated and consumed on site. Additionally construction of such devices was further encouraged by tax incentives and subsidies.

The main challenge is to link all these decentralized electricity generation capacities in a way that it can be used to provide power to the grid. There are companies nowadays specialised in operating such decentralized installation to maximum effect and profit.

2.5.3 Impact on Use Pattern

The changes in electricity generation demand a change in energy consumption. The biggest challenge today is to match volatile energy consumption with volatile energy generation. The matching has been achieved in the last years by only varying energy generation in conventional power plants. Gas turbines were the means to an end as they are highly flexible in operation. They can shed load

in a matter of seconds and thus balance changes in electricity generation by renewable energy sources.

Since 2012 energy prices at the energy exchange (EEX) are decreasing due to increasing amounts of renewable energy that have to be integrated into the grid. The additional cost of renewable energies is levied onto all electricity consumers in a separate allocation system. This has led to gas turbines not being feasible anymore as the number of hours with energy prices above full costs are diminishing.

There is additional demand for regulatory power capacity that cannot be provided on the generation side. Thus there is an incentive for the consumers to investigate their ability to operate with varying load.

The aluminium industry as a major power consumer has to be at the forefront.

3 Material and Thermal Balances

Synopsis:

This chapter expands on the operational constraints given in the objectives of the thesis. To elaborate on those, a detailed material and thermal balance for the cell as it is operated at Trimet Hamburg is compiled, detailing main and side reactions as well as material streams and all associated energy requirements. Including side reaction an energy demand of 6.455 MWh/t_{Al} at 93.55 current efficiency is determined. Lastly heat loss from the cell is discussed based on heat loss measurements conducted on-site. These show an error of 10% or less compared to the theoretical values.

All thermal calculations are done with or use data from the HSC Chemistry 5.0 software (Roine 2002).

3.1 Process Fundamentals

3.1.1 Operational Constraints

In the Introduction, the objectives of this thesis and the major constraints for operating the process continuously and successfully were described. These major constraints that span the process area need further explanation. Figure 3.1 illustrates these.

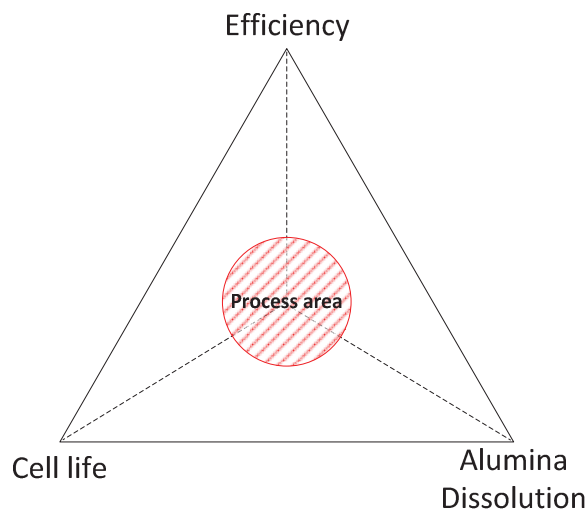


Figure 3.1: Constraints of aluminium production

3.1.1.1 Alumina Solubility

The ability to dissolve alumina is essential for an uninterrupted process. Even though the cryolitic electrolyte is able to dissolve alumina up to 8 %, the typical alumina content is between 2 – 4 %. With 5.15 t of liquid bath as inventory, this equates to about max. 100 kg of alumina that is freely available for the process if it swings within the full range of alumina concentration. For a production rate of 56.5 kg_{Al}/h this is less than one hour of raw material supply in the best case.

If the cell is not able to dissolve the continuously added alumina, alumina sludge will form on the bottom of the cell hindering a uniform current flow. More damaging to a stable process is that if the alumina content of the bath drops below the lower limit, the electrolyte will be decomposed, forming PFC gases and pushing the cell into an anode effect.

Alumina is fed at – or close to – room temperature into the electrolyte. Before dissolving, the alumina has to be heated to process temperature. The only readily available heat source is the superheat of the electrolyte. To propagate heat transfer from the electrolyte to the added alumina good stirring of the bath is essential. This is achieved by natural bath movement induced by the metal movement as well as by bubble formation underneath the anode and the subsequent release. If there is free space between the top crust of the cell and the surface of the bath, alumina is known to spread out along the bath surface before dissolving. This increases the volume of bath in contact with the alumina.

The cell at Trimet Hamburg adds 6 kg of alumina each shot. The alumina addition is distributed over 4 feeding locations which are all activated together. 3.54 kWh are needed to heat and dissolve this mass of alumina. Eq. 3.1 details how much liquid bath at a given superheat is needed to supply this amount of energy without freezing bath.

Figure 3.2 represents the equation graphically. The necessary bath mass increases hyperbolically with decreasing superheat. It should be noted that at 1.3 °C superheat the entire energy of the liquid bath would be necessary to

dissolve a single shot of alumina. The addition of 6 kg of alumina to the bath increases the alumina content by 0.11 % as calculated by the Solheim equation. This lowers the liquidus in the given operational range by approximately 0.7 °C, compensating half the needed energy (Solheim, Rolseth et al. 1995).

$$m_{Na_3AlF_6} = \frac{(Q_{Al_2O_3,heat} \cdot (T_{bath} - T_{ambient}) + Q_{Al_2O_3,dissolve}) \cdot M_{Al_2O_3}}{Q_{Na_3AlF_6,heat} \cdot \Delta T} \quad \text{Eq. 3.1}$$

With	$m_{Na_3AlF_6}$	bath mass necessary to supply heat for dissolution
	$Q_{Al_2O_3,heat}$	specific heat capacity of Al_2O_3
	$Q_{Al_2O_3,dissolve}$	specific dissolution energy of Al_2O_3
	$Q_{Na_3AlF_6,heat}$	specific heat capacity of molten Na_3AlF_6
	$M_{Al_2O_3}$	mass of one shot alumina
	$T_{ambient}$	ambient temperature of the alumina
	T_{bath}	bath temperature
	ΔT	superheat

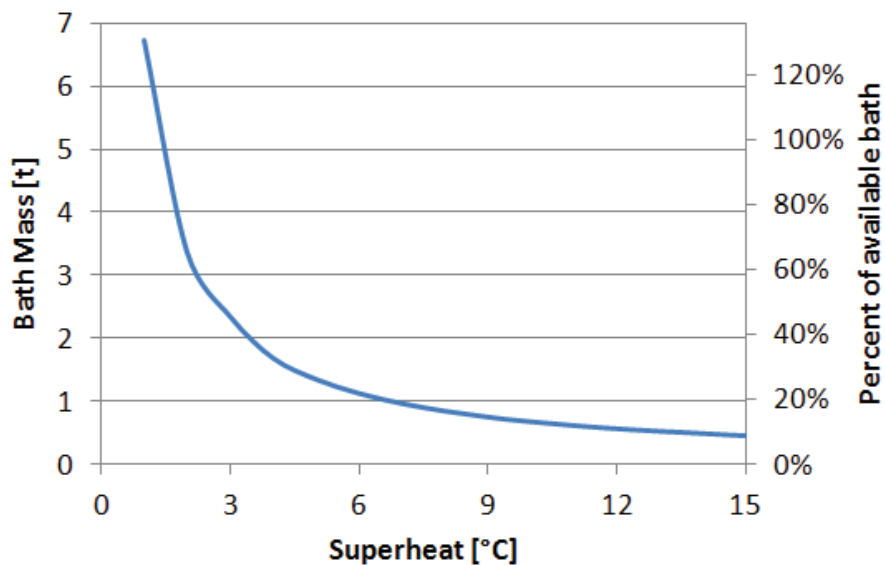


Figure 3.2: Bath mass necessary to heat and dissolve one shot of alumina weighing 6 kg

The above calculation is only valid if no side ledge is melting or freezing to provide heat for alumina dissolution. Even though the cell's energy input is capable of supplying enough heat to dissolve the average amount of alumina added, during a feeding cycle of overfeeding and underfeeding alumina the energy content in the cell and thus the temperature varies. As a consequence this leads to a melting and freezing of ledge during a feed cycle. During overfeed additional energy is needed. A solidification of bath would be expected to release the heat needed for dissolution. Iffert however found an increase in liquid bath mass during an extended overfeed period (Iffert 2008). His explanation is a superimposed lowering of the liquidus temperature due to the increasing alumina concentration as can be seen in Figure 3.3. With a lower liquidus he found an increase in superheat and thus melting of ledge.

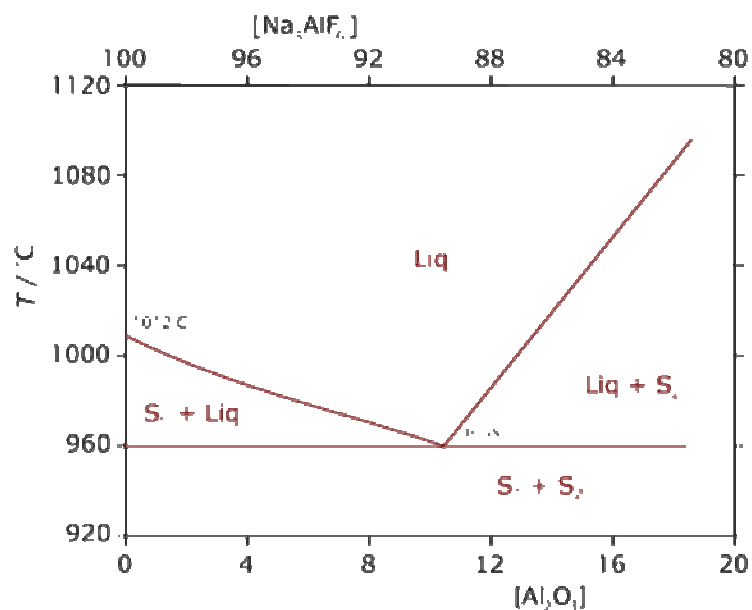


Figure 3.3: Phase diagram $\text{Na}_3\text{AlF}_6 - \text{Al}_2\text{O}_3$

3.1.1.2 The Ability to Retain Ledge

The electrolyte used in the aluminium production electrolysis is a fluoride molten salt, consisting of NaF and AlF_3 . This molten salt is highly corrosive. Besides dissolving alumina, it attacks all refractory materials and eventually dissolves them. Internal exposure tests have shown that silicon carbide refractory used as side wall refractory can withstand direct contact with molten electrolyte for approximately one week.

Typically cells are in operation 5 to 7 years. To achieve this life time the side wall has to be covered by a frozen layer of electrolyte at all times. If the internal energy of the system is too high, e.g. the superheat is above average, side ledge will melt. This will increase heat flux through the side wall to compensate for the increased energy. Additionally the cryolite from the side ledge will dilute the additives in the bulk of the bath by increasing the available liquid material. This increases the liquidus temperature and thus decreases the superheat. Figure 3.4 illustrates this effect.

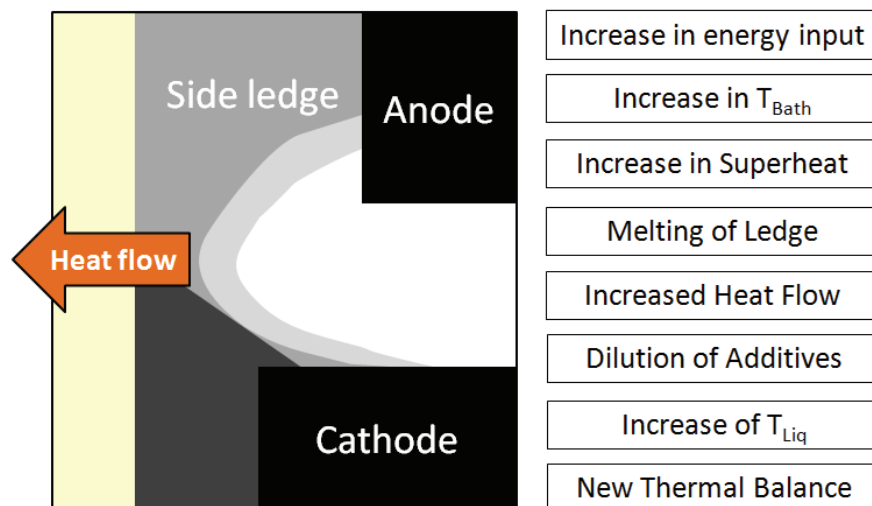


Figure 3.4: Effect of increased internal energy

If this compensatory effect is not sufficient to stabilize the cell – e.g. the root cause for increased heat input is not removed – all side ledge will melt. Then the side wall refractory will be in direct contact with the molten electrolyte and eventually the cell will fail. Due to the high costs associated with relining a cell, this has to be avoided.

3.1.1.3 Current Efficiency and Energy Consumption

According to Faraday's Law the amount of electrolytic deposit is proportional to current and time. In an aluminium reduction cell the reaction is not free of losses. A significant characteristic is the current efficiency, the quotient of produced aluminium and the theoretical maximum:

$$\eta = \frac{M_{Al}}{I \cdot n \cdot t_s \cdot \frac{m_{Al}}{n_e \cdot F}} = \frac{M_{Al}}{I \cdot n \cdot t_h \cdot 0.3356}$$

Eq. 3.2

With	η	current efficiency
	M_{Al}	mass of aluminium produced
	I	line current
	n	number of cells in line
	n_e	number of electrons transferred, 3
	t_s	time in seconds
	t_h	time in hours
	m_{Al}	molar mass of aluminium
	F	Faraday's Constant

A well run modern smelter operates at above 93 % current efficiency (Rieck, Iffert et al. 2003). Newest technologies report values above 95 % as achievable (Benkahla, Caratini et al. 2008, Kalban, Alfarsi et al. 2008, Zarouni, Zarouni et al. 2011).

Increasing current efficiency has been the main goal for an easy way to increase metal output without need for expansion. Increasing current efficiency also mitigates fixed costs per ton of aluminium produced as a cell does not require any different handling or maintenance if current efficiency is increased. In fact only additional alumina and to some degree additional energy is needed, whereas gross carbon consumption is fixed to line amperage and the size of the anode. This results in extremely low marginal costs. For this reason operating at higher line currents at increased current efficiency has been and still is a driving force in the industry.

However a change of philosophy from productivity towards least specific energy consumption is happening at present (Welch 2011). This is due to increased energy costs for many smelters, especially established smelters in western countries – such as the smelters operated by Trimet in Germany.

Populace and less energy intensive industries are competing with aluminium smelters for energy. This – in addition to politically motivated taxes and tariffs on energy – leads to increased energy prices which are threatening the continued operation of many smelters (Kruse 2004). As a consequence the focus is shifting from producing the maximum amount of metal to minimizing cost per ton produced – especially minimum energy cost per ton. The effect can be seen in reduction of global energy consumption shown in Table 2.7. In only 5 years the global average energy consumption for producing aluminium decreased by 3.4 %. This figure includes both a replacement of older capacity with modern technology, as well as the reduction in energy consumption of existing technology.

The specific energy consumption can be calculated by dividing the energy consumed by the metal produced. The equation can be simplified to depend on cell voltage on the one hand and current efficiency on the other:

$$E_{Al} = \frac{U \cdot I \cdot t}{M_{Al}} = 2.9797 \cdot \frac{U}{\eta_{CE}} \quad \text{Eq. 3.3}$$

With	E_{Al}	specific energy consumption
	U	cell voltage
	M_{Al}	mass of aluminium produced
	I	line current
	η_{CE}	current efficiency

If efficiency decreases, more carbon monoxide evolves in the anode gas. This can occur through various means. The mechanics are detailed in chapter 3.2. The loss in efficiency can be initiated by operating patterns as well as by temporal effects. Current efficiency varies with interpolar distance, decreasing if the distance is too small as a clear separation between anode gas and reduced metal is no longer given.

The same effect occurs if the metal pad stability decreases. Wave patterns on top of the metal pad lead to variations in interpolar distance with the top of the wave being too close to the anode.

The operating point of the cell may cause decreases in efficiency as well. If the superheat is too large, the solubility of the electrolyte for reduced metal is increased, deteriorating separation of anode gas and produced metal. The same effect can occur if the chemical composition of the bath favours metal dissolution.

Operating practice has a major impact on efficiency as well. For example if after an anode change an anode is in direct contact with the liquid aluminium, the anode partially shorts the cell. Current may pass through the anode into the aluminium without taking part in the electrolytic process, effectively resistance heating the cell.

As decreases in efficiency typically lead to additional heat being introduced to the cell and thus increasing superheat, efficiency losses are self amplifying.

For typical smelters today the ranges of current efficiencies between 93 % and 95 % and specific energy consumptions between 12.5 and 14.0 kWh_{DC}/kg_{Al} constitute a narrow window to operate within. This range has been stable for the last two decades, as the emphasis was towards producing more metal instead of reducing energy consumption (Welch 2011). Lower values will make a smelter uncompetitive under normal circumstances. If the process is run with a different philosophy – as is the case with power modulation – losses in efficiency have to be offset by higher gains in energy price or other revenues associated with providing energy services to grid operators for example.

If the gains cannot compensate increased inefficiencies an already bad situation is turned worse.

3.1.2 The Challenge of Power Modulation

Power modulation is strictly speaking not novel to the Hall-Héroult-Process. Novel is the perception of process instabilities as desirable instances for generating additional revenue in an aluminium smelter. Even if the amount and occurrence is optimized to minimize the effect on production and process efficiency, there will still be a negative impact. The essential issue is to determine the point at which the loss of efficiency accelerates. It is expected that within a narrow band around the optimum operation point efficiency losses will be acceptable and the losses will increase exponentially when the process is pushed beyond a certain point. Figure 3.5 illustrates this theory. Even if the cell is not operating at an optimum point for constant energy input, efficiency will deteriorate if the energy input is modulated.



Figure 3.5: Effect of power modulation on process efficiency

The difficulty is to keep the process within profitable operation limits while inducing an additional variance. To date all process control strategies aim at keeping the cell in thermal balance. This is determined by keeping the cell within a limited defined bath temperature and liquidus temperature band. This is only meaningful if the energy input to the cell is constant. Only then can energy loss and the thermal state of the cell be targeted as constant as well. This dictum does not hold true anymore if the energy input is deliberately modulated. Tracking the energy state of the cell becomes a sophisticated problem. Energy input, energy content, energy loss and used process heat become parameters that have to be determined continuously. At the moment this is only possible for the energy input. All other coefficients can vary significantly without being detected immediately.

3.2 Material and Thermal Balances

The principle of conservation of mass and energy leads to a mass and energy balance which is given by Eq. 3.4 and Eq. 3.5 respectively.

$$m_{\text{accumulation}} = m_{\text{in}} - m_{\text{out}} \quad \text{Eq. 3.4}$$

$$Q_{\text{accumulation}} = Q_{\text{in}} - Q_{\text{out}} + Q_{\text{conversion}} \quad \text{Eq. 3.5}$$

With m mass
 Q energy

Over any reasonable time the mass accumulation in any reduction cell is zero. At certain times however mass can accumulate or be removed operationally from any given cell.

3.2.1 Envelope of the Material and Thermal Balance

The main reaction is taking place between the underside of the carbon anode and the top surface of the liquid aluminium pool. Due to the encapsulated nature of the cell, it can be assumed that the underside of the crust, the electrolyte and the gas between both have the same temperature and exchange heat continuously and uniformly. All reactions happening in this zone have to be included in both the thermal and material balance. Reactions occurring outside of this boundary, such as partial reaction of gases with ambient oxygen cannot be included in the thermal balance as the generated heat is immediately lost to the off gas. They are also outside the boundary for the material balance as ambient oxygen is in excess. This defines the top part of the boundary to include the crust covering the electrolyte and the anodes, but not reactions occurring above the crust using ambient media such as oxygen.

By this definition, the reaction of anode carbon with ambient oxygen – commonly called anode air burn – is not included in the thermal balance. Even though one reactant is anode carbon, which indicates that the reaction should be included in the thermal balance, ambient air is penetrating into the cell. This is only possible to a significant extent if the cover integrity is compromised. This

will also create an additional heat sink due to increased radiation balancing the additionally generated heat.

For the thermal balance, ohmic heat generated in the anode and in the contact resistance from anode rod to cast iron to anode has to be included. The resistance of the rod and yoke can be excluded as they are in contact with ambient air.

The other boundary for the balance has to include the body of the cell, including the refractory and steel shell. For balance purposes it is not possible to distinguish between the liquid media contained in the cell and the refractory itself. There is no temperature gradient associated with the various interfaces. This indicates that heat transfer is imminent and balanced. On the vertical interface on the side of the cell, the first medium of contact is solid cryolite that can melt and solidify during the process, effectively moving the boundary. Even though melting and solidification itself has to be included in any thermal model, for the material model it is more sensible to include both the molten and the solid phase.

For the thermal balance the ohmic heat generated in the cathode and the cathode collector bars has to be included in the thermal balance. It is not possible to discern if heat is transmitted from the metal pad into the carbon refractory and vice versa.

Figure 3.6 illustrates the boundary for the heat balance calculation (Bruggeman 1998).

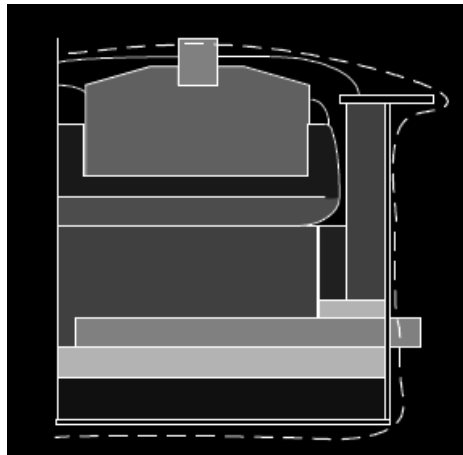


Figure 3.6: Heat Balance Boundary (Bruggeman 1998)

3.2.2 Main Reactions

The dominant reaction is given in Eq. 3.6 and describes the overall reaction given for the Hall-Héroult-Process in standard literature as well as the associated reaction enthalpy (Grjotheim and Kvande 1993).



$$\Delta H^0 = 5,587 \text{ kWh } t_{Al}$$

This neglects significant side reactions and does not consider spatial differences in partial reactions. Some reactions are split into partial reactions one of which occurs within the boundary of balance and the other does not.

In addition, material streams that are returned via external facilities such as the dry scrubber are neglected. Typically these materials exit the cell as a heated, gaseous material and return as a condensed phase at – or close to – room temperature. In effect this is heat lost from the cell that has to be reintroduced. As the net material balance is zero, these streams typically are neglected.

Besides the evolution of CO₂ at the anode, there are other reactions occurring. These include:



$$\Delta H^0 = 6,437 \text{ kWh/t}_{Al}$$

Eq. 3.7 is the resulting reaction equation from sulphur contained in the anode carbon. Typical Sulphur content of the anode is in the range of 1.5 – 2.5 %.

Eq. 3.8 is a net reaction. There are three individual reactions possible leading to this net reaction. Firstly, the reaction happens as stated. Due to reaction kinetics, for higher current densities the formation of CO₂ as given in Eq. 3.6 is favoured. Reaction potentials are given in Figure 3.7. A certain fraction of CO evolves nevertheless.

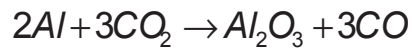


$$\Delta H^0 = 6,918 \text{ kWh/t}_{Al}$$

This is more pronounced at lower anodic current densities. If the different types of carbon used in manufacturing the anode – e.g. coke and binder pitch – have different reaction potentials, the anode can develop a porous surface. This will result in a lower true anodic current density and increased CO formation. Figure 3.7 shows the relevant anode over potentials and their dependency on current density (Welch 2010). Fischer et al describes this phenomenon in detail. Figure 3.8 illustrates this effect (Fischer, Meier et al. 2006).

Other reactions resulting in the formation of CO are given in Eq. 3.9 and Eq. 3.10.





Eq. 3.10

The first reaction is the consequence of converting some of the generated CO_2 with anode carbon to CO. The second reaction is the re-oxidation of produced aluminium with carbon dioxide. In both cases one reactant is a product from Eq. 3.6. As both reactions take place within the defined envelope, the reactions can be combined into the reaction given in Eq. 3.8. As the reaction enthalpy is not dependent on any intermediate products, it is sufficient to consider the resultant equation for the overall balance.

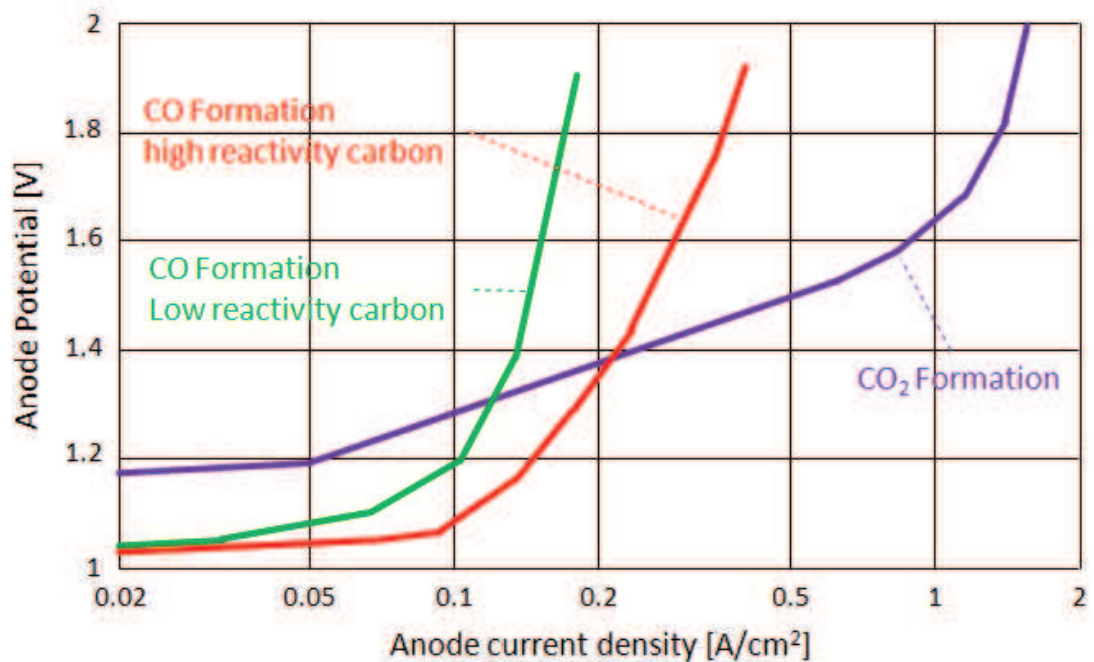


Figure 3.7: Reaction potentials for CO_2 and CO formation depending on current density (Welch 2010)

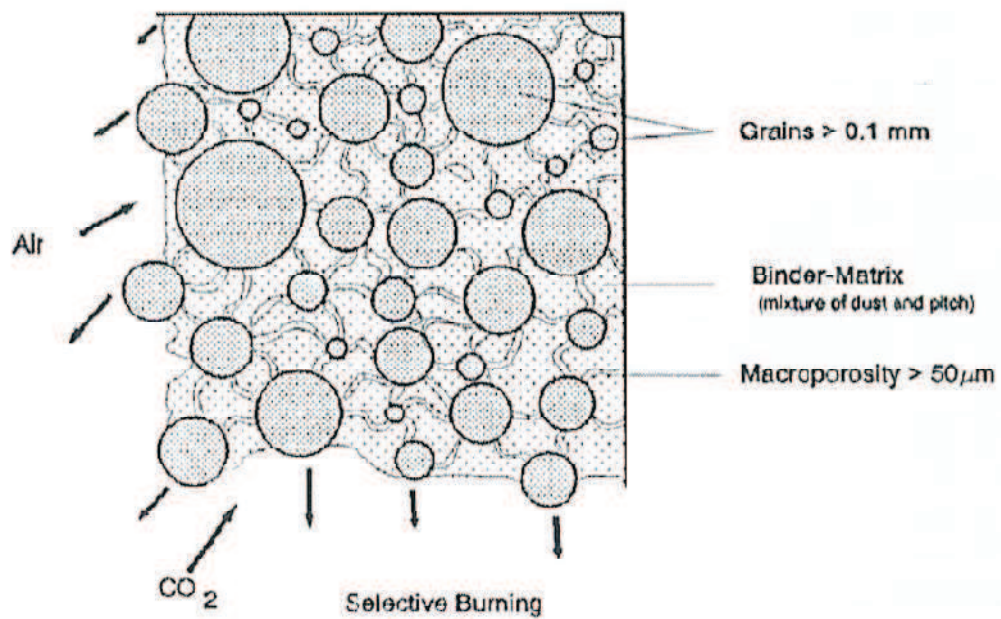
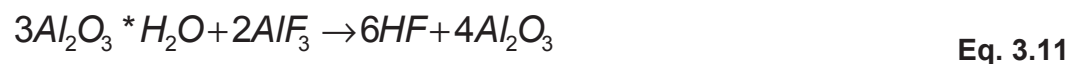


Figure 3.8: Preferential reaction of different carbons in an anode (Fischer, Meier et al. 2006)

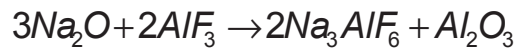
3.2.3 Side Reactions

In the process HF is typically formed by the reaction of water with AlF_3 . The reaction is given in Eq. 3.11. Water is introduced as either moisture or as structurally bound water in the alumina ($\text{Al}_2\text{O}_3 \cdot \text{H}_2\text{O}$) which dissolves or reacts to generate the HF.



$$\Delta H^0 = -7,880 \text{ kWh/t}_{\text{H}_2\text{O}}$$

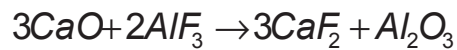
A major impurity in the alumina is Na_2O . Sodium oxide is a residue from the Bayer process. A typical content is in the range of 0.28 to 0.40 wt%. In the process it reacts with AlF_3 to form cryolite and alumina, effectively producing excess electrolyte.



Eq. 3.12

$$\Delta H^0 = -6,044 \text{ kWh/t}_{\text{Na}_2\text{O}}$$

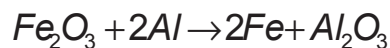
Similar reactions occur for other oxide impurities, such as CaO. These reactions are negligible due to the concentration of the oxide. CaO is the second most common species with 0.003 to 0.053 wt% with an average of 0.020 wt%. Its concentration is typically one order of magnitude lower than that of Na₂O.



Eq. 3.13

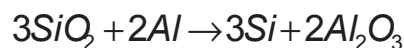
$$\Delta H^0 = -515 \text{ kWh/t}_{\text{CaO}}$$

Other impurities in the alumina are iron and silicon oxides. These do not accumulate in the bath, but are reduced to their elemental form and are removed from the process together with the produced aluminium. In both cases the concentration can be as high as 0.050 wt% in the alumina, but is typically 0.020 % or lower.



Eq. 3.14

$$\Delta H^0 = -2,120 \text{ kWh/t}_{\text{Fe}}$$



Eq. 3.15

$$\Delta H^0 = -2,040 \text{ kWh/t}_{\text{CaO}}$$

3.2.4 Material Balance

Besides the main reaction and the side reactions occurring to form aluminium in a cell, various material streams are entering and exiting the cell continuously. Typically the material enters the cell at or close to room temperature and exits the cell at process temperature. This chapter covers the amount of material entering and exiting the cell, setting up the material balance. The following chapter includes the start and end temperatures to complete a thermal balance.

3.2.4.1 Alumina

To produce 1.0 ton of aluminium, one needs 1.889 t of pure aluminium oxide.



$$m_{Al_2O_3} = 101.96 \text{ g / mol}$$

$$m_{Al} = 26.98 \text{ g / mol}$$

$$1,889 \text{ kg } Al_2O_3$$

$$1,000 \text{ kg } Al$$

Alumina however is not pure aluminium oxide. Major impurities are sodium, iron and silicon in their oxide form and a significant portion of moisture and crystal water. When alumina is used in the dry scrubber to adsorb HF, typically 2.2 % fluorides are present in the so-called secondary alumina. This represents both cryolite particles condensed in the off gas stream and adsorbed by the alumina in the dry scrubber as well as HF reacted in the dry scrubber with alumina to form water and aluminium fluoride. This is the reverse reaction given in Eq. 3.11.

To differentiate between bonded HF and condensed cryolite, aluminium fluoride additions of primary alumina cells and secondary alumina cells were compared over a 3 month average. The additions of soda ash (Na_2CO_3) were subtracted from the AlF_3 additions as soda ash neutralizes AlF_3 . As primary alumina cells do not receive any AlF_3 from the dry scrubber, the difference in addition levels

indicates the AlF_3 load of the secondary alumina. The rest of the fluoride content in the secondary alumina is thus cryolite:

$$m(\text{Na}_3\text{AlF}_6) = \left(m(\text{alumina}) \cdot c_F - m(\text{AlF}_3) \cdot \frac{3 \cdot M(\text{F})}{M(\text{AlF}_3)} \right) \cdot \frac{M(\text{Na}_3\text{AlF}_6)}{6 \cdot M(\text{F})} \quad \text{Eq. 3.17}$$

With $m()$ total mass of a substance
 $M()$ molar mass of a specie
 c_F fluoride concentration in secondary alumina

The remaining fluoride adsorbed in the alumina corresponds to 43.2 kg of cryolite per ton aluminium. On a mole ratio this split represents 46.2 % of the fluoride being present as AlF_3 . As the main source for AlF_3 is HF, this is in correspondence with the general rule, that 50 % of the total fluoride emissions are based on HF emissions (Hyland, Patterson et al. 2004).

Table 3.1: Difference in AlF_3 additions in primary and secondary alumina cells

	Daily AlF_3 addition	AlF_3 addition per t_{Al}
Primary alumina	36 kg	29.5 kg
Secondary alumina	-0.3 kg	-0.25 kg
Total difference		29.75 kg

The compositions for the different alumina grades are given Table 3.2. In total 1,986 kg of secondary alumina are added to produce 1,000 kg of aluminium.

Table 3.2: Average analysis of alumina used by Trimet

Substance	Dry primary alumina	Total primary alumina	Total secondary alumina	Addition per ton aluminium
Al ₂ O ₃	99.54 %	98.75 %	95.54 %	1,889 kg
Na ₂ O	0.37 %	0.37 %	0.36 %	7,02 kg
Fe ₂ O ₃	0.02 %	0.02 %	0.02 %	0.38 kg
SiO ₂	0.02 %	0.02 %	0.02 %	0.38 kg
CaO	0.02 %	0.02 %	0.02 %	0.38 kg
Others	0.03 %	0.03 %	0.03 %	0.57 kg
Moisture and crystal water	0.80%	0.79 %	0.77 %	15.18 kg
F from dry scrubber	--	--	2.2 %	--
AlF ₃ from dry scrubber	--	--	--	29.7 kg
Na ₃ AlF ₆ from dry scrubber	--	--	--	43.2 kg
Total mass				1,986 kg

3.2.4.2 Anode Carbon

The gross carbon consumption is 532 kg/t_{Al} as is given in Table 2.6. A rest of each anode is removed at the end of its life cycle. The mass of this rest is 255 kg on average. The net carbon consumption is therefore 419 kg/t_{Al}. To determine the anode consumption relevant to the thermal balance, the amount of anode that reacts with ambient oxygen has to be subtracted. This amount is hard to determine. In a cell that is properly covered, the effect of air burn is minimized. Even though an exact figure is hard to estimate, an indication is the

number of anode changes out of schedule that are air burn related and unrelated to other anode incidents like spikes and cracks. The percentage of such anode changes is typically minor. The assumption is made that not more than 3 % of the anode is lost to air burn.

Table 3.3: Anode consumption

Gross anode consumption	532 kg/t _{Al}
Net anode consumption	419 kg/t _{Al}
Air burn	16 kg/t _{Al}
Anode consumption with the balance envelope	403 kg/t _{Al}

Table 3.4: Impurities of a carbon anode

Substance	Content	Gross consumption per t _{Al}	Net Consumption per t _{Al}	Net consumption without air burn
Anode		532 kg	419 kg	403 kg
Carbon	96.76 %	514.7 kg	405.4 kg	390 kg
Nitrogen	0.86 %	4.6 kg	3.6 kg	3.5 kg
Sulphur	1.25 %	6.6 kg	5.2 kg	5.0 kg
Oxygen	0.55 %	2.9 kg	2.3 kg	2.2 kg
Ash	0.60 %	3.2 kg	2.5 kg	2.4 kg

The carbon of the anode contains impurities as well. The main impurities are given in Table 3.4. Data is taken from an analysis of a certified laboratory (Fresenius 2013). Other impurities, such as iron, silicon and other metals amount to 0.01 % and can be neglected.

Whereas carbon and sulphur are oxidized according to Eq. 3.6 and Eq. 3.7, ash and nitrogen are just heated to process temperature.

3.2.4.3 Anode Change

During an anode change not only is the spent anode replaced with a new one, but in addition anode cover material is removed along with the spent anode and new cover material is applied onto the new anode. A typical cover composition is 50 % alumina and 50 % crushed bath material. Some material spills into the bath during both anode change and covering. As the alumina spilling from anode covering into the bath is reduced to aluminium and replaces alumina added on purpose, it can be disregarded for the purpose of the thermal balance.

The bath material added is heated, molten and will eventually be removed from the cell. It has to be included in the thermal balance calculation. Table 3.5 gives detailed data on the amounts of material moved in reference to one anode change.

Table 3.6 shows the same data, but referred to the aluminium production of 1 ton.

Table 3.5: Material movement during one anode change

Substance	Content	Applied material	Removed material	Material consumed
Cover material		400 kg	320 kg	80 kg
alumina	50 %	200 kg	160 kg	40 kg
Na ₃ AlF ₆	50 %	200 kg	160 kg	40 kg

Table 3.6: Material movement during anode change per ton of aluminium produced

Substance	Applied material	Removed material	Material consumed
alumina	89 kg	71 kg	18 kg
Na ₃ AlF ₆	89 kg	71 kg	18 kg

3.2.4.4 Additives and Bath Production

Depending on the sodium oxide concentration in the alumina, AlF₃ is added to compensate for the reaction given in Eq. 3.12. This amounts typically to 13 kg_{AlF₃}/t_{Al}. With neutralization of sodium oxide with aluminium fluoride, cryolite is produced. Effectively, each cell is producing bath at a steady state. Part of this bath is absorbed into the carbon material of the cathode (Sorlie and Oye 2010). The remaining excess bath has to be removed from the cell manually.

3.2.5 Thermal Balance

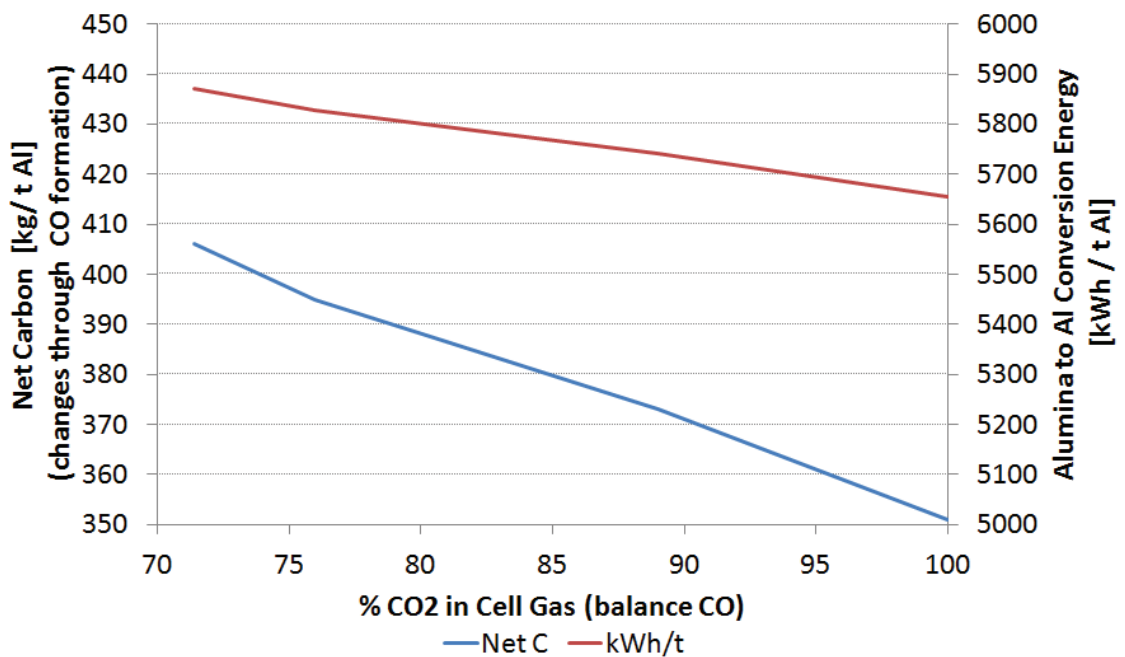
3.2.5.1 Aluminium Reduction and Carbon Consumption

There are three reactions possible to produce aluminium. These reactions were given in Eq. 3.6 to Eq. 3.8. Reaction products are CO_2 , CO and COS besides aluminium. The proportion of occurrence is in reference to the available material. All sulphur reacts to COS . The remaining carbon is oxidized with the available oxygen resulting in a distribution of carbon monoxide and carbon dioxide. Table 3.7 gives an overview of the reaction products.

The resulting anode gas consists of 0.5 mol% COS , 71.6 mol % CO_2 and 27.9 mol % CO . Contrary to what is commonly published, a significant portion of the anode gas is carbon monoxide which is only subsequently oxidized to CO_2 (Welch 2013b). Figure 3.9 illustrates the relation between increased carbon consumption and energy consumption as well as the composition of evolved anode gas (Welch 2013a). The exact relation between carbon consumption and energy consumption is linked by the specific production data of the cell, mainly net anode consumption and thus current efficiency. In a stable process the main variable to change net carbon consumption is the rate of back reaction according to Eq. 3.8 to Eq. 3.10. The energy needed to reduce aluminium oxide varies depending on the available carbon. The more carbon taking part in the reaction, the more energy is needed, as the CO content in the anode gas increases significantly.

Table 3.7: Proportion for the reaction to produce aluminium

Reactant			Product			
	kmol	kg		kmol	kg	mol/mol
Al ₂ O ₃	18.53	1,889.5	Al	37.062	1,000.0	--
S	0.156	5.0	COS	0.157	9.4	0.007
C	32.47	390.0	CO ₂	23.267	1,024.0	0.796
O	0.138	2.2	CO	9.042	253.3	0.197

**Figure 3.9: Exemplary increase in energy consumption as a result of increased carbon consumption (Welch 2013a)**

Accordingly, the total enthalpy for the reduction of 1 ton of aluminium can be calculated with these percentages and the individual ΔH^0 given with Eq. 3.6 to Eq. 3.8:

$$\begin{aligned}\Delta H_{Al}^0 &= 0.007 \cdot \Delta H_{COs}^0 + 0.796 \cdot \Delta H_{CO_2}^0 + 0.197 \cdot \Delta H_{CO}^0 \\ &= 5,855 \text{ kWh} / t_{Al}\end{aligned}\tag{Eq. 3.18}$$

This is 268 kWh/t_{Al} or 4.8 % higher than in case of only CO₂ evolution. Additionally the reactants have to be heated to process temperature. This results for the given current efficiency of 93.5 % in:

$$\Delta H_{Al} = 6,455 \text{ kWh} / t_{Al}\tag{Eq. 3.19}$$

This is the energy needed to just sustain the reactions. Heat requirements for side reactions and the heating of additional material needed for the process but not converted in the reaction have to be added to determine the overall energy demand.

As the anode gas composition changes with a change in current efficiency, the energy need shifts accordingly as illustrated by Figure 3.9. For a decrease in current efficiency, the fraction of carbon monoxide in anode gas will increase, leading to an increase in the required energy. Due to the reaction mechanisms given in Eq. 3.8 to Eq. 3.10 and discussed earlier, the carbon consumption changes linearly with a change in current efficiency:

$$m_{net\ carbon} = 657 - 298.4 \cdot \eta_{CE} \left(\frac{kg\ C}{t\ Al} \right) \quad \text{Eq. 3.20}$$

With $m_{net\ carbon}$ mass of carbon consumed
 η_{CE} current efficiency

Accordingly the necessary energy to produce metal changes linearly with current efficiency:

$$Q_{metal} = 8323.9 - 1989.8 \cdot \eta_{CE} \left(\frac{kWh}{t\ Al} \right) \quad \text{Eq. 3.21}$$

With Q_{metal} energy to produce metal
 η_{CE} current efficiency

Figure 3.10 shows the relation graphically. The relations are according to Figure 3.9, but show relevant data for the P19 cell in Hamburg.

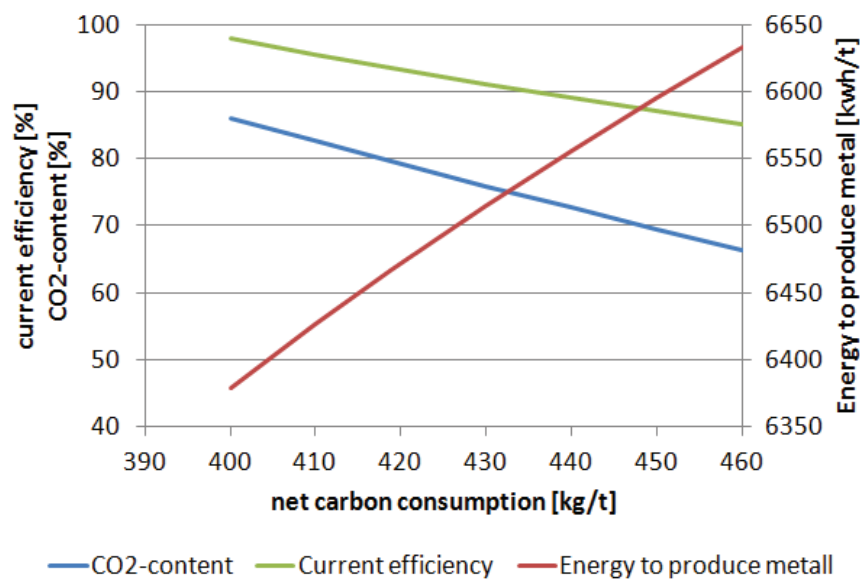


Figure 3.10: Relation between net carbon consumption, current efficiency and energy to produce metal for the Hamburg cell

3.2.5.2 Anode Change

In addition to the anode carbon that reacts with the oxygen from alumina, there is the rest of the anode that is removed at the end of the life cycle. This material has to be heated to process temperature. Cover material applied onto the anode has to be preheated to an intermediate temperature. Studies have determined this temperature as 325 °C (Depree, Agbe nyegah et al. 2012). Of the cover material spilled into the electrolyte during anode covering, only Na_3AlF_6 has to be considered. It is heated to process temperature and molten. Alumina is consumed in the regular process and is thus covered in the previous chapter.

Table 3.8 details both the associated masses and heat capacities for the relevant materials. The process energy needed for the anode change is:

$$\Delta H_{\text{anode change}} = 68.80 \text{ kWh} / t_{\text{Al}}$$

Eq. 3.22

Table 3.8: Material and heat balance for anode butts and cover

	Mass (absolute)	Mass (per t_{Al})	Input Temp	Output Temp	Heat capacity (per t_{Al})
C (anode)	255 kg	113 kg	25 °C	960 °C	44.4 kWh
Al_2O_3 (cover)	180 kg	80 kg	25 °C	325 °C	6.5 kWh
Na_3AlF_6 (cover)	180 kg	80 kg	25 °C	325 °C	7.7 kWh
Na_3AlF_6 (spillage)	20 kg	9 kg	25 °C	960 °C	10.2 kWh

3.2.5.3 Water and Additives

With the alumina a substantial amount of water is introduced into the system. Free water rapidly and easily evolves from monohydrates as commented on in chapter 3.2.3. HF gas exits the cell. Conversion from HF back to AlF_3 probably occurs outside boundaries of the discussed balances when alumina is added to the off gas stream in the dry scrubber.



Water leaves the loop of cell to dry scrubber through the off gas while aluminium compounds are recycled to the cell with the alumina stream. This is in line with the plant observation that the HF load changes primarily when the source of alumina is changed (Patterson 2001). This results in a reduction of water through the alumina from 15.18 kg/t_{Al} to 9.55 kg/t_{Al}. This corresponds to a reduction of water content of 37 %. All additives are at ambient temperature when they enter the process and are heated to process temperature.

The process energy for this process is:

$$\Delta H_{\text{water dry scrubber}} = 75.90 \text{ kWh} / t_{\text{Al}} \quad \text{Eq. 3.24}$$

The material streams are detailed in Table 3.9.

Table 3.9: Material and heat for the dry scrubber process and AlF₃-additions

Reactant			Product		
	kmol	kg		kmol	kg
H ₂ O	0.53	9.55	HF(g)	1.060	21.21
AlF ₃ (dry scrubber)	0.354	29.70	Al ₂ O ₃ (l)	0.281	28.64
Na ₃ AlF ₆ (dry scrubber)	0.206	43.20	Na ₃ AlF ₆ (l)	0.206	43.20
AlF ₃ (addition)	0.155	13.00	AlF ₃ (l)	0.155	13.00

3.2.5.4 Impurities in the Alumina

Impurities in the alumina can be divided into two subgroups. The first group spans those impurities that react to fluoride salts. These are Na₂O and CaO. The reactions with AlF₃ are given in Eq. 3.12 and Eq. 3.13 respectively and the mass balance is shown in Table 3.10. For the heat calculation it was assumed, that the reactant AlF₃ is already at process temperature. It does not have to be subtracted from the AlF₃ mass in any of the other calculations. The products are all molten and at process temperature. The process energy is then:

$$\Delta H_{\text{impurities Na Ca}} = -8.03 \text{ kWh} / t_{\text{Al}}$$

Eq. 3.25

Table 3.10: Impurity reactions forming fluoride salts per t_{Al}

Reactant			Product		
	kmol	kg		kmol	kg
Na ₂ O	0.113	7.02	Na ₃ AlF ₆ (l)	0.076	15.85
CaO	0.007	0.38	CaF ₂ (l)	0.007	0.53
AlF ₃ (l)	0.156	13.06	Al ₂ O ₃ (l)	0.040	4.08

The second group of impurities is made up of iron and silicon oxide. These react with aluminium to form their elements and aluminium oxide. The overall components are given in Table 3.11. Their contribution towards the overall thermal balance is minor:

$$\Delta H_{\text{impurities Fe Si}} = -0.48 \text{ kWh} / t_{Al}$$

Eq. 3.26**Table 3.11: Impurity reactions forming elements per t_{Al}**

Reactant			Product		
	kmol	kg		kmol	kg
Fe ₂ O ₃	0.002	0.38	Fe(l)	0.005	0.23
SiO ₂	0.006	0.38	Si(l)	0.006	0.18
Al(l)	0.013	0.36	Al ₂ O ₃ (l)	0.007	0.67

3.2.5.5 Summary on Thermal Balance

Table 3.12 summarizes the energy needed to keep the aluminium production in operation. It includes heat losses associated with material removed from the cell, such as HF gas or anode butts that are removed from the process but are essentially necessary.

Table 3.12: Total energy needed in the reduction process for 93.5 % current efficiency

ΔH_{Al}	6,455.00 kWh/t _{Al}
$\Delta H_{anode\ change}$	68.80 kWh/t _{Al}
$\Delta H_{water\ dry\ scrubber}$	75.90 kWh/t _{Al}
$\Delta H_{impurities\ Na\ Ca}$	-8.03 kWh/t _{Al}
$\Delta H_{impurities\ Fe\ Si}$	-0.48 kWh/t _{Al}
ΔH_{total}	6,591.19 kWh/t _{Al}

With 6,591 kWh/t_{Al} the energy demand is considerably higher than the energy needed for the dominant reaction between aluminium oxide and carbon to form aluminium and CO₂. The energy demand for this reaction is 6,324 kWh/t_{Al}.

Within the operating cell the actual required energy demand is scaled in proportion to the production rate of the aluminium. While the associated energy demands detailed in Table 3.12 change with current efficiency, these changes are minor when compared to the total energy demand and the changes induced by variation in the main reaction and the anode gas composition. Thus they are neglected in the further discussion.

Based on Faraday's Law the hourly energy consumption for materials heating and chemical conversion is given by the following equation:

$$Q_{total\ process} = \frac{6.591}{0.3356 \cdot I \cdot \eta_{CE}} (kW) \quad \text{Eq. 3.27}$$

With $Q_{total\ process}$ energy consumption for heating and chemical conversion
 I amperage
 η_{CE} current efficiency

Using this data the equivalent voltage to produce aluminium can be calculated by Eq. 3.28. Due to the amount of metal produced changing with line current, the voltage to produce metal is independent from line current:

$$U_{eq} = 2.213 \cdot \eta_{CE} (V_{equiv.}) \quad \text{Eq. 3.28}$$

With U_{eq} Equivalent voltage
 η_{CE} current efficiency

Since the total energy applied to the cell is given by the relationship

$$Q_{cell} = (U_{cell} - I \cdot R_{external}) \cdot I \quad \text{Eq. 3.29}$$

With Q_{cell} total energy
 U_{cell} cell voltage
 I amperage
 $R_{external}$ external cell resistance

The energy available for heat losses and transient processes associated with the modulation is given by

$$Q_{\text{heat loss \& transient}} = (U_{\text{cell}} - I \cdot R_{\text{external}} - 2.213V \cdot \eta_{\text{CE}}) \cdot I \quad \text{Eq. 3.30}$$

With $Q_{\text{heat loss \& transient}}$ energy for heat loss and transient processes

U_{cell} cell voltage

I amperage

R_{external} external cell resistance

η_{CE} current efficiency

3.3 Heat Loss

Energy that is introduced into the process but not used for aluminium reduction or preheating raw materials and products has to be removed from the cell. This is by heat loss through all surfaces and interfaces of the heat balance boundary.

Figure 3.11 details a typical heat loss breakdown as given by Bruggeman expressing the individual heat losses as a percentage (Bruggeman 1998). Different cell designs can have widely different heat loss distributions, especially when considering diverse current densities. There can also be a wide variation between cells of the same design due to different operating parameters and cell states.

In addition to the components in Figure 3.11, there are other minor heat losses (Bruggeman 1998):

- the heat loss with anode butt removal
- vapour losses
- metal removal and bath level adjustment

While included in the previous chapter, these are often neglected in a steady state heat balance.

Bruggeman states several points concerning the individual heat losses in Figure 3.11:

- The sum of the crust and anode heat losses often exceeds 30% of the total cell heat loss. Hence, anode covering practices provide an important ability to regulate the heat balance of the pot.
- The bottom heat losses are a strong function of lining integrity. For fully deteriorated insulation the heat loss can be twice as high as for new cells.
- Heat losses from holes in the crust are significant if the hole areas total more than 0.2 m^2 .
- Conduction up through the anode rods and collector bar connections account for about half of the heat losses from the anode stubs and collector bars, respectively.
- Changes in the heat loss are accommodated primarily by the side wall and end wall heat losses.

While this is correct, the heat loss through the top of cell increases significantly, if cell temperature exceed a critical limit. At this point large holes appear in the crust and the integrity of the cover is lost nearly completely. Typically this happens at cell temperatures exceeding $990 \text{ }^\circ\text{C}$.

For the side wall heat loss during steady state conditions Haupin introduced a one dimensional model. The ledge thickness is derived assuming only horizontal heat flux by (Haupin 1971):

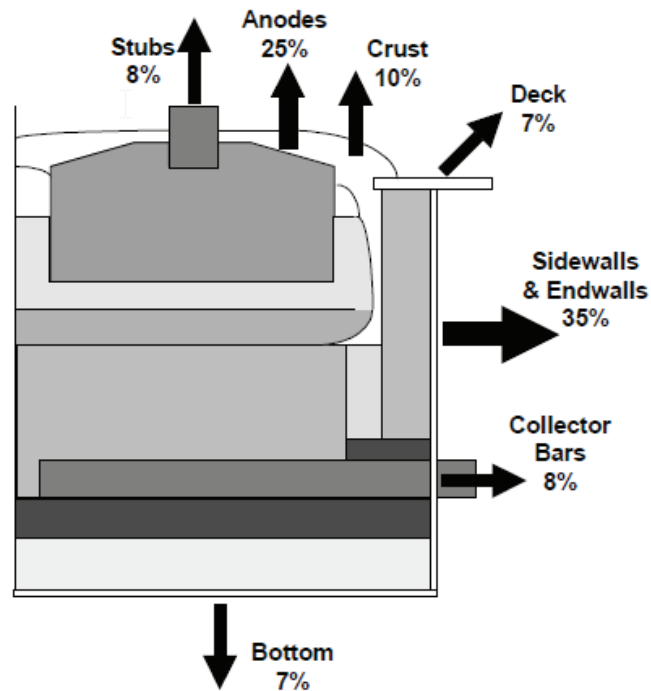


Figure 3.11: Typical heat loss distribution as given by Bruggeman (Bruggeman 1998)

$$I_{ledge} = \frac{k_{ledge}}{A} \cdot \left(\frac{T_{liq} - T_{amb}}{h_{ledge} \cdot A \cdot (T_{bath} - T_{liq})} - \sum_i R_{wall}^i - \frac{1}{h_{shell} \cdot A} \right) \quad \text{Eq. 3.31}$$

With	l_{ledge}	ledge thickness
	k_{ledge}	thermal conductivity of ledge
	h_{ledge}	bath/metal to ledge heat transfer coefficient
	h_{shell}	shell to ambient air pseudo-heat transfer coefficient, as this includes radiant heat loss from the steel shell
	A	heat flow area
	R_{wall}^i	thermal resistance for each side wall lining material steel shell, cement, refractory
	T_{liq}	liquidus temperature
	T_{amb}	ambient temperature
	T_{bath}	bath temperature

The heat flux from the electrolyte to the side wall in this model is equal to $h_{ledge} \cdot A \cdot (T_{bath} - T_{liq})$. The driving force for heat loss is the superheat ΔT . A higher superheat will produce a greater heat loss through the side wall even before decreasing the side ledge thickness.

Eq. 3.31 constitutes a uniform ledge thickness in first approximation as it is only dependent on superheat. The heat transfer coefficients are not constant however. They depend on the geometry of the interface as well as the local mass transfer. If convection is the predominant mechanism for heat transfer, the coefficient h_{ledge} will also depend on metal and bath velocities. To estimate the dominance of either convection or thermal conduction the Péclet number can be used:

$$p_e = \frac{l \cdot v \cdot \rho \cdot c_p}{\lambda}$$

Eq. 3.32

With	l	characteristic length
	v	velocity
	ρ	specific density
	c_p	specific heat capacity
	λ	thermal conductivity

If the Péclet number goes to infinity, convection is dominant. If it converges to zero, conduction is prevalent.

The characteristic length of the cell can be defined as the height of the respective medium, which is 0.2 m. The density of the bath can be calculated by formulas published by Welch and Haupin as 2.1 g/cm^3 (Burkin 1987, Welch and Gjortheim 1988). The specific heat capacity of cryolite melt is $1.89 \text{ J/g}\cdot\text{K}$. Iffert gives the thermal conductivity of bath as $0.4 \text{ W/m}\cdot\text{K}$ (Iffert 2008).

For aluminium in the respective values are 2.4 g/cm³ for the density (Burkin 1987), 1.18 J/g*K for the specific heat capacity and 237 W/m*K for the thermal conductivity.

This results in the following equations for the Péclet number:

$$p_{e \text{ bath}} = v \cdot 1,984,500 \frac{\text{S}}{\text{m}} \quad \text{Eq. 3.33}$$

$$p_{e \text{ metal}} = v \cdot 2,390 \frac{\text{S}}{\text{m}} \quad \text{Eq. 3.34}$$

With $p_{e \text{ ()}}$ Péclet number
 v velocity

Typical velocities of bath and metal are 0.15 to 0.10 m/s maximum with 0.05 m/s given as average (Potočnik and Laroche 2001). Models for the P19 cell in Hamburg result in similar conditions with an average metal velocity of 0.056 m/s and a maximum velocity of 0.169 m/s (Droste 2001). Bath velocities are reported slightly below these values.

For the bath area it is probable that mass transfer and convection dominate the heat transfer as long as any bath velocity is present. In the case of the metal-ledge interface this is not so easily discernible. For average conditions the Péclet number is only 134. This indicates a much stronger balance between convection and conduction. If the metal velocity is well below average – either due to local conditions or due to a power outage removing the driving force for the metal velocity – conduction will become the dominating force for heat loss in the metal pad.

3.3.1 Experimental Cross-Check on the Cell Heat Loss Distribution

To verify the heat loss distribution found in the literature and given in Figure 3.11, heat loss measurements were performed on the P19 cell. This was also in preparation to investigate the changes in heat loss under varying heat input. The heat loss measurement boundary was different to the boundaries given in Figure 3.6 as the superstructure was included. This is due to the difficulty of measuring the heat loss on the top side of the anode cover. In this area, the following exothermic reactions are occurring additionally to the oxidation of anode carbon with ambient air (airburn):



Combining anode airburn given in Table 3.3 and product quantities given in Table 3.7 the additional heat loss amounts to 703 kWh/t_{Al} or 41.2 kW. Additionally the ohmic resistance of the anode beam to the yoke has to be included with 60mV. The total heat loss then is 393.1 kW for a cell voltage of 4.20 V at 180 kA. For the measurement the cell was subdivided into components. Heat flux was measured at representative points with a KEM heat flux meter (Kyoto Electronics Manufacturing Co Ltd 2013). The positions of the sensor were confirmed to be representative in a separate measurements campaign. Figure 3.12 illustrates this process at the example of the cell bottom. Measurement points were reduced from 13 to 5 at the underside of the cell, indicated in red. Average heat flux derived from the reduced number of measurement points was in good agreement with the heat loss from the larger number of measurement points.

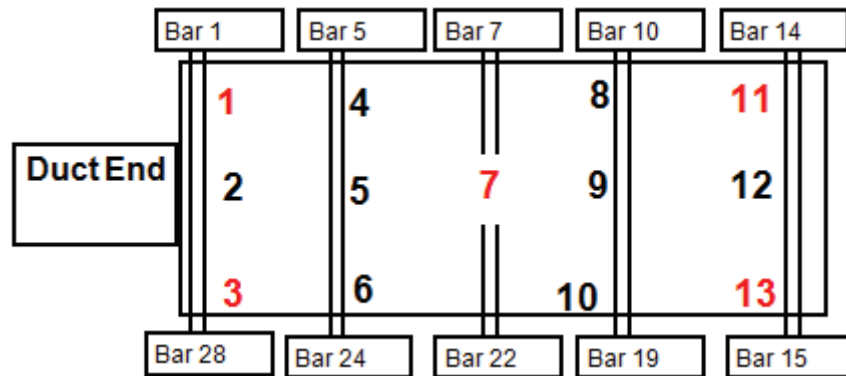


Figure 3.12: Heat flux measurement points at the cell bottom

The heat loss was calculated as:

$$\dot{Q} = A \cdot \frac{1}{n} \sum_{i=1}^n \dot{q}$$

Eq. 3.37

With:

- \dot{Q} total heat loss through one part of a cell
- A relevant surface area
- n number of measurement points
- \dot{q} heat flux as measured

The same system was used for the other cell components. The cell components and the measurement values are given in Table 3.13. Most measurement points were direct heat flux measurements. The heat loss through the off-gas was a combined temperature and velocity measurement:

$$\dot{Q}_{off\ gas} = v \cdot A \cdot \rho \cdot c_p \cdot (T_{off\ gas} - T_{amb}) \quad \text{Eq. 3.38}$$

With	$\dot{Q}_{off\ gas}$	heat content of the off gas
	v	gas velocity
	A	cross section of the duct
	ρ	specific density of air at 140 °C
	c_p	specific heat content of air
	T_{amb}	ambient temperature close to the cell
	$T_{off\ gas}$	temperature of the off gas

To calculate the heat loss through both collector bars and cooling fins, the temperature gradient over a fixed distance was determined. The following formula was used to determine the heat loss:

$$\dot{Q} = \frac{\Delta T \cdot A \cdot \lambda_{steel}}{l} \quad \text{Eq. 3.39}$$

With	\dot{Q}	heat loss
	ΔT	temperature gradient measured over distance l
	A	surface area
	l	distance of the relevant measurement points
	λ_{steel}	thermal conductivity of steel, 49 W/m*K

Table 3.13: Results of 4 consecutive heat loss measurements

	Cell 333 a	Cell 332 a	Cell 332 b	Cell 333 b	Calculated
Super structure	24,613 W	25,078 W	26,842 W	29,443 W	
Cell hooding	32,763 W	33,439 W	33,901 W	30,645 W	
Off-gas	136,675 W	149,686 W	149,033 W	114,005 W	
Deck plate	16,733 W	14,830 W	18,426 W	19,322 W	
SiC - area	39,384 W	35,116 W	38,102 W	34,992 W	
Cooling fins	8,592 W	9,025 W	8,132 W	7,237 W	
Short sides (duct + tap end)	30,677 W	32,481 W	26,065 W	21,454 W	
Collector bars dT	13,830 W	24,368 W	21,225 W	20,637 W	
Refractory area	10,475 W	10,203 W	9,903 W	10,788 W	
Insulation area	15,193 W	12,231 W	13,665 W	16,856 W	
Shell bottom	39,162 W	37,515 W	43,730 W	45,407 W	
Total	368,097 W	383,972 W	389,024 W	350,786 W	393,100 W
Cell voltage	4.10 V	4.18 V	4.18 V	4.09 V	
Line current	177.3 kA	177.3 kA	177.3 kA	177.3 kA	

To get more accurate measurements the collector bar was insulated with rock wool to minimize heat loss along the respective length. Due to the geometry of the cooling fins insulation was not possible.

The measurements are within reasonable repeatability if the complexity of the measurement is considered. Heat losses recorded are 1 % to 12 % lower than the theoretical value. It should be noted that both actual line current as well as actual cell voltage were below the case used for the heat loss calculation. If compensated for this, the calculated heat loss is 18 kW lower if the efficiency is the same. This would result in a measurement error between +3.6 % and -6.9 %.

Notable variations are in the off gas heat loss – values spread 26 % compared to the mean value of all measurements. Here a single measurement is done for the velocity of the off gas. It is assumed that the velocity is uniform within the off-gas duct.

The heat loss attributed to the short sides of the cell varies considerably. This can be attributed to different weather conditions, mainly wind direction, temperature and speed. The duct side of pot room 3 is a weather side and susceptible to changing wind conditions. Keeping the inevitability of changing weather in mind, the effect on cell heat loss is considerable.

Collector bar heat loss was recorded considerably lower in the first measurement than in the others. This is due to the fact that only a single insulated collector bar was measured at this time. To get more reliable and repeatable data, in the measurements 2 – 4 half the collector bars were measured.

All other variations in heat loss may appear relevant if compared to the average value, if compared to the total heat loss of the cell, the contribution of these variations are minor.

It should be noted that the heat loss distribution is significantly different to the one given by Bruggeman in Figure 3.11. More than 50 % of the heat is lost through the top of cell, compared to 33 % stated by Bruggeman. Accordingly, less heat is lost through the side walls of the cell – only 26 % compared to 35 %. The reason for this distribution is the wide side channel between the

anodes and the side lining of the P19 cell. There is sufficient space to develop a thick side ledge restricting heat flow. Accordingly, the other heat losses have to increase to compensate for this insulation.

4 Power Modulation

Synopsis:

This chapter contains details on the history of power modulation. In addition theoretical aspects are detailed such as maximum heat deviation that is possible for a P19 cell. The maximum heat deviation while remaining within the process envelop was determined as 0.7 MWh. External constraints such as work procedures are discussed. Parts of this chapter were published as a TMS paper in 2011. (Reek 2011a) and a paper presented at the 10th Australasian Smelter Technology Conference, Launceston, Australia (Reek 2011b).

4.1 History of Power Modulation

4.1.1 First Applications of Power Modulation

The idea to modulate the energy input into aluminium reduction cells is not a new one. Brant Filho and Pinheiro Leal Nunes published papers on work done in Brazilian smelters in the 1990s (Brant Filho, Queiroz et al. 1992, Pinheiro Leal Nunes, Vianna da Silva et al. 1998). Brant Filho even mentions and references correspondence about power modulation with Nippon Light Metals Co dating back to the 1980s. Unfortunately, these documents are not publicly available.

In both papers the data presented is quite similar. Whereas Brant Filho details a peak power reduction of 34 % over a 3 hour period and the results achieved, Pinheiro describes two modulation steps - a very small power modulation of just 4 % and a drastic cut back of 50 %, both on peak power uptake. He deduced that an amperage reduction of 30 % – again for 3 hours – is the most feasible. The time period however is more likely to be linked to a high energy price window at this time in Brazil than for the technical reasons they ascertained. A period of increased power input to mitigate the energy deficit is not mentioned in either case. Even though only Filho's paper mentions it explicitly, in both papers the modulation worked with a constant pseudo-resistance setting. The aim was

to keep the average line amperage constant. This goal is not met exactly. The resulting reduction of energy input and the shift in energy introduced is detailed in Table 4.1. While the first is the total reduction of the energy input during modulation compared to normal operation, the latter is amount of energy shifted away from constant energy input. The amount of shifted energy is calculated as:

Table 4.1: Details for power modulation at Alcanbrazil and Valesul

	Alcan Brazil	Valesul
Source	(Brant Filho, Queiroz et al. 1992)	(Pinheiro Leal Nunes, Vianna da Silva et al. 1998)
Line current before modulation	61.0 kA	161.3 kA
Average line current during modulation	60.4 kA	159.6 kA
Peak line current	62.2 kA	163.0 kA
Off peak line current	48.0 kA	129.0 kA
Total energy deviation	-1.25 %	-1.4 %
Total energy shift	7.7 %	5.2 %
Comments		Constant line current on weekends

$$P_{shift} = \frac{\int |P_t - P_{avg}| dt}{\int P_t dt} \quad \text{Eq. 4.1}$$

With P_{shift} energy shifted
 P_t energy input at a given time
 P_{avg} average energy input for the respective time period

In terms of measures taken to enable the cells to cope with this drastic cut in energy input Brant Filho is extremely brief. He points out the postponing of scheduled anode effects as his only measure. On the reduction line behaviour, he notes a drop in bath temperature from 960°C to 945°C. Even though he records a drop in cathode collector bar temperature, he records a constant heat flux through the side wall. He gives no explanation why this might be the case.

Pinheiro is more detailed in his paper. He notes an increase in cell resistance the longer the low amperage period continued. He attributes this effect to cell cooling. He details strategies used for alumina feeding during the low energy period as the trend of increasing resistance overlays the usual correlation between resistance and alumina concentration. He implements a fixed feed time for this interval. He also introduces preventive feeding to reduce the number of anode effects directly after amperage increase reverting to the high energy level. He takes note of bath cooling of only 6°C during three hours of energy reduction, but he erroneously attributes this decrease only to a reduction in superheat. He does not consider that the composition of the bath and thus the liquidus temperature will change as the cells cools and bath material solidifies. More recent publications document an immediate response in ledge thickness and bath volume when outside parameters change (Iffert 2008).

Both papers come to the conclusion that while not desirable, the power modulation has a negligible negative impact on the reduction line. Both smelters publish an achieved current efficiency below today's standard. Thus it cannot be excluded that there is an impact on a smelter operating at a higher efficiency.

It is not published however that both smelters discontinued power modulation at the moment they signed new energy contracts. Unpublished private correspondence suggested that both plants had problems with bottom freezes in their cells, disturbing the metal flow and resulting in unstable cell operation and losses in efficiency (HAW 2008).

4.1.2 Energy Input Reduction

Another technique that has been used in the industry to cope with extreme situations is the permanent decrease in power consumption of the smelter. One example is Hydro Aluminium Karmøy (Rolland, Furu et al. 2004). This is a smelter supplied by hydro-electrical power. Due to insufficient rain in autumn 2002 the amount of electrical energy with which the plant could be supplied was severely reduced. As a consequence the smelter was forced to reduce operating current from 135kA to 120kA as well as reducing all target cell voltages for a period of 4 months. A specific value for the reduction of target voltage is not given, but assuming a constant pseudo-resistance setting in the process control system. A decrease in cell voltage by approximately 0.25 V would result if Eq. 2.8 is applied. This would lead to a total energy reduction of 16 % from nominal input. It appears unlikely that cell voltages were reduced further than this limit. The details of this energy reduction are compiled in Table 4.2.

In his paper Rolland describes the measures taken to stabilize the cells at this low energy input as well as the cell behaviour he recorded. Most notable is a crusting in of the cells to a degree that threatened normal operation. Alumina solubility decreased considerably and significant bottom freeze was recorded beneath the feeder positions. The other notable experience he describes is an increase in the number as well as the maximum voltage of anode effects. Based on the energy requirements summarized in Chapter 3.2.5, and the general behaviour of a given cell design having almost constant heat loss unless essential preventative actions are taken, these adverse cooling effects could be anticipated. Effectively the cells were operated close to minimal superheat. This

resulted in the loss of alumina solubility leading to an increased number of anode effects. The cells were cooled to an extent that even during an anode effect, dissolving and distributing alumina enriched bath in the cell was not rapidly done, leading to the increased voltage of the anode effects.

Table 4.2: Details for power modulation at Hydro Aluminium Karmøy

	Karmøy
Source	(Rolland, Furu et al. 2004)
Line current before modulation	135.0 kA
Average line current during modulation	120.0 kA
Peak line current	120.0 kA
Off peak line current	120.0 kA
Total energy deviation	-16 %
Total energy shift	n/a
Comments	3 months duration

4.1.3 Modern Power Modulation

After the publications of Brant Filho and Pinheiro, no further information on modulating power has been found in the literature up until Stam and Eisma published their papers in 2007 and 2009 respectively (Stam and Schaafsma 2007, Eisma and Patel 2009).

The details for all these modulations are given in Table 4.3.

Stam discusses a minor modulation referring to the procedure as a “day-night-rhythm”. He adopts a +5 kA step during the night at constant control resistance. The biggest difference to former work is that he applies the modulation step for 12 hours. This corresponds to a modulation of roughly 2.9 %. His analysis of resultant data is very thorough. He suggests that the bath temperature changes according to the deviation from normal energy input. For his cell technology he determines a factor of 0.125°C/kWh.

While Eisma details similar experiences, he applies power modulation in the range of -20 kA for up to 24 hours. These were mitigated by a target voltage increase of +0.20 V. He also reports data on +10 kA for 10 hours during the night. The energy deficit or surplus is not immediately compensated. Cells are just returned to normal operation. Effective modulation is used in both cases to significantly shift the operating point away from the origin.

He determines the correlation between temperature change and energy deficit to be 0.0046 °C/kWh for his cell design. Even though the latter cell is to some extent larger and thus has more thermal mass, it is surprising to find values more than 20 times different.

Eisma’s lower coefficient of 0.0046 °C/kWh can be explained with his stronger deviation from nominal heat input as well as an extended trial time. With an increased heat input, heat loss will increase. This will lead to a dampening of the temperature increase. This effect will be more pronounced if the trial is over an extended period of time. Another explanation for Stam’s significantly larger temperature increase of 0.125 °C/kWh would be a massive degradation in process efficiency. This is contrary to both the relatively minor deviation of 5 kA and his paper stating no negative impact on the process.

Lastly, a larger temperature increase would result if there is less side ledge to melt in the cell. As the main heat capacitor is the melting of side ledge, cells with significantly less ledge volume will be increasing in temperature more rapidly. This would necessitate a decoupling of bath and liquidus temperature and an overproportional increase in superheat. Unfortunately, values for the change in superheat are not reported in both papers. If such a behaviour was observed, Stam would have been endangering the potline as all protective side ledge would have been molten.

Table 4.3: Details for power modulation at Trimet Essen and AIDel

	Trimet Essen		AIDel
Source	(Eisma and Patel 2009)		(Stam and Schaafsma 2007)
Line current before modulation	167.0 kA	167.0 kA	142.0 kA
Average line current during modulation	147.0 kA	171.2 kA	144.5 kA
Peak line current	147.0 kA	167.0 kA	142.0 kA
Off peak line current	147.0 kA	177.0 kA	147.0 kA
Total energy deviation	-15 %	+4.1 %	+2.9 %
Total energy shift	n/a	4.6 %	2.8 %
Comments	24h duration		--

Eisma is also the only author investigating the change of bath mass. He determines the solidification of 787 kg of bath during one modulation period. This is in contrast to only 305 kg being molten afterwards. He indicates that continued modulation can lead to a build-up of ledge on both the cathode and the side wall leading to cell instabilities as mentioned above. Interestingly he observes a stronger reaction for the move out of normal operation on each trial – for an energy increase, he reports more ledge melting immediately than is solidifying when the cell is returned to normal voltage. If the energy is decreased, he reports more ledge solidifying than is molten when the cell is returned to normal operation. As a conclusion this indicates that the cell behaviour is following a hysteresis.

4.2 Possible Scope of Power Modulation

Most of the industry still tries to operate at a current that is as constant as possible. Nevertheless there are regular incidents which indicate that a certain degree of modulation of the power input is in fact the norm.

For example, line amperage drops if there is an anode effect on the line. Depending on the duration and magnitude of the anode effect, the decrease can exceed 10 kA and last for several minutes. This happens routinely and it is not known to have a negative impact on the rest of the pot line.

The most severe case of power modulation is a line shutdown, e.g. to cut out a cell for relining or to cut a cell back in. Measures are taken to reduce the time needed for that operation, but a shutdown of a line for 10 to 15 min is quite common. Depending on the number of cells in line and the average life time of a cell such outages happen approximately once a week. These procedures are not referred to as power modulation routinely as the incentive is very different. Looked upon from a different angle, perception can shift. It is common practice in Germany that in times of grid instabilities, the grid operators, after consulting with the smelter management, may take a smelter off the grid as a substitution for fast-starting a peak load power plant to stabilize the electrical grid.

Also, over the past years, a practice called peak shaving has been used repeatedly. This is practiced mainly during summer, when energy demand around midday peaks and prices at the EEX preclude economical aluminium production as well. In consultation with the grid operators, the smelters cut out one or several lines to reduce their electricity uptake for one hour or more. The energy is sold back to the market. Smelters have been able to generate a profit of several tens of thousands Euros on each occasion.

4.2.1 Thermal Operation Range for a Reduction Cell

Looking at the cell side of power modulation, cells can attain different energy states. The control of a cell always works to keep the cell within a very limited range of bath temperature and bath composition. In some instances, the control even works towards a set, single value temperature. However, looking at publications over the last years, there is no general agreement on the optimum temperature. Typically, target temperatures in the range of 955 to 970 °C are cited, depending on cell technology, process control and operating philosophy (Utigard 1999, Rieck, Iffert et al. 2003, Stam, Taylor et al. 2007). If the bath is lithium modified, temperatures as low as 945 °C are quoted. The general agreement is that cells perform optimum in that range and efficiency decreases if you operate at bath temperatures considerably below or above. On the lower temperature this is due to decreasing alumina solubility and a less stable cell resulting from the steeper gradient of the liquidus temperature. On the higher temperature, metal solubility in the electrolyte increases leading to an increase in back reaction and thus loss of current efficiency.

4.2.2 Aim of Process Control Systems

The aim of process control is to drive the cells back into their respective target range and keep them there. With increased effectiveness of process control, the distribution of cell states – represented by bath temperature and superheat or

liquidus temperature – has narrowed, leading to a better operation (Rieck, Iffert et al. 2003, Gao, Gustafsson et al. 2007, Stam, Taylor et al. 2007). Maintaining a smaller variability of cell states to a fixed range for optimum target bath temperature results in a variation of cell states that still leads to optimum performance. Figure 4.1 illustrates this concept.

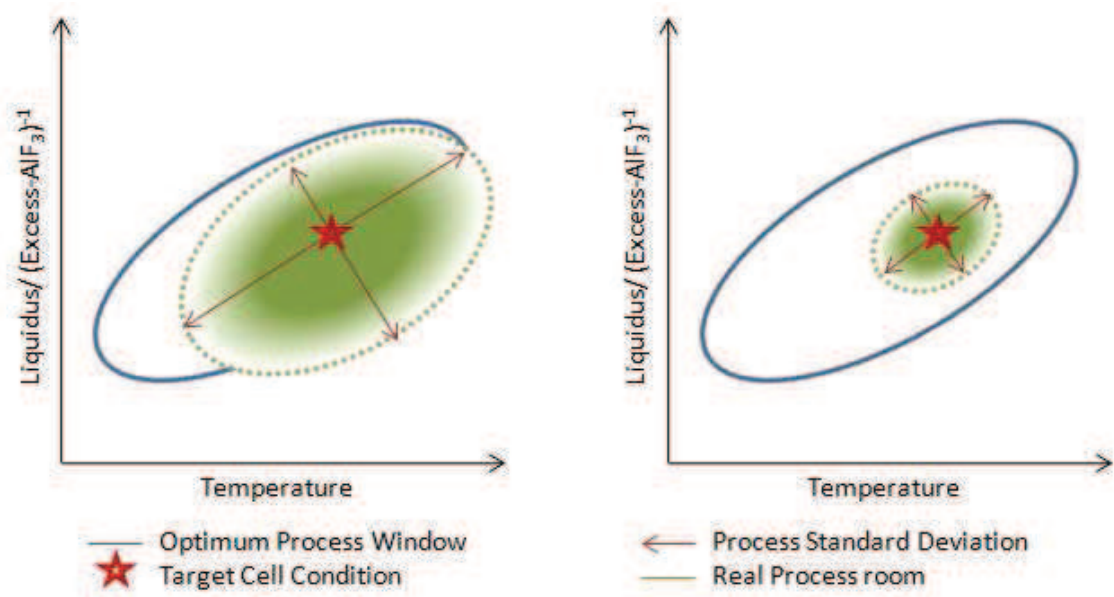


Figure 4.1: Comparison of the process Window of optimum performance with the real process room of a classical control system (left) and a modern one (right)

Variability cannot be eliminated completely however. If means are taken to operate at differing target conditions and if these target conditions are close enough to the boundary of optimum efficiency, individual cells will start to show indicators of being beyond the boundary even though the majority of cells are not affected significantly.

4.2.3 Heat Capacity of an Calculation for the Aluminium Reduction Cell as it is installed in Hamburg

If temperature swings between 955 °C and 970 °C are accepted, assumptions can be made as to the energy differences between these cell states. Table 4.4 shows the different temperatures for various materials located in the cell operating at two different temperatures of 955 °C and 970 °C, together with the energy needed to heat the material from room temperature to the given temperature and – if applicable – melt it. The minimum energy needed to heat the cell from one state to the other was deduced from the different heat contents. This calculation did not take into account that a heated cell will have an increased heat loss, but focused on the different heat content in the cell.

The data given in Table 4.4 represents data from cell reconstruction, bath and metal inventory measurements and sub-cathodic temperature measurements for a P19 cell performed at HAW and Trimet Hamburg (HAW 1999, Abbe and Reek 2008). To simplify the calculation, materials which have a definite temperature gradient – such as current collector bars, anodes and cathodes – were still treated as having an average, uniform temperature. Care was taken for the collector bars to avoid temperature swings beyond the recrystallization temperature. When evaluating the data it should be kept in mind that absolute temperatures are less important than the temperature difference between the heated and cooled state.

Table 4.4: Mass, temperature and energy of materials used in the cell at 955 °C and 970 °C

	Substance	Amount [kg]	Temp. [°C]	Energy contained [kWh]	Amount [kg]	Temp [°C]	Energy contained [kWh]
		Cell at 955 °C			Cell at 970 °C		
Anode	C	13,230	850	4,438	13,230	858	4,493
Cathode	C	14,000	935	5,282	14,000	940	5,355
Ramming paste	C	7,500	935	2,829	7,500	940	2,869
Collector bars	Fe	12,400	750	1,603	12,400	760	1,638
Side ledge	Na ₃ AlF ₆	5,000	890	1,623	2,689	908	883
Metal pad	Al	8,500	955	3,344	8,500	970	3,386
Total Bath		5200			7,511		
Cryolite	Na ₃ AlF ₆	4,134	955	2,099	6,271	970	3,232
Al ₂ O ₃		130	955	76	188	970	111
AlF ₃		676	955	399	676	970	403
CaF ₂		260	955	112	376	970	163
Sum		21,805			22,533		
Delta					728		

The metal pad will increase in temperature the same amount as the bath because of the high heat transfer rate between the two liquids (Whitfield, Skyllas-Kazacos et al. 2004).

Anodes and cathode carbon change will be equivalent to a 7.5 °C swing as bath/metal side interfaces will be at temperature, and the other boundaries are assumed to remain unchanged.

The change in liquid bath mass is the result of the melting of side ledge. In this scenario, the AlF_3 content dropped from 13 % to 9 %, which is a common occurrence for the stated temperature change as long as the superheat remains stable. The change in liquid bath mass can then be easily calculated by:

$$M_{\text{bath new}} = M_{\text{bath old}} \cdot \frac{C_{\text{AlF}_3 \text{ old}}}{C_{\text{AlF}_3 \text{ new}}} \quad \text{Eq. 4.2}$$

With	$M_{\text{bath new}}$	bath mass after change
	$M_{\text{bath old}}$	bath mass before change
	$C_{\text{AlF}_3 \text{ new}}$	AlF_3 concentration before change
	$C_{\text{AlF}_3 \text{ old}}$	AlF_3 concentration before change

Alumina concentration is not changing as alumina is added continuously to the bath. CaF_2 is not changing in correspondence to AlF_3 as shown in Table 4.5.

The table shows the AlF_3 and CaF_2 levels of a cell before and after an incident resulting in an increase in temperature. The CaF_2 remained stable while the AlF_3 concentration changed significantly. This implies that the CaF_2 content in solid ledge is similar to the content in the liquid bulk. For this reason, the amount of CaF_2 increases in the liquid bath in Table 4.4.

Table 4.5: Bath chemistry development on cell 113 without AlF_3 additions (Reek 2013)

Date	AlF_3	CaF_2
07.05.13	15.2	4.9
09.05.13	14.3	5.0
12.05.13	8.7	4.4
13.05.13	8.4	4.6
14.05.13	8.7	4.7
15.05.13	8.9	4.5

The energy data is represented in Figure 4.2, while Figure 4.3 details the change of energy content of the described cell materials during heat up and cooling. It is evident that the major shift in heat content is in the change-over from solid side ledge to molten bath. The changes of heat content of all other materials are insignificant in comparison.

The calculation also shows that cells operated on power modulation are very susceptible to hot or red side walls due to the thinning of side. If the cell has been driven to maximum amperage, this danger is increased manifold. Due to constraints mainly in the anode bake furnace and also in anodic current density, the TRIMET Hamburg P19 cell is operated with a wide side channel and sufficient side ledge mitigating this danger.

Due to the cooling of the cell, it is also susceptible to ridging of the cell bottom. This has to be kept in mind when designing power modulation cycles.

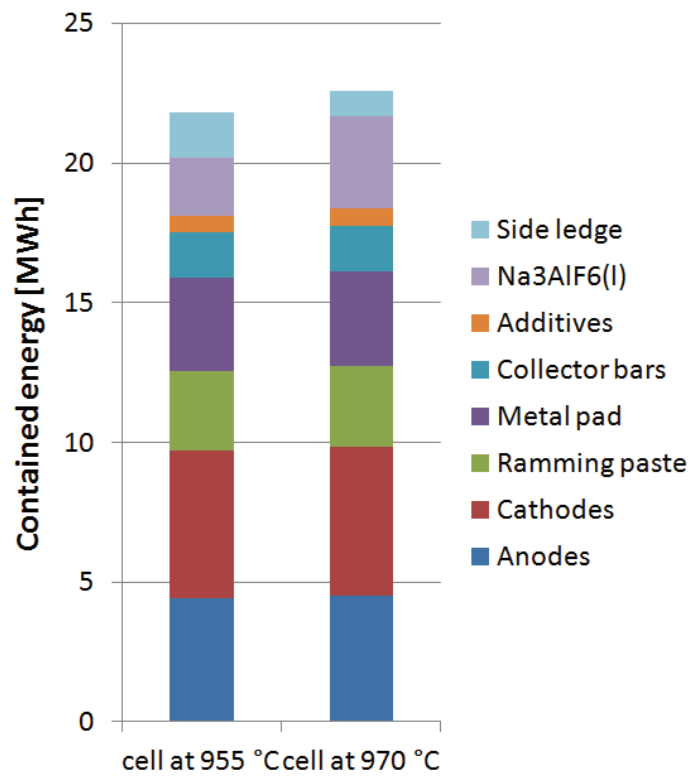


Figure 4.2: Energy content of a reduction cell at 955 °C and 970 °C

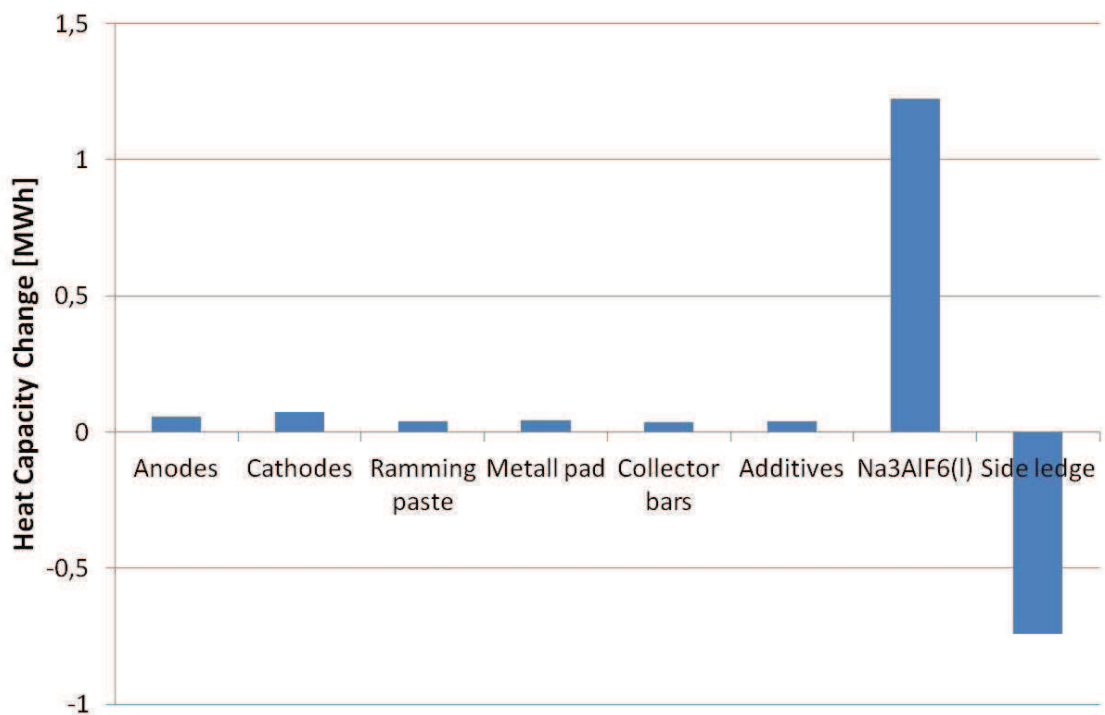


Figure 4.3: Shift in energy content while heating up from 955 °C to 970 °C

As is shown in Table 4.4, a theoretical limit of roughly 0.7 MWh was calculated for the energy difference that can be stored in the cell. This does not include any additional heat losses incurred during heating up of the cell and during operation at an elevated temperature. The storage efficiency cannot be expected to be 100 %.

Based on the operating constraints, trials of power modulation were conducted under the following conditions:

- The average power introduced into the cell shall average to an energy input that is similar to the energy input with which the cell was operated previously on continuous amperage. This should keep both, energy needed for metal production as well as heat loss in mind.
- The maximum deviation from continuous power input shall not exceed the theoretical maximum.

The assumption is that the process efficiency will decrease significantly if you exceed these boundaries. In 2008 TRIMET Hamburg operated on a modulation scheme that was significantly below nominal energy input. During this time, significant losses in current efficiency were recorded, as will be discussed in Chapter 6.

4.3 Affected Cell Voltage Components

Changing the line amperage is one of the major – if not the one major – change a pot line can undergo. Because many of the cell voltage components are either ohmic in nature or dependent on current density, a change in line current also means that cell voltage will also change.

If there is no additional action taken when changing line current, cell voltage will change accordingly because of the ohmic contributions, and hence the energy introduced to the cell will change by the same factor to the power of two.

However the electrochemical potential gradients at the two electrodes will also change even though within the band in which variations can be made the change in the decomposition potential will be negligible.

Likewise the operating electrode potential constraint to avoid PFCs will not change significantly and there is still the need to maintain the anode potential below ~ 1.8 V to avoid formation of such.

The major change that can occur due to changes in current is in the electrode over-potentials since these have been shown to be a function of:

- the anode current density
- the anode gas composition
- the temperature
- dissolved alumina concentration

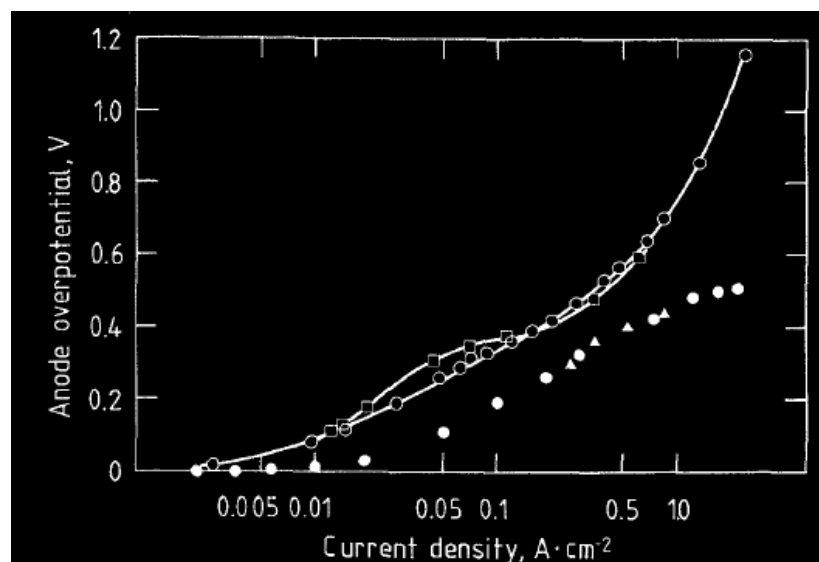


Figure 4.4: Different investigations of anode polarization at 980 °C for cryolite-alumina melts with graphitic carbon electrodes (Welch 2003)

While the published data all shows similar trends, predicting the magnitude of change is unfortunately more difficult because of this strong dependence on carbon type and quality. According to Welch reproducibility is limited due to the inhomogeneous properties of industrial anodes (Welch 2003). Coke and binder matrix in an industrial anode show preferential reaction and uneven wear. Laboratory tests typically use graphitic, glassy or pyrolytic carbon for this reason. The results will differ from each other as well as from industrial grade anodes, but trends are assumed to be similar. Figure 4.4 shows results from several laboratory trials using graphitic carbon (Welch 2003).

In the literature, there have been discussions if anode polarization follows a Tafel behaviour or not. Earlier works explicitly report non-conformity, which indicates the author expected to find adherence to Tafel behaviour. (Haupin 1956). Other work report conformity (Thonstad 1970, Zuca, Herdlicka et al. 1980). The range of coefficients given for the Tafel equation as detailed in Eq. 4.3 must be considered wide with values for coefficient b between 0.13 and 0.6.

$$\eta = a + b \cdot \log\left(\frac{i}{i_0}\right)$$

Eq. 4.3

with:

η	over potential
i	current density
i_0	exchange current density
a, b	reaction specific constants

Tafel behaviour can be questioned as most of the published curves have inflexions similar to that in one of the curves in Figure 4.4. There is another possible explanation however.

There are two distinctly different anode reactions occurring depending on current density. This is the formation of carbon monoxide at low current densities on the one hand and carbon dioxide on the other hand. The

generation of both gases is overlapping however and each over-potential curve is following an exponential trend as is shown in Figure 3.7. Carbon dioxide formation has a higher over potential and is thus only favoured at a higher current density. As such the data presented in Figure 4.4 could also be an overlay of these two exponential curves. The attributed Tafel equation relationship would then be only an approximation based on experimental results.

For the line currents of 160 kA to 195 kA realized during power modulation in Hamburg, anodic current densities between 0.75 and 0.91 A/cm² can be calculated. This would induce a change in anode polarization voltage between 50 mV and 130 mV, if the data from Figure 4.4 is used. As a medium anode polarization voltage is assumed a medium change of 90 mV will be assumed for the given range.

The saturated alumina concentration is lowered by decreasing temperature, and this in turn lowers the kinetics of dissolution.

At lower current densities the proportion of carbon monoxide formed would increase and consequently it would have an impact on the change in the anode gas composition but a very negligible impact on electrode potential.

The major change will be in the ohmic voltage drop through the electrolyte which is the other largest single ohmic voltage component.

Since the energy required for metal production according to the various reactions given in Chapters 3.2.2 and 3.2.3 will only change by the proportion of the current, then a current reduction usually results in an energy deficit since the cell heat loss is driven by the temperatures rather than the operating current. Accordingly, an increase in amperage will result in a surplus of heat being introduced.

The accumulation of deviation from nominal heat input will lead to a decrease of cell temperature for current reductions and an increase in temperature for line current increases. This will have an according impact on heat loss from the cell.

4.3.1 Compensating Voltage Adjustments

Accordingly, the cell resistance has to be adjusted anti-proportional to the line current to counteract the change in line current. The boundaries for these actions are the instability for ACD reductions on the one hand and the available bath volume on the other.

The lower the ACD, the higher is the back reaction due to insufficient separation of metal droplets formed at the cathode and CO_2 formed at the anode. Also, ripples on the liquid metal surface will lead to an uneven current distribution, if the height of said ripples is large enough compared to the ACD. As the magnetic fields increase with increased current, the so-called magneto-hydrodynamic stability (MHD) decreases.

An increase in ACD to counteract a decrease in current is facing hard limits as well. As the ACD increases, the total bath height is decreased overproportionally. This is due to the different areas for the total area of the cell relevant for the ACD on the one hand and the area of the channels between the anodes themselves and between the anodes and the side of the cell relevant for the bath height above ACD on the other hand. For the Hamburg cell, an increase of ACD of 1 cm leads to a bath height decrease of 3 cm.

If the ACD is increased, the conductive anode surface decreases as the immersion depths of the anode decreases. This can have a major impact on anodic current density as well as on the functioning of the equipment such as the alumina feeders and breakers.

Likewise if the current is being increased and the voltage reduced in accordance with the need to maintain heat balance, the rise in height of the electrolyte around the sides of the anodes can also become a constraint.

Another issue when balancing energy following amperage change is the change in current efficiency with the inter-electrode distance which will automatically change. There is a non-linear dependence so prediction is difficult.

4.3.2 Bath Voltage Drop

The bath voltage drop is dependent on a variety of factors. Most notable among these is the ACD. Even if the ACD is kept constant, as is the target for most modulation scenarios, the conductivity of the bath changes with temperature and chemical composition.

In the literature there are several publications on the empirical determination of electrical conductivity. The most used are published by Wang X, Hives and Wang L (Wang, Peterson et al. 1993, Híveš, Thonstad et al. 1994, Wang, Tabereaux et al. 1994).

The equation given by these three sources differ for the given cell and electrolyte composition. Hives gives two equations in his publication as follows:

$$\begin{aligned} \kappa = & -1.66 \cdot x_{AlF_3} - 0.942 \cdot x_{AlF_3} \cdot x_{Li_3AlF_6} - 0.76 \cdot x_{CaF_2} \\ & - 1.80 \cdot x_{CaF_2} \cdot x_{Al_2O_3} - 2.53 \cdot x_{Al_2O_3} - 2.59 \cdot x_{Al_2O_3} \cdot x_{MgF_2} \\ & + 0.97 \cdot x_{Li_3AlF_6} - 1.07 \cdot x_{MgF_2} + 7.22 \cdot e^{\frac{-1204.3}{T}} \end{aligned} \quad \text{Eq. 4.4}$$

$$\begin{aligned} \kappa = & 1.977 - 0.0131 \cdot c_{AlF_3} - 0.0060 \cdot c_{CaF_2} - 0.0200 \cdot c_{Al_2O_3} \\ & + 0.0121 \cdot c_{LiF} - 0.0106 \cdot c_{MgF_2} - \frac{1204.3}{T} \end{aligned} \quad \text{Eq. 4.5}$$

The first equation uses mole fractions and is including terms for interdependencies of species. The other uses mass fractions and simplified

coefficients. Wang, X. reports values slightly higher than Hives using the cryolite ratio as given by:

$$\begin{aligned} \ln \kappa = & 1.9105 + 0.1620 \cdot CR - 3.955 \cdot 10^{-3} \cdot c_{CaF_2} \\ & - 1.738 \cdot 10^{-2} \cdot c_{Al_2O_3} + 2.155 \cdot 10^{-2} \cdot c_{LiF} - 9.227 \cdot 10^{-3} \cdot c_{MgF_2} \\ & - \frac{1745.7}{T} \end{aligned} \quad \text{Eq. 4.6}$$

With $CR = \frac{n_{NaF}}{n_{AlF_3}}$ cryolite ratio

On the other hand Wang, L. reports values slightly lower according to Eq. 4.7. He includes a term for aluminium carbide and uses the equivalent weight ratio of Tabereaux as input (Tabereaux, Alcorn et al. 1993).

$$\begin{aligned} \ln \kappa = & 1.7738 + 0.3351 \cdot EWR - 1.75 \cdot 10^{-2} \cdot c_{CaF_2} \\ & - 2.13 \cdot 10^{-2} \cdot c_{Al_2O_3} + 2.73 \cdot 10^{-2} \cdot c_{LiF} - 3.21 \cdot 10^{-1} \cdot c_{MgF_2} \\ & - 1.211 \cdot 10^{-1} \cdot c_{Al_3C_4} - \frac{1553.7}{T} \end{aligned} \quad \text{Eq. 4.7}$$

With $EWR = \frac{1}{2} \cdot \frac{n_{NaF} + n_{LiF} - n_{MgF_2}}{n_{AlF_3}}$ equivalent weight ratio

Figure 4.5 compares the equations for the given temperature range at a constant composition consisting of 13 % AlF_3 , 4.5 % CaF_2 , 0.3 % LiF and 3 % Al_2O_3 , which is the composition used in Hamburg. LiF is still present from a time when it was actively added, which is not the case anymore. Figure 4.6 compares the same equations for a change in AlF_3 -content at a bath temperature of 965 °C and a content of other additives as used in Figure 4.5. In reality both changes are superimposed.

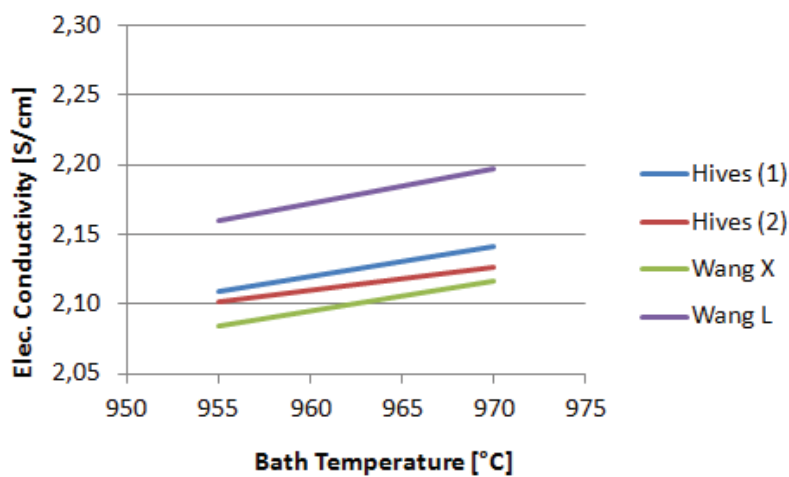


Figure 4.5: Electrical conductivity of the bath depending on bath temperature

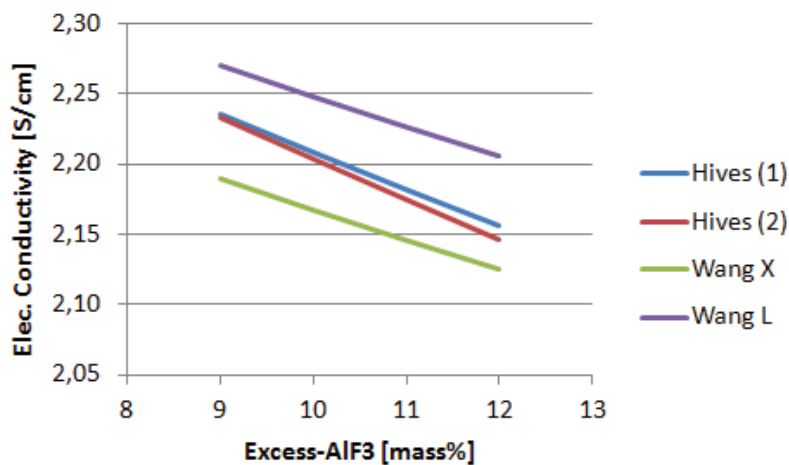


Figure 4.6: Electrical conductivity of the bath depending on bath composition

Both figures show a nearly linear trend in the given temperature and composition range. Superimposing both effects leads to a change in bath voltage drop of 80 – 90 mV for an ACD of 45mm, depending on which equation is used for the given change in cell condition.

It is difficult to ascertain which equation is the most reliable. The first equation given by Hives detailed in Eq. 4.4 seems to be used most often nowadays,

4.3.2.1 Bubble Layer Voltage Drop

The gas bubble layer is a topic of various publications. Voltage drop values that are reported vary greatly depending on determining method. Typically measurements are either performed in an industrial cell or the bubble layer voltage drop is modelled. (Solheim and Thonstad 1986, Zoric and Solheim 2000).

It is dependent on bubble formation speed and the speed of release from underneath the anode. As such the following properties play a role in the resulting bubble resistance:

- anodic current density as it influences anode gas composition
- anode gas composition as it influences generated gas volume
- anode width and length as well as number, width and depth of slots in the anode as they determine release distance for the bubbles
- anode wear profile as it influences the bottom slope of the anode
- bath height as it influences local pressure and thus anode gas volume
- bath composition and temperature as they influence bath viscosity

The individual effects these variables have are difficult to distinguish and their dependency on current density and changes of cell state caused by power modulation is difficult to assess. For this work it is thus assumed that the voltage drop is constant.

4.3.3 Cell Voltages Changes Induced by Changes of Line Current

In chapter 4.3 the individual cell voltage components were discussed. The components were categorised into ones following Ohm's Law and are affected linearly by changes in line current and those behaving differently. Table 4.6 lists the voltage components from Table 2.4 and expands this data in accordance with the discussed effects.

Cell voltage is expected to change from 4.20 V at 180 kA to 4.00 V at 160 kA or 4.35 V at 195 kA if the anode position remains stable. This is a change in cell voltage of approximately 350 mV. This calculation includes only first order reactions. The change in cell voltage can be quantified in dependence on line current with a linear regression to:

$$U_{cell} = 2.114 + 0.0155 \cdot I \text{ (V)} \quad \text{Eq. 4.8}$$

With: U_{cell} cell voltage
 I line current in kA

Changes beyond the given range will occur due to solidification and melting of bath and the changes in resistance due to changes of temperature for ohmic conductors. These changes are not only limited to cell temperature and chemical composition of the molten bath. The change in line current will interact with flow patterns of bath, metal and current distribution; thus influencing the magnetic field as well.

These changes are even harder to investigate and quantify. For that reason differences from the given range of approximately 350 mV are to be expected.

Table 4.6: Comparison of voltage breakdown for different line currents

	Low Amp	Normal Amp	High Amp
Temperature	955 °C	965°C	970 °C
Line Current	160 kA	180 kA	195 kA
Total Cell Voltage	4.007 V	4.200 V	4.351 V
Cell Electrochemical Voltage	1.760 V	1.810 V	1.850V
Decomposition Potential	1.220 V	1.220 V	1.220 V
Anode Polarization Voltage	0.510 V	0.560 V	0.600 V
Cathode Polarization Voltage	0.030 V	0.030 V	0.030 V
Total Anode Voltage Drop	0.430 V	0.485 V	0.525 V
Anode clamp + Beam	0.053 V	0.060 V	0.065 V
Anode Rod to Yoke	0.053 V	0.060 V	0.065 V
Stub – Carbon Contact	0.111 V	0.125 V	0.135 V
Carbon	0.213 V	0.240 V	0.260 V
Total Bath Voltage Drop	1.501 V	1.550 V	1.591 V
Electrolyte Voltage Drop	1.380 V	1.430 V	1.470 V
Bubble Voltage Drop	0.121 V	0.121 V	0.121 V
Total Cathode Voltage Drop	0.316 V	0.355 V	0.385 V
Cathode + Collector Bar	0.240 V	0.270 V	0.293 V
CVD externals bus bar	0.076 V	0.085 V	0.092 V

The equation used in process control units to compensate fluctuations in line current is given in Eq. 2.8. This equation gives cell voltages of 3.91 V at 160 kA and 4.416 V for 195 kA. These deviations are considerably higher than the ones given in Table 4.6. This infers that the non-ohmic part of the cell voltage is larger than is taken into account in the process control system.

Figure 4.7 compares cell voltage for different line amperages obtained from Table 4.6 and the calculated control voltage used in the process control units over the given amperage range. The change in calculated process control voltage is larger than the actual change in cell voltage. Thus the anode cathode distance is increased slightly for increased line currents, and respectively decreased if the line current is lowered.

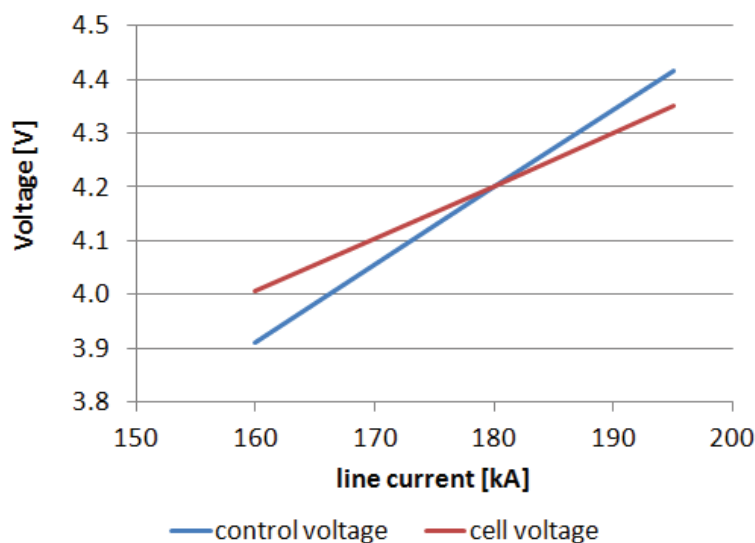


Figure 4.7: Cell voltage compared to calculated control voltage

4.4 Practical Limitations

Whereas the previous part of this chapter discussed the constraints the process itself imposes on operation with a non-constant energy input, outside factors like equipment availability, operational personnel and organisational issues act as constraints as well. Figure 4.8 illustrates a modulation cycle and the resulting energy state of the cell. A positive energy state is indicated by the green curve being above the base line while a negative state is indicated by the green curve being below the baseline. There is a time lag between the change in energy input and the actual change of the energy state of the cell. For this discussion it is irrelevant if the modulation is induced by changes in line current, cell voltage or a combination of both. The resulting energy state of the cell is of interest in this chapter.

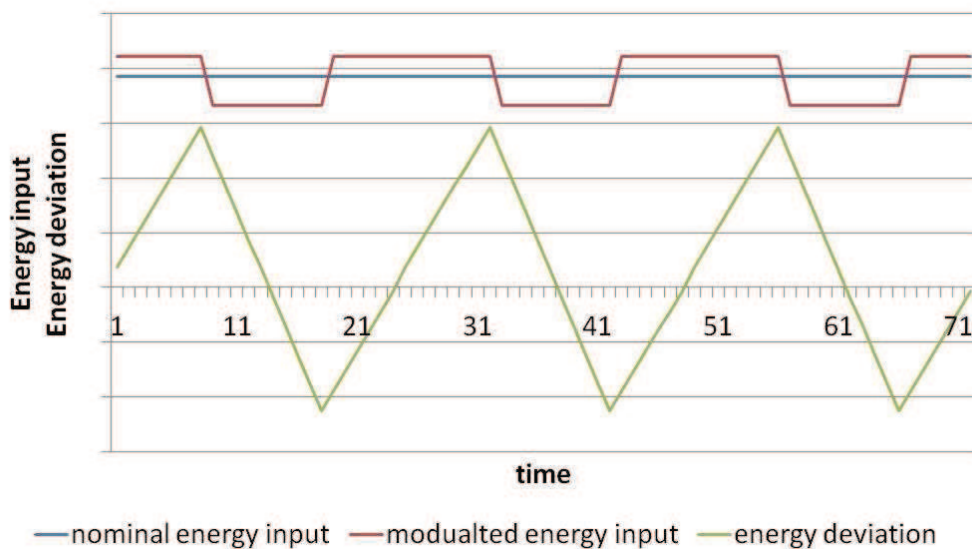


Figure 4.8: Schematic of modulated energy input and resulting energy states

Such issues come to bear if power modulation is practised to an extent that it has an immediate impact on work practices. Certain work practices can be linked to defined energy states of the cell. Anode change on the one hand

introduces a large mass of cold material into the cell. That material has to be heated to operating temperature. If the available energy is insufficient for heating, the anode may develop spikes and the cell might not have enough energy to dissolve alumina, leading to sludging and anode effects. Therefore anode change should be limited to the period of high energy content.

On the other hand metal tapping reduces the heat loss from the cell by decreasing the liquid level in the cell and thus the heat transmitting surface on the side walls. Thus even though removing hot metal decreases the energy content, it also decreases the heat loss from the cell. This results in a measureable increase in bath temperature (Reek 2003).

Thus it would complement a period of lower energy content. Additionally, lower energy input will be realized by lowering pot line current. This leads to a decrease of magnetic forces in the cell. This may enable a smelter to temporarily operate with slightly lower metal inventories than during operation with normal amperage. It should be optimized in a way that normal metal levels are regained within the time of low amperage. As metal production is within 1.5 to 2 centimetres of metal height increase per day and typical modulation cycles are expected to be considerably shorter, the magnitude for such action is within 1 cm.

4.4.1 Restraints in Equipment and Organisation

If modulation is practiced to an extent that work procedures have to be shifted, available equipment may pose a limiting constraint. The two main work procedures that can be shifted are metal tapping and anode changing. Typically anode changing would be shifted into the high energy period and metal tapping would be shifted into the low energy period. This arrangement would necessitate different availability of equipment and – at a certain point - even personnel.

Typically a smelter is equipped in a way to service a continuous load of work – the number of anodes changed and the amount of metal tapped does not vary significantly from shift to shift.

If metal is to be tapped during the low energy period, there has to be enough equipment – such as crucibles – to deliver the same amount of metal in a significantly shorter time to the cast house. Additionally, the cast house has to be able to process the liquid metal in a shorter time. The same is valid for anode change.

Even if the needed man hours are the same if you rearrange the work practice, there may be limits which are not easy to overcome on a short term. For a smelter with crane operation – like Trimet Hamburg – that problem may not be as pronounced as for a vehicle operated smelter. The cranes servicing a half-pot room in Hamburg are used for both metal tapping and anode changing. Rearranging the work practices will not have a significant impact. If metal is tapped by trucks, the availability of tapping trucks may impose a hard limit on metal delivery to the cast house.

4.4.2 Constraints Imposed through Interfaces

If looking at changing overall work routines, interfacing plant sections have to be taken into consideration as well.

4.4.2.1 Pot Room – Cast House Interface

The interface between pot rooms and cast house needs to be discussed in that regard. The cast house operation is only feasible if it is supplied with liquid metal from the pot room. If only scrap metal or primary ingots are used for cast house operation, the cast house suffers from increased melting times and metal loss during melting. The additional energy delivered into the cast house by liquid metal from the pot room heated to 250 °C above melting point is taken out of the process.

In Hamburg there is an additional barrier. The cast house is operated by a different company and it was contractually agreed that metal is delivered uniformly throughout the day. Thus changing from a continuous metal supply to a metal supply covering only the major part of the day would necessitate a renegotiation of the metal delivery contract.

If the cast house is considering non-continuous shift rotas anyway, the idea of shifting metal delivery is not prohibitive any more.

4.4.2.2 Rodding Shop – Pot Room Interface

Considering the other major interface of the pot room, anode supply from the rodding shop is less critical. In Hamburg rodded anodes are stored in the pot room for several shifts and anode supply is non continuous. Rearranging anode changing is not impacting on this interface.

4.5 Concepts of Implementing Power Modulation

To modulate the energy input of an aluminium reducing cell, two parameters can be manipulated. The first parameter is cell voltage, the second line amperage. Whereas the cell voltage only influences the heat generation in the cell, the line current influences both heat generation by acting upon the cell voltage, and the production rate of metal and thus one heat sink.

If a cell is operated at different currents the balance between metal production and heat loss has to be kept in mind. Two extreme strategies are possible to approach the changing heat balance. These are:

- modulation with minimal impact on thermal balance
- modulation with minimal impact on the cell

4.5.1 Modulation with Minimal Impact on Thermal Balance

In this scenario, the cell voltage is adapted to facilitate constant heat loss from a cell. For the base case detailed in chapter 3.2 at 93.5 % current efficiency, the heat loss is:

$$\begin{aligned} Q_{heat\ loss} &= (U_{cell} - U_{ext} - U_{metal}) \cdot I \\ &= (4.20V - 0.355V - 2.069V) \cdot 180\text{ kA} = 319.68\text{ kW} \end{aligned} \quad \text{Eq. 4.9}$$

The same amount of surplus energy has to be introduced into the cell to enable it to remain in heat balance. For this theoretical discussion, it is assumed that the metal production voltage is independent of current density and the current efficiency of the process does not change as well as that the bubble resistance remains unchanged.

If the line current varies, the cell voltage has to be adapted to enable a constant heat loss as follows:

$$U_{I_{target}} = \frac{Q_{heat\ loss}}{I_{target}} + U_{metal} + U_{ext} \cdot \frac{I_{target}}{I_{base}} \quad \text{Eq. 4.10}$$

With	$U_{I_{target}}$	new set point voltage
	I_{target}	new line current
	U_{metal}	voltage to produce metal; 2.069 V at $\eta_{CE} = 0.935$
	U_{ext}	external (ohmic) voltage drops, 0.355V
	I_{base}	base line current; 180 kA
	$Q_{heat\ loss}$	heat loss from the cell

The formula is similar in setup to the one used in standard control systems to compensate for fluctuations in line amperage given in chapter 2.1.4.

For 160 kA this results in a set point voltage of 4.38 V and for 195 kA the result is 4.009 V.

The natural changes in cell voltage as given in Table 4.6 result in cell voltages of 4.007 V and 4.351 V for 160 kA and 195 kA respectively. This would require the following voltage changes to enable a constant heat loss:

$$\Delta U_{195kA} = 4.009V - 4.351V = -0.342V \quad \text{Eq. 4.11}$$

$$\Delta U_{160kA} = 4.380V - 4.007V = +0.373V \quad \text{Eq. 4.12}$$

Comparing these findings with the natural changes in cell voltage given in Table 4.6, voltage changes of +0.403 V and -0.281 V would be necessary for current decrease and increase respectively to maintain constant heat balance at said amperages. This would only be achievable by significant movement of the beam and changing of the ACD as the bath voltage drop is the only one that can be influenced. As the bath voltage drop changes linearly with the ACD, the change in ACD can be calculated as follows:

$$\Delta ACD_{195kA} = \frac{-0.342V}{1.380V} = -24.8\% \quad \text{Eq. 4.13}$$

$$\Delta ACD_{160kA} = \frac{+0.373V}{1.380V} = +27,0\% \quad \text{Eq. 4.14}$$

Assuming an ACD of 45 mm, this would necessitate a beam movement of -11.2 mm and +12.2 mm respectively. The change in bath level is 3 times as high for the Hamburg cell due to the bath replacement by the anodes. This change of bath level cannot be tolerated for an extended period of time.

Addition and removal of liquid bath would be necessary for each modulation step. As liquid bath has to be removed for high amperage operation and re-introduced for low amperage modulation, storage of liquid bath outside of the process would be necessary. With the low superheat and the corrosive nature of the electrolyte, this would present a new set of challenges besides the logistics involved.

As the change in set point voltage is counteracting the energy increase and decrease, the achieved spread in energy uptake is diminished. In addition to the scenario with increased current, the ACD would drop below the critical limit necessary for stable operation.

The following advantages and disadvantages can be summarized for modulation within thermal balance:

- + can operate with these settings indefinitely as heat balance is not influenced

- bath handling increases dramatically
- ACD too small for stable operation for high current scenario
- anode cover deteriorates due to beam movements
- spread of energy uptake partly compensated by voltage adjustment

4.5.2 Modulation with Minimal Impact on the Cell

This scenario aims at keeping the cell – especially the beam – as unchanged as possible. The line current is changed, but any compensator action taken by the process control system is suppressed. This is only necessary if the control system is controlling by raw voltage and not by (pseudo-)resistance or normalized cell voltage. If the control system operates using Eq. 2.8 given in Chapter 2.1.4, it will not determine a change in the operational state, even though measured cell voltage will change according to the change in line current. The anode beam is not moved as the cell resistance does not change.

The disadvantages are on the thermal balance of the cell. The energy input to the cell decreases dramatically if the current is reduced. As the heat loss is not changed immediately the cell will start cooling. If cooling of the cell is insufficient to compensate for the heat loss, the cell will lose current efficiency to supply enough heat for heat loss. Accordingly if the current is increased, the cell will heat up and lose more heat. As this will eventually also decrease efficiency, the cell may become a hot cell with all associated problems, up to premature failure. To counteract the adverse effects of both cooling and heating, the modulation cycle has to be enveloped by the maximum amplitude of energy input as developed in chapter 4.2. A very detailed control of the cell with regards to a cumulative energy input is needed. Also the control of bath and liquidus temperature is no longer straight forward, as temperature will shift depending on the deviation from nominal energy input.

As the line resistance remains stable, the energy uptake increases or decreases by the power of two with a change in line current.

The following advantages and disadvantages can be summarized for modulation outside thermal balance:

- + no beam movement necessary
- + maximizing the effect on power price if current is modulated in counter current

- operation only possible for a limited time
- cell forced into cooling/heating cycle
- traditional process control towards constant target temperatures no longer valid

4.5.3 Changes in Alumina Feeding

The Celtrol process control system uses a base feed time (BFT) to adjust alumina additions. The base feed time is the time distance between two dumps of alumina with 6 kg each. All feeding cycles are calculated based on the BFT. Average base feed time for a cell at 180 kA is 195 s. The base feed time is reduced to 76 % during overfeed for 40 min as a standard during normal operation. Overfeed is followed by 15 min on base feed where beam adjustments are executed. When a new phase begins, the first shot is added immediately and the timer is started. The number of shots in a feeding phase can thus be calculated as:

$$n_{shots} = \left[\frac{t_{phase}}{t_{feeding}} \right] \quad \text{Eq. 4.15}$$

With:

- n_{shots} number of alumina additions
- t_{phase} duration of the feeding phase
- $t_{feeding}$ feed time during the phase

When changing line current the alumina consumption of the cell changes accordingly and the alumina addition has to be adapted. The best way to do this is by adjusting the base feed time. As can be seen from Eq. 4.15 the alumina addition only changes if the change in feeding time results in a change of the integer part of the equation. Figure 4.9 illustrates this for both base feed and overfeed. The vertical lines indicate the needed feeding rates for 160 kA (88 %) and 190 kA (108 %) respectively. While the number of shots during base feed time does not change at all, during overfeed the number of shots varies from -2 to +1. Considering the volumetric design of the feeder which is prone to error, the change is small.

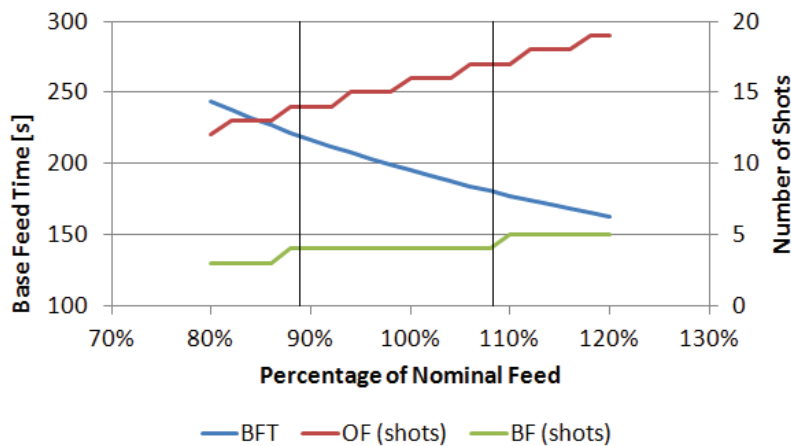


Figure 4.9: Effects of varying BFT on number of shots

4.5.4 Implementation at Trimet Hamburg

In this work the aim was to investigate the cell reaction to different energy inputs. The target was operation out of heat balance for a limited time period. The omission of any additional bath handling as well as the maximum spread in energy uptake was considered beneficial. For this reason, the respective modulation scheme as detailed in chapter 4.5.2 was adopted.

The maximum amplitude was stepwise increased towards the theoretical maximum as developed in chapter 4.2, resulting in operation between 160 kA and 195 kA. Even though the effect of adapted feeding times was considered minor, nevertheless it was implemented. The main reason for this was the natural distribution of base feed times in a pot line. Base feed time was adjusted proportional to the change in line current.

Before line current increases a forced overfeed was found to be beneficial as indicated by Pinheiro et al (Pinheiro Leal Nunes, Vianna da Silva et al. 1998). Figure 4.10 shows the critical current density in relation to the alumina concentration (Entner 1998). The blue area indicates the usual window of operation for a P19 cell in Hamburg. If the current density is increased rapidly by increasing line amperage, cells which are close to the critical current density will be pushed beyond it into an anode effect. With a forced overfeed just before

an amperage increase, cells are moved away from the critical current density and the risk of having anode effects is less when the current is increased.

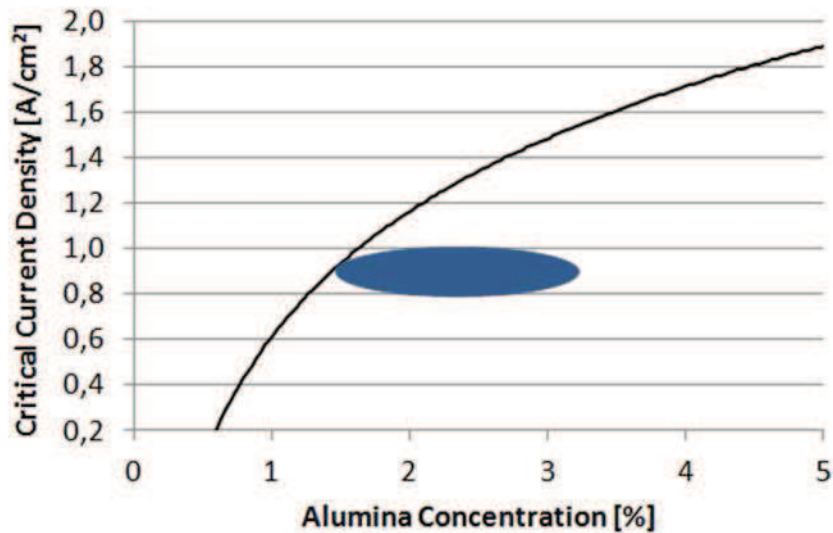


Figure 4.10: Critical anodic current density

As current increases take place after operating with decreased energy input for an extend period of them, the cell is on energy deficit and the superheat will be low in general. Forcing an overfeed may result in more alumina added than the cell can dissolve. Even if enough alumina is added in such a case, the cell may still go into an anode effect due to low alumina concentration in the bath. An overfeed of 120 % of nominal demand for 15 min was found to be sufficient of reducing the number of anode effects while simultaneously not sludging the cell.

5 Cell Reaction to Altered Operating Conditions

Synopsis:

To determine ledge dynamics and thus operational constraints, cells were subjected to both changes in line current as well as changes in operating voltage. The majority of these experiments use one single incident of deviating energy input to determine and evaluate cell and ledge reaction as well as the capability of recovery for a cell.

In addition several modulation schemes were run over an extended period of time in one reduction line to determine long term effects on the reduction line.

It was found that side ledge in contact with bath was reacting spontaneously to energy deviations, while side ledge in contact with the metal pad did not react as readily.

Part of the data presented in this chapter was already published at the Postgraduate Reduction Course in Hamburg and Essen organized by the LMRC, Auckland in 2012 (Reek 2012).

For multivariate regression analysis NLREG software was used (Sherrod 2014).

5.1 Measurement Systems Used

In this thesis cell data is measured by various means. The different measurement systems and techniques are detailed in this chapter.

5.1.1 Bath, Liquidus Temperature and Superheat

Bath temperature and liquidus temperature are measured using the Cry-O-Therm system developed by Heraeus. The company published several papers detailing the design of the sensor and discussing measuring accuracy (Verstreken and Benninghoff 1996, Rolseth, Verstreken et al. 1998).

Accuracy of the used Type S thermocouple wire is given with ± 0.5 °C. For laboratory tests a precision is given of ± 1 °C for bath temperature and ± 2 °C for liquidus temperature. These values were determined in a 5 kg bath sample

molten in an induction furnace. The disposable sensors need no calibration before use.

For industrial application the measurement system is precise enough to determine small changes in the cell such as the feeding cycle or individual alumina shots. Repeatability of the measurements is within the postulated range if such influences can be avoided (Reek 2003).

5.1.2 Side Ledge Measurement

Measuring side ledge is a difficult task. Due to the multi-layered set-up of the cell lining and the physical similarity between side ledge and liquid bath there is no known method to measure the thickness of the side ledge from outside of the cell. Similarly due to the aggressive bath there is no technology to determine the contour of the side ledge contact-free from inside the cell. The only viable method for measuring side ledge is to use a metal hook contacting the frozen ledge inside the cell and record the geometry of the suspension to calculate the position of the solid/liquid interface. There are two reference means in use in the industry. One references from the steel shell, the other uses the anode ring bus as a reference. For this thesis the steel shell was used as a reference. The method is described by Angwafor in his thesis in detail (Angwafor III. 2000).

A suspended rotatable metal hook is dipping into the bath as illustrated in Figure 5.1. The hook is rotated until it is touching the solid side ledge. The angle which the hook turns is measured. The geometry of the hook and the suspension together with the angle of rotation can be used to calculate the position of the bath/ledge interface. The ledge thickness is the distance from the SiC-side wall to the bath/ledge interface. Even though the ramming of the seam also extends into this area, ledge thickness is not calculated as ledge deposited on top of the ramming paste. Ramming paste erodes fast if exposed to the bath. As can be seen in the following diagrams, the ledge profile intersects the outline

of the ramming of a new cell. It is not possible to determine reliably the ramming/ledge interface.

5.1.2.1 Ledge Measurement System

Figure 5.1 shows the ledge measurement system positioned on a newly relined cell. As can be seen, the handle at the top is in the same position as the metal hook inside the cell. Due to this construction the rotation of the handle is equivalent to the rotation of the hook. Figure 5.2 shows details of the dial used to measure the rotation of the handle. A laser pointer projects the exact position of the handle onto the dial. The other picture shows the hook in the cell positioned perpendicular towards the side lining.



Figure 5.1: Ledge measurement system in a new cell



Figure 5.2: Dial used for determination of the angle (left) and hook inside the cell (right)

It is possible to calculate the exact position of the tip of the hook from the geometry of the suspension. It is easier to measure the minimum distance from the tip of the hook to the side lining, when the hook is perpendicular to the side wall of the cell. As all cells are constructed according to the same drawing, the distance is the same for all cells if the geometry of the suspension is not changed. In case of the Hamburg cell, the side ledge can thus be calculated by the following equation. Figure 5.3 illustrates the measurement geometry for the calculation.

$$l = l_0 + l_{hook} \cdot (1 - \sin\alpha) \quad \text{Eq. 5.1}$$

With:

- l thickness of side ledge
- l_0 minimum distance from hook to side wall
- l_{hook} length of the bottom part of the hook
- α angle of rotation

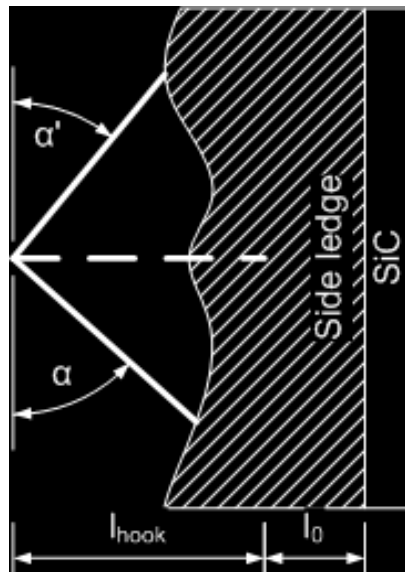


Figure 5.3: Sketch of the set-up of the side ledge measurement

To determine the ledge thickness over the height of the cell, the hook is raised incrementally and the measurement is repeated. Serrations on the hook holder indicate 50 mm increments of height. The measurement is repeated at each increment to give a complete coverage of the side ledge. Additionally, the measurement is done rotating the hook once clockwise and then counter clockwise (α and α' in Figure 5.3) resulting in two distinct measurements for each location and height. To avoid errors due to torsion of the system, both resulting ledge thickness are averaged, resulting in one ledge profile per insertion point.

5.1.2.2 Error Estimation of the Side Ledge Measurement

Due to the industrial nature of the measurement, there are errors associated with it. The following errors are possible:

Positioning of the System

The system has two attachment points located at the bottom of the base plate. These help to ensure that the system is always positioned in parallel to the deck plate of the cell. To avoid positioning with an inclination, the deck plate had to be swept clean from alumina and bath material. If these precautions are taken, an error transferred from positioning to the measurement is negligible.

If the deck plate is askew, the positioning will be askew to a similar extent. The angle of skewness will be transferred to the hook of the measurement rod. The side ledge will be influenced by:

$$l_{err} = l_{hook} \cdot (1 - \cos\vartheta) \quad \text{Eq. 5.2}$$

With: l_{hook} length of the bottom part of the hook
 ϑ skewness of the deck plate

Measuring the skewness of the deck plate on the test cells resulted in values of less than 2°. This results in a maximum error of 0.2 mm for the thickness of the side ledge. This error is negligible.

Torsion and Slack on the Measurement Rod

The measurement hook was connected to an upper rod using a splint pin. This is necessary to be able to change the hook after a few measurements. If this is not done, the hook will soften due to heat up, leading to an increased error. Eventually it will dissolve in the cryolitic melt.

Inevitably there is some slack in the connection. This combined with the torsion applied by the person conducting the measurement will introduce an error to the measurement. On trial measurements the maximum deviation on readings was found to be less than 5°. In this case the formula to calculate the maximum error is as follows:

$$I_{err} = I_{hook} \cdot \sin\alpha \quad \text{Eq. 5.3}$$

With: I_{hook} length of the bottom part of the hook
 α deviation on measurements

The maximum error is achieved if the measurement hook is parallel to the side wall of the cell. Using 5° as a maximum error results a maximum error of ± 30 mm for the thickness of the side ledge. If the hook is perpendicular to the side wall, the error would be only 1.4 mm. In the normal measurement range of about 45° an error of 1 – 2cm must be assumed.

The best precaution against this error is to have a limited number of people conducting the measurement. This is based on the assumption that the same person is always using the same force for rotating the measurement rod and thus will generate a similar reading. This was found to be valid during test measurements.

Limits of the Measurement Range

The side ledge measurement system can only detect side ledges that are within the ability of the hook to touch. If the side ledge is too thin, the hook will rotate freely within the bath.

Accordingly if the side ledge is too thick to introduce the vertical rod, no measurement is possible. This is typically found at the bottom of the cell if the cell has bottom ridge. In this case the measurement started at the lowest possible position and a side ledge thickness of the distance from the vertical rod to the SiC-side wall was recorded. In only a very limited number of cases, the ledge was so thin, that the hook did not touch the side wall. In these cases the thickness of the side ledge was assumed to be 100 mm, 10 mm less than the minimal measurable side ledge, to avoid disregarding the whole set of data.

With the equipment used and with the given cell geometry, side ledge thickness from the SiC refractory between 110 mm and 470 mm could be measured. It should be noted again that the measurement extended well into the side ramming, if it had been eroded. For reference purposes the original profile of the side ramming is given in all following figures.

Preparation of the Measuring Holes

To perform side ledge measurements, the top crust has to be broken. During this operation, lumps will fall into the bath. If they are still present during the measurement, erroneous results will be reported. Either the vertical rod cannot be introduced to the bottom of the cell, or the lump might sit in front of the side ledge. The measurement will report increased ledge thickness.

To avoid such errors, the holes were broken one shift before the measurement was performed. Immediately before the measurement, the holes were cleaned using a skimming scoop.

Conclusion on the Error Estimation

The main error comes from the torsion and slack of the measurement system. Other errors of the measurement system are significant or can be avoided by thorough preparation of the measurement. Nevertheless, accuracy of the ledge measurement is at an accuracy of ± 1 cm in the measurement range of the instrument.

To compensate for this accuracy, the measurements were performed at several cells and at several positions in each cell for each experiment. This resulted in typically 60 to 65 data points per height above the cathode for each experiment – e.g. 16 values for the ledge thickness at each anode pair were obtained before and after each of the energy increase trials detailed in the following chapter. The results show a scatter as is shown in Figure 5.4. To avoid a single

value being over influenced by individual outliers the median was used to represent these measurement points instead of an average value.

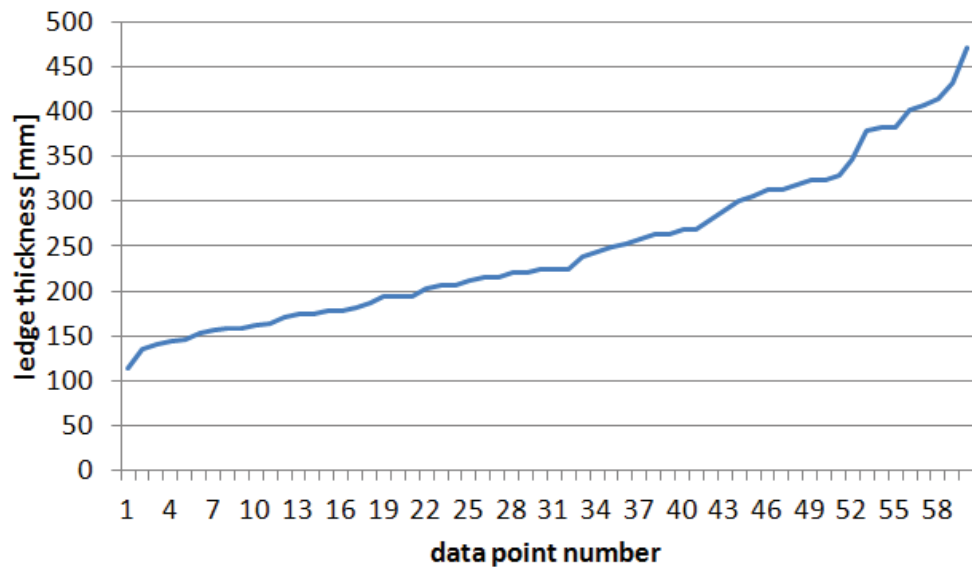


Figure 5.4: Distribution of measured ledge thicknesses 10 cm above the cathode surface on all cells before an energy increase trial

To manage the workload during the experiments, the number of measurement locations had to be limited. 8 out of 18 anodes were chosen to represent the total ledge thickness. The difference in measured ledge thickness is shown in Figure 5.5. The average difference over the total height of the cell is 4.5 mm, while the maximum difference is 22 mm at 10 cm above the cathode surface. This difference was found acceptable as the alternative would have been to limit the number of cells which could be measured in each trial.

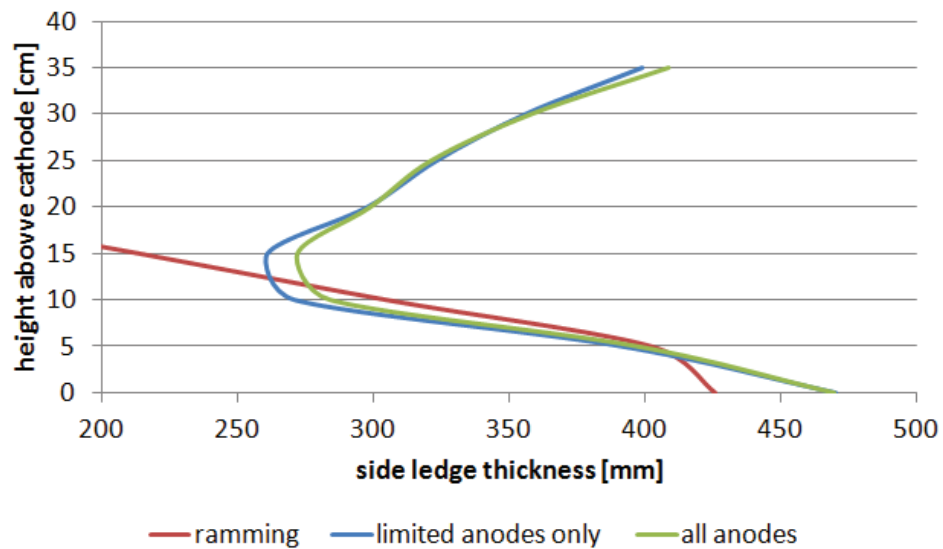


Figure 5.5: Comparison of the ledge thickness of all anodes and the selected measurement location for the January 2010 base case

5.1.3 Bath Inventory Measurement

In addition during one trial the change in bath inventory was determined using the Strontium tracer method described by Iffert and Stam (Iffert, Skyllas-Kazacos et al. 2005, Stam, Taylor et al. 2008).

The method detailed by Iffert was used. 5 kg of SrCO_3 were introduced into each cell, as well as using 3 samples before and 1 hour after addition to determine measuring accuracy and to be able to determine and disregard outliers. By comparing strontium levels before and after the addition, the bath volume can be calculated by:

$$M_{\text{bath}} = \frac{M_{\text{SrCO}_3}}{(c_{\text{after}} - c_{\text{before}})} \cdot \frac{m_{\text{Sr}}}{m_{\text{SrCO}_3}} \quad \text{Eq. 5.4}$$

with: M_{bath} inventory of liquid bath

M_{SrCO_3}	added mass of SrCO_3
c_0	concentration of Sr in the bath before and after the addition
m_0	molar mass of Sr and SrCO_3 respectively

It was found that if not introduced carefully, strontium carbonate suffers from heavy dust discharging due to the evolving CO_2 when in contact with liquid cryolite. This can lead to biased measurements resulting in increased inventory results if the addition is not done carefully. The method found to be most effective is to wrap 1 kg of SrCO_3 powder into several layers of aluminium foil and submerge it in the electrolyte using a ladle to keep it submerged until fully dissolved. Nevertheless careless addition of SrCO_3 resulted in several sets of data that was not usable.

5.2 Base Case Studies

5.2.1 Sensitivity of Side Ledge to Outside Temperature

Before modulation was introduced in Trimet Hamburg, the base case of side ledge was investigated. For this purpose side ledge measurements on four cells were taken in January and April. Measurements were performed between each anode as is shown in Figure 5.6.

According to German weather the service average temperature in January was $-3.1\text{ }^{\circ}\text{C}$. In April the average temperature was $8.9\text{ }^{\circ}\text{C}$ (Anonymous 2013b). The pot line was operating with the same operating parameters. The measured side ledge is shown in Figure 5.7.

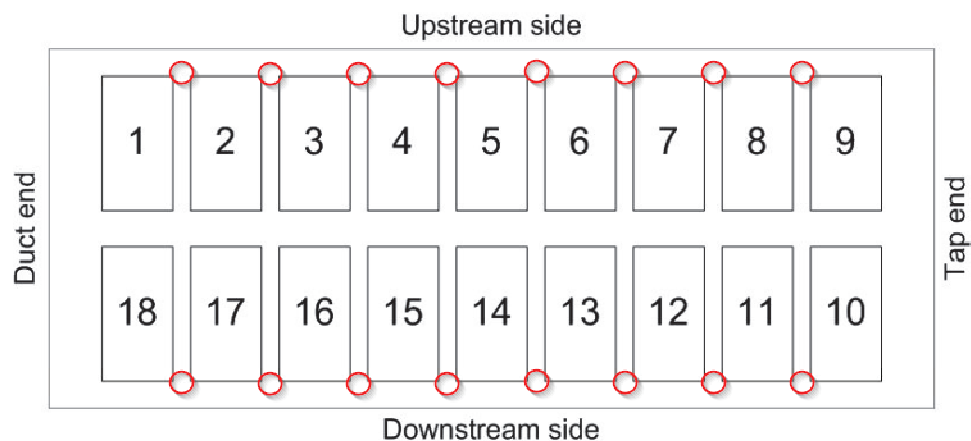


Figure 5.6: Measurement positions for the base case side ledge measurement

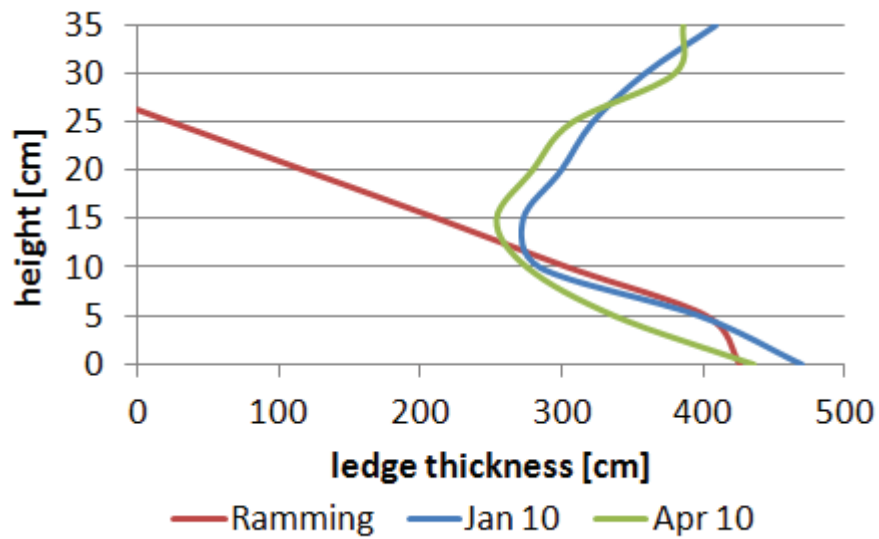


Figure 5.7: Effect of different seasons on side ledge

As expected, the side ledge is considerably thinner during the warmer month. In total the side ledge thinned by 20 mm as is shown in Table 5.1. Calculated for the total inner surface of the cell this corresponds to a loss of side ledge in the amount of 0.224 m³ or 605 kg of side ledge:

$$V = 2 \cdot (l_{cell\ length} + l_{cell\ width}) \cdot h \cdot \Delta d$$

Eq. 5.5

With:

- V ledge volume
- $l_{cell\ length}$ length of the cell
- $l_{cell\ width}$ width of the cell
- h height of the liquid phase; 0.4 m
- Δd reduction in thickness; 0.02 m as per Table 5.1

Table 5.1: Measurement data for Figure 5.7

Height	Jan 2010	Apr 2010
0 cm	470 mm	435 mm
5 cm	397 mm	337 mm
10 cm	284 mm	275 mm
15 cm	272 mm	253 mm
20 cm	299 mm	278 mm
25 cm	321 mm	307 mm
30 cm	358 mm	379 mm
35 cm	409 mm	385 mm
Average	351 mm	331 mm

The metal height is recognizable by the pinch point where the side ledge is thinnest. This is due to turbulence in the metal-bath-interface introduced through the bubble release at the corner of the anode (Taylor 2012). Figure 5.8 illustrates this effect.

It is notable that the height of the thinnest side ledge is not exactly corresponding to the recorded metal height of the cell of 18 to 20 cm. The pinch point is typically recorded at 10 or 15 cm above the cathode surface as is depicted in Figure 5.7 and most of the following measurements. This is possible due to the uneven metal pad in the cell. Metal level is typically measured well within the anode shadow in Hamburg, between anodes 9 and 10 as shown in Figure 2.6. Due to the metal upheaval, the metal pad is higher at the measuring position than at the surface of the side ledge. The metal upheaval of the P19 cell is reported with 6 cm (Droste 2001). This in combination with a measured

metal level of 18 to 20 cm will result in the phase border of the bath-metal interface being between 10 and 15 cm above the cathode at the side ledge.

It is notable, that the melting of ledge was more pronounced in the metal pad. 31 mm of side ledge was molten in the metal pad compared to only 9 mm within the bath area.

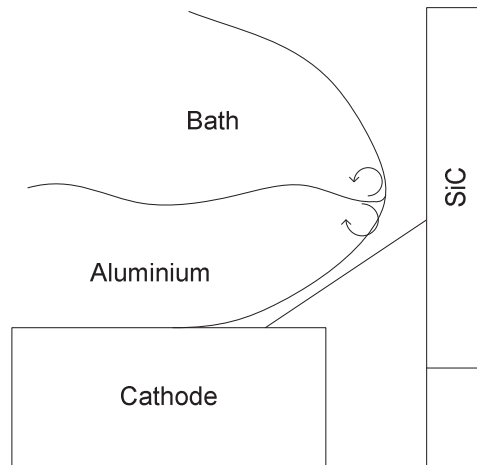


Figure 5.8: Pinch point of the side ledge

5.2.2 Distribution of Ledge Thickness in a Cell

Ledge is not uniformly distributed in the cell. Depending on metal and bath movement, the heat transfer coefficient from bath and metal into the side ledge will differ. If a higher metal and bath velocity or greater turbulence act upon the side ledge, there will be a higher temperature gradient due to the material flow. This should lead to a thinner side ledge. This corresponds with the empirical observation that cell will develop red side walls and tap-outs typically occur at fixed places. These are spots where the metal vortex hits the side wall and maximum heat is transferred into the side wall.

Figure 5.9 depicts the side ledge distribution for particular anode positions. These positions were measurement points for all experiments detailed in the following part of this chapter. Anode numbering is depicted in Figure 2.6 on page 32 and is indicated in the following figure. Figure 5.10 depicts the metal

velocity according to an internal MHD modelling report (Droste 1999). It is discernible that metal velocity at the upstream side of the cell is higher than on the downstream side. This accounts for the thinner ledge at anode position 6/7. At anode position 3/4 there is a zone of increased turbulence as metal streams from both vortexes collide. At anode position 15/16 the metal stream hits the side wall of the cell. However as the velocity is small, the side ledge thickness is greater than at the upstream side.

The flow profile given in Figure 5.10 is specific for a given line amperage. If the line amperage changes, the flow profile changes along the magnetic fields that induce the metal movement. If the characteristic distribution of side ledge remains constant over the experimental current, range is a significant indicator for changes in the flow characteristics.

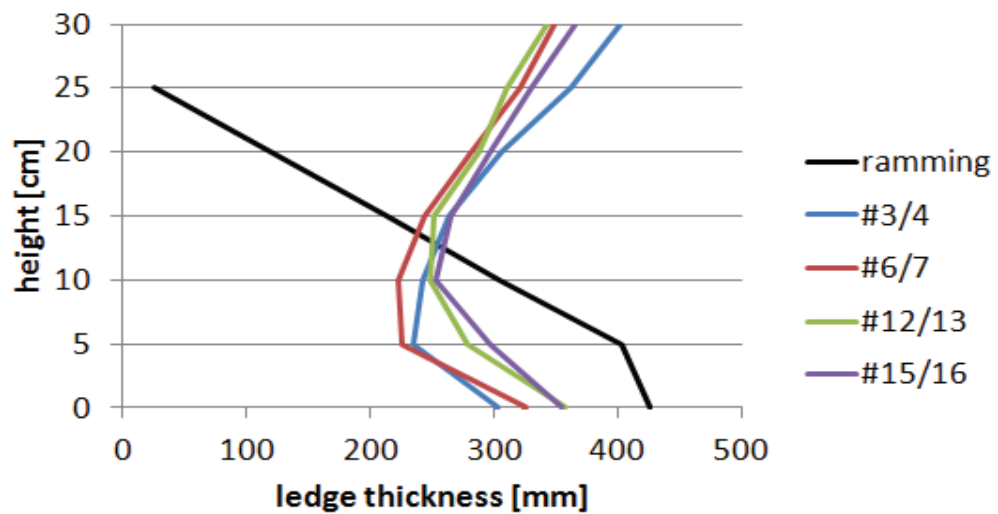


Figure 5.9: Distribution of ledge thickness in a cell

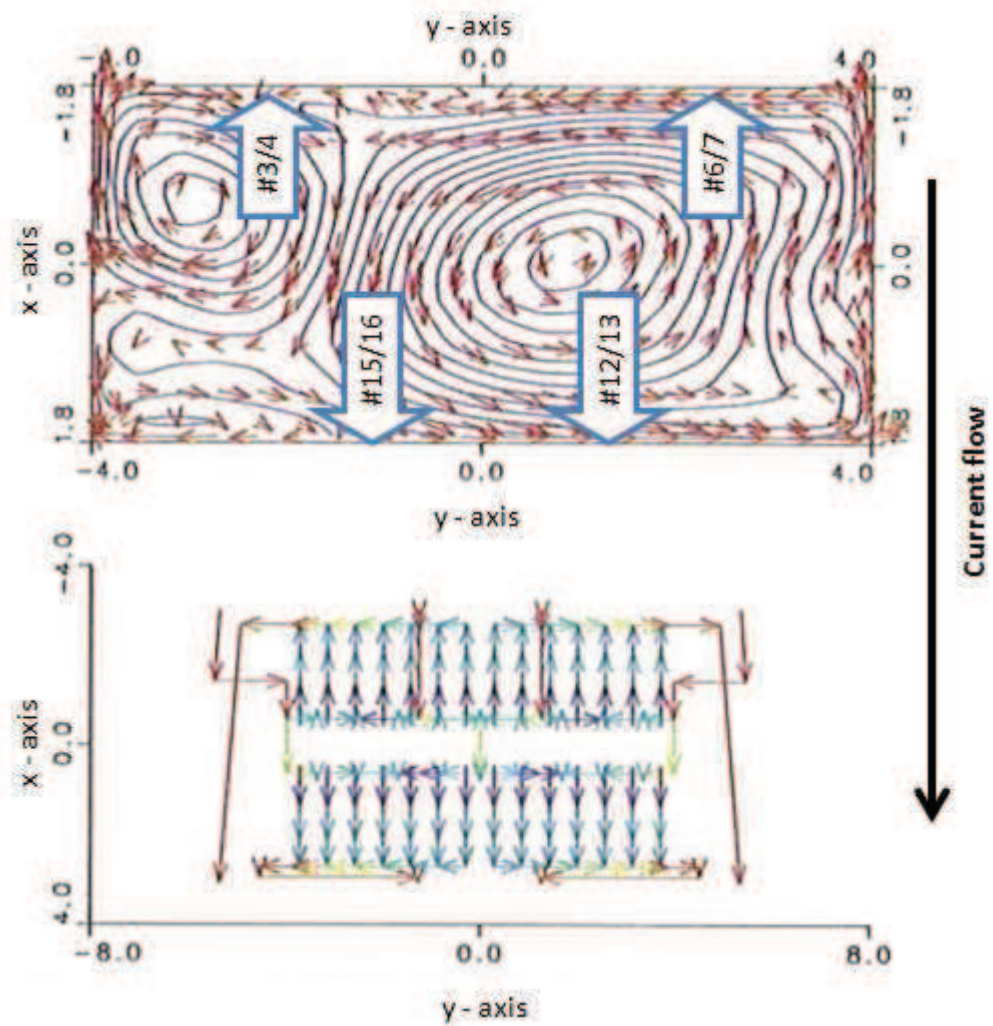


Figure 5.10: Metal velocity diagram of the Hamburg cell and bus bar schematics (Droste 1999)

5.3 Cell Reactions to Single Periods of Increased Energy Input

5.3.1 Experimental Setup

5.3.1.1 Line Current Modulation

To validate the cell reactions assumed in chapter 4.2 in operation, a pot line was exposed to several line current increases and one line current decrease for a limited time. The additional heat input was set up to cover situations up to the estimated maximum heat deviation. The individual experiments are detailed in Table 5.2. Base line current for these trials was 178 kA with a base cell voltage of 4.20 V. Data for four individual cells was collected. The trial was repeated twice with 48 hours in between each repetition to provide a solid database consisting of eight data points per current increase that could be averaged.

The additional heat input is calculated by subtracting the energy to produce metal from the total heat input as given by Eq. 5.6. Even though the process control voltage does not vary as it is normalised according to Eq. 2.8, the actual cell voltage has to be used in the calculation of the additional heat input.

$$\Delta P = (U_{trial} - U_{Al}) \cdot I_{trial} - (U_o - U_{Al}) \cdot I_o \quad \text{Eq. 5.6}$$

with:	ΔP	additional heat input to the cell
	U_o	base voltage before trial
	I_o	base amperage
	U_{trial}	voltage during the trail, calculated by Eq. 2.8
	I_{trial}	line amperage during trail
	U_{Al}	voltage to produce metal, calculated as 2.069 V by Eq. 3.28

Table 5.2: Additional heat input for investigating cell reactions

Amperage Change	Duration	Change in Heat Input
+10 kA	4 h	192 kWh
+10 kA	8 h	384 kWh
+15 kA	4 h	292 kWh
+15 kA	8 h	584 kWh
-10 kA	4 h	-180 kWh

It was assumed that cell efficiency does not change during the period of increased or decreased line amperage. Thus the voltage to produce metal is considered constant.

Measurements of bath temperature, superheat and side ledge were performed before and immediately after the end of the line current change.

It should be noted that several cells in the reduction line developed spikes during the +15 kA for 8 hours trial. These spikes resulted in an increased temperature over several days as well as additional anode changes out of schedule. One of the cells closely monitored for the experiment was affected by spikes as well. The process data for this cell was removed from the experimental data to avoid falsification of the results.

This indicates that the estimated energy increase is indeed a threshold that should not be exceeded if a serious impact on performance is to be avoided. This is also an indication that cells should be operated with an energy deficit pushing them towards the lower end of the optimum process window before a massive amount of additional energy is introduced as was the case during the trial with +584 kWh additional energy input, which is close to the maximum amount that can be stored in a cell given as 0.7 MWh. For the full amount to be

available, cells have to start at a temperature below normal operational temperature.

5.3.1.2 Voltage Modulation

To investigate the alternate approach for modulating energy input of reduction cells, a total of six cells were subjected to 3 different levels of increased voltage for 8 hours.

A modulation of cell voltage was also chosen to operate several levels of energy increase at the same time in one reduction line at a later date. The levels of voltage increase applied are detailed in Table 5.3. As metal production is assumed to be constant when increasing energy input, the energy increase can be calculated by:

$$Q = \Delta U \cdot I \cdot t \quad \text{Eq. 5.7}$$

With	Q	change in energy
	ΔU	voltage change
	I	amperage
	t	duration

Additionally the aim of this series was to determine the speed with which the cells rebalance themselves. For this reason regular measurements of bath temperature, superheat and side ledge thickness were continued for up to 50 hours after the end of the energy increase.

Table 5.3: Voltage increase applied to study self-rebalancing

Voltage increase	Duration	Line amperage	Energy increase
+150 mV	8 h	178 kA	214 kWh
+250 mV	8 h	178 kA	356 kWh
+350 mV	8 h	178 kA	498 kWh

5.3.2 Discussion of Experimental Results

5.3.2.1 Relation of Cell Temperature and Superheat to Energy Input

For the current modulation experiment, temperature and superheat measurements before and after energy increase were compared. In addition during one trial the change in bath inventory was determined using the strontium tracer method. A detailed discussion of the change in liquid bath mass is given in chapter 5.3.2.3.

Table 5.4 details the temperature, superheat and liquid bath mass changes determined during the trials. Figure 5.11 plots these findings against the additional energy increase and compares the experimental data with the hypothesis given in chapter 4.2.3. Expected cell temperature increase is plotted in red and expected bath inventory increase is plotted in blue.

The figure clearly shows the close correlation between expected and found changes in cell temperature. A temperature gradient of 0.01953 °C/kWh was expected and a gradient of 0.020 °C was determined. Thus the findings match the expected value exactly. This is in between the findings of Eisma and Stam detailed in chapter 4.1.

Table 5.4: Temperature and superheat measurements from energy input trials.

Add. Heat Input	Temp increase	SH increase	Bath inv. increase
192 kWh	3.5 °C	0.1 °C	--
292 kWh	4.8 °C	2.6 °C	--
384 kWh	8.2 °C	0.4 °C	1410 kg
584 kWh	12.0 °C	4.1 °C	--
-180 kWh	-1.6 °C	-0.3 °C	--

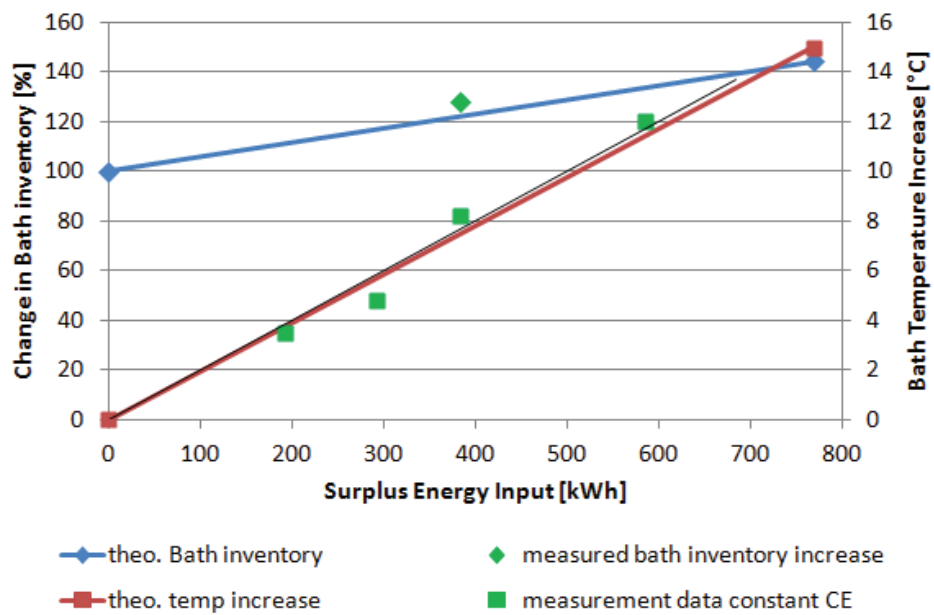


Figure 5.11: Comparison of predicted and measured temperature Increase and bath inventory change

Even though the applied additional energy input is still within the theoretical limit, no precautions were taken to remain within the outside boundaries for optimum process efficiency. As the cells in a reduction line are normally distributed, a certain fraction of cells will be pushed beyond said boundaries.

The closer the actual energy input is to the theoretical maximum, the more cells show indications of less than optimum operation. For cells with a surplus of energy these indicators include spiking anodes.

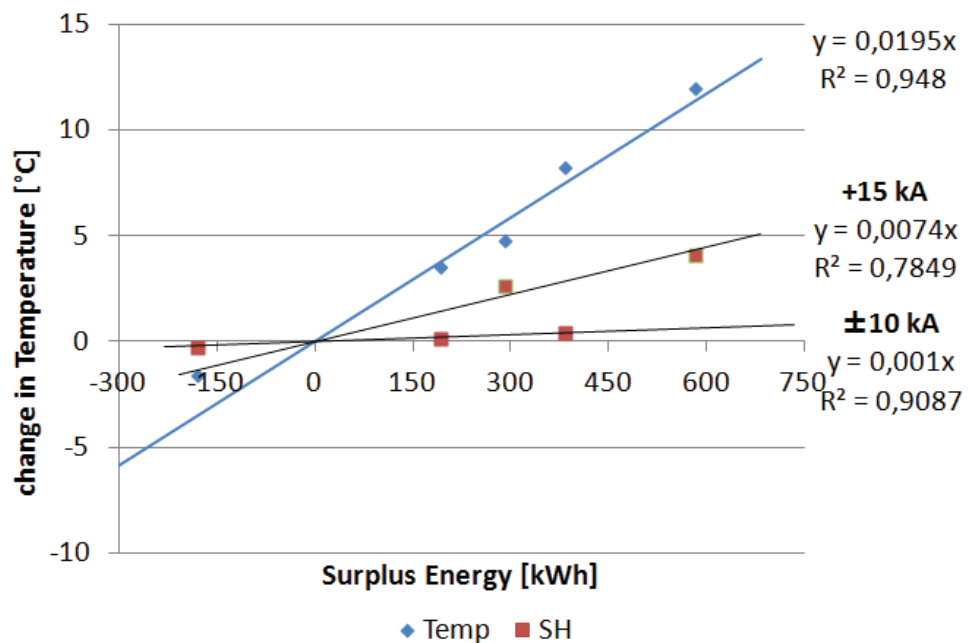


Figure 5.12: Change in temperature and superheat vs deviation from nominal energy input introduced by current

As was already shown in Figure 5.11, the temperature increase follows a linear trend depending on surplus energy. Figure 5.12 expands on this data by including the change in superheat determined during the trials. Changes in superheat do not follow a single linear trend. To evaluate the changes found, a differentiation between ± 10 kA experiments and $+15$ kA experiments is necessary.

For the series of experiments exposing the cells to +10 kA there is little change in superheat detected. Linear regression shows a change in superheat of 0.001 °C/kWh. For the given energy range from -180 kWh to +384 kWh this equates to a total of 0.56 °C change in superheat. Considering a measurement accuracy of ± 2 °C, the change measured is not statistically significant.

As the superheat can be described as a measure of the free energy of the system, it can be concluded that the additional energy introduced into the cell at +10 kA can be translated into molten electrolyte completely and continuously, as long as solid cryolite is present.

Regarding the experiments where +15 kA was applied to the cells, a significant increase in superheat was determined. The coefficient for superheat increase is 0.0074 °C/kWh. For the given range of energy increase this equates to 4.3 °C superheat increase at 584 kWh.

During these experiments the cells are exposed to a higher energy density than they can absorb and translate immediately. Thus the free energy in the system increases. It is significant that the limit is not only on the total amount of energy increase but also on the rate or density at which the energy is introduced into the cell. This is evident as the trial introducing 292 kWh in 4 hours increases the superheat while the trial introducing 384 kWh in 8 hours does not increase superheat. It is plausible to assume that the increase in superheat will be more pronounced if the energy density is increased beyond +15 kA.

Increased bath temperature in a cell will lead to an increased metal solubility in the electrolyte. This will decrease efficiency due to the back reaction given in Eq. 3.10. Figure 5.13 indicates the surface curve of superheat in relation to the change of power input and trial duration. Even though the number of data points used for this graph is limited, an exponential or power trend with increasing energy density is readily visible. The impact of trial duration is less pronounced

but still visible. An exponential or power trend line behaviour in superheat is expected for longer trial durations as well.

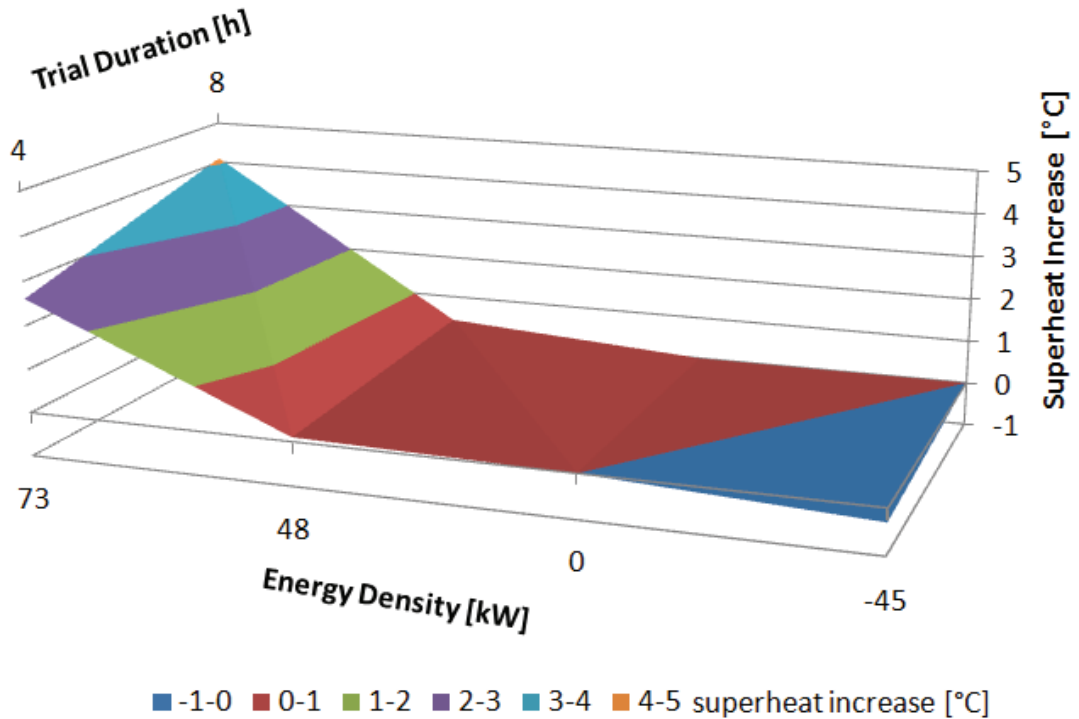


Figure 5.13: Superheat surface curve of energy density and trial time

Cells subjected to voltage increases as detailed in Table 5.3 show a similar behaviour. Figure 5.14 shows the temperature and superheat increase as measured immediately after the voltage increase. Independent of the actual voltage increase a significant reaction in both bath temperature and superheat is detected. The cell heating coefficients are 0.045 °C/kWh for bath temperature and 0.0152 °C/kWh for superheat. The coefficient for temperature change is twice as high as the one found for current increases.

The superheat coefficient is not as easy to compare, as the current increase experiments resulted in two discrete values for different energy densities. The voltage addition experiments were set up to use the same duration and different

voltage addition. This results in different energy densities as well. The superheat trend depending on energy density is given in Figure 5.15. A power trend line is fitted to the data, in accordance with Figure 5.13 for current increases. The power trend line shows a slightly better fit than a linear trend line would. The data gained in the experiments is not sufficient to support this without doubt however. The trend is not as visible as for the experiment using line current increases.

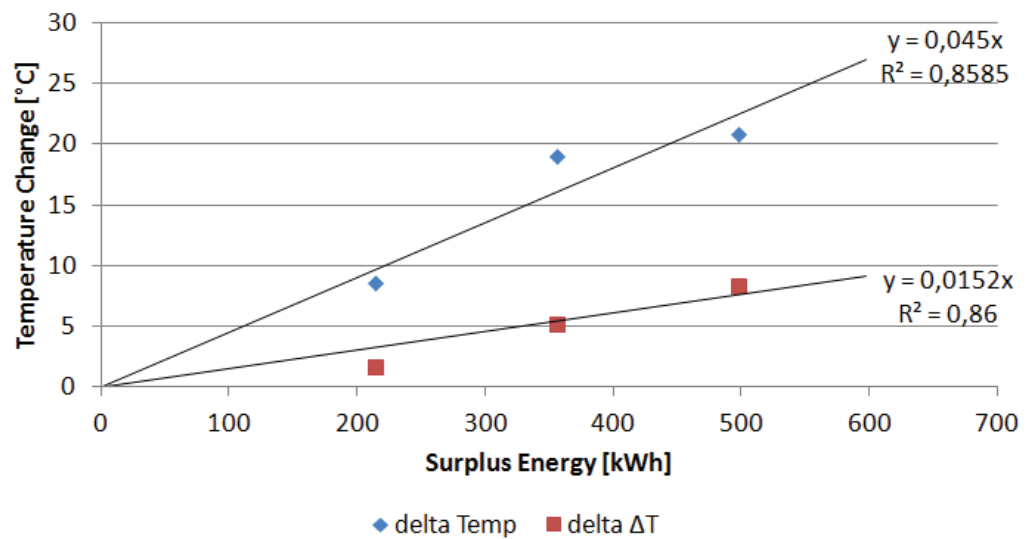


Figure 5.14: Coefficients of temperature and superheat increase per kWh of energy increase introduced by voltage addition

The data is a strong indication that models trying to predict and track power modulation should use a potency formula to calculate the change of superheat in dependence to the magnitude of change in energy density and the time for which it is applied. For the purpose of cell control, a linear regression has been used most of the time (Rieck, Iffert et al. 2003). For the needed accuracy for calculating measures to bring the cell back within control limits, this might have been accurate enough so far, especially as the application of a voltage increase or decrease was always for a predetermined duration. From the viewpoint of power modulation and predicting cell behaviour for a long term and repeated prediction, new approaches are necessary.

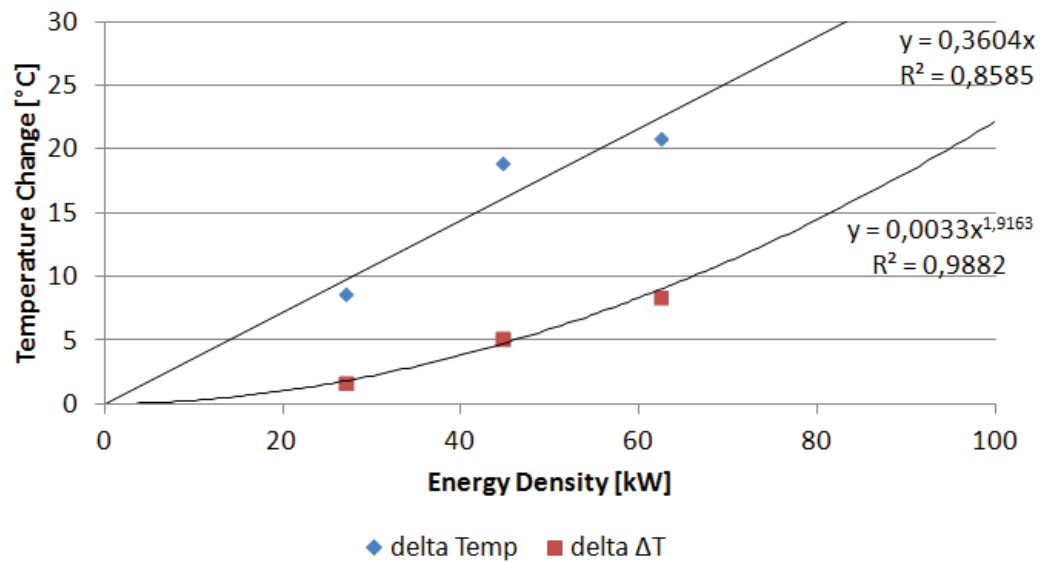


Figure 5.15: Temperature and superheat reaction in relation to energy density introduced by voltage addition

5.3.2.2 Self-Rebalancing of the Cell

The experiments using changes in line amperage were repeated twice each with 48 hours between the repetitions. The experiments were set up as single, uncompensated deviations from nominal energy input. By comparing cell data at the beginning of each energy increase, the capability of rebalancing of the cell can be determined.

Table 5.5 details cell temperatures and superheat before the 1st and 2nd trial. Figure 5.16 shows the data graphically. Superheat is changing between -0.9 °C and +1.78 °C. This is within measuring accuracy. Also, there is no distinction in the cell reaction in the ±10 kA and +15 kA experiments. Both groups show increases in superheat as well as decreases. This signifies that within this time distance from the energy input deviation the melting and solidifying of side ledge had reached equilibrium again.

Bath temperature shows a significantly different trend. For intermediate energy increase – from 0 kWh to 400 kWh surplus energy – the cells have returned to

normal operating conditions within ± 2 °C of the starting values for both bath temperature and superheat.

Table 5.5: Temperature and superheat before 1st and 2nd trial

Trial	Surplus energy	1 st trial		2 nd trial		Delta	
		T _{bath}	ΔT	T _{bath}	ΔT	T _{bath}	ΔT
+10 kA 4 h	192 kWh	963.0	5.1	962.0	6.8	-1.0	1.7
+10 kA 8 h	384 kWh	963.7	4.3	961.8	5.8	-1.9	1.5
+15 kA 4 h	292 kWh	960.8	3.5	960.2	2.6	-0.6	-0.9
+15 kA 8 h	584 kWh	960.4	2.5	965.9	4.1	5.5	1.6
-10 kA 4 h	-180 kWh	966.9	4.2	960.0	3.8	-6.9	-0.4

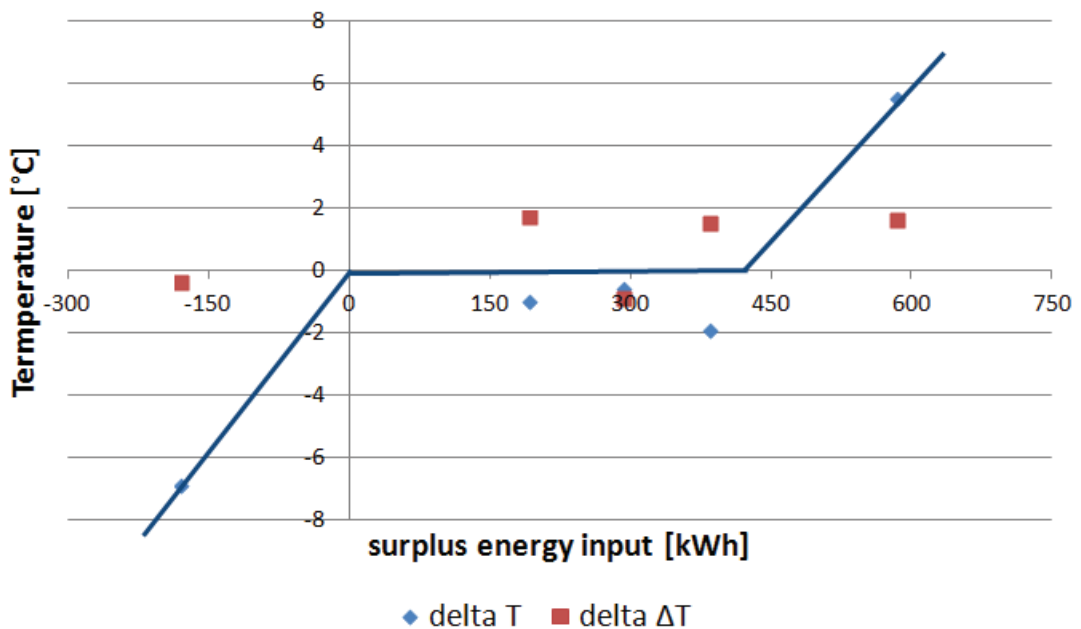


Figure 5.16: Temperature and superheat difference before 1st and 2nd repetition

The experiments outside of this scope show a different trend. For the trial subjecting the cell to +584 kWh of additional energy, temperature increases by +5.5 °C. This is significantly above starting temperature and in line with the observation described in chapter 5.3.2.1 that several cells in the reduction line developed spikes during this trial.

Between both energy reduction trials the temperature decreased by -6.9 °C. It should be noted that the temperature continued decreasing even after the energy input returned to normal. Immediately after the energy input reduction cell temperature had decreased by only -1.4 °C for the 1st repetition (compared to -1.6 °C for the average of both repetitions). The energy decrease initiated a cooling trend that continued even with nominal heat input!

Stam attributes such a self-accelerating cooling trend to a change in AlF_3 and/or liquid bath balance (Stam, Taylor et al. 2007). He gives various examples for mechanisms producing this effect, but under this circumstance sludge or ledge formation with a significant decrease in liquid bath inventory is most plausible. With a decreased energy input side ledge starts to solidify to compensate for the lower energy input. Pure cryolite solidifies out of liquid electrolyte, thus the AlF_3 -content of the remaining bath increases. This leads to a decreased solubility of alumina. When alumina is fed into the electrolyte and does not spread out along the surface of the electrolyte, cryolite can solidify around the alumina, increasing the trend started with the solidification of side ledge. The undissolved alumina/cryolite mix is deposited onto the cathode as sludge.

This indicates that cells are more susceptible to suffer from long term effects after energy decreases, if the deficit is not compensated within an acceptable time frame. This is in line with the general process target to operate cells at minimum specific energy consumption as detailed in chapter 2.3.1.1. Consequently an energy reduction will move a cell out of optimum performance more easily than an energy increase.

The experiment detailed in Table 5.3 using voltage addition also covers the same range of additional energy inputs as the previous experiments using

increased line currents. Each voltage increase is applied to two cells. To determine the rate at which the cells return to previous operating temperature, the cells were measured repeatedly for up to 50 hours after the return to normal operating voltage. The first measurement was immediately before the voltage increase, the second measurement immediately after the voltage increase was removed. Table 5.6 shows the resulting measurement data. The corresponding graphs are shown in Figure 5.17 and Figure 5.18.

Table 5.6: Temperature and superheat development after voltage increase

Bath Temperature [°C]						
	0.0 h	8.5 h	24.0 h	34.5 h	48.0 h	58.5 h
150 mV; 8h	959.4	968.0	956.8	955.6	953.5	956.5
250 mV; 8h	950.9	969.9	956.3	956.9	956.0	957.0
350 mV; 8h	968.5	989.3	973.0	975.5	974.1	970.5
Superheat [°C]						
	0.0 h	8.5 h	24.0 h	34.5 h	48.0 h	58.5 h
150 mV; 8h	2.6	4.3	1.9	3.4	3.4	5.0
250 mV; 8h	1.2	6.4	3.5	3.6	3.3	3.2
350 mV; 8h	7.3	15.7	5.4	4.8	3.7	4.5

It is notable that cell temperatures and superheats have returned to normal operational level within 16 hours after the end of the increased energy input. It was not possible to determine an actual cooling rate during this experiment as

the cells had shed all additional energy at the first following measurement. This highlights that cells cannot store additional energy for any significant amount of time with their current construction.

The cells subjected to +250 mV had an average starting temperature of 950.0 °C. This is below the target operating band of 955 – 965 °C. After the trial the cells settled at an average bath temperature and superheat comparable to the cells exposed to +150 mV. The cells subjected to +350 mV started at an elevated bath temperature and superheat. After the energy increase the superheat settled in a range found at the other cells as well. Temperature stayed at an elevated level at +4.5 to +7 °C above starting temperature however.

Considering the low superheat and elevated bath temperature of the +350 mV cells after the energy increase, this indicates lower AlF_3 -levels than targeted. This is confirmed with the AlF_3 -data presented in Figure 5.19. Whereas AlF_3 appears stable for the +150 mV and +250 mV trials, AlF_3 -content starts at a lower level for the +350 mV trials and continues to drop. Combined with the severe temperature and superheat increase during the voltage addition, this indicates a loss of AlF_3 to the vapour phase. This loss of AlF_3 cannot be recovered immediately by the cell on its own.

If a full reduction line is subjected to such power modulation, AlF_3 -level would return to normal when the alumina used in the dry scrubbing system at the moment of modulation is fed into the cells. Depending on silo capacity between the GTC and the pot line, this can take only a few hours or several days. If the time delay is long enough for the process control system to start increasing AlF_3 -additions, swings are induced that can unbalance the pot line.

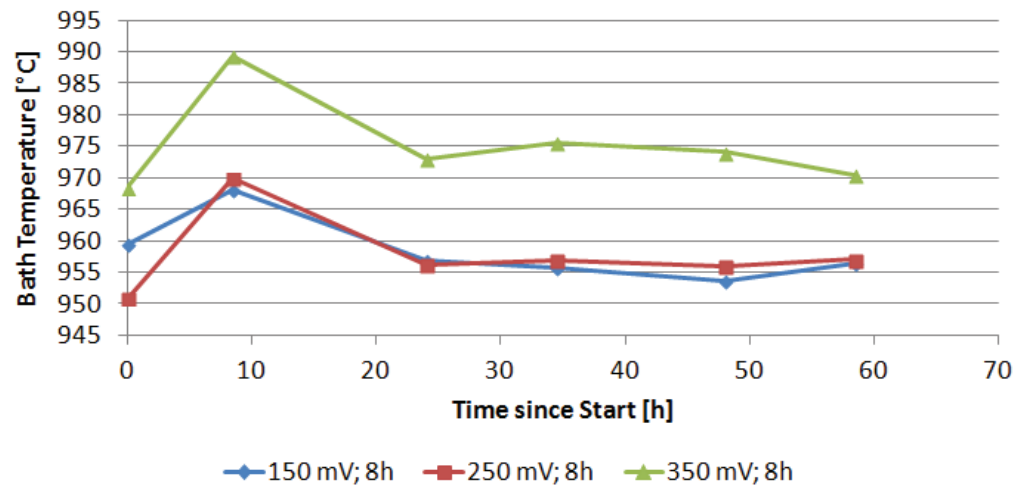


Figure 5.17: Temperature curve after voltage increase

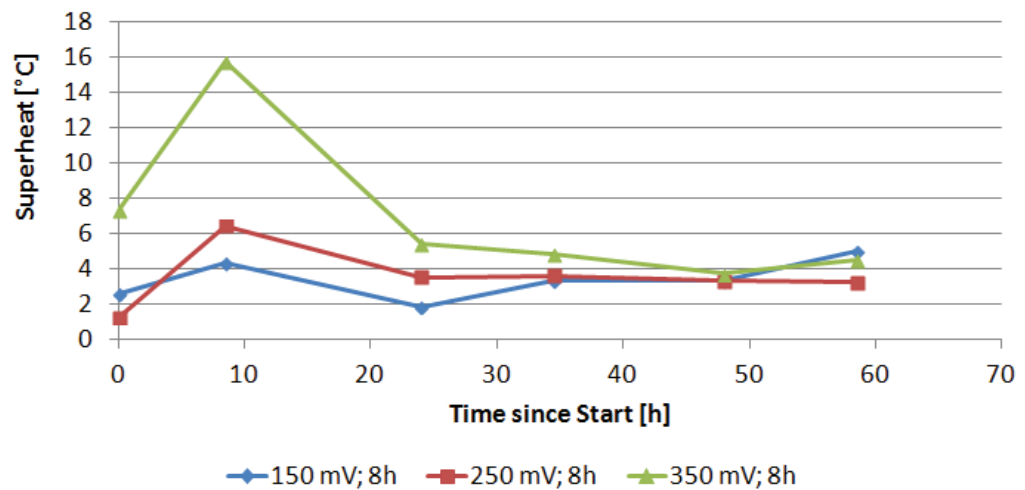


Figure 5.18: Superheat curve after voltage increase

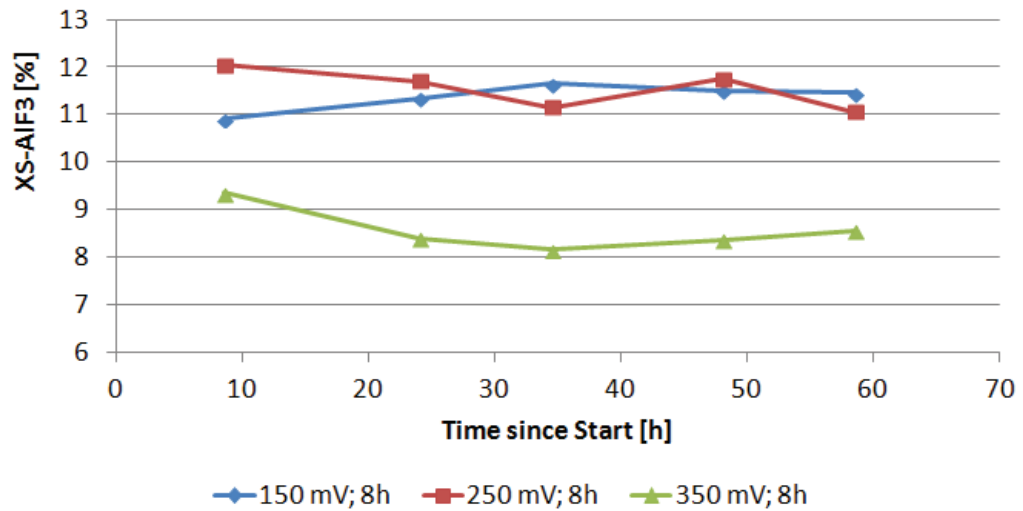


Figure 5.19: AIF₃-Levels during voltage increase

The immediate return to lower bath temperatures at the end of increased energy input suggests that the standard operating procedure to raise the cell voltage for cold cells is only helpful on a short term during the actual application of additional voltage. As soon as the voltage is removed, the cell will return to the previous operating temperature. A combined effort of voltage increase and corrective measures for the chemical composition of the bath is necessary.

5.3.2.3 Development of Side Ledge in Relation to Energy Input

Ledge measurements were performed during the energy input trials detailed in chapter 5.3.1.1. Measurements were taken on four positions covering 8 of 18 anodes on four pots. All trials were conducted twice. The resulting overall ledge profile is shown in Figure 5.21. The numerical data is shown in the following table:

Table 5.7: Ledge profile in mm after energy increase

Height above cathode	-180 kWh	+0 kWh	+192 kWh	+292 kWh	+384 kWh	+584 kWh
30 cm	377	361	361	337	339	336
25 cm	331	331	336	314	293	284
20 cm	294	294	294	279	263	275
15 cm	264	256	247	238	239	236
10 cm	250	242	232	218	216	219
5 cm	249	259	247	254	243	241
0 cm	305	326	363	351	317	348
Average	296	295	297	285	273	277

In the range of ± 200 kWh there is little total change in ledge thickness measurable. For the energy reduction, the ledge thickness distribution shifts. Ledge is gained just below the metal–bath interface situated between 15 cm and 20 cm. Closer to the cathode, ledge is lost even though the energy input is reduced. For +192 kWh ledge is also lost at the metal-bath interface; directly above the cathode an increase in ledge thickness is registered. For stronger energy increases, ledge is lost uniformly, except immediately at the cathode surface.

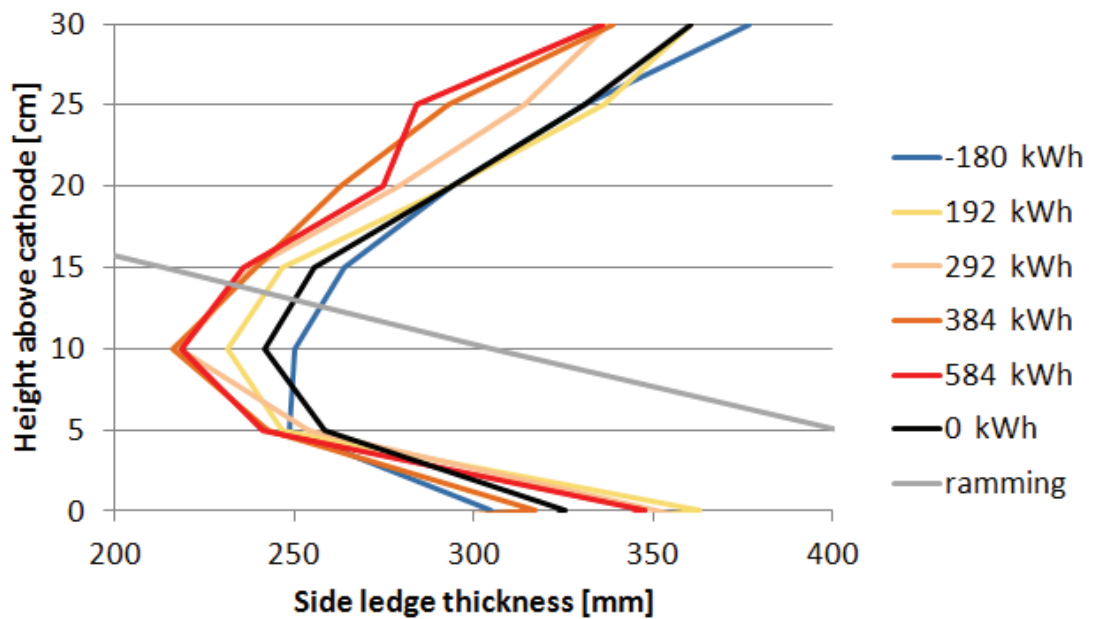


Figure 5.20: Ledge profile after energy increase

With regards to the ledge thickness at the bottom of the cell, only two measurements show a ledge melting. The second largest energy increase and the only energy decrease. All other trials show a ledge increase of 20 – 40 mm, as detailed in Figure 5.21. While there are valid explanations that could explain this trend on single measurements, each data point is based on 64 individual measurements. To avoid overrating single measurements the median of all measurements is used, not the mean. This in combination with the fact that the ledge thickness 5 cm above the cathode is also decreasing for the energy reduction trials implies that ledge mechanics are not as straight forward as assumed so far, especially if ledge dynamics within the metal pad are investigated.

It is also notable that there seems to be a holding point in ledge melting in the upper part of the metal pad if an energy threshold is exceeded. There is little difference in recorded ledge melting 5 – 15 cm above the cathode surface as soon as 300 kWh of additional energy input are exceeded. It appears that the turbulence at the metal–bath interface results in a heat transfer into the side ledge that is not depending linearly on the energy increase.

All additional ledge melting at increased energy input is happening in the bath area of the ledge. Ledge melting in this area appears to be highly dynamic and depending on energy input.

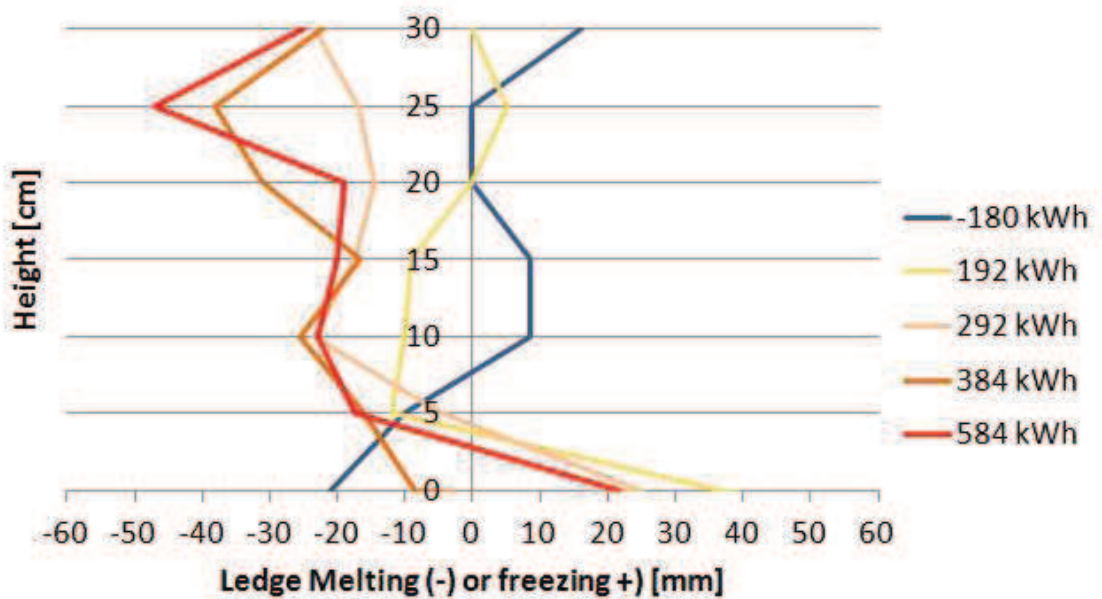


Figure 5.21: Ledge movement for different energy increases

Figure 5.22 shows the different trends of ledge melting in the bath and metal area depending on the energy increase. Ledge movement in the bath area – given as 20 - 30 cm above the cathode surface – is following a linear trend with 0.04 mm/kWh. The R^2 -value with 0.74 gives a very strong correlation in the given trial area. Overall ledge movement in the metal area – given as 0 - 15 cm above the cathode – appears to follow rather an exponential trend. The correlation is given with R^2 as 0.24 which indicates only a weak correlation however.

Cross checking these findings with a linear regression for the total ledge movement for the given trials results in an R^2 -value of 0.59. The corresponding

data is given in Figure 5.23. Comparing both regression parameters shows that a split metal/bath regression is the better fitting.

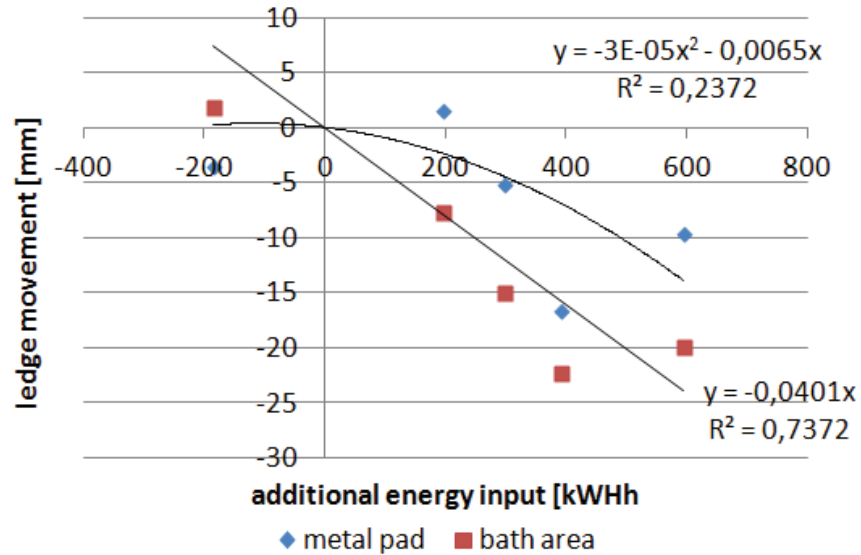


Figure 5.22: Ledge melting in the metal pad and bath area depending on additional energy input

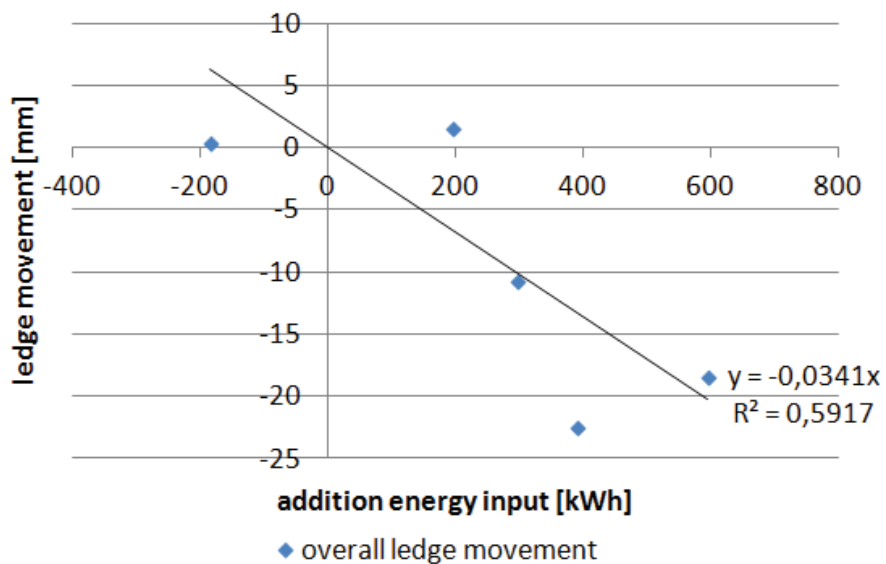


Figure 5.23: Linear regression for the overall ledge melting

While the change of ledge in the bath area shows a linear trend, the ledge in the metal pad shows a delayed reaction to increased energy inputs with virtually no change in ledge thickness for energy increases below +200 kWh. For Figure 5.22 a polynomial regression of the 2nd degree is used as it was the best fit for the found data. It cannot be excluded that a linear regression with a significant offset models the found reaction more precisely if more data is available.

However, a definite conclusion is that ledge behaviour is following two distinctly different behaviour mechanisms, depending on whether the ledge is in direct contact with molten bath or not. These are discussed in more detail in chapter 5.6.

5.3.2.4 Correlation of Ledge Melting and Bath Inventory Increase

During normal operation the Hamburg cell has 5,140 kg of liquid bath. Introducing +384 kWh of additional energy for heating up the cell, the bath inventory increased by 27.4 % to 6,550 kg. This is in close agreement with the expected mass increase of liquid bath of 22 % stated in chapter 4.2.3.

Only 22.5 mm of side ledge was found to be molten at the end of the trial however. With Eq. 5.5 this results in 0.252 m³ of molten ledge. Using the specific density of solid cryolite given as 2.7 g/cm³ (Roine 2002), this corresponds to 680 kg. Compared to the increase of liquid bath of 1,410 kg this is just below 50 % of the bath inventory increase accounted for.

The only possible explanation is that not only side ledge melts. Other possible sources of solid bath material are the cell cover as well as sludge. Even though sludge is present in every cell to varying degrees, in this case it can be disregarded as it is unlikely that sludge levels will decrease rapidly after a change in line current as long as the metal pad remains stable. This leaves the top crust as the other source of solid bath material. Using Eq. 5.8 gives a crust area at the top of the cell of 18.9 m².

Table 5.8: Bath inventory before and after the +10 kA for 8 hours trials

Cell	Bath inventory before trial	Bath inventory after trial
331; 1 st trial	5,240 kg	6,100 kg
331; 2 nd trial	4,880 kg	6,840 kg
332; 1 st trial	5,060 kg	5,240 kg
332; 2 nd trial	5,120 kg	6,900 kg
333; 1 st trial	4,970 kg	6,900 kg
333; 2 nd trial	5,210 kg	6,500 kg
334; 1 st trial	5,430 kg	6,500 kg
334; 2 nd trial	5,210 kg	7,420 kg
Average	5,140 kg	6,550 kg

$$\begin{aligned}
 A_{crust} &= A_{cell} - A_{anodes} \\
 &= l_{cell \ length} \cdot l_{cell \ lwidth} - n_{anodes} \cdot l_{anode \ length} \cdot l_{anode \ lwidth}
 \end{aligned}$$

Eq. 5.8

With:

- $A_{()}$ corresponding surface area
- $l_{cell \ length}$ length of the cell
- $l_{cell \ lwidth}$ width of the cell
- n_{anodes} number of anode; 18
- $l_{anode \ length}$ length of the anode
- $l_{anode \ lwidth}$ width of the anode

This is twice the active area of the side ledge. Considering that good cover material has an alumina content of about 50 % this relates to 1,460 kg of cover material melting. Assuming the same specific density for calcined cover material as for solid cryolite, during the same trial the top crust would have been reduced by 28.6 mm in addition to a melting of 22.5 mm of side ledge.

The top crust is thus contributing considerably towards the amount of bath melting during increased energy inputs. It is reasonable to expect this to be in the same order of magnitude than the typical ledge melting as is indicated by the collected data. This was confirmed by an observed but not quantifiable degradation of cover integrity during the increased energy input trials.

5.4 Reversibility of Energy Increases

5.4.1 Experimental Setup

In order to further investigate the reversibility of ledge melting during increased energy input, a trial was devised that switches from increased energy input to reduced energy input. To minimize the exposure of the pot line, cell voltage increase and decrease were used to simulate varying energy inputs.

This setup is not identical to an increase or decrease in line current. During line amperage changes heat generation varies in each part of the cell – e.g. in the anode and anode assembly, bath and relining. With a variation in cell voltage, heat generation is only changed in the bath. Even though the direct impact on the cell from a current increase to a voltage increase is less intense, the principles appear to be same for both scenarios. To avoid subjecting a full pot line to the experiment, a change of cell voltage was therefore chosen.

Different voltage steps for increase and decrease were used to simulate similar energy differences compared to previous tests. Table 5.9 shows the details of voltage variations and Figure 5.24 shows a graphical representation of the experimental setup.

For calculating the energy deviation Eq. 5.6 is used. Ledge measurements were conducted at the same anode positions used in the other experiments. The trial was repeated twice. The duration of the experiment was restricted to two times 3 hours to be able to integrate it into normal working routines.

Table 5.9: Experimental setup for 3 h voltage changes

Voltage addition	Voltage reduction	Equiv. amperage change	Total energy deviation
+270 mV	- 250 mV	± 10 kA	+204 kWh -195 kWh

**Figure 5.24: Cell voltage over the experiment**

The trials were conducted about one month apart, on May 9th 2008 and June 19th 2008 respectively.

5.4.2 Discussion of Experimental Results

Even though the tests were set up identically, the two cells were at different operating points before the start of each trial. One cell was operating within the

normal process window with a starting temperature of 958 °C, while the other cell suffered from carbon dust increasing the starting temperature to 982 °C.

The development of bath temperature, measured in parallel to the side ledge, and side ledge itself shows a similar trend for both cells. Development of the liquidus temperature is differing however.

The results of the bath temperature measurement are shown in Table 5.10. The temperature curve follows the expected trend with a temperature increase during the increased voltage period. Cell 138 increased temperature by 11 °C while cell 139 increased temperature by 7 °C. The smaller temperature increase occurred at the cell with the elevated starting temperature. As the higher temperature cell with a higher superheat suffered from increased heat loss, the smaller temperature increase is to be expected. Applying the coefficient for cell heating derived from the previous trial using increased voltage of 0.045 °C/kWh suggests an increased bath temperature of 9.18 °C. Even though the cells differ from that value, the average of both cells is in line with this expectation.

Table 5.10: Temperatures during the voltage compensation trial

Cell 138	09.05.2012	Start	Mid	End
Bath temperature		958.0 °C	969.0 °C	963.0 °C
Liquidus temperature		951.0 °C	957.0 °C	963.0 °C
Superheat		7.0 °C	12.0 °C	0.0 °C
Cell 139	19.06.2012	Start	Mid	End
Bath temperature		982.0 °C	989.0 °C	972.0 °C
Liquidus temperature		963.4 °C	969.1 °C	966.2 °C
Superheat		18.6 °C	19.9 °C	5.8 °C

The trend was reversed during the energy decrease. Both cells decrease cell temperature, the hotter cell dropped considerably more with $-17\text{ }^{\circ}\text{C}$ compared to $-6\text{ }^{\circ}\text{C}$. During the previous experiments no coefficient for cooling of bath temperature was determined. The given data points are not sufficient enough to ascertain one as the results differ considerably. The magnitude of the temperature change suggests a coefficient similar or slightly larger than to the voltage heating coefficient. This is in-line with the one trial with a current decrease indicating a slight cooling. The cooling trend found during that trial was not evident here.

Superheat follows the expected trend as well, increasing and decreasing with the respective change in voltage. For cell 139 the drop in superheat during the energy decrease period was surprisingly high with $-14.1\text{ }^{\circ}\text{C}$. Liquidus temperature was behaving as expected during the increased voltage. For cell 138 liquidus temperature continued to increase during the voltage reduction period. This indicates the previously discussed cooling trend described by Stam (Stam and Schaafsma 2007).

The resulting side ledge development of both repetitions of the trial is shown in Figure 5.25 and Figure 5.26. The ledge thickness is extremely different in both cases due to different cell temperatures at the beginning of each trial; the resulting change in ledge thickness also differs considerably. The data is shown in Table 5.11.

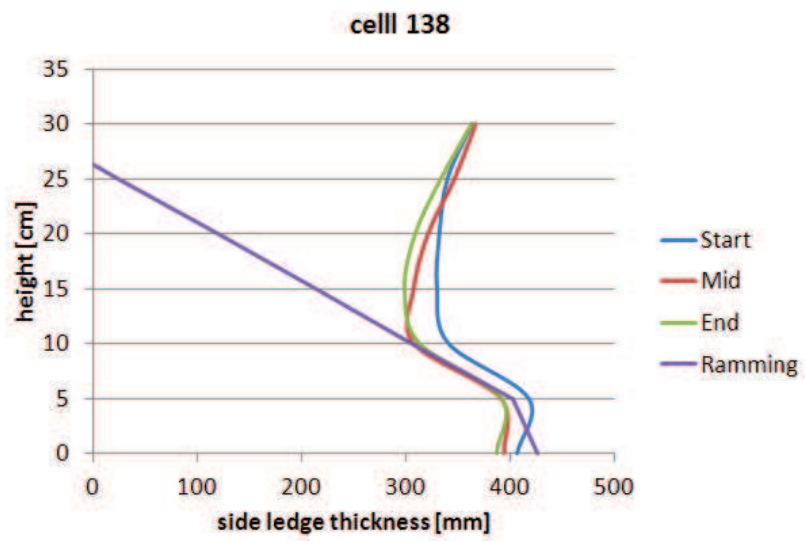


Figure 5.25: Side ledge development during the trial, cell 138

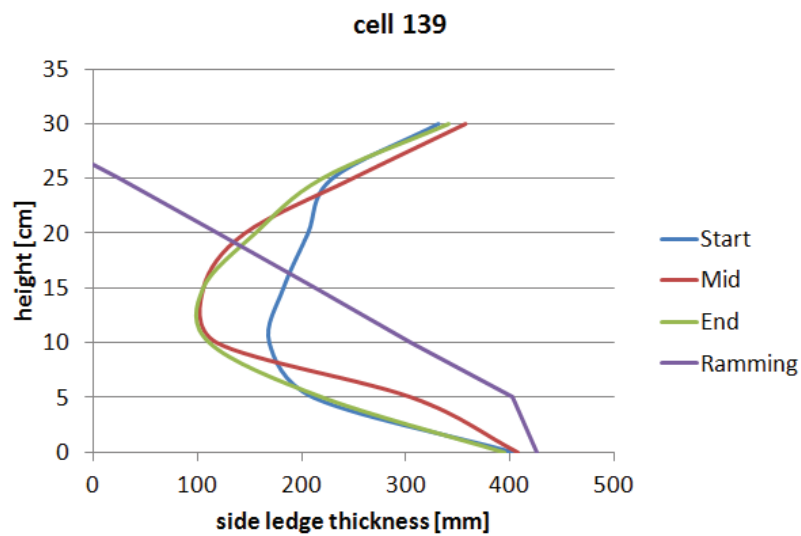


Figure 5.26: Side ledge development during the trial, cell 139

Table 5.11: Side ledge dimension during the trials

	Start	Mid	End
Cell 138	361.4 mm	347.3 mm	342.6 mm
		- 14.1 mm	- 4.7 mm
Cell 138	247.3 mm	241.5 mm	221.1 mm
		- 5.8 mm	- 20.4 mm

During both phases of the experiment – voltage increase and decrease – ledge is melting. This differs from the expectation that with an energy decrease ledge solidifies immediately. Latent energy reserves in the cell lead to continued ledge melting even though the energy input is severely reduced below normal operation.

The absolute melting of ledge is different from repetition to repetition. Also the magnitude of loss of ledge in each phase of the experiment is varying from repetition to repetition. This indicates that magnitude of ledge loss is dependent on starting cell state.

The characteristic of ledge loss is different in both repetitions. In the first trial ledge is lost over the whole height of the cell. During the 2nd trial ledge movement is more variable. During the increased energy input ledge is lost around the metal-bath interface, but ledge thickness is gained deeper within the metal pad. This results in a small net loss of ledge thickness. The trend for solidification of ledge in the metal pad during energy increases has been noted on several experiments discussed earlier.

A more detailed breakdown of the change in ledge thickness is given in Table 5.12 and Figure 5.27. A differentiation between ledge thickness in bath and in

metal is given. Interestingly in both experiments the ledge thickness in the metal is decreasing more than the ledge thickness in the bath area. For cell 138 this is -25.6 mm in the metal compared to -9.5 mm in the bath. For cell 139 this is -33.3 mm compared to -16.8 mm respectively over the total duration of the experiment.

With the detected ledge increase during experiments with only an energy increase, it can be concluded that side ledge in the metal pad reacts more strongly to energy imbalances than to a shift in operating set point.

Table 5.12: Development of ledge thickness in the bath and metal

Cell 138	Start	Mid	End
Metal	373.6 mm	349.5 mm	348.0 mm
		-24.1 mm	-1.5 mm
Bath	345.1 mm	344.4 mm	335.5 mm
		-0.6 mm	-8.9 mm
cell 139	Start	Mid	End
metal	241.4 mm	234.9 mm	208.2 mm
		-6.6 mm	-26.7 mm
Bath	255.1 mm	250.3 mm	238.4 mm
		-4.8 mm	-12.0 mm

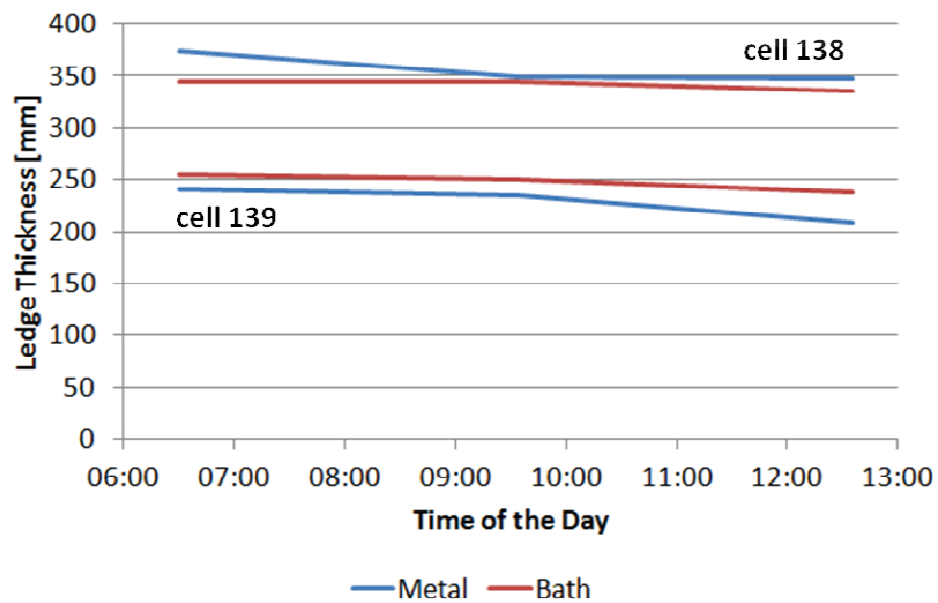


Figure 5.27: Development of ledge thickness in the bath and metal

5.5 Potline Behaviour under Repeated Modulation

5.5.1 Experimental Setup

During 2008 several power modulation schemes were trialed. Each consecutive step aimed at increasing the maximum delta energy with which the cells were operated. The overall energy input was intended to be slightly higher than during constant operation if averaged over each modulation cycle. Maximum and minimum amperage and cell voltage varied considerably. The delta energy was calculated by assuming a constant heat loss from the cell and a constant current efficiency. The delta energy for each quarter hour was calculated and integrated. The resulting cumulative sum can be used to characterise the amount of modulation by determining the maximum amplitude between peaks. Data characterising the different modulation schemes is given in Table 5.13. Even though modulations 1 to 3 have the same minimum and maximum amperages, the amplitude is significantly different. This is achieved by varying the time the pot line is operating at maximum and minimum line amperage.

Table 5.13: Characterisation of four modulation schemes

	Min amperage	Max Amperage	Amplitude	Energy balancing
Modulation 1	160 kA	185 kA	302 kWh	1/day
Modulation 2	160 kA	185 kA	321 kWh	1/day
Modulation 3	160 kA	185 kA	360 kWh	1/day
Modulation 4	160 kA	190 kA	405 kWh	1/day

Eq. 5.9 details the calculation of the energy amplitude given in Table 5.13. The actual energy to produce aluminium is subtracted from the actual energy input from the cell. This leaves the energy either stored in the cell or removed from the cell as heat loss. Assuming a constant heat loss from the cell based on average operational data, the cumulative energy deviation for a given modulation scheme can be calculated. To determine the amplitude, the minimum energy state is subtracted from the maximum energy state.

For the modulation schemes detailed in Figure 5.28 this results in an energy amplitude between 302 kWh and 405 kWh per day.

$$Q_{cusum} = \sum_{i=0}^{95} (I_i \cdot U_i \cdot t_i - Q_{Al\ i} - Q_{avg\ heat\ loss})$$

$$\Delta Q_{cusum} = \max(Q_{cusum}) - \min(Q_{cusum})$$

Eq. 5.9

With	i	time increment
	I_i	average line current during on time period
	U_i	average cell voltage during on time period
	t_i	duration of one time increment; 15 min
	$Q_{Al\ i}$	energy to make metal at said line current and current efficiency
	$Q_{avg\ heat\ loss}$	average heat loss during the modulation
	ΔQ_{cusum}	energy amplitude of the modulation as given in Table 5.13

In each case the modulation was set up to result in a nearly constant average energy input throughout each day. Basically the time of minimum energy was during the middle of the day. The high amperage was placed in the early hours of morning. Figure 5.28 shows the line current curves for the modulation schemes. The difference from one modulation to the next is not large in terms of amperage change and duration, but in reality the maximum energy cumulative sum is changing more significantly.

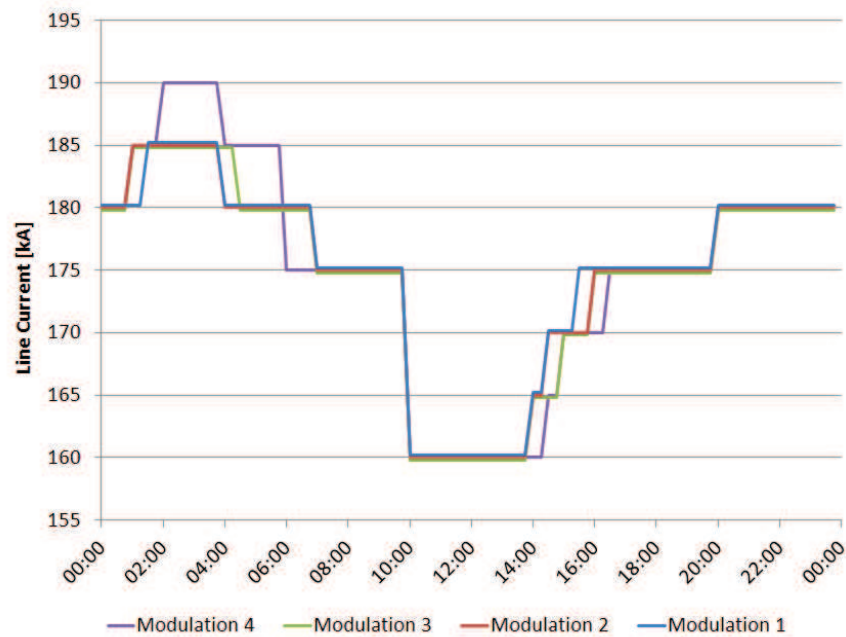


Figure 5.28: Line current curve for the modulation schemes

Figure 5.29 shows the resulting energy cumulative sum of one modulation scheme. The increasing trend in the cumulative sum is intentional. Due to anticipated additional heat loss the modulation scheme was set up with a small surplus of energy.

In the figure the vertical lines indicate the time of ledge measurement. Ledge measurements were performed on the same cells detailed in the previous chapters.

The timing of the measurements was at the end of the phase with the highest amperage and at the end of the phase with the lowest amperage even though these times do not correspond with the points of the lowest and highest energy cumulative sum. This decision was mainly taken due to the availability of manpower to perform the measurements. As the offset is systematic, results should be influenced systematically as well.

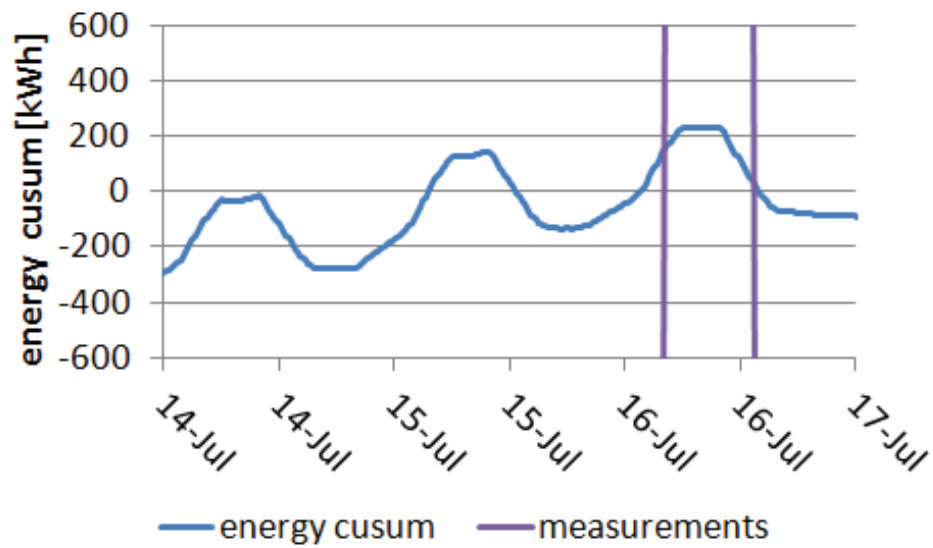


Figure 5.29: Energy cumulative sum for continuous modulation

5.5.2 Discussion of Experimental Results

Figure 5.31 shows the resulting ledge profile from modulation 4. There is a pronounced ledge movement recordable associated with the change in energy input. The difference between ledge in the bath and ledge in the metal that was found in the first experiments was found in these trials as well. Table 5.14 details the total ledge movement as well as the breakdown of the ledge movement in the metal and in the bath area for all modulation schemes. It is notable that during all modulation schemes, the ledge thickness in the metal pad increased. The magnitude of ledge growth in the metal pad during modulation 1 is extreme and not consistent with the data from the other measurements. Considering the nearly constant level of ledge increase in all other modulation schemes, the data seems to represent an outlier.

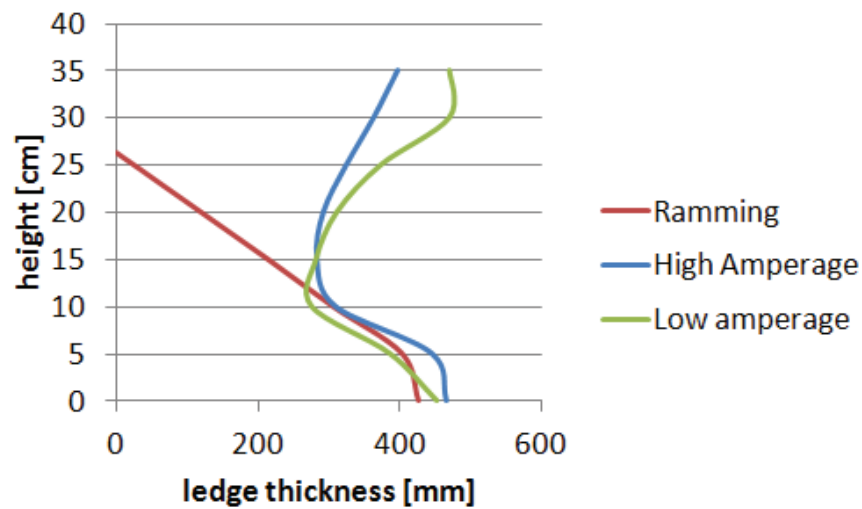


Figure 5.30: Shape of the side ledge after the high and low amperage phase

Table 5.14: Ledge movement during modulation

	Total ledge movement	Metal ledge movement	Bath ledge movement
Modulation 1	+62 mm	+59 mm	+3 mm
Modulation 2	+3 mm	+26 mm	-23 mm
Modulation 3	-8 mm	+28 mm	-36 mm
Modulation 4	-35 mm	+27 mm	-62 mm

The remaining data shows two distinct trends. The ledge growth in the metal pad during increased energy input shows little variation – except the already mentioned data from modulation 1. It is consistent at 27 ± 1 mm. Ledge melting in the bath area however seems to follow a linear trend if plotted against the

maximum delta energy of the modulation cycle. Figure 5.31 shows the resulting trends graphically.

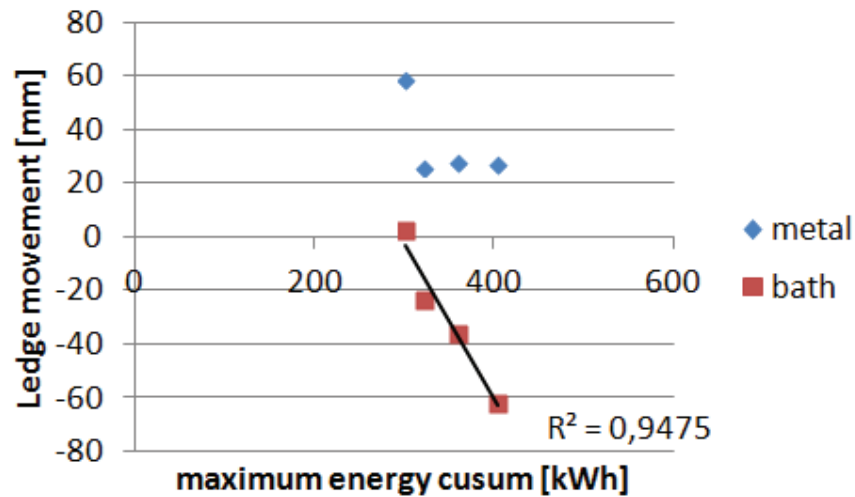


Figure 5.31: Ledge movement (ledge growth positive) depending on maximum energy cumulative sum

Ledge formation in the metal pad is not so much influenced by the energy imbalances of the cell. There must be another driving factor for ledge movement. As the solid phase is not in direct contact with a corresponding melt, availability of liquid electrolyte for both formation and dissolution appears to have a superior influence. This will be discussed in more detail in chapter 5.6.2.

For ledge movement in the bath area, it is surprising that ledge melting and solidifying is in equilibrium for modulation 1 with an energy cumulative sum of 300 kWh and for the subsequent modulation schemes with increasing energy cumulative sum, ledge is readily melting and staying molten. Of these facts it can be deduced that solidification dynamics are inhibited beyond a threshold energy shift. This seems to be the case when the P19 cell is driven beyond 300 kWh energy cumulative sum. Consequently, modulation below this critical point should have minimal impact on cell performance.

5.6 Conclusions on Cell Behaviour

Most comprehensive studies performed and published on aluminium reduction cells are done for or close to steady state operation. Published modelling scenarios always assume a steady state of the cell. In cases of the study of individual changes – most notably cell voltage adaption as a corrective tool for bath temperature control – the studies have not been comprehensive, but focused on the controlled process variable and the shift towards another steady state with the newly set parameters.

5.6.1 Regression Analysis for Cell Reactions

The aim of this work is to investigate the differences in the cell behaviour in between two different steady states and the dynamics that are detectable in this transition period. To enable further models to be constructed of non-steady-state scenarios, the measured data on cell behaviour was analysed using NLREG, a software tool for non linear regression (Sherrod 2014).

During the experiments it was determined that the cell response to changes of the energy input depends on several key factors. The most obvious and notable one is the dependency on additional energy input. For changes of cell voltage the calculation is straight forward using standard formula for calculating electrical energy and subtracting a base value:

$$E = \int (U(t) - U_{base}) \cdot I \cdot c \cdot dt \quad \text{Eq. 5.10}$$

With	$U(t)$	actual cell voltage
	U_{base}	cell base voltage
	I	line amperage
	c	cell design constant

When looking at the resulting changes in bath temperature and superheat, the effects are linearly dependent on surplus energy input if the additional voltage is applied for a fixed time. Looking at the energy density that is applied – in terms of the magnitude of voltage increase – the bath temperature is still linearly dependent on the change in energy density, but the superheat follows a 2nd degree polynomial as shown in Figure 5.15. To verify this, the following equations for modelling bath temperature and superheat change as a result of a change in cell voltage at constant line amperage are used for the regression:

$$\Delta T_{bath} = k_{T_{bath}} \cdot \Delta U \cdot I \cdot t \quad \text{Eq. 5.11}$$

$$\Delta(\Delta T) = k_1 \cdot (\Delta U \cdot I)^{k_2} \cdot t^{k_3} \quad \text{Eq. 5.12}$$

With	ΔU	cell voltage increase
	k_i	cell specific constants
	I	constant line amperage
	t	duration of the cell voltage increase (hours)

For the cell in Hamburg the following, unit-less coefficients were determined using the experimental data to perform a regression to the above equations. Coefficient k_3 could not be determined with the experimental data as time was not varied during these experiments. The found coefficients indicate as well the assumed 2nd degree polynomial dependence for the change of superheat.

$$k_{T_{bath}} = 0.045$$

$$k_{1 \Delta T} = 0.0033$$

$$k_{2 \Delta T} = 1.916$$

For changes in line current the calculation of the surplus energy input is more difficult as the measured cell voltage drop changes. Part of this voltage drop is compensated by the process control system. As the control system uses a simplified approach to normalise cell voltage deviations are to be expected. The

comparison of cell voltage and control voltage at varying line currents is given in Figure 4.7. Eq. 5.6 gives the relation between additional energy input and changes in line current.

Bath temperature again is in a linear correlation to the additional energy input:

$$\Delta T_{bath} = k_{T_{bath}} \cdot Q \quad \text{Eq. 5.13}$$

$$\Delta(\Delta T) = k_1 \cdot \dot{Q}^{k_2} \cdot t^{k_3} \quad \text{Eq. 5.14}$$

$$k_{T_{bath}} = 0.020$$

$$k_{1 \Delta T} = 6.69 \cdot 10^{-12}$$

$$k_{2 \Delta T} = 6.00$$

$$k_{3 \Delta T} = 0.66$$

With coefficient $k_{3 \Delta T} < 1$ the indicated trend is not polynomial as suggested earlier. There are two explanations to consider. Firstly with increasing time the impact is indeed decreasing as suggested by $k_{3 \Delta T}$. Practically this means that the cell is approaching a new equilibrium. Alternately there is an increase as expected, but the limited data used for regression for Eq. 5.14 does not show this increase. A more detailed analysis of time dependency of energy increases should be performed in subsequent work.

As only one experiment was conducted using an energy decrease, there is not enough data for a regression. The coefficients for immediate cooling during the decreasing line amperage were:

$$k_{T_{bath}} = 0.0089$$

$$k_{\Delta T} = 0.0017$$

The coefficient for bath temperature decrease is notably smaller with 0.01 °C/kWh than the one for temperature increase with 0.02 °C/kWh. The heating coefficient is more than twice as high. This indicates that either the cell immediately operates at a decreased current efficiency to compensate for the decreased heat input, or ledge starts forming as soon as the energy input is decreased. As an increased ledge thickness was not detected during the trials, the assumption of decreased efficiency appears more likely.

More notable is the continued decrease in cell temperature during the days following the first trial with energy decrease, leading to bath temperatures 7 °C lower for the beginning of the second trial. This proves an over sensitivity for current decreases especially if the cells already operate at a minimized energy input.

The general difference of cell behaviour between current induced modulation and voltage induced modulation is significant. In all experiments, cells react stronger to energy changes induced by voltage adjustments than to changes induced by changes in line current.

Whereas the calculation of the delta energy input is rather straight forward during voltage adjustments, the calculation of the energy deviation is more difficult for the changes in line current. For the former, the assumption was always that there is only a change in ohmic resistance. For the latter, with the change in line current the amount of metal produced changes directly as well as the electrode overpotentials. This changes the amount of energy available for process heat.

The data presented in this thesis is contrary to these assumptions to some degree. As the amount of heat applied to the cell as voltage shows a larger

heating coefficient, either the efficiency of the cell is more strongly affected when changing line current, or the energy to produce metal is changing to a larger extent than anticipated. This can be the case if the efficiency increases – the cell operating more efficient – if the current is increased. This would imply operating well below the energetic optimum of the cell. Alternatively a larger than anticipated change in anodic and cathodic reactions is occurring when the anodic current density is changed. This would increase the electrode polarization over-voltages and thus leave less energy for heating the cell available.

Lastly, the heat input during voltage increases is only generated in the ACD. For the current increase, the additional heat is generated over the whole current pass through the cell – in the anodes as well as in the ACD, the metal pad and the cathode and finally the collector bars. This may lead to an imbalanced temperature distribution during voltage increases which results in an over proportional heating of bath.

If the low superheat level at which the Hamburg cell is operating is taken into account, an increased current efficiency when increasing amperage appears to be a major contributor to the observed data.

5.6.2 Ledge Dynamics during Power Modulation

Reaction of the side ledge to changes in energy input are more differentiated than reported so far in the literature. The usual assumption was that the same mechanisms act upon the ledge uniformly over the whole height. The assumption is that ledge thickness in equilibrium is dependent on the superheat of the bath and heat transfer coefficients. In FEM models the concave occurrence of the ledge is achieved by varying the heat transfer coefficients over the height of the ledge (Fraser, Taylor et al. 1990, Chen, Taylor et al. 1998, Kholklov, Filatov et al. 1998).

The data presented in this thesis shows that this assumption is not valid. There is a clear distinction between the reaction in the metal pad and in the bath area.

Considering the actual immediate surroundings in each phase, one major difference can be ascertained:

- In the bath area ledge is in equilibrium with the bulk of liquid bath.
- In the metal area, there is no direct contact between solid cryolite and a corresponding melt.

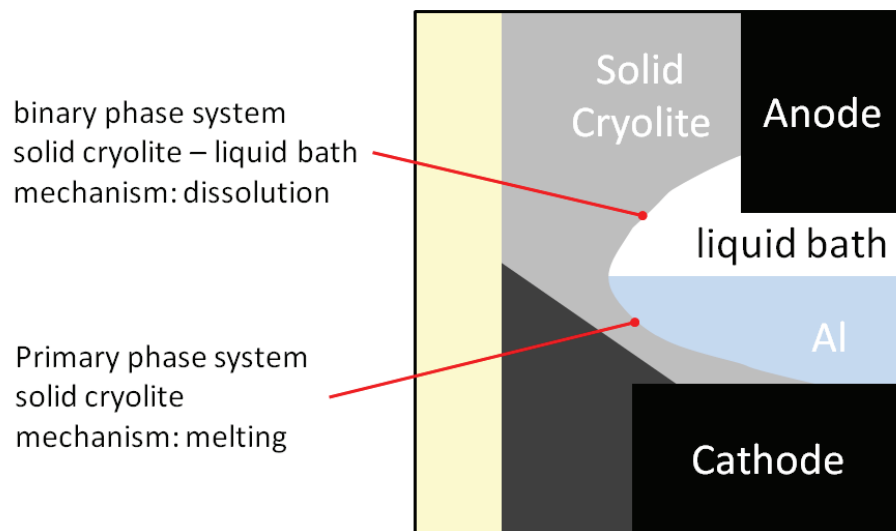


Figure 5.32: Areas for mechanisms of dissolving and melting ledge

This leads to two different mechanisms of solid cryolite converting to its liquid form. Figure 5.32 illustrates the area in which each mechanism is taking place.

In the bath area, the predominant mechanism is dissolution as in any area where a solid and a corresponding liquid phase are in contact. The overall rate of dissolution is dependent on the dissolution rate in the boundary layer and the diffusion rate resulting from the concentration gradients. The process is spontaneous and reversible as solid and liquid are in continuous contact. The assumed dependency on the superheat of the bath is valid.

In the metal area, the solid cryolite is in contact with molten aluminium. As molten aluminium is not able to dissolve any cryolite, another mechanism for changing ledge thickness must be in place.

The most obvious one takes place if the ambient temperature exceeds the melting point of the material the ledge is composed of. For the case of pure cryolite this temperature is given as 1013 °C (Roin e 2002). Depending on impurities in the ledge this temperature may be up to 20 °C lower. In this case, the ledge would melt and the resulting liquid would rise to the top of the metal pad and mix with the bulk material of the bath. While this theory does explain the little change of ledge thickness in the metal pad during single power modulations, it doesn't explain a slow change of ledge thickness or even the build up of ledge in the metal pad at all, especially not during repetitive modulation.

In the literature there are publications on the existence on a liquid bath film between ledge and liquid metal. While the general consensus is that said film exists, its characteristics and driving force are under discussion. Solheim summarizes the possible driving forces for such a film in one of his publications (Solheim 2006). He discusses three separate hypotheses. These are:

- a drag of bath along a downwards metal flow at the metal ledge interface;
- a flow of bath along the interface due to interfacial tension;
- an upwards bath flow from a liquid bath reservoir at the bottom of the cell.

He disregards the first two mechanisms as they cannot result in a bath film thick enough to justify the side ledge thickness found. He concludes that the only viable means to have a bath film of sufficient thickness to result in a change of ledge is the theory of a liquid bath pool beneath the metal pad. Solheim postulated the existence of such a reservoir in an earlier publication (Solheim 2002). The liquid forms from low AlF_3 bath that solidifies at the metal-bath-interface and sinks to the bottom of the cell. In contact with alumina

rich sludge, it forms an alumina-saturated liquid that may creep up along the ledge-metal boundary.

He defines four states for cell reactions. These are quoted here (Solheim 2006):

- At steady-state, the bath temperature is about 960 °C at 12 % AlF_3 in the bath. The bath in the film is alumina saturated and has a somewhat lower AlF_3 -content (*e.g.*, 5 % [...]), and the film temperature is assumed to be slightly lower than the bath temperature. Neither melting nor freezing takes place in this situation, and it is not possible to define a “superheat”.
- In periods without a source of liquid at the bottom of the film (absence of sludge), the ledge will act as an “inert container” for molten aluminium, as long as the metal temperature is lower than the solidus temperature of the ledge. Neither melting nor freezing takes place.
- If the bath temperature decreases by lowering the superheat or by increasing the alumina content in the bath, the metal temperature, as well as the film temperature decreases. If the temperature falls below the eutectic temperature, cryolite and alumina present in the film crystallize until the liquid source at the cell bottom “dries out”, and the ledge grows.
- If the bath and metal temperature increase, the side ledge starts to melt once the temperature exceeds the eutectic temperature of the ledge facing the metal.

These states do not explain why the measured ledge grows during energy increases however. These can be explained by the induced temperature gradients during modulation. The assumption is that the bath melting at the bottom of the cell will be close to saturation with no discernible superheat. If the temperature at the ledge-metal-interface is slightly cooler than at the position where the liquid formed, the melt will crystallize again resulting in building side ledge. In essence this is the third mechanism described by Solheim. If such a

temperature difference is not induced by cooling of the cell, but by heating of the center of the cell, the effect would be essentially the same. Ledge thickness would increase.

During prolonged heating of the cell, the temperature difference would diminish and the melting of side ledge as described by Solheim would ascertain itself. The time dependency on ledge thickness is shown exemplarily in Figure 5.33. Unfortunately it was not possible to determine an exact time after which the solidification of ledge after an energy increase stopped. Thus there is no time scale given in the figure.

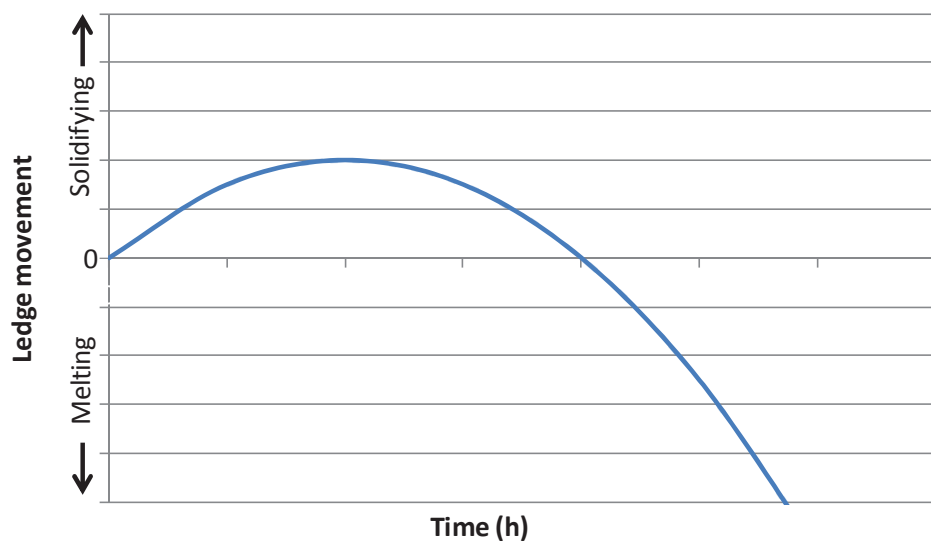


Figure 5.33: Time dependency of ledge in the metal pad after a change of heat input

5.6.3 Impact of Melting Cover Material on Bath Inventory and Ledge Development

During the experiment that encompassed the determination of bath inventories before and after the energy increase, it was shown that the anode cover is a major contributor to increases of bath inventory.

When the energy stored in additional liquid bath during an energy increase is released, the bath cannot attach itself to the cover material again as there is no direct contact between the cover material and the liquid phase due to a gas layer created by the evolving anode gases.

The cryolite has to solidify along the side of the cell. As there is equilibrium between the upper side ledge in bath area and the liquid phase, the ledge thickness is determined by the heat flow through the upper side wall.

The only surface it can attach to without being immediately re-dissolved is the side ledge below the metal pad.

In summary, there is a mass transfer from the cover material to the lower part of the side ledge during power modulation, resulting in a build up of bottom ridging and decreased process efficiency. Due to the decrease in cell volume on the lower part of the cell, metal inventory will decrease. Due to this good production figures will be recorded if the metal inventory is not monitored closely.

6 Economic Impact of Power Modulation

Synopsis:

In this chapter price fluctuations of the electricity price experienced in Germany in 2008 are detailed. Applied scenarios for power modulation are discussed with this data as the modulation was applied at this time. In addition, an estimate on the effect of power modulation on process efficiencies is given based on the operational data of Trimet Hamburg while applying continuous modulation. It is shown that power modulation is an employable means to reduce energy cost.

The application of power modulation with the current market situation as well as other approaches to generate extra revenue for primary aluminium plants from participating in more flexible energy markets are discussed.

6.1 Energy Price Spread

With the liberalisation of the energy market in Europe starting in 1998, Germany was on the forefront to comply with the guidelines set by the EU. The liberalisation led to a separation of electrical energy generation and transmission. As the grid operating companies continued to hold a monopoly on the transmission grid, a free market only existed for production and purchasing of electrical energy. This led to a minimum in energy costs in 2000. Since then the prices have increased continuously, both in price quoted on the European Energy Exchange (EEX) as well as the cost for levies and taxes applied (Kruse 2004).

The inception of the EEX in 2000 led to a visible pricing instrument for electrical energy. Energy prices were not discussed any longer between the consumer and the producer of electricity individually, but are arbitrated in view of the public market. This leads to a uniform price for all market participants taking into account the overall demand as well as generation capacity. As this lead to all energy being sold at the cost of the last MWh generated, an increase in price went along with the new regulation. In addition a price for electricity for every

hour of a day was fixed at the EEX. Figure 6.1 shows the average price curve of June 2008.

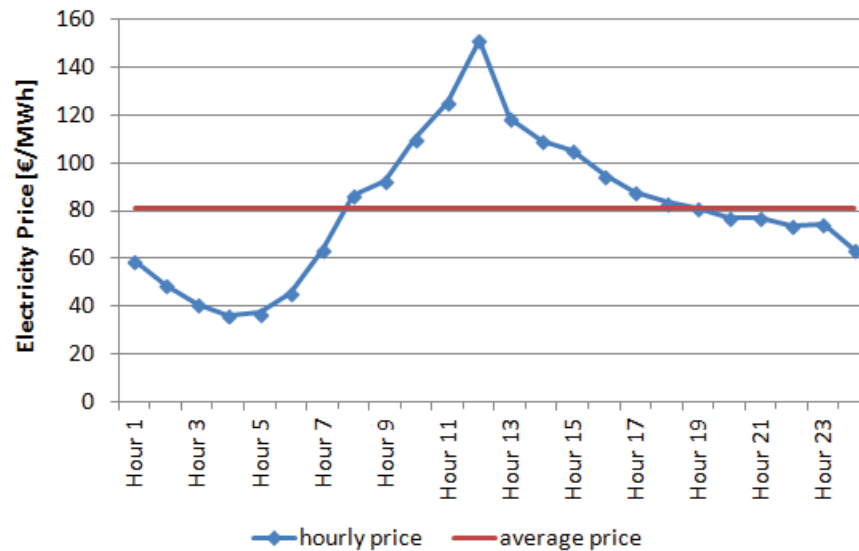


Figure 6.1: Average power price on a weekday in June 2008

Blocks of hours were marketed as well, like a base price for a 24 hour uptake of electricity as well as night time blocks, morning or rush hour. Due to the nature of the trading platform, prices for blocks were effectively the average of the individual prices for each hour contained in a given block. Effectively it was not possible any longer to realize a price for electricity below EEX market price.

Similar to the intraday price spread, price differences can be determined for other changes in electricity usage patterns such as the difference between working days and weekends as shown in Figure 6.2. The intraday spread is less pronounced on the weekends as the usage profile is more uniform throughout the day with less commercial and industrial activity driving the price during daytime.

Also significant shifts in the price curve are visible with changes in seasons. While the highest price during summer time occurs during noon time, in winter

there is a pronounced peak in electricity price in the late afternoon and early evening as is shown in Figure 6.3.

Possible usage profiles of a primary aluminium smelter have to take these shifts into account to maximize the gain from power modulation.

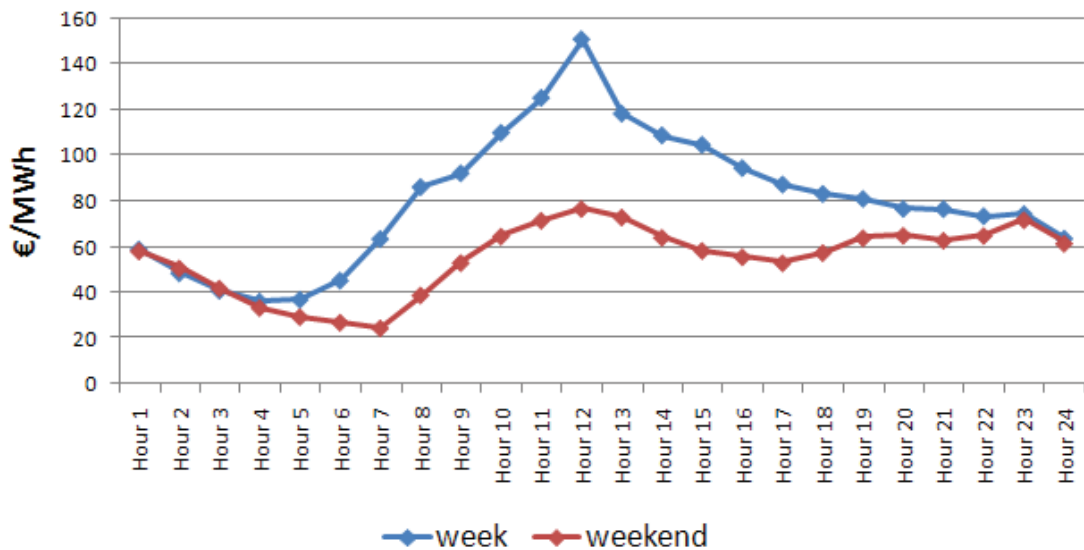


Figure 6.2: Power price on weekdays and weekends in June 2008 (Anonymous)

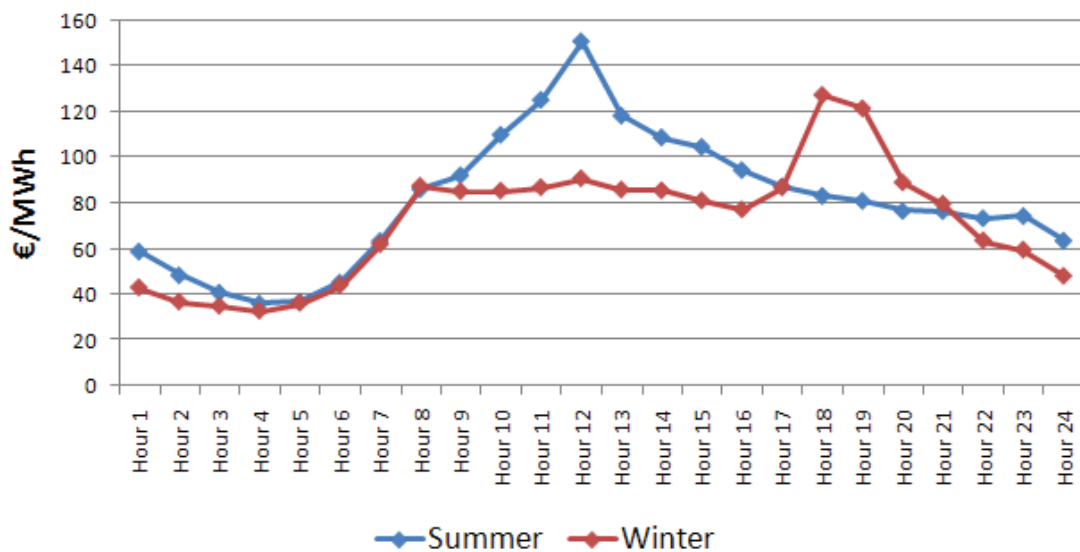


Figure 6.3: Power prices during seasons in 2008 (Anonymous)

Considering the price spread between the most and least expensive hour during a day, a substantial reduction in average energy price is realizable if the traditional load profile of a primary aluminium plant is disregarded in favor of a modulated energy uptake.

The price curve shown in Figure 6.1 and the line current of modulation 4 shown in Figure 5.28 are plotted together in Figure 6.4. The reduction in average energy cost can be calculated from the line current and the resulting shift in cell voltage. The reduction in energy price corresponds to 2.68 % or 2.17 €/MWh. This corresponds to savings of more than 30 €/t_{Al} considering the energy price level and an energy consumption of 14.5 MWh_{AC}/t_{Al}.

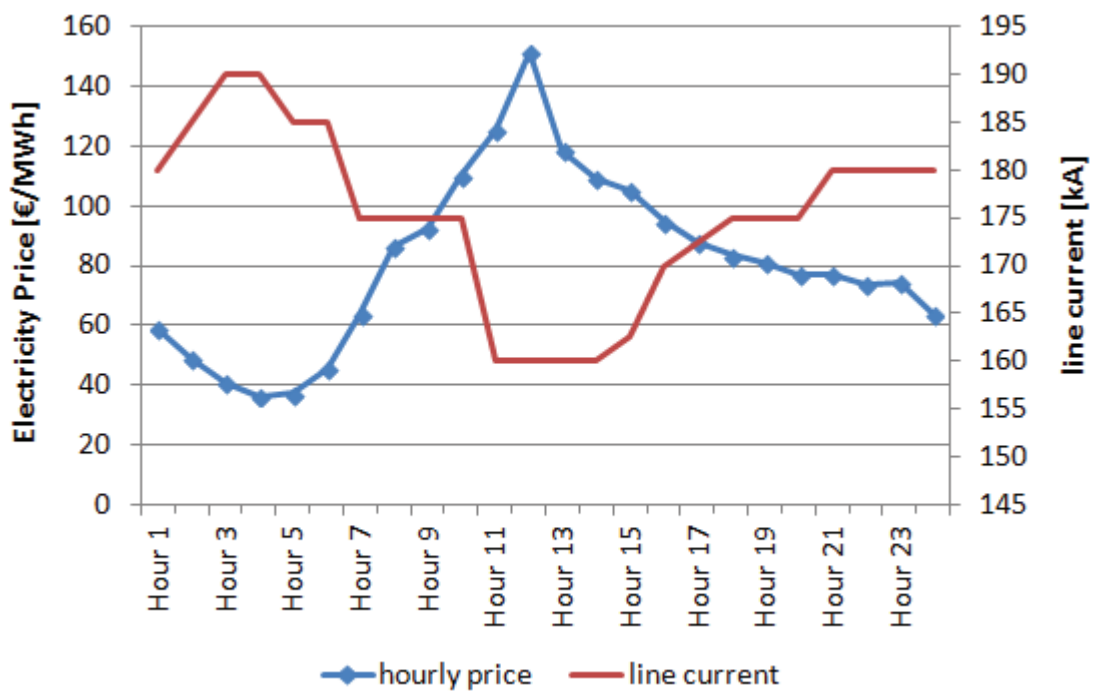


Figure 6.4: Price curve and resulting line current

6.2 Power Modulation with the Current Market Situation

Since the power modulation was practiced on full scale in 2008, the market changed considerably. Figure 6.5 shows the average price for a normal working day in November 2013. The average power price decreased by nearly 50 % from 80 €/MWh to just above 40 €/MWh. The spread in energy price is still on a similar level – from 50 % of the base price in the cheapest period to nearly 200 % in the most expensive period. The deviation is however smaller as the main period of the day from 10:00 h to 18:00 h is close to the average price of the day. Thus, the potential for modulation is limited.

It should be noted, that, even though the energy price decreased considerably, the percentage of energy cost on total production cost has not changed significantly, since anode prices are heavily linked to calcined petrol coke prices. As CPC can substitute fuel in power plants, its price is linked to the global energy price. Alumina is traditionally traded at a percentage of aluminium price. As such, all raw material prices are linked to the price of the finished product. As raw material costs contribute with 90 % to the production costs, these are the dominant factors.

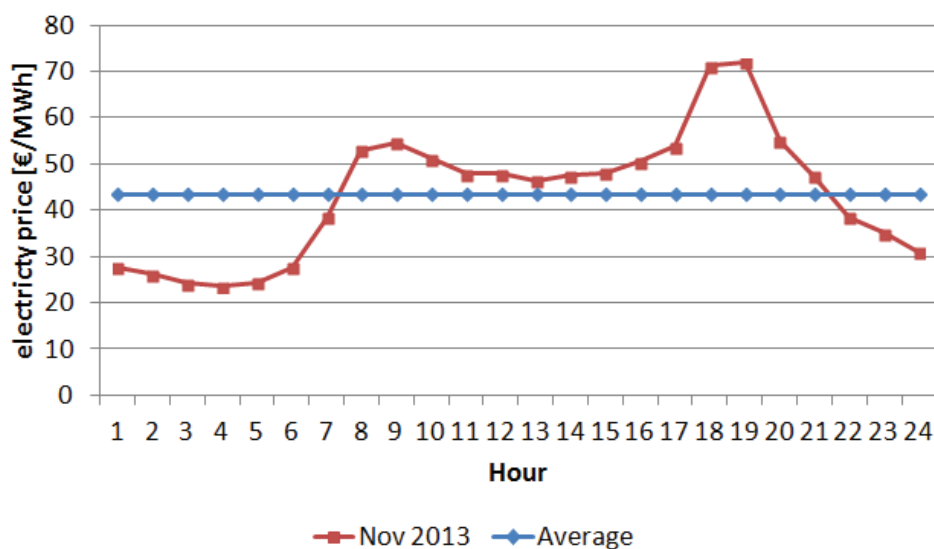


Figure 6.5: Average power price on a weekday in November 2013

A potential modulation curve is given in Figure 6.6. The modulation scheme is shedding load during the small early morning peak as well as during the significant early evening peak. It is taking advantage of the usual low energy price during the night. This results in a modulation of 31 MWh per cell per month. This is 5.70 % of the nominal energy input or slightly more than half the modulations practiced in 2008. The maximum shift of energy is 347 kWh and thus well within the capabilities of the cell.

Energy cost would decrease by 2.75 %. This is in a similar range than the price reduction achieved in 2008. Power modulation was not practiced at this time as the Hamburg smelter provided a frequency response service detailed in Chapter 6.4 at this time. The revenue achieved by these was exceeding the projected earnings from classic load management. A combination of both is not practical due to restrictions in the energy market.

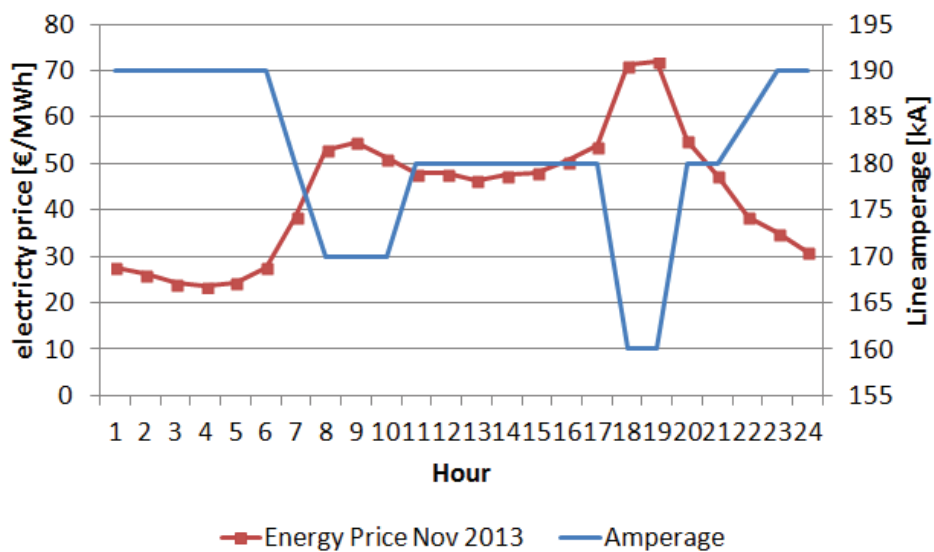


Figure 6.6: Resulting modulation profile

6.3 Effect of Power Modulation on Productivity

As discussed earlier in this thesis, a reduction in efficiency is to be expected when a reduction line is operated with power modulation. Exceeding a certain level of power modulation, the loss of productivity is expected to increase over proportionally. An attempt is made to determine the effect of power modulation as conducted at Trimet Hamburg based on the production data of the period from late 2007 until early 2009. This data, however, is heavily biased and superimposed with several other effects.

Firstly, in 2007 the plant was restarted after being idled for more than one year. While potline 1 was fully operational by the end of June 2007, potline 2 was restarted in the second half of 2007, with the last cell being taken into operation just before Christmas. The standard operation procedure aimed at an increased metal inventory immediately following start-up of a cell. The metal inventory was reduced to normal operating level within the first month of operation. This resulted in an increased metal tapping in the first month of operation. While the effect on the discussed period was minimal in potline 1, potline 2 recorded above average production in the respective period due to this effect.

Secondly, at the end of the investigated period, production was cut severely by 50 % due to the economical situation in 2009. Production in pot line 1 was cut in late 2008 and in potline 2 in February 2009. Cells were shut down and metal inventory was tapped and recorded as production in the monthly reports. Subtracting a nominal metal inventory per shut down cell is not constructive as the actual metal inventory of a cell can vary considerably from nominal. To explain the significantly reduced current efficiencies at the end of 2009 and beginning of 2010 it should be noted that the metal added after start up of a cell is not recorded in the monthly reports as well.

Thirdly, the enactment of power modulation was in conjunction with a slight but noticeable reduction in average line current and thus heat input. This was done without any compensation on cell voltage. No means were taken to reduce heat loss from the cell besides the natural formation of side ledge to regulate heat flow through the side of cell. Any resulting change of metal inventory due to

sludging of cells and formation (or dissolution) of bottom freeze cannot be regarded in this discussion.

In spite of these biases the resulting production data for the production lines at Trimet Hamburg is given in Figure 6.7 and Figure 6.8 as well as Table 6.1 and Table 6.2. Months with significant changes in the number of operating cells were omitted from the averages presented in both tables. These are October to December 2008 in potline 1 and February 2009 in pot line 2. The amount of power modulation is calculated as the absolute sum of energy deviating from a constant energy input.

Despite these omissions a significant drop in current efficiency is detectable in both potlines. The drop is 1.09 % in potline 1 and 2.68 % in potline 2. This effect is more pronounced in potline 2 as the starting level of current efficiency is significantly higher in potline 2 (95.41 % compared to 93.32 %). As the relevant time frame includes data from the start-up and immediately after, it seems likely the bias due to reducing metal inventory after start-up is significantly more pronounced in pot line 2.

Further information is critical for further discussion of the data. It is noted that in both cases the recorded heat loss from the cell is larger during the period of power modulation and reduced heat input than during normal operation. As the energy introduced to the cell is either used to produce metal or lost as heat, an increased heat loss is a strong indicator for decreased current efficiency.

The experimental part of this thesis has shown that cells have a significant capacity for shedding additional heat if heated beyond nominal operating temperature. It is therefore assumed that the additional heat loss is attributed to power modulation exclusively.

To differentiate between the effect of power modulation and the general reduction of heat input by reducing the line current, the drop of current efficiency is calculated which would result in the same increased heat loss from the cell if the overall heat input to the cell would remain stable.

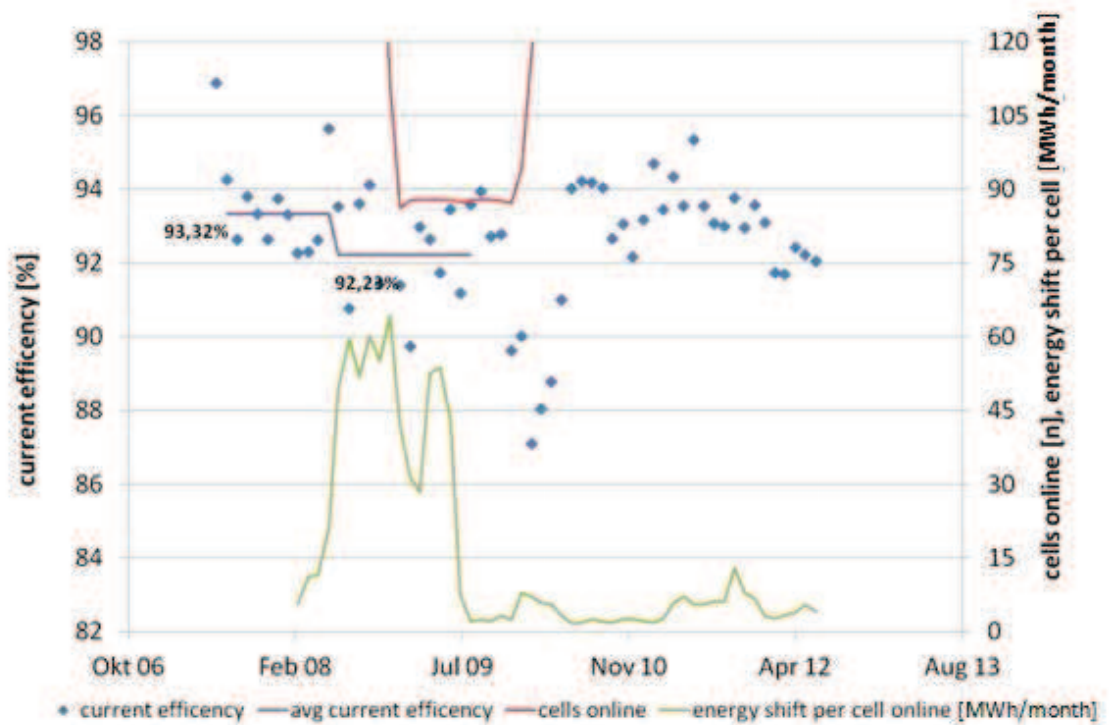


Figure 6.7: Production data System I

Table 6.1: Production data System I

Time period	η [%]	I [kA]	Heat input [kW]	Energy for Al [kW]	Heat loss [kW]
Aug 07 – Jun 08	93.32	175.19	721.3	361.9	359.4
Jul 08 – Aug 09	92.23	173.77	716.0	354.8	361.2
Delta	1.09				1.8

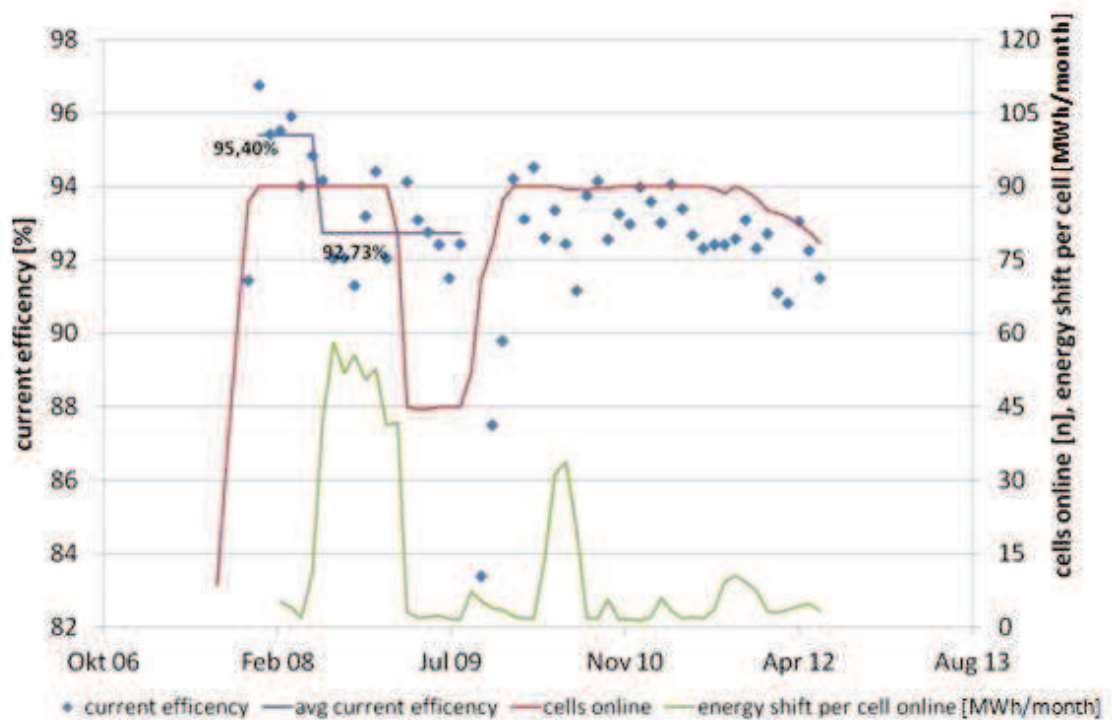


Figure 6.8: Production data System II

Table 6.2: Production data System II

Time period	η [%]	I [kA]	Heat input [kW]	Energy for Al [kW]	Heat loss [kW]
Jan 08 – Jun 08	95.41	175.53	719.4	370.8	348.6
Jul 08 – Aug 09	92.73	173.91	711.1	356.4	354.7
Delta	2.68				6.1

The calculation is based on a constant heat input:

$$d\eta_{CE} = \eta_{CE} \cdot \left(\frac{1 - d\dot{Q}_{heat\ loss}}{\dot{Q}_{Al}} \right) \quad \text{Eq. 6.1}$$

With:

- $d\eta_{CE}$ change current efficiency
- η_{CE} current efficiency
- $d\dot{Q}_{heat\ loss}$ change in heat loss
- \dot{Q}_{Al} energy to produce aluminium

The resulting data is shown in Table 6.3:

Table 6.3: Adjusted productivity loss during power modulation

	System I	System II
Loss in current efficiency	1.09 %	2.68 %
Increase in heat loss	1.8 kW	6.1 kW
Adjusted loss in current efficiency	0.45 %	1.54 %

Even though the examined data is heavily biased, in the given scenario it can be assumed that the efficiency loss due to power modulation is less than 1 %. For continuous operation the loss of current efficiency due to a shift of 10 % of the energy from average input can be as low as 0.5 %, as is shown by the data from pot line 1.

Using both the reduced current efficiency and the reduced energy cost, the effect on production cost can be calculated. The result is presented in Table 6.4 for a variation of energy price decreases and losses of current efficiency. The assumptions used in this table are an energy cost percentage of 40 % of total production cost and an alumina cost percentage of 30 %. Decreases in current efficiency are calculated as increasing the full production price minus alumina cost. The resulting percentage is a change of total production cost – a decrease if the value is negative.

The results achieved at Trimet Hamburg are highlighted in the table. For the given decrease in energy price of 2.68 % and a loss of current efficiency between 0.5 % and 1 % the reduction in production cost is between 0.36 % and 0.72 %. The threshold of profitability can be calculated as loss of current efficiency of 1.51 % if a cost reduction in energy cost of 2.68 % is achieved. Even though the data presented for potline 2 is heavily biased due to the start up and shut down in the respective time frame, the recorded loss in current efficiency of 1.54 % is in this range.

Table 6.4: Net benefit of power modulation on production cost

		Decrease in electricity cost								
		0.00%	-0.50%	-1.00%	-1.50%	-2.00%	-2.50%	-3.00%	-3.50%	-4.00%
Loss in current efficiency	0.00%	0.00%	-0.20%	-0.40%	-0.60%	-0.80%	-1.00%	-1.20%	-1.40%	-1.60%
	-0.50%	0.35%	0.15%	-0.05%	-0.25%	-0.45%	-0.65%	-0.85%	-1.05%	-1.25%
	-1.00%	0.71%	0.51%	0.31%	0.11%	-0.09%	-0.29%	-0.49%	-0.69%	-0.89%
	-1.50%	1.07%	0.87%	0.67%	0.47%	0.27%	0.07%	-0.13%	-0.33%	-0.53%
	-2.00%	1.43%	1.23%	1.03%	0.83%	0.63%	0.43%	0.23%	0.03%	-0.17%
	-2.50%	1.79%	1.59%	1.39%	1.19%	0.99%	0.79%	0.59%	0.39%	0.19%
	-3.00%	2.16%	1.96%	1.76%	1.56%	1.36%	1.16%	0.96%	0.76%	0.56%

6.4 Conclusions on Economical Impact and Future Prospects

The practical work conducted during this study has shown that it is possible to operate a smelter with varying energy input. In 2008 the price spread of electricity within each day was large enough to enable a beneficial operation of power modulation on its own. Since then the price spread has decreased to a more normal level. In a conjunction with benefits on levies for an as constant energy uptake as possible, this has limited opportunities for reducing energy cost by load management.

If the process philosophy of keeping the energy input to a cell as constant as possible is overcome, there are other ways to profit from flexible smelter operation. In an environment with a rapidly increasing share of highly variable renewable energy generation, either balancing power plants are needed or consumers of electricity have to fill the same role. Whereas the advantage of self-directed power modulation is the fixed schedule, externally controlled energy services yield a premium even for the provision of service independent of the actual release order.

Within the German energy market there are several energy services that are handled by power plants nearly exclusively today which can be profitable markets for aluminium smelters to enter. In all cases the aluminium smelter would act as a negative (or virtual) power plant shedding load to the grid when a regular power plant would increase energy output. Possible markets are:

Emergency Grid Stabilisation

Time-limited emergency shut downs of smelters have been employed throughout the history to stabilize grid operation. Power outages of 30 to 60 minutes are the norm as this is approximately the time needed to start a contingency power plant. Typically one or all potlines are dropped off the grid simultaneously.

When there is a major incident limiting electricity available in the grid, fast response power plants have to come online or large consumers must be dropped off the grid. Incidents can be failures in other power plants as well as failures in transmission lines or substations. An occurrence appearing more frequent recently is a significant deviation from the actual production of renewable energies to its forecast. This typically leads to short time energy deficits in the thousands of MW in the grid (Trimet 2014). These deviations will occur more regularly the more generation capacity of solar and wind power is installed.

In 2013 a market system was implemented in Germany to remunerate major consumers of electricity for this service.

Operating Reserve

Each grid operator must source an operating reserve in relation to the electric consumption in his grid zone. The operating reserve adjusts the energy supply to match demand within a short time frame. Operating reserve adjustments typically take less than 10 minutes to enact and can last from at least one to several hours.

Using a smelter in the operating reserve implies that the smelter must increase or decrease power consumption within the given time frame on demand of the grid operator. The advantage is that the amount of load shed or taken on additionally can be agreed on individually. Effectively the impact on operation can result from a few kA for a single hour to substantial changes in line current for 4 hours or more.

Today the operating reserve is provided exclusively by power plants. These are pump storage hydro power plants, gas turbines or margin capacity of base load power plants.

Frequency Response

The most challenging energy service is the frequency response or primary control power. Providers of this service match their load to the measured grid frequency with the aim of keeping the frequency within a small band around the target. A loss of frequency corresponds to too little energy available in the grid. An increase in frequency consequently means an oversupply to the grid.

Effectively the provider has to match their load profile to the grid frequency every second. As very few power plants offer such technical service, the premium is substantial. For a smelter, the benefits are that typically the frequency response swings around zero demand on short notice. The energy imbalance of the cell is therefore negligible.

Trimet Hamburg was the first provider of frequency response power that is not a power plant in Germany in 2012 (Lützerath 2013).

7 Engineering Solutions to Promote Sustained Power Modulation

Synopsis:

Experimental setup for this thesis was an unmodified cell as it is installed in the Hamburg plant. Heat loss from the cell was not influenced. Possible modifications with the aim to control heat loss from the cell are discussed in this chapter.

In modulation scenarios investigated in this thesis, no modifications were made to the existing cell. As such heat loss from the cell was not varied beyond the natural, self regulating amount. The results showed a strong capacity for losing additional heat introduced by line current or voltage increases. Cell temperatures had returned to normal level in less than one day after the end of increased energy input period.

During one trial the convectional air flow along the side wall of the cell was blocked by applying a layer of rock wool to cover the gap between the steel shell and the concrete floor. The cell heated up to 990 °C within 12 hours. The ambient temperature in the basement had increased to 250 °C as well. While this means appears to be very effective, the resulting temperature in the basement is damaging to the concrete structure of the pot line. In addition, the bimetal clads connecting the cathode collector bars with the bus bar system have a service temperature of 300 °C maximum. For this reason no further trials were undertaken.

In a similar way, the cell reacted very sensitively to reduced energy inputs, resulting in a prolonged period of operation on lower temperature levels if the energy deficit was not balanced within a short time frame.

This highlights major constraints on the magnitude of power modulation that is realizable with an unmodified aluminium reduction cell before encountering severe losses in production efficiency or worse. To further increase both the amount of energy to be modulated and the time distance between shifting the

cell out of normal heat balance and rebalancing the cell, means have to be investigated to directly vary and control the amount of heat lost from the cell.

7.1 Controlled Side Wall Heat Loss

Modifying heat loss through the side of the cell has been employed in recent years repeatedly to boost heat loss to facilitate current increases and thus increases in productivity. Typically, air lances are installed at regular intervals along the side of the cell. They are connected to a low pressure fan via a network of tubing. The flow of air is varied by modifying the power of the fan. This design is subject to several patents (Bos, Feve et al. 1999, Bos, Feve et al. 2001) and has been implemented repeatedly successfully (Fiot, Jamey et al. 2004). The capability of this system to retain energy in the cell is nonexistent however. By shutting down the forced cooling network, the cell is just returned to its original un-boosted state.

A different design is the inclusion of a heat exchanger inside the steel shell of cell. This design was patented by Ingo Bayer (Bayer 2007). In this set up, air ducts are installed horizontally between the steel shell and silicon carbide refractory. Air is pumped through the ducts according to a temperature profile measured on a normal cell. The difficulty of this set-up is that it can only be installed during relining of the cell. A conversion of an existing smelter would take 6 to 7 years, depending on the average cell life. As far as it is determinable, there is no smelter using the system on a production scale today.

Another alternative is similar to the one described by Bayer, but offers several distinct advantages. Heat exchangers are clamped onto the outside of the cell. Air is sucked vertically along the side wall of cell. Employing suction and opening the heat exchangers at the bottom of the design reduces the number of ducts needed as the ambient air at the cell is used as coolant. Figure 7.1 shows a sketch of the shell heat exchanger (Lavoie, Namboothiri et al. 2011).

The major benefits of this system are the ease of installation. The air flow can be adjusted on each heat exchanger by adjustable dampers optimizing the heat

extracted at each point along the side wall of the cell. Furthermore, the heat exchanger can be used as an insulator as well. Reducing air flow below a certain threshold will result in less heat being extracted from the cell than without the heat exchanger. The heat exchangers create air pockets at the outside of the shell, blocking self-contained convection.

This can be a disadvantage as well. If the suction fan fails due to mechanical problems or power outage, the heat exchanger goes into insulation mode as well. Side wall temperatures will increase beyond 400 °C within minutes.

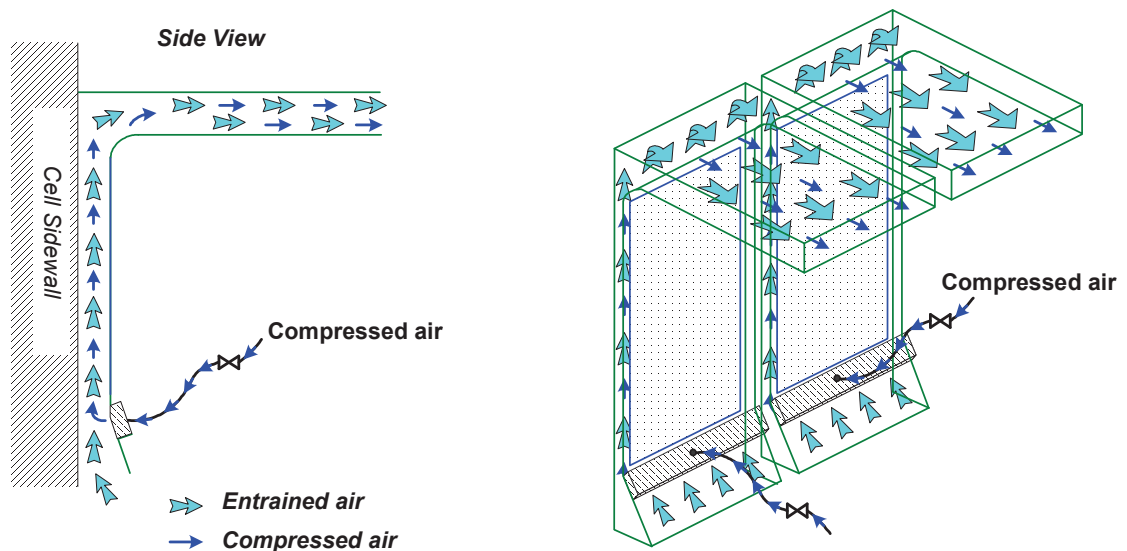


Figure 7.1: Sketch of the working principle of the shell heat exchanger (Lavoie, Namboothiri et al. 2011)

At Trimet Essen a single cell was equipped with such a shell heat exchanger to determine the operation window achievable. Data was collected over an extended period of time using both approaches of extracting a varying amount of heat from a normally operating cell as well as adapting cell operation to the heat loss controlled with the SHE. The resulting data is shown in Figure 7.2. One data point represents an hourly average of cell operation. Black data points

represent normal and constant heat input to the cell with varying suction rates and red data points represent cell operation adapted to the controlled heat loss.

Nominal heat loss through the side walls is 100 kW for the installed cells. This was achieved with 20.3 m/s air flow through the heat exchanger. Operating the heat exchanger with minimum and maximum air flow resulted in a change of ± 50 kW heat loss through the side wall. This shows that the heat exchanger is a valid approach for controlling the side wall heat loss of a reduction cell and thus increasing the modulation window of aluminium reduction cells.

Increasing the air velocity in the heat exchanger beyond a certain threshold resulted in a worsening of convective heat flow. Effectively less heat was extracted due to an over proportional decrease in outlet air temperature. This was the case if 35 m/s were exceeded in the main duct.

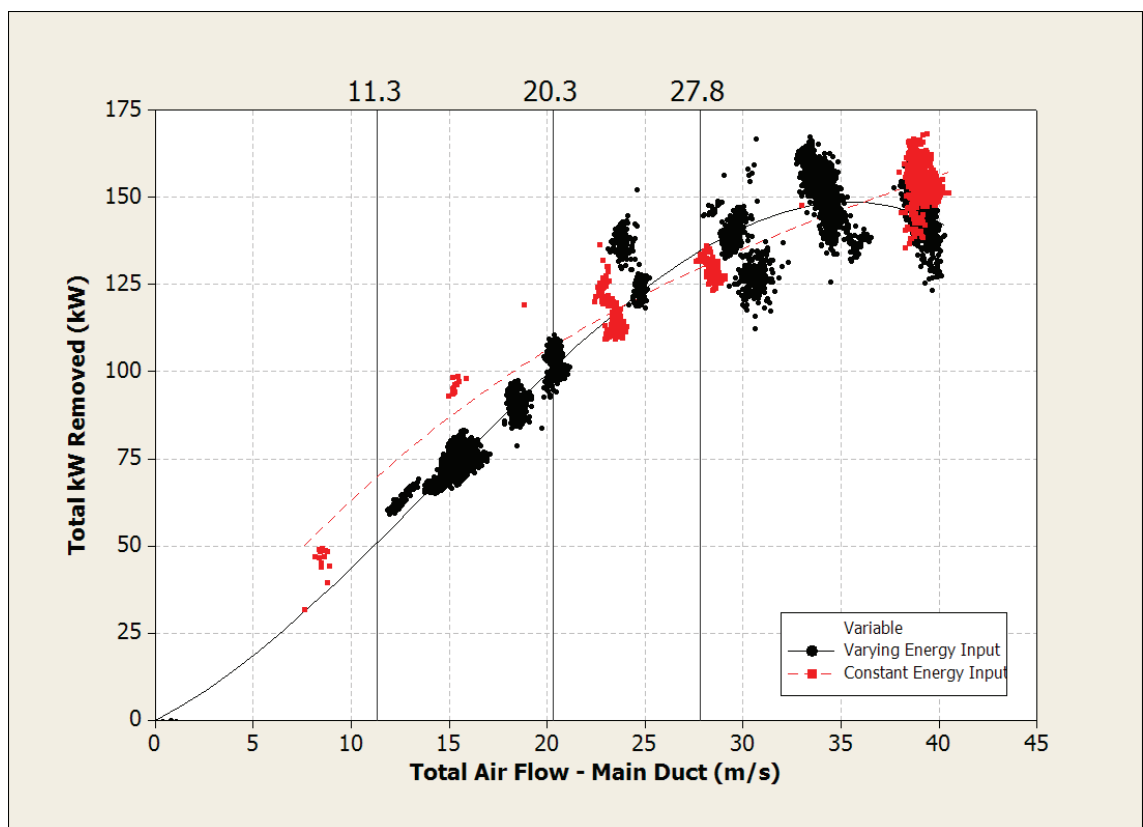


Figure 7.2: Heat loss achievable with a shell heat exchanger

7.2 Controlled Top Heat Loss

The other main route for heat loss from the cell is the top side. As was shown in chapter 3.3.1, about half the heat is lost from the top of the cell. The largest part of this heat is removed with the off-gas of the cell. The off-gas heat flow amounts to $2/3$ of the heat loss from the top of the cell or about $1/3$ of the cell's total heat loss, as is shown in Chapter 0.

Within limits it's possible to adjust the suction rate to control the heat loss from the top of the cell. Constraints are on one side the capabilities of the dry scrubbing system. The filter units must be able to operate with the generated under pressure and throughput. Also, existing governmental limits of maximum throughput must not be exceeded. As dry scrubbing units are typically operated close to those limits, the capacity for increasing suction rate without investments is limited. On the other side, reduced suction rates result in higher diffuse emissions escaping through the roof of the pot line. Governmental limits are imposing a hard constraint here as well. Typically there is some room for improvement with regards to maintaining the hooding of the cell to improve capture efficiency. In addition, if the reduction of suction rate is in correspondence with a decrease in line current, HF generation is reduced as well, as has been shown by Iffert (Iffert 2008).

The Hamburg cell is equipped with a damper system on each cell to equalize suction rate during normal operation. When work is performed on a given cell, the damper is opened to boost suction. To investigate the effect on extracted heat by varying the suction, on two cells air flow and off-gas temperature has been measured at incremental positions of the damper. The results are shown in Figure 7.3.

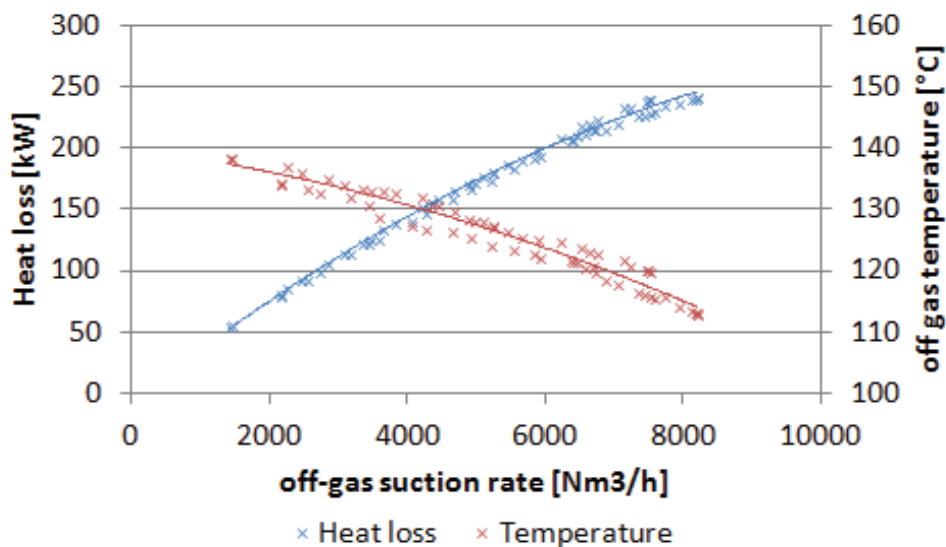


Figure 7.3: Heat loss through the top of the cell at various suction rates

The variability of the heat extracted through the off gas is significant if the variability in suction rate is large enough. The full width cannot be realized in real production due to the constraints discussed above. Normal suction rate is about 3800 Nm³/h for the Hamburg cell. This equates to 137.5 kW heat loss through the off gas.

A variation of 10 % of the suction rate would equate to 12 kW change in heat loss. A change like this will not be significant for energy increases, if it can be realized at all due to the constraints of increasing suction rate in the dry scrubber.

For line current decreases the HF generation will decrease as well. As such a slight reduction in suction rate will not increase diffuse emission and can benefit heat conservation in the cell. The potential is limited in comparison to the potential offered by a shell heat exchanger.

8 Conclusions and Future Work

Synopsis:

The final chapter of this thesis presents a summary of the major points of this work as well as the conclusions drawn herein. It is shown that it is feasible and economical to operate a smelter with continuous power modulation, even though a loss of efficiency is unavoidable.

There are fields for improvement if the challenge of flexible pot line operation is accepted. Even though the market environment is currently not driving for an increased modulation, there are energy services that provide additional revenue if integrated successfully into day-to-day operation. How to achieve this is outlined as work to do in the near future to be prepared for even more competitive energy markets that will arise in the future.

In this thesis capabilities of aluminium reduction cells, specifically the side-riser modified P19 cell as it is installed in Trimet Hamburg, to act as a storage of energy are reviewed. Even though the work focuses on this specific type of cell, the systematic approach is easily transferable to cells of other design and size.

Modern cells like the AP3X or DubAl's DX and DX+ will most likely show less storage capabilities as those cells tend to have smaller side channels than the older technologies like Reynold's P19 cell. This results in less side ledge and accordingly less cryolite to melt and solidify per operational amperage. This also implies that during temperature excursions – intentional like during power modulation or unintentionally during process excursions – it is much easier to have molten cryolite in contact with the side lining material. This will damage the lining permanently and may lead to premature cell failure if it is happening repeatedly.

In the introduction, several questions were raised. In the following, a short answer is given to each of those. A more detailed summary of the findings is given in the following chapters.

Q: How much energy can you store in each cell while maintaining thermal balance constraints?

A: For the Hamburg P19 cell a storage capacity of 0.7 MWh was determined with the cell staying in the optimum process envelope.

Q: What are the limiting constraints existing in cell design and process organisation?

A: The limits in process operation and cell design are the necessity to retain side ledge on the high energy side and the loss of sufficient alumina dissolution on the low energy side. The process organisation is limited mainly by interfaces like metal delivery to the cast house and availability of rodded anodes if modulation is undertaken to an extent that necessitates shifts in work routine.

Q: What is the effect on process efficiency?

A: With increased power modulation, a degradation of process efficiency is noticeable. This is over-compensated by reduced energy costs even in moderately variable energy markets.

Q: Which simple, economical and retrofittable design variations exist that increase the feasibility of power modulation?

A: For regulating the heat loss through the side wall, a heat exchanger design that can both insulate and increase heat loss is available and can be installed at reasonable costs. For plant wide modulation varying the suction rate of the dry scrubber is very attractive, especially for conserving energy in the cell as long as environmental limits can be met.

8.1 Capability of Energy Storage

A significant constraint is the maximum energy deviation that signifies the difference between a cold and a hot cell that are at the border of optimum operation. This energy was determined as 0.7 MWh, or 4 kWh/kA.

Small amounts of energy are stored in the cell by heating all relevant materials, including relining, metal stock and liquid bath. The major part of the energy is stored in dissolution of side ledge into liquid bath. Nearly 2/3 – or 485 kWh – of the stored energy is retained in the mechanism of ledge melting.

The second largest energy storage in the cell is the heat up of the cathode and the ramming paste. These combine another 113 kWh of storage capacity.

For cells with less side channel and less side ledge, the maximum amount of storable energy will be considerable less, probably about 3 kWh/kA or even slightly lower. This would result in storage capacities of 1 MWh or slightly above for modern 350 to 400 kA cells.

One major finding of this thesis is that the storage time that can be achieved with an unmodified reduction cell is extremely limited. If periods of energy decrease can be scheduled by the smelter management, these have to be implemented immediately after periods of increased energy. During the experiments cells had lost all additional heat within 16 hours. Thus, a balanced energy input as to be achieved within 24 hours latest, with a maximum peak deviation not exceeding the afore mentioned value of 0.7 MWh.

Cells reacted significantly stronger to energy decreases than they react to energy increases. Process instabilities were found to decrease significantly if an energy increase was scheduled before decreasing energy input. It is therefore detrimental to schedule additional heat input before executing a severe cut in energy input.

8.2 Limiting Constraints for Power Modulation

The major limiting constraint is the maximum amount of energy that can be stored in the cell. This was determined to be 0.7 MWh per cell resulting from the energy needed to heat a slightly cold cell to a temperature just below the threshold above which a cell is considered in need of special attention and checks. As there is always a distribution of cell stated in a given reduction line, this theoretical threshold is practically not achievable as a certain number of cells is always pushed beyond the envelope of optimum performance.

If cells are pushed beyond this envelope, the efficiency of the process will decrease significantly as described above. Additionally there are significant outer limits which have to be avoided under all circumstances.

The upper limit for increased energy input is the dissolution of all side ledge in a cell. This results in a decoupling of bath temperature and chemical composition of the bath. The superheat of the cell will increase significantly, resulting in a significantly less efficient process. If the cell is in this state for an extended period of time, premature cell failure by corrosion of the lining material is inevitable.

The lower limit for overall energy input is indicated by a low superheat. This will lead to insufficient dissolution of alumina. This can lead to either anode effects during the low energy period due to too little dissolved alumina in the electrolyte. Alternately electrolyte solidifies to provide energy for dissolution. This leads to ridging in the cell disturbing the current flow as well as decreasing electrolyte levels. The smaller amount of liquid electrolyte is then again not able to dissolve the added alumina completely, leading to sludging of the cell bottom.

Other constraints are imposed if rescheduling work practices becomes necessary due to the extent of power modulation.

Work routines have to be shifted to avoid combinations that will destabilize the cell, such as changing anodes on cells that are operating on the low side of the

energy balance already. This will lead to an increased number of unstable cells and subsequently to greater losses in process efficiency.

However, if work practices are rescheduled, interfaces and logistics may pose a major constraint. The cast house will not receive liquid metal equally spread throughout the day. While this may not pose a problem if the cast house is not operating continuously, in Hamburg this is a criterion for exclusion as the cast house is operated by a different company.

Other interfaces are with the rodding shop and with equipment availability such as cranes for anode change, equipment for tapping or shift personnel. In Hamburg these points would not pose any bottlenecks.

8.3 Side Ledge Variability during Power Modulation

It was hypothesized that the melting and dissolution of side ledge is the major mechanism for a cell to store additional energy. This hypothesis was proven to be correct. However, significant unexpected behaviour of the side ledge was found during the experiments.

A significant, repeatable difference in side ledge reaction was found depending on the position in the cell. Whereas side ledge in contact with bath reached an equilibrium state easily, the first reaction to energy increase within the metal pad was a build up of ledge. On a longer term, the cell achieved equilibrium again. Equilibrium was not nearly as instantaneous achieved as was assumed.

The reason for this was found in the lack of a corresponding melt able to dissolve the cryolite of the side ledge. A mechanism postulated by Solheim for explaining a sufficient bath film between side ledge and metal to facilitate a slow formation of side ledge is supported by these findings.

To explain the increase of side ledge during energy increases, Solheim's hypothesis was expanded by an imbalanced case where an alumina saturated melt forms at the bottom of the cell and solidifies when it reaches the ledge/metal interface due to temperature imbalances induced by cell heating.

Additionally it was found that the melting of cover constitutes a significant factor in changes of liquid bath mass. As the material cannot solidify at the top crust again, but can only build side ledge or be removed from the cell by tapping liquid bath, a reason for increased ledge and bottom ridge build up during power modulation was found.

8.4 Effects on Process Efficiency and Means of Generating Additional Revenue

Swings beyond the maximum energy deviation promise a significant decrease in process efficiency. Even continuous modulation within that range showed a decrease between 0.5 % and 1.0 % in current efficiency as was shown on operational data obtained in Hamburg in 2008. Considering the intraday price spread that was listed at the EEX during this period, the overall effect of adopting power modulation was beneficial as the reduction in energy price over-compensated the decrease in efficiency.

Since then the intraday price spread has decreased. Nevertheless, there are other energy services that are typically provided by power plants that smelters can supply as easily. This spans from providing backup power as a negative power plant in emergency situations to frequency response services.

The upside of providing energy services is that a premium is paid independently of the actual release order. A smelter that is operating with understanding of the market can set margins to generate revenue and limit the number of actions it is called upon to perform.

8.5 Design Improvements

Two design solutions for improving the modulation window are discussed in this thesis. These are side wall heat exchangers and the modulation of the suction

rate of the dry scrubber. Both show significant possibilities for varying the heat loss from the cell. Due to environmental constraints and the limits on the dry scrubbers to increase throughput, the possibility of utilizing the second solution proves limited.

Implementation of an easily installable shell heat exchanger promises a cost effective upgrade with which the heat loss from the cell can be increased or decreased by approximately 12 % or ± 50 kW.

A simpler way for regulating heat loss through the side wall by blocking the air flow from the basement along the side wall of the cell was trialled but immediately discontinued as the heat build up in the basement was found to be too high, endangering both the concrete structure as well as the steel-aluminium-clads used to connect the cathode collector bars to the external bus bar.

8.6 Future Work

This work has shown that it is feasible to operate a smelter with non-continuous energy input. However, it has also shown that there are several areas of interest that need further work. These are outlined here.

8.6.1 Process Control of Power Modulation

Traditional process control has always assumed that heat loss from the cell is either not differing very much or not determinable anyway. With power modulation these assumptions are not valid anymore and have to be overcome. It is not sufficient to judge measured cell temperatures according to a fixed set of limits anymore. A cell operating 960 °C would have always been considered as optimum performance before.

8.6.1.1 Energy Counter

With power modulation, 960 °C at the end of a low energy period might constitute a hot cell, and at the end of a high energy period it might be considered cold.

To keep track of this, an energy counter has to be developed. The energy counter has to keep track of the energy input of the cell, as well as cell operations heavily influencing the energy content such as anode change, anode covering but also anode effects. This data is readily available from the process control system today.

It has to include the ability of a cell to shed additional heat. While this thesis showed that additional heat is lost rapidly, further investigation has to follow to understand how quickly this is happening and where the limiting boundaries are as well. For this, better understanding of varying efficiencies during operation will be necessary. Under which circumstances is the cell losing efficiency and to what extend?

Considering only the heat input as has been the case in the recent decades will not be sufficient any more. A more accurate dynamic heat balance distinguishing between process heat eventually lost from the cell and energy to produce metal has to be developed.

8.6.1.2 Heat Exchanger Process Control

If pot lines are equipped with heat exchanger technology, one other variable becomes available for process control. For the first time in process history a system will be available to variably adapt heat loss from the cell depending on both heat input and process state. This demands new guide lines on how to integrate this additional degree of freedom into existing process control strategies and process control units. Will draft of the heat exchanger be controlled on a cell to cell basis? Will the whole pot line operate with the same settings? When is draft through the heat exchanger adapted?

These are but the first questions surfacing when considering operation with a means to control heat loss. Currently Trimet Essen is installing heat exchangers on a test section with 12 cells. Start-up of the system is scheduled for the 3rd quarter of this year. It will be fascinating to open this new dimension for the process.

8.6.2 Impact on Cathode Performance

One major unknown factor when considering power modulation is the impact a varying energy state of the cell has on the life time of the lining material. One erosion mechanism for carbon cathodes discussed in the industry is the penetration, solidification and subsequent remelting of bath in the cathode. Solidification and remelting are associated with the shifting of isotherms in the cathode lining material. These are governed by the overall cell temperature.

Modulation induces repeated and more frequent swings in bath temperature when compared to normal operation. If these swings lead to a faster degradation of lining material than before, the gains from reduced energy price are offset by a significant cost increase for cell linings.

It would be devastating to a smelter if this effect would be discovered after operating on power modulation for an extended period of time. While power modulation was applied in Hamburg, no decrease in life time of the lining was experienced beyond the expected. As modulation was in conjunction with restart of the smelter and a cut and subsequent ramp up of production, there are many other influences that affected cell life besides modulation.

It would be favourable to devise a laboratory test simulating the effect of repeatedly moving isotherms in the cathode material. As the Rappaport test determines bath penetration into cathode material, this test appears to be a good starting point for developing a new testing system.

9 Bibliography

Abbe, A. and Reek, T. (2008). Internal Measurement Report on Subcathodic Temperature Measurement.

Angwafor III., J.P.C. (2000). Untersuchung zu den Auswirkungen des Energieeintrags von Aluminium-Elektrolysezellen. Mechanical Engineering. Berlin. **Dipl.-Ing. Thesis**.

Anonymous. "European Energy Exchange." from www.eex.de.

Anonymous (2010). "European Power Exchange website." European Power Exchange. Retrieved Jan 12th 2010, from www.eex.com.

Anonymous (2011). "Weltkarte / Europakarte der Industriestrompreise." VIK Verband der Industriellen Energie- und Kraftwirtschaft e.V. Retrieved 2011, from <http://www.vik.de>.

Anonymous (2012). "UAE buys four nuclear power plants." Retrieved Oct 31st 2012, from <http://weekly.ahram.org.eg/2010/981/re9.htm>.

Anonymous (2013a). "Image Library." Retrieved Dec 7th 2013, from <http://www.alcoa.com>.

Anonymous (2013b). "Klimadaten Monatswerte." Wetter und Klima - Deutscher Wetterdienst. Retrieved Oct 31st 2013, from <http://www.dwd.de>.

Anonymous (2013c). "NetElectricityGenerationAllCountriesTotal.xls." US Energy Information Administration. Retrieved Apr 14th 2013, from <http://www.eia.gov>.

Anonymous (2013d). "Primary Aluminium Production." International Aluminium Institute. Retrieved Apr 14th 2013, from <http://www.world-aluminium.org>.

Automated Systems Group (2007). "Manual of the Celtrol control system." Internal Dokumentation.

Bayer, I. (2007). Internal Cooling of Electrolytic Smelting Cell. Patent No US20070187230 A1. USA.

Beck, T. (2008, May 2008). "Electrochemistry Encyclopedia - ELECTROLYTIC PRODUCTION OF ALUMINUM <http://electrochem.cwru.edu/encycl/art-a01-al-prod.htm>." Retrieved Dec 7th 2013.

Benkahla, B., Caratini, Y., Mezin, H., Renaudier, S. and Fardeau, S. (2008). "Last development in AP50 cell." Light Metals 2008: 451-455.

Bos, J., Feve, B. and Homsy, P. (1999). Fused bath electrolysis cell for producing aluminium by hall-heroult process comprising cooling means. Patent No WO1999054526 A1.

Bos, J., Feve, B. and Homsy, P. (2001). Electrolytic pot for production of aluminum using the Hall-Héroult process comprising cooling means. Patent No US 6,251,237.

Brant Filho, A.C., Queiroz, A.A.B., Macedo, E., Pena, J.E. and Mol Santos, M.A. (1992). "The operation of a smelter with power modulation." Light Metals 1992: 357 - 362.

Bruggeman, J. (1998). Pot Heat Balance Fundamentals. 6th Australasian Aluminium Smelting Technology Conference and Workshop, Queenstown, New Zealand.

Burkin, A., Ed. (1987). Production of Aluminum and Alumina. Critical Reports on Applied Chemistry Volume 20, John Wiley & Sons,.

Cannova, F., Sadler, B. and Vitichus, B. (2007). Challenges and Opportunities for Calcined Petroleum Coke. Ninth Australasian Aluminium Smelting Technology Conference.

Chen, Z.D., Taylor, M.P. and Chen, J.J.J. (1998). "Heat Transfer on a Surface Affected by an Air/Water Interface Undergoing Wave Motion." Light Metals 1998: 429-435.

Depree, N., Agbenyegah, G., Narayanan, A., Barret, M. and Patel, P. (2012). Thermo-Electric Modelling Report. LMRC - Internal Report. Auckland, LMRC.

Droste, C. (1999). MHD Stability Report. Internal Modelling Report.

Droste, C. (2001). Simulationsberechnung zum Betrieb von System I, HAW, bei 180 kA, VAW ATG.

Eisma, D. and Patel, P. (2009). "Challenges in power modulation." Light Metals 2009: 327 - 332.

Ekeberg, L., Schaumburg-Müller, J., Laudrup, U., Schmidt, E.M., Mattila, T., Virtanen, V., Stefansson, S., Ankner, S.A., Kvinge, V.S. and Slinde, M. (2007). Capacity for Competition - Investing for an Efficient Nordic Electricity Market. N. C. Authorities.

Entner, P.M. (1998). "ElyseSem, The Electrolysis Seminar Book on Computer Screen." Alusuisse Technology & Management Ltd.

Fiot, L., Jamey, C., Backhouse, N. and Vanvoren, C. (2004). "Tomago Aluminium AP22 Project." Light Metals 2004: 173 - 178.

Fischer, W., Meier, M., Mannweiler, U. and Perruchoud, R. (2006). Anodes for the Aluminium Industry. Sierre, Switzerland, R&D Carbon.

Fraser, K.J., Taylor, M.P. and Jenkin, A.M. (1990). "Bath Heat Transfer and Mass Transport Processes in H-H Cells." Light Metals 1990.

Fresenius (2013). SGS Institut Fresenius GmbH - Analysis Report. Herlen.

Gao, Y.S., Gustafsson, M., Taylor, M.P. and Chen, J.J.J. (2007). "The control ellipse as a decision making tool to control temperature and aluminium fluoride in aluminium reduction." proceedings 9th Australasian Aluminium Smelting Conference.

Grjotheim, K. and Kvande, H., Eds. (1993). Introduction to Aluminium Electrolysis.

Hall, C.M. (1889). Process of Reducing Aluminium from Its Fluoride Salts by Electrolysis. Patent No US400,664. USA.

Haupin, W. (1956). "Polarization in an Aluminum Reduction Cell." Journal of The Electrochemical Society.

Haupin, W. (1971). "A scanning reference electrode for voltage contours in aluminum smelting cells." Journal of Metals, Vol. 23, No. 10, p.46.

Haupin, W. (1980). Fundamentals of Aluminium Production. Fundamentals of Aluminium Production. Trondheim.

HAW (1999). Internal Measurement Report on Subcathodic Temperature Measurement.

HAW (2008). Personal Communication.

Héroult, P. (1886). Proceeded electrolytic for the production of aluminium. Patent No 175 711. France.

Híveš, J., Thonstad, J., Sterten, Å. and Fellner, P. (1994). "Electrical conductivity of molten cryolite-based mixtures obtained with a tube-type cell made of pyrolytic boron nitride." Light Metals 1994: 187-194.

Hoff, R. (2011). Thermische Speicher für Solarthermische Kraftwerke: Übersicht und aktuelle Projekte. Arbeitskreis Energie der DPG. Bad Honnef.

Hume, S., Fischer, W. and Perruchoud, R. (2006). Influence of Petroleum Coke Sulphur Content on the Sodium Sensitivity of Carbon Anodes. Anodes for the Aluminium Industry. R&D Carbon. Sierre: 83-100.

Hyland, M., Patterson, E. and Welch, B. (2004). "Alumina structural hydroxyl as a continuous source of HF." Light Metals 2004: 361-366.

Iffert, M. (2008). Aluminium Smelting Cell Control and Optimisation. Sydney, UNSW. **PhD Thesis**.

Iffert, M., Kuenkel, M. and Skyllas-Kazacos, M. (2006). "Reduction in HF Emissions from the TRIMET Aluminium smelter." Light Metals 2006: 195-201.

Iffert, M., Skyllas-Kazacos, M. and Welch, B. (2005). "Challenges in mass balance control." Light Metals 2005: 385-391.

Kalban, A., Alfarsi, Y. and Meghlaoui, A. (2008). "DX TECHNOLOGY: THE DEVELOPMENT AND THE WAY FORWARD." Light Metals 2008: 383-388.

Kholklov, V.A., Filatov, E.A., Solheim, A. and Thonstad, J. (1998). "Thermal Conductivity in Cryolitic Melts - New Data and Its Influence on Heat Transfer in Aluminium Cells." Light Metals 1998: 501-506.

Krause, F., Bossel, H. and Müller-Reißmann, K. (1980). Energiewende – Wachstum und Wohlstand ohne Erdöl und Uran, S. Fischer Verlag.

Kruse, H. (2004). "German power market - Final count down for the aluminium smelters." proceedings 8th Australasian Aluminium Smelting Conference.

Kvande, H. (1983). "Vapour-phase studies of NaF-AlF₃ melts. IV: Activity data." High Temperatures. High Pressures **15**(6): 685-691.

Kyoto Electronics Manufacturing Co Ltd (2013). "Multi Point Heat Flow Meter HFM 215N."

Lavoie, P., Namboothiri, S., Dorreen, M., Chen, J.J., Zeigler, D.P. and Taylor, M.P. (2011). "Increasing the Power Modulation Window of Aluminium Smelter Pots with Shell Heat Exchanger Technology." Light Metals 2011: 367-374.

Lindsay, S. (2013). "Raw Material Impurities and The Challenges Ahead." Light Metals 2013: 5-8.

LMRC (2012). "internal correspondence."

Lützerath, A. (2012). Aluminiumproduktion in Deutschland - Chancen und Risiken. AEC Seminar, Aachen.

Lützerath, A. (2013). "High Frequency Power Modulation - TRIMET smelters provide primary control power for stabilizing the frequency in the electricity grid." Light Metals 2013: 659-662.

Martin, O., Fiot, L., Ritter, C., Santerre, R. and Vermette, H. (2009). "AP30 toward 400 kA." Light Metals 2009: 445-450.

Patterson, E.C. (2001). Fluoride Emissions from Aluminium Electrolysis Cells, The University of Auckland. **PhD Thesis**.

Perruchoud, R., Meier, M. and Fischer, W. (2006). Coke Characteristics from the Refiners to the Smelters. Anodes for the Aluminium Industry. R&D Carbon. Sierre: 35-58.

Pieper, T., Fleckenstein, H. and Rosen, M. (2007). "Das Wohl und Wehe des Windes." EMW 01-2007.

Pinheiro Leal Nunes, L.J., Vianna da Silva, A. and Soutinho, G. (1998). "Power modulation on Valesul P-19 pots." Light Metals 1998: 1267 - 1271.

Potočník, V. and Laroche, F. (2001). "Comparison of measured and calculated metal pad velocities for different prebake cell designs." Light Metals 2001: 419-425.

Reek, T. (2003). Optimierung der Steuerstrategie von Aluminiumelektrolysezellen durch Messung der Superheat. Aachen, Germany, RWTH Aachen. **Dipl.-Ing. Thesis**.

Reek, T. (2011a). "New approaches to power modulation at TRIMET Hamburg." Light Metals 2011: 375-379.

Reek, T. (2011b). A NOVEL APPROACH TO POWER MODULATION. 10th Australasian Smelter Technology Conference, Launceston, Australia.

Reek, T. (2012). Power Modulation. PostGraduate Certificate in Light Metals Reduction Technology 2012, University Auckland. Trimet Essen/Hamburg.

Reek, T. (2013). Plant data analysis Trimet Essen.

Richards, N.E. and Welch, B.J. (1964). Anodic Overpotentials and Mechanisms of the Anode Process on Carbon in Cryolite-Alumina Electrolytes. Electrochemistry Proc. 1st Australian Conference.

Rieck, T., Iffert, M., White, P., Rodrigo, R. and Kelchtermans, R. (2003). "Increased current efficiency and reduced energy consumption at the TRIMET smelter Essen using 9 Box Matrix Control." Light Metals 2003: 449 - 456.

Roine, A. (2002). HSC Chemistry 5.0 software. Outocompu.

Rolland, W.K., Furu, E., Paulsen, K.A., Bugge, M. and Tratteberg, O. (2004). "Experience with power savings in the Soederberg lines at Hydro aluminium Karmøy." Light Metals 2004: 179-183.

Rolseth, S., Verstreken, P. and Kobbeltvedt, O. (1998). "Liquidus temperature measurements in molten salts." Light Metals 1998: 359 - 366.

Schulz, T. (2012). Demand Response coming to Germany and Europe. EcoSummit 2012, Berlin.

SGL Carbon (2013). technical data sheets for cathode grades for aluminium smelting SGL Group.

Sherrod, P. (2014). "NLREG - Nonlinear Regression Analysis Program." Retrieved 25 Feb 2014, from <http://www.nlreg.com/>.

Simonsen (2012). technical data sheets for SiC side wall bricks, Simonsen.

Solheim, A. (2002). "Crystallization of Cryolite and Alumina at the Metal-Bath Interface in Aluminium Reduction Cells." Light Metals 2002: ?

Solheim, A. (2006). "TOWARDS A PROPER UNDERSTANDING OF SIDELEDGE FACING THE METAL IN ALUMINIUM CELLS?" Light Metals 2006: 439-443.

Solheim, A., Rolseth, S., Skybakmoen, E., Støen, L., Sterten, Å. and Støre, T. (1995). "Liquidus Temperature and Alumina Solubility in the System Na₃-AlF₆-AlF₃-LiF-CaF₂-MgF₂." Essential Readings in Light Metals: Aluminum Reduction Technology, Volume 2: 73-82.

Solheim, A. and Thonstad, J. (1986). Light Metals 1986: 397 - 403.

Sorlie, M. and Oye, H.A., Eds. (1994). Cathodes in Aluminium Electrolysis. Düsseldorf, Aluminium Verlag.

Sorlie, M. and Oye, H.A. (2010). Cathodes in Aluminium Electrolysis (3rd Edition). Düsseldorf, Germany, Aluminium Verlag.

Stam, M. and Schaafsma, J. (2007). "The impact of power modulation on cell dynamics." proceedings 9th Australasian Aluminium Smelting Conference.

Stam, M., Taylor, M.P., Chen, J.J.J., Mulder, A. and Rodrigo, R. (2008). "Common behaviour and abnormalities in aluminium reduction cells." Light Metals 2008: 309-314.

Stam, M., Taylor, M.P., Chen, J.J.J. and van Dellen, S. (2007). "Operational and control improvements in reduction lines at Aluminium Delfzijl." Light Metals 2007: 243-247.

Tabereaux, A. (2000). "Prebake cell technology: A global review." JOM **52**(2): 23-29.

Tabereaux, A., Alcorn, T.R. and Trembley, L. (1993). "Lithium-Modified Low Ratio Electrolyte Chemistry for Improved Performance in Modern Reduction Cells." Light Metals 1993: 221-226.

Tarcy, G.P., Kvande, H. and Tabereaux, A. (2011). "Advancing the industrial aluminum process: 20th century breakthrough inventions and developments." JOM **63**(8): 101-108.

Taylor, M.P. (2012). Dynamics of Cell Mass Balance. Post Graduate Course in Light Metal Reduction, Essen and Hamburg, Germany, LMRC.

Thibeault, P., Bécasse, S., Blais, A., Côté, P., Fiot, L. and Laflamme, F. "Rio Tinto Alcan AP4X Low Energy Cell Development." Light Metals 2013: 543-547.

Thonstad, J. (1970). "The electrode reaction on the C, CO₂ electrode in cryolite-alumina melts—I. Steady state measurements." Electrochimica Acta.

Thonstad, J., Fellner, P., Haarberg, G.M., Híveš, J., Kvannd, H. and Sterten, Å. (2001). Aluminium Electrolysis – Fundamentals of the Hall-Héroult Process. Düsseldorf, Aluminium Verlag.

Trimet (2014). "internal communication."

Utigard, T.A. (1999). "Why best pots operate between 955 and 970 °C." Light Metals 1999: 319 – 326.

Vanvoren, C., Homsí, P., Basquin, J. and Beheregaray, T. (2001a). "AP50: The Pechiney 500kA cell." Light Metals 2001: ?

Vanvoren, C., Homsí, P., Fève, B., Molinier, B. and di Giovanni, Y. (2001b). "AP35: THE LATEST HIGH PERFORMANCE INDUSTRIALLY AVAILABLE NEW CELL TECHNOLOGY." Light Metals 2001: ?

Verstreken, P. and Benninghoff, S. (1996). "Bath- and Liquidussensor for molten salts." Light Metals 1996: 437-444.

Wang, L., Tabereaux, A. and Richards, N. (1994). "The Electrical Conductivity of Molten Cryolitic Melts Containing Aluminum Carbide." Light Metals 1994: 177-184.

Wang, X., Peterson, R. and Tabereaux, A. (1993). "A multiple regression equation for the electrical conductivity of cryolitic melts." Light Metals 1993: 247-255.

Welch, B. (2010). Electrochemical Engineering. UNSW course material, Sydney, Australia.

Welch, B. (2011). THE FUTURE OF ALUMINIUM SMELTING - CONTINUE ADAPTATION OR INTRODUCE DESIGN AND OPERATING INNOVATIONS? 10th Australasian Smelter Technology Conference, Launceston, Australia.

Welch, B. (2013a). Constraints and options for reducing energy consumption in aluminium smelting. ICSOBA 2013, Krasnoyarsk, Russia.

Welch, B. (2013b). The importance of fundamental understanding for high amperage high performance cell operation. ICSOBA 2013, Krasnoyarsk, Russia.

Welch, B. and Gjortheim, K. (1988). Aluminum Smelter Technology 2nd Edition. Düsseldorf, Aluminium-Verlag.

Welch, B. and James, B. (2003). Anode Yoke Design and Stub Sizing – Some Practical and Operating Issues. 2nd International Conf. and Workshop on Anode Rodding, Reykjavik.

Welch, B.J., Ed. (2003). Aluminium Smelter Technology - Theory and Practice: unpublished revision draft of 'Aluminium Smelter technology - a pure and applied approach'. Auckland/Sydney.

Welch, B.J. (2009). "Inert Anodes - the Status of the Materials Science, the Opportunities they present and the Challenges that need resolving before Commercial Implementation." Light Metals 2009: 972-978.

Whitfield, D., Skyllas-Kazacos, M., Welch, B. and White, P. (2004). "Metal pad temperatures in aluminium reduction cells." Light Metals 2004: 239-244.

Zarouni, A., Zarouni, A., Ahli, N., Mishra, L., Kakkar, B., Spencer, D. and Reverdy, M. (2011). Dubal High Amperage Pot Technology From Dx To Dx+. 10th Australasian Smelter Technology Conference, Launceston, Australia.

Zoric, J. and Solheim, A. (2000). "On gas bubbles in industrial aluminium cells with prebaked anodes and their influence on the current distribution." Journal of applied electrochemistry **30**(7): 787-794.

Zuca, S., Herdlicka, C. and Terzi, M. (1980). "On porosity-overvoltage correlation for carbon anodes in cryolite-alumina melts." Electrochimica Acta.